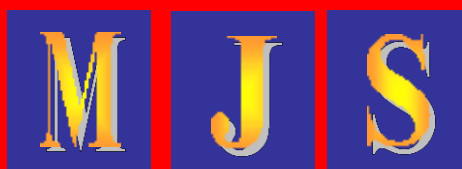


MALAYSIAN JOURNAL OF SCIENCE

Vol. 42 ● No 3 ● October 2023

JURNAL SAINS MALAYSIA



ISSN 1394 - 3065

The Malaysian Journal of Science is indexed or cited in the following Scientific Databases: Elsevier Bibliographic Databases (ACI, Scopus, EMBASE, Compendex, GEOBASE, EMBiology, Elsevier BIOBASE, FLUIDEX and World Textiles); CAB Abstracts and Chemical Abstracts Service Database

<http://www.myjournal.my/public/browse-journal-view.php?id=194>
www.mjs.um.edu.my

POLYMER-BASED IONIC CONDUCTORS

A.K.Arof^{1a}

Abstract: Polymer electrolytes consist of polymer matrices with ion transport capabilities and can exist in either a solid or gel state. In both states, the incorporation of plasticizers and fillers will enhance the ionic conductivity. Gel polymer electrolytes (GPEs) exhibit ionic conductivity levels remarkably akin to those of liquid electrolytes, owing to the direct solvation of salts within solid polymer electrolytes.

Keywords: Polymer electrolytes, gel polymer electrolytes, ionic conductivity, filler and plasticizers

1. Introduction

The term “solid state ionics” (SSI) was initially used by Takehiko Takahashi in 1967 (Yamamoto, 2017). SSI is a multi-disciplinary subject that includes various aspects of science and engineering. SSI also covers research related to charge transfer in electrolytes that are in the solid and gel states. Solid-state electrolytes comprise inorganic as well as polymer electrolytes. In this article, discussion is restricted to polymer electrolytes.

Polymer electrolytes are highly flexible films that conduct ions when acted on by an electric field. Electrode-electrolyte contact is excellent and the cost is low (Liu et al., 2020). Ion transport is achieved by means of ion hopping and segmental motion. Ionic conductivity (σ) depends on the availability of free ions (n) and ion mobility (μ) as in the equation $\sigma = n\mu e$ with e being 1.6×10^{-19} C. Solid polymer electrolytes ensures high safety (Zhang et al., 2021). However, the ionic conductivity of solid polymer electrolytes is low and they exhibit high interfacial resistance with the electrodes. Apart from these, the cycling performance is also poor (Chae & Lucht, 2023). Gel polymer electrolytes (GPEs) exhibit good flexibility, processability and ensures high safety features (Aruchamy et al., 2023). GPEs are used in devices. The possibility that the device will encounter leakage problems is slim. The device will also be thermally stable (Long et al., 2022). Poor safety and unstable electrochemical performance are some disadvantages of liquid electrolytes (Yao et al., 2019). These greatly limits its further development and wider applications.

2. Polymer Electrolytes

Authors information:

^aCenter for Ionics University Malaya, Universiti Malaya, 50603 Kuala Lumpur, MALAYSIA. E-mail: akarof@um.edu.my¹

*Corresponding Author: akarof@um.edu.my

For application as an electrolyte, a polymer must have polar groups with electron donor atoms to coordinate with cation of the salt. Ion conduction in polymer electrolytes was initially demonstrated using dye-sensitized solar cells (DSSCs) (Hagfeldt, Boschloo, Sun, Kloo, & Pettersson, 2010). In a DSSC, the electrons that make up the current are returned to the dye material by way of the reduction-oxidation (redox) reactions that occur in the electrolyte. The electrolyte electrically connects the positive and negative terminals of the solar cell.

There are many polymers used in polymer electrolyte research. These include chitosan (Arof et al., 2001; Khiar, Puteh, & Arif, 2006; Morni & Arif, 1999), poly (ethylene oxide) (Quartarone, Mustarelli, & Magistris, 1998; Yan et al., 2023), poly (vinylidene fluoride) (Zhou et al., 2023), poly (vinyl alcohol) (Moorthy, Sivasubramanian, Kannaiyan, & Deivanayagam, 2023), poly (methyl methacrylate) (S Ramesh & Arif, 2021; Uktamaliyev et al., 2023), poly (vinyl pyrrolidone) (Sangwan, Mathela, Dhapola, Singh, & Tomar, 2022), poly (caprolactone) (Li et al., 2022) and poly (vinyl chloride) (Subramaniam Ramesh & Arif, 2000). In all these polymers there are atoms with unused electrons. These electrons are not shared with other atoms from the same molecule. In chitosan and poly (vinyl pyrrolidone), the oxygen and nitrogen atoms have unused electrons. In poly (ethylene oxide) or PEO, poly (methyl methacrylate) or PMMA, poly (caprolactone) and poly (vinyl alcohol) or PVA, the oxygen atoms are the sites that contain the unused or what is also known as “lone pair” electrons. In poly (vinylidene fluoride), the unused electrons are at the fluorine atoms and in poly (vinyl chloride) at the chlorine atoms. Cations from the added salt can form “loose” bonds with atoms that contain these lone pair electrons. In the presence of an electric field, these ions will be transported to the appropriate terminal. Thus ion conduction occurs.

2.1 Types of Polymer Electrolyte

Polymer electrolytes can be divided into four groups: (i) solid, (ii) gel, (iii) plasticized and (iv) composite polymer electrolytes.

2.1.1 Solid Polymer Electrolytes (SPEs) Or Polymer-Salt Complexes

A polymer-salt complex or SPE is a solvent-free salt solution in a polymer host. An example of a solid polymer electrolyte (SPE) is 65 wt.% chitosan–35 wt.% adipic acid. Room temperature conductivity of the SPE was only $1.4 \times 10^{-7} \text{ S m}^{-1}$ (Idris, Aziz, Zambri, Zakaria, & Isa, 2009). The conductivity was attributed to protons from the acid. The protons hop from one nitrogen to the next or via the oxygen atoms in the hydroxyl groups in the polymer. As another example, consider the solid electrolyte 69 mol% PEO-23 mol% PVC-8 mol% LiBF_4 (Rajendran, Babu, & Usha Rani, 2011) that contains two types of polymers. The room temperature ion conductivity was $7.9 \times 10^{-4} \text{ S m}^{-1}$. The Li^+ ion is transported between the electrodes via hopping along the oxygen atoms in PEO and along the chlorine atoms in PVC. The availability of more active sites for ion hopping is probably the reason conductivity is able to reach the order 10^{-4} S m^{-1} .

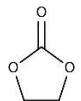
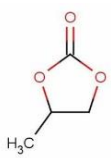
2.1.2 Gel polymer electrolyte

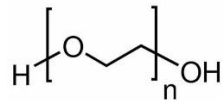
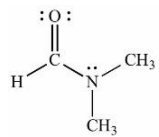
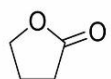
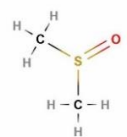
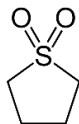
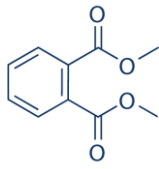
Gel polymer electrolyte (GPE) was first proposed by Feullade and Perche in 1975 (Feullade & Perche, 1975). The physical phase of a GPE is between that of solid and liquid electrolytes. Thus, the ionic conductivity of GPEs is higher than that of solid electrolytes. As stated above, GPEs are safe as leakage is less likely to occur in devices employing GPEs. It has been demonstrated that a GPE containing LiPF_6 salt exhibited a conductivity of 0.888 S m^{-1} at 25°C (Wang, Qiu, Peng, Li, & Zhai, 2017).

2.1.3 Plasticized polymer electrolyte

Plasticized polymer electrolyte is a mixture containing at least a polymer, a salt and a material that when added in the suitable amount can increase ionic conductivity. The added material that helped to increase ionic conductivity of the polymer-salt electrolyte is known as plasticizer. The plasticizer enhances ion conduction in the polymer electrolyte by weakening the interactions within and among the polymer molecules that compete with ion-polymer interactions. Some examples of plasticizers are listed in Table 1.

Table 1. Listed of common plasticizers used as additive in polymer electrolyte

Plasticizer	Molecule Structure	Molecular Weight (g mol^{-1})
Ethylene carbonate	 $(\text{CH}_2\text{O})_2\text{CO}$	88.1
Propylene carbonate	 $\text{C}_4\text{H}_6\text{O}_3$	102.1

Polyethylene glycol	 $\text{C}_2\text{H}_6\text{O}_2$	62.07
Dimethyl formamide	 $(\text{CH}_3)_2\text{NC(O)H}$	73.09
γ -butyrolactone	 $\text{C}_4\text{H}_8\text{O}_2$	164.99
Dimethyl sulfoxide	 $(\text{CH}_3)_2\text{SO}$	78.13
Sulfolane	 $\text{C}_4\text{H}_8\text{O}_2\text{S}$	120.17
Dimethyl phthalate	 $\text{C}_{10}\text{H}_{10}\text{O}_4$	194.18

The oxygen atoms in ethylene carbonate (EC) contain unused electrons just as in the atoms with unused electrons in the polymers for preparing the electrolytes. It is to be noted that plasticizers do not bond covalently with the polymer chain. With the addition of plasticizer such as EC, the cation of the salt has more transit sites to move or hop along the electrolyte. The energy required by the cations, i.e. the activation energy to hop along the electrolyte in the absence of EC is more than the activation energy of the cations in electrolytes containing plasticizers (Banitaba, Semnani, Heydari-Soureshjani, Rezaei, & Ensafi, 2020). Activation energy is the minimum energy required by the cations to hop from one site to another in an electrolyte. The activation energy can be obtained from the gradient of the $\ln(\sigma T)$ versus $1000/T$, which is known as the Arrhenius plot. Here T is absolute temperature. In the Arrhenius plot for the GPE with tetrabutyl ammonium iodide (TBAI) salt, the lowest activation energy is $\sim 13 \text{ kJ mol}^{-1}$ (Chowdhury et al., 2020). This was the highest conducting sample.

Since plasticizers can weaken the forces within and between the polymer chains, they make the polymer electrolyte films less rigid, more amorphous and more salt can be dissociated in the electrolytes. The glass transition temperature is also reduced (Storck, Dotter, Brockhagen, & Grothe, 2020). With increase in salt dissociation, more free ions will be available. The presence of more free ions will increase ion conductivity. Although plasticizer addition can increase ion conductivity, it also lowers the mechanical strength of the electrolyte.

Polymer electrolytes utilizing plasticized polyacrylonitrile (PAN) have demonstrated impressive ion conductivity levels exceeding 10^{-3} S cm^{-1} at a temperature of 30 °C (Singh et al., 2020). In this study, the researchers employed propylene carbonate (PC) as the plasticizing agent, resulting in a notable ionic conductivity of 0.328 S cm^{-1} for PAN-Mg(ClO₄)₂-PC.

2.1.4 Composite polymer electrolytes (CPEs)

CPEs contain inorganic fillers, which are typically ceramic materials. Examples of these inorganic fillers are Al₂O₃ (Kotobuki, 2020), BaTiO₃ (Sadiq, Arya, Ali, Singh, & Sharma, 2020), CeO₂ (Augustine, Zahid, Hasan, Dalvi, & Jacob, 2020), ZrO₂ (Xiao, Song, Huang, Yang, & Qiao, 2020), TiO₂ (Ruiz Gómez, Mina Hernández, & Diosa Astaiza, 2020), SiO₂ (Lyu, He, & Liu, 2020), ZnO (Chan et al., 2018), carbon nanotubes (Alateyah, 2019) and boehmite (AlOOH) nanoparticles (Meera & Ramesan, 2022). They have high dielectric constants that can enhance ion conductivity by preventing the formation of ion-pairs and ion-triplets in the electrolyte. Boehmite is a crystalline mineral that contains Al₂O₃ and Al(OH)₃. Boehmite is found in bauxite. The addition of inorganic filler is effective in increasing the amorphousness and segmental motion of a polymer electrolyte and improves mobility of the Li⁺ cation (Lyu et al., 2020) and hence cationic conductivity. The increase in amorphousness creates the formation of more ionic conductivity pathways in the polymer matrix. T_g of the polymer phase also decreased (Fu, Li, Zhou, & Guo, 2022). The addition of fillers only lead to conductivity enhancement up to a maximum concentration. Beyond the maximum filler concentration, the conductivity shows a decrease.

In all the electrolytes described above, the conductivity is observed to decrease after a maximum value is attained at a particular salt, plasticizer or filler concentration. When the quantity of these materials is increased, there will be more charge carrying ions and the conductivity is observed to increase. If the number of ions has increased above a certain concentration, conductivity decreased. This is because, above a certain concentration of these materials, the ions will be closer together and begin to interact with each other leading to recombination. Thus, although more salt, plasticizer or filler is added, there will be less free ion concentration, and this led to the decrease in ionic conductivity.

3. Conclusion

In this article we have shown how the conductivity of a polymer electrolyte can be maximized. Conductivity can be increased by adding the right amount of salt concentration, using more than one polymer, gelling the electrolyte and adding plasticizers and fillers.

4. References

- Alateyah, A. (2019). High-Density Polyethylene Based on Exfoliated Graphite Nanoplatelets/Nano-Magnesium Oxide: An Investigation of Thermal Properties and Morphology. *Materials Sciences and Applications*, 10, 159-169. doi:10.4236/msa.2019.103013
- Arof, A. K., Osman, Z., Morni, N., Kamarulzaman, N., Ibrahim, Z., & Muhamad, M. (2001). Chitosan-based electrolyte for secondary lithium cells. *Journal of materials science*, 36, 791-793.
- Aruchamy, K., Ramasundaram, S., Divya, S., Chandran, M., Yun, K., & Oh, T. H. (2023). Gel Polymer Electrolytes: Advancing Solid-State Batteries for High-Performance Applications. *Gels*, 9(7), 585.
- Augustine, R., Zahid, A. A., Hasan, A., Dalvi, Y. B., & Jacob, J. (2020). Cerium oxide nanoparticle-loaded gelatin methacryloyl hydrogel wound-healing patch with free radical scavenging activity. *ACS Biomaterials Science & Engineering*, 7(1), 279-290.
- Banitaba, S. N., Semnani, D., Heydari-Soureshjani, E., Rezaei, B., & Ensafi, A. A. (2020). The effect of concentration and ratio of ethylene carbonate and propylene carbonate plasticizers on characteristics of the electrospun PEO-based electrolytes applicable in lithium-ion batteries. *Solid State Ionics*, 347, 115252.
- Chae, O. B., & Lucht, B. L. (2023). Interfacial issues and modification of solid electrolyte interphase for Li metal anode in liquid and solid electrolytes. *Advanced Energy Materials*, 13(14), 2203791.
- Chan, X. H., Khanmirzaei, M. H., Omar, F. S., Ramesh, K., Ramesh, S., & Ramesh, S. (2018). Enhanced efficiency in dye-sensitized solar cell based on zinc oxide-modified poly(ethylene oxide) gel electrolyte. *Ionics*, 24(4), 1221-1226. doi:10.1007/s11581-017-2271-y
- Chowdhury, F. I., Khalil, I., Khandaker, M., Rabbani, M., Uddin, J., & Arof, A. (2020). Electrochemical and structural characterization of polyacrylonitrile (PAN)-based gel polymer electrolytes blended with tetrabutylammonium iodide for possible application in dye-sensitized solar cells. *Ionics*, 26(9), 4737-4746.
- Feuillade, G., & Perche, P. (1975). Ion-conductive macromolecular gels and membranes for solid lithium cells. *Journal of Applied Electrochemistry*, 5, 63-69.
- Fu, J., Li, Z., Zhou, X., & Guo, X. (2022). Ion transport in composite polymer electrolytes. *Materials Advances*, 3(9), 3809-3819. doi:10.1039/D2MA00215A

- Hagfeldt, A., Boschloo, G., Sun, L., Kloo, L., & Pettersson, H. (2010). Dye-sensitized solar cells. *Chemical Reviews*, *110*(11), 6595-6663.
- Idris, N. K., Aziz, N. A. N., Zambri, M. S. M., Zakaria, N. A., & Isa, M. I. N. (2009). Ionic conductivity studies of chitosan-based polymer electrolytes doped with adipic acid. *Ionics*, *15*(5), 643-646. doi:10.1007/s11581-009-0318-4
- Khair, A., Puteh, R., & Arof, A. (2006). Conductivity studies of a chitosan-based polymer electrolyte. *Physica B: Condensed Matter*, *373*(1), 23-27.
- Kotobuki, M. (2020). Polymer Electrolytes. *Polymer Electrolytes: Characterization Techniques and Energy Applications*, 1-21.
- Li, Y., Wang, F., Huang, B., Huang, C., Pei, D., Liu, Z., . . . Jin, H. (2022). A high power density solid electrolyte based on polycaprolactone for high-performance all-solid-state flexible lithium batteries. *Electrochimica Acta*, *424*, 140624.
- Liu, M., Wang, Y., Li, M., Li, G., Li, B., Zhang, S., . . . Zhao, P. (2020). A new composite gel polymer electrolyte based on matrix of PEGDA with high ionic conductivity for lithium-ion batteries. *Electrochimica Acta*, *354*, 136622.
- Long, M.-C., Wang, T., Duan, P.-H., Gao, Y., Wang, X.-L., Wu, G., & Wang, Y.-Z. (2022). Thermotolerant and fireproof gel polymer electrolyte toward high-performance and safe lithium-ion battery. *Journal of Energy Chemistry*, *65*, 9-18.
- Lyu, W., He, G., & Liu, T. (2020). PEO-LITFSI-SiO₂-SN System Promotes the Application of Polymer Electrolytes in All-Solid-State Lithium-ion Batteries. *ChemistryOpen*, *9*(6), 713-718.
- Meera, K., & Ramesan, M. T. (2022). Performance of Boehmite Nanoparticles Reinforced Carboxymethyl Chitosan/Polyvinyl Alcohol Blend Nanocomposites Tailored Through Green Synthesis. *Journal of Polymers and the Environment*, *31*, 1-14. doi:10.1007/s10924-022-02649-1
- Moorthy, S., Sivasubramanian, G., Kannaiyan, D., & Deivanayagam, P. (2023). Neoteric advancements in polybenzimidazole based polymer electrolytes for high-temperature proton exchange membrane fuel cells-A versatile review. *International Journal of Hydrogen Energy*.
- Morni, N., & Arof, A. (1999). Chitosan-lithium triflate electrolyte in secondary lithium cells. *Journal of Power sources*, *77*(1), 42-48.
- Quartarone, E., Mustarelli, P., & Magistris, A. (1998). PEO-based composite polymer electrolytes. *Solid State Ionics*, *110*(1-2), 1-14.
- Rajendran, S., Babu, R. S., & Usha Rani, M. (2011). Effect of complexing salt on conductivity of PVC/PEO polymer blend electrolytes. *Bulletin of Materials Science*, *34*, 1525-1530.
- Ramesh, S., & Arof, A. (2021). PMMA-LiTFSI based gel polymer electrolyte for lithium-oxygen cell application. *Optical Materials*, *120*, 111418.
- Ramesh, S., & Arof, A. K. (2000). Electrical conductivity studies of polyvinyl chloride-based electrolytes with double salt system. *Solid State Ionics*, *136*, 1197-1200.
- Ruiz Gómez, E. E., Mina Hernández, J. H., & Dios Astaiza, J. E. (2020). Development of a Chitosan/PVA/TiO₂ nanocomposite for application as a solid polymeric electrolyte in fuel cells. *Polymers*, *12*(8), 1691.
- Sadiq, M., Arya, A., Ali, J., Singh, N. P., & Sharma, A. (2020). Electrical conductivity and dielectric properties of solid polymer nanocomposite films: Effect of BaTiO₃ nanofiller. *Materials Today: Proceedings*, *32*, 476-482.
- Sangwan, B., Mathela, S., Dhapola, P. S., Singh, P. K., & Tomar, R. (2022). Ionic liquid incorporated polyvinylpyrrolidone (PVP) doped with ammonium iodide (NH₄I) doped solid polymer electrolyte for energy device. *Materials Today: Proceedings*, *49*, 3306-3309.
- Singh, R., Janakiraman, S., Khalifa, M., Anandhan, S., Ghosh, S., Venimadhav, A., & Biswas, K. (2020). A high thermally stable polyacrylonitrile (PAN)-based gel polymer electrolyte for rechargeable Mg-ion battery. *Journal of Materials Science: Materials in Electronics*, *31*, 22912-22925.
- Storck, J. L., Dotter, M., Brockhagen, B., & Grothe, T. (2020). Evaluation of novel glycerol/PEO gel polymer electrolytes for non-toxic dye-sensitized solar cells with natural dyes regarding long-term stability and reproducibility. *Crystals*, *10*(12), 1158.
- Uktamaliyev, B., Kufian, M., Abdulkarimov, A., Harudin, N., Mamatkarimov, O., Abidin, Z., . . . Arof, A. (2023). Determination of transport properties for polymer electrolytes containing LiTf and MgTf₂ salts. *Molecular Crystals and Liquid Crystals*, 1-11.
- Wang, Y., Qiu, J., Peng, J., Li, J., & Zhai, M. (2017). One-step radiation synthesis of gel polymer electrolytes with high ionic conductivity for lithium-ion batteries. *Journal of Materials Chemistry A*, *5*(24), 12393-12399.
- Xiao, W., Song, J., Huang, L., Yang, Z., & Qiao, Q. (2020). PVA-ZrO₂ multilayer composite separator with enhanced electrolyte property and mechanical strength for lithium-ion batteries. *Ceramics International*, *46*(18), 29212-29221.
- Yamamoto, O. (2017). Solid state ionics: a Japan perspective. *Science and Technology of advanced Materials*, *18*(1), 504-527.
- Yan, H., Wang, T., Liu, L., Song, T., Li, C., Sun, L., . . . Dai, Y. (2023). High voltage stable cycling of all-solid-state lithium metal batteries enabled by top-down direct fluorinated poly(ethylene oxide)-based electrolytes. *Journal of Power sources*, *557*, 232559.
- Yao, P., Yu, H., Ding, Z., Liu, Y., Lu, J., Lavorgna, M., . . . Liu, X. (2019). Review on polymer-based composite electrolytes for lithium batteries. *Frontiers in chemistry*, *7*, 522.
- Zhang, D., Li, L., Wu, X., Wang, J., Li, Q., Pan, K., & He, J. (2021). Research progress and application of PEO-based solid state polymer composite electrolytes. *Frontiers in Energy Research*, *9*, 726738.
- Zhou, S., Zhong, S., Dong, Y., Liu, Z., Dong, L., Yuan, B., . . . Han, J. (2023). Composition and Structure Design of Poly(vinylidene fluoride)-Based Solid Polymer Electrolytes for Lithium Batteries. *Advanced Functional Materials*, *33*(20), 2214432.

A COMPUTATIONAL DENSITY FUNCTIONAL THEORY INVESTIGATION OF THE INTERACTION OF BORON NITRIDE NANOSHEETS WITH MULTIPLE MOLECULAR HYDROGENS

Pek-Lan Toh^{1a*}, Syed Amir Abbas Shah Naqvi^{2a}, Suh-Miin Wang^{3a}, Yao-Cong Lim^{4a}, Lee-Sin Ang^{5b} and Lan-Ching^{6c}

Abstract: In this study, the adsorption of molecular hydrogens (H₂) on boron nitride (BN) frameworks was investigated using the density functional theory (DFT) technique. The results of optimized geometric structures revealed that molecular hydrogens were favourably adsorbed on top of nitrogen atoms in the BN monolayers. In addition, the optimized equilibrium geometries were utilized to calculate the electronic structures, including binding energies, energies of the highest and lowest occupied molecular orbitals (HOMO and LUMO), molecular electrostatic potentials (MEPs), and Mulliken atomic charges (MACs). The binding energy values were calculated to be approximately 0.01 eV per molecular hydrogen based on the results. As the number of molecular hydrogens increased in the BN framework, a slight increase was observed in the binding energy value per hydrogen molecule. Furthermore, the HOMO–LUMO gaps were determined with the corresponding energy values of about 6 eV. Regarding the Frontier molecular orbitals (FMOs) diagrams, the electron densities for the HOMOs of the studied systems were primarily focused on the N-edges. Conversely, for the LUMO, the electron density distribution was localized in the B-edges of titled systems. In the context of hydrogen adsorption on BN nanosheets, the MEP maps indicated that hydrogen atoms at the N-edges of the studied systems exhibited the most positive electrostatic potentials in this research. In contrast, surfaces with negative electrostatic potential surfaces were situated in the region close to B-edges. The computed results are consistent with the corresponding Mulliken atomic charge distributions. From the analyses of the Mulliken scheme, all nitrogen atoms displayed negative charge values, and positive charges were found on the boron atoms. The DFT results obtained in this report may serve as the foundation for developing hydrogen storage materials..

Keywords: Density functional theory, boron nitride frameworks, hydrogen molecules, electronic structures

1. Introduction

Boron nitride (BN) is an inorganic compound composed of equal numbers of nitrogen (N) and boron (B) atoms (Mukasyan, 2017). According to literature studies, BN finds significant use in electronic and optoelectronic devices (Izyumskaya et al., 2017; Gonzalez–Ortiz, 2020). For instance, Izyumskaya et al. (2017) summarized an overview of the structural and physical properties of various polymorphs of BNs. Four crystal phase forms of BN exist cubic, hexagonal, wurtzite, and rhombohedral. Among these, hexagonal boron nitride (h-BN) stands out due to its wide bandgap energy, rendering it increasingly attractive for electronic and optoelectronic applications. Recent years have witnessed a growing interest in exploring the applications of BNs due to their

unique chemical and physical structures, including excellent thermal shock resistance, low toxicity, favourable dielectric properties, high hydrogen storage capacity, and more (Izyumskaya et al., 2017; Gonzalez–Ortiz, 2020). In 2020, Gonzalez–Ortiz et al. discussed ongoing advancements in optimal synthesis methods and applications of BN-based materials. Their work presented four synthesis methods of BN-based nanostructured materials: in situ intercalative polymerization, melt-intercalation, solvent mixing, and template synthesis.

Numerous experimental studies have been conducted on BN nanomaterials (Kannan et al., 2013; Ansaloni & Sousa, 2013). For example, Kannan et al. (2013) employed a novel combustion synthesis method, glycine-nitrate, to synthesize h-BN crystals. For this purpose, they utilized Fourier transform infrared (FT-IR) spectroscopy and X-ray powder diffraction (XRD) to identify and characterize the h-BN compounds. Their experimental findings revealed the successful production of pure h-BN, which holds promise for high–temperature applications. Similarly, Ansaloni and Sousa, in the same year, synthesized and characterized the h-BN nanostructured sample. Their findings indicated that h-BN nanomaterial could be obtained through high–temperature treatment at 1600 °C. Notably, h-Bn nanostructures exhibit

Authors information:

^aFaculty of Engineering and Green Technology, Universiti Tunku Abdul Rahman, 31900 Kampar, Perak, MALAYSIA. E-mail: tohpl@utar.edu.my;

syedamirnaqvi.51214@1utar.my;

wangsm456@1utar.my; yaocong61@1utar.my

^bFakulti Sains Gunaan, Universiti Teknologi MARA Cawangan Perlis, MALAYSIA. E-mail: anglee631@uitm.edu.my

^cLee Kong Chian Faculty of Engineering and Science, Universiti Tunku Abdul Rahman, 43200 Kajang, MALAYSIA. E-mail: simcl@utar.edu.my

*Corresponding Author: tohpl@utar.edu.my

Received: May 17, 2022

Accepted: September 6, 2022

Published: October 31, 2023

potential for future applications in the cosmetic industry, particularly in sunscreen products.

Among other initial studies, density functional theory (DFT) is one of the most widely used computational methods in recent years. Numerous DFT studies have been conducted to explore the electronic structures of BN systems (Roohi et al., 2010; Esrafil & Behzadi, 2012; Seyed-Talebi & Neek-Amal, 2014; Denis & Iribarne, 2019; Shuaibu et al., 2019; Toh & Wang, 2019). For example, Roohi et al. (2010) reported on the geometric structures and electronic properties of CH₃CO molecules absorbed on the various surface sites of boron nitride nanotubes (BNNTs) at B3LYP/6-31G* level of theory. The DFT calculations indicated a preference for CH₃CO molecules to absorb perpendicularly on the outer surfaces of BNNTs. In 2012, Esrafil and Behzadi presented the structural and electronic properties of carbon-doped BNNT using DFT/B3LYP/6-31G* level of calculation. In the context of carbon-doped BNNT, the obtained HOMO-LUMO energies were smaller than those of pure BNNT framework. Similarly, in 2014, Seyed-Talebi and Neek-Amal studied the absorption of methane molecules on the surfaces of BN and graphene sheets using B3LYP/6-31G* calculation. Computational results suggested a higher likelihood for methane molecules to absorb onto the surface of the BN monolayer than graphene. Similar findings were reported by Denis and Iribarne (2019). They investigated the adsorption of aryl, benzynes, ethyne, ethane, and azomethine on the surfaces of graphene and BN nanosheets using DFT/M06-L/6-31G* level of theory. The results for binding energy (BE) revealed a greater propensity for aryl, benzynes, ethyne, ethane, and azomethine molecules to absorb onto the BN system's surface rather than that of graphene. In the same year, Shuaibu et al. reported the elastic properties and electronic structures of h-BN monolayers through computational DFT investigations implemented in the Quantum-ESPRESSO program package. The computed findings identified a narrow band from the band structure calculations for the single layer of h-BN.

Furthermore, all elastic modulus constants, including shear strength and Young's modulus, strongly concur with the existing literature data. In 2019, Toh and Wang conducted computational studies on the structural and electronic structures of the h-BN nanosheet using the DFT technique, which was implemented within the Gaussian 09 software suite. They observed that the computed HOMO-LUMO energy gaps are about 6.0 eV - 7.7 eV, using B3LYP functional and four different basis sets. These energy values of HOMO-LUMO gaps were in excellent agreement with available experimental and computational data from prior studies

(Oku, 2015; Lale et al., 2018; Chettri et al., 2021). In addition, Shah-Naqvi et al. (2022) also studied the structural and electronic properties of h-BN monolayers doped with or without group IV elements, i.e., carbon (C), silicon (Si), and germanium (Ge) atoms. The DFT results presented that the germanium-substituted BN system has the highest stability among all consideration BN frameworks.

In recent years, the literature on hydrogen storage materials has significantly increased in experimental and computational studies. This surge in research is attributed to hydrogen being a clean and renewable energy source. For example, using the DFT technique, Chettri et al. (2021) investigated the hydrogen storage capacity of monolayer h-BN nanosheets. The computed results indicated that the maximum hydrogen gravimetric density obtained in the studied h-BN nanosheet is about 6.7%, slightly higher than the Department of Energy (DOE) hydrogen storage targets of 6.0%. Therefore, numerous researchers have been interested in hydrogen as an energy source due to the growing role of hydrogen energy storage systems in future energy solutions, especially in transport, industry, cosmetics, and other sectors. From a literature survey, numerous studies have examined the technical and economic aspects of hydrogen energy systems (Oku, 2015; Lale et al., 2018). In 2015, Oku synthesized BN nanotubes, nano capsules, and nanocages and analysed their hydrogen storage capacity using thermogravimetric analysis (TGA). The experiment revealed that the BN nanostructures could only store hydrogen up to about 3 wt %.

Furthermore, semi-empirical molecular orbital calculations were conducted on the BN nanomaterials, yielding computed results that reported a hydrogen gravimetric capacity of approximately 6.5 wt%, in agreement with the DOE's target value. Lale et al. (2018) summarized BN nanostructures' potential for molecular hydrogen storage using the DFT technique, finding that among BN structures, the oxygen-doped BN nanosheet exhibits excellent material properties, providing the highest hydrogen storage capacity (about 5.8 wt%) in the literature survey. In 2021, Shah-Naqvi et al. reported a computational DFT investigation of two molecular hydrogen molecules adsorbed on the surfaces of BN nanostructures doped with or without group IV elements. The calculated binding energies of all the studied structures in the work were approximately 0.01 eV - 0.05 eV per molecular hydrogen. Motivated by the recent experimental and theoretical progress, conducting a computational DFT investigation into the adsorption of varying numbers of molecular hydrogens (H₂) onto boron nitride (BN) nanosheets is of great interest in this study.

2. Computational Methodology

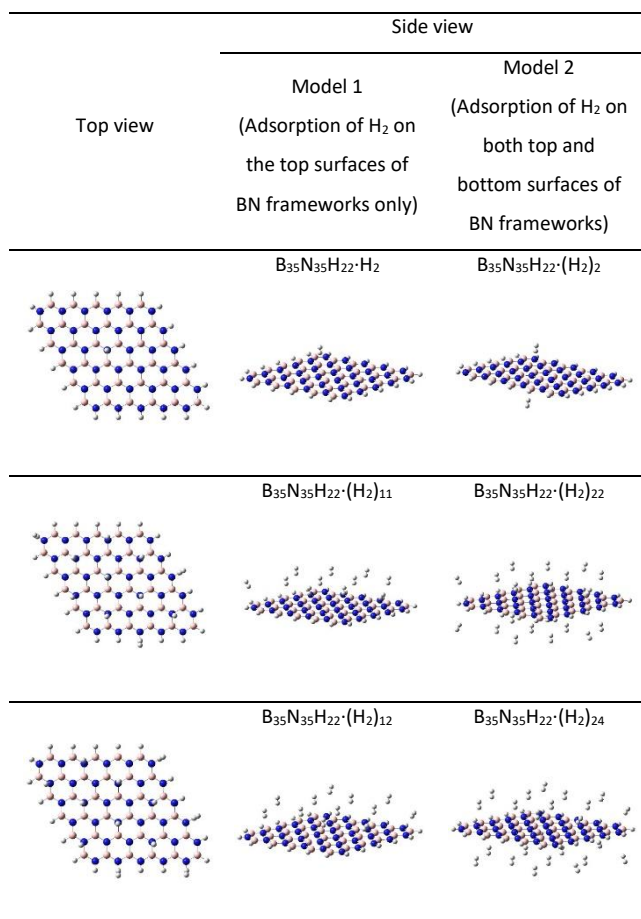


Figure 1. Top and side views for the adsorption of molecular hydrogens on the surfaces of BN monolayers.

All first principle DFT-based calculations were conducted using the Gaussian 09 software program (Frisch et al., 2016). Initially, the BN nanomaterial was selected for the study. Due to the absence of periodic boundary conditions in the DFT calculations, hydrogen (H) atoms were added to saturate the dangling bonds of B and N atoms in the BN structure (Zheng et al., 2011). Consequently, the cluster model of boron nitride B₃₅N₃₅H₂₂ was chosen as the local environment for this study. The molecular hydrogens (H₂) were also introduced to the surfaces of BN nanosheets. There are two H₂ adsorption configuration models employed in this study. Model 1 allows hydrogen molecules to adsorb solely on the BN sheets' top surfaces (one side). Conversely, model 2 assumes that the adsorption of molecular hydrogens on both surfaces (i.e., top and bottom sides) of BN monolayers. For both models (i.e., models 1 and 2), the H₂ molecules were sequentially added until the respective BN models reached their maximum H₂ capacity. Due to issues with self-consistent field convergence (SCF) in this work, geometry optimization calculations were employed to determine the

precise locations of H₂ molecules adsorption on the BN nanostructures at the DFT/B3LYP/6–31G level of theory.

Figure 1 illustrates three numbers of H₂ molecules (designated as 1, 11, and 12 in model 1) being adsorbed onto the top surfaces of BN frameworks. Additionally, three sets of molecular hydrogens (numbered 2, 22, and 24 in model 2) were placed on BN nanostructures' top and bottom surfaces. Single-point calculations were performed at the B3LYP/6–31G* level of theory to achieve more accurate energy levels. The equilibrium geometric structures resulting from the adsorption of H₂ molecules onto the studied BN systems were subsequently utilized to determine binding energies and various other electronic properties, including Frontier molecular orbitals (FMOs), molecular electrostatic potentials (MEPs), and others.

3. Results and Discussions

In this study, the DFT technique is utilized to investigate the adsorption of hydrogen molecules on BN surfaces. Analysing the equilibrium structures of H₂ molecules adsorbed onto BN, as depicted in Figure 1, the computational results reveal optimized B–N bond lengths ranging from approximately 1.42 Å – 1.46 Å. These bond distances of BN closely align with experimental and previous theoretical findings (Anota et al., 2013; Thomas et al., 2020). Moreover, the results of the DFT calculations demonstrate a preference for hydrogen molecule adsorption on top of the nitrogen atoms. The molecular hydrogens are adsorbed to the surfaces of BN structures, with corresponding equilibrium distance ranging from 3.23 Å to 3.26 Å. The calculated H–H bond distances for hydrogen molecules in this study average around 0.74 Å.

Table 1 presents the binding energies of six numbers of H₂ (i.e., 1, 2, 11, 12, 22, and 24) adsorbed onto the surfaces of BN monolayers, yielding values around about 0.01 eV. In addition, the DFT results reveal that the computed binding energies of BN frameworks are found depending on the quantity of adsorbed molecular hydrogen. In model 1, the binding energies follow this sequence: B₃₅N₃₅H₂₂·H₂ > B₃₅N₃₅H₂₂·(H₂)₁₁ > B₃₅N₃₅H₂₂·(H₂)₁₂. Similarly, in model 2, the order is as follows: B₃₅N₃₅H₂₂·(H₂)₂ > B₃₅N₃₅H₂₂·(H₂)₂₂ > B₃₅N₃₅H₂₂·(H₂)₂₄. Nevertheless, the computed binding energy values remain notably lower than the literature data (Chettri et al., 2021).

Table 1. Optimized hydrogen binding, BSSE, and Frontier molecular orbital energies (in eV) of BN nanostructures with the six numbers of molecular hydrogens.

Numbers of hydrogen molecules	Model 1			Model 2		
	B ₃₅ N ₃₅ H ₂₂ ·H ₂	B ₃₅ N ₃₅ H ₂₂ ·(H ₂) ₁₁	B ₃₅ N ₃₅ H ₂₂ ·(H ₂) ₁₂	B ₃₅ N ₃₅ H ₂₂ ·(H ₂) ₂	B ₃₅ N ₃₅ H ₂₂ ·(H ₂) ₂₂	B ₃₅ N ₃₅ H ₂₂ ·(H ₂) ₂₄
Binding energy	0.0085	0.0077	0.0074	0.0085	0.0078	0.0074
BSSE	0.0135	0.1759	0.2011	0.0269	0.3476	0.3962
HOMO	-6.3147	-6.3544	-6.3781	-6.3158	-6.3917	-6.4325
LUMO	-0.3146	-0.3491	-0.3475	-0.3154	-0.3826	-0.3793
HOMO–LUMO energy	6.0001	6.0053	6.0306	6.0004	6.0091	6.0532

In Table 1, the HOMO–LUMO energies are determined to range between 6.00 eV – 6.05 eV. In the case of model 1, the HOMO–LUMO energy values exhibit an increase in the order as follows: B₃₅N₃₅H₂₂·H₂ < B₃₅N₃₅H₂₂·(H₂)₁₁ < B₃₅N₃₅H₂₂·(H₂)₁₂. A similar pattern is observed in model 2, where the energy gap of HOMO–LUMO follows this progression: B₃₅N₃₅H₂₂·(H₂)₂ < B₃₅N₃₅H₂₂·(H₂)₂₂ < B₃₅N₃₅H₂₂·(H₂)₂₄. Overall, as the number of molecular hydrogens in the investigated BN systems increases, there is a minimal alteration in the HOMO–LUMO energy values. The minimal alteration is attributed to the relatively modest interaction between the 1s-orbital of H and 2p_z-orbitals of B and N atoms within the studied systems (Thomas et al., 2020).

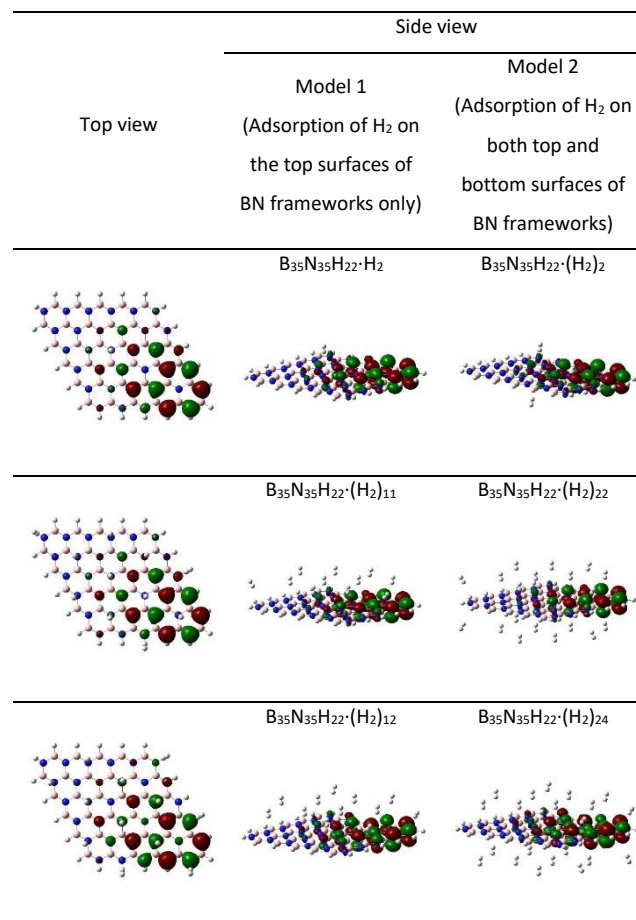


Figure 2. The diagrams of HOMO molecular orbitals for the various numbers of H₂ molecules absorbed on the surfaces of BN models.

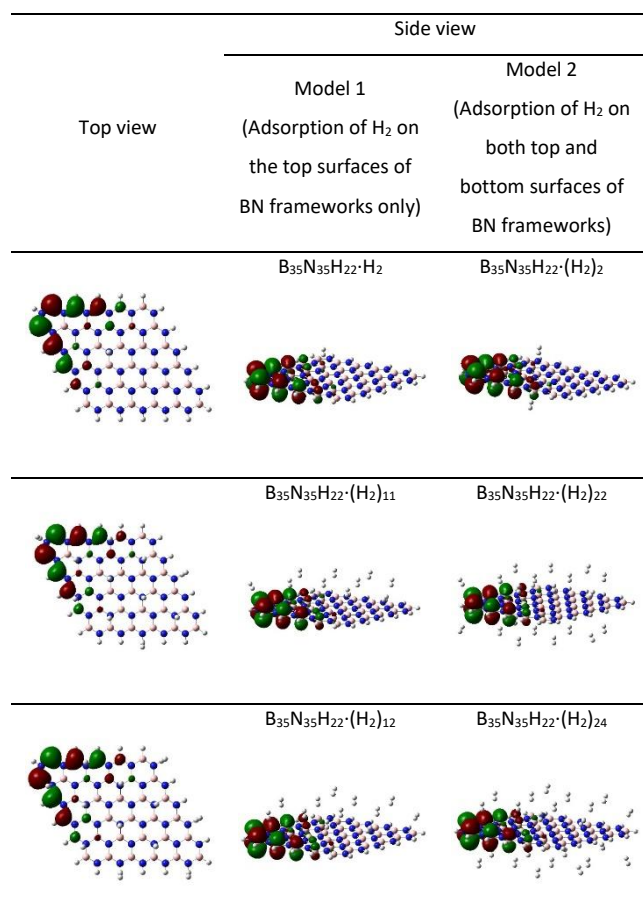


Figure 3. The molecular orbital diagrams of LUMOs for the adsorption of H₂ molecules on the surfaces of BN monolayers.

Thus, these HOMO–LUMO gap values closely resemble the bandgap obtained from previous literature studies (Toh & Wang, 2019; Chettri et al., 2021). To understand the adsorption interaction between molecular hydrogens and BN frameworks, the surface diagrams of the Frontier molecular orbitals of H₂ molecules adsorbed onto BN nanostructures are depicted in Figures 2 and 3. Our findings indicate that the distributions of Frontier molecular orbitals exhibit nearly identical patterns across all examined BN models (i.e., B₃₅N₃₅H₂₂·H₂, B₃₅N₃₅H₂₂·(H₂)₂, B₃₅N₃₅H₂₂·(H₂)₁₁, B₃₅N₃₅H₂₂·(H₂)₁₂, B₃₅N₃₅H₂₂·(H₂)₂₂, and B₃₅N₃₅H₂₂·(H₂)₂₄). The electron densities of HOMO orbitals, as shown in Figure 2, are localized in the N–edges of the studied BN systems. Conversely, for the LUMO orbitals illustrated in Figure 3,

the electron density distribution predominantly centers around the B–edges. The HOMO predominantly exhibits p–character, originating from the p_z–orbitals of nitrogen atoms, while the LUMO primarily comprises p_z–orbitals from boron atoms at the edges. The results align with the findings presented by Javan et al. (2017). However, our findings explicitly indicate that an increase in the number of molecular hydrogens results in a minor but significant interaction between the 1s–orbital of H and 2p_z–orbitals of B and N atoms within the studied BN systems (Anota et al., 2013).

Based on the Mulliken population analysis (MPA) shown in Figure 4, it is evident that the calculated results distribute negative charges (ranging from -0.626 a.u. and -0.434 a.u.) onto the nitrogen atoms within the BN frameworks. In contrast, the boron atoms exhibit notable high positive charges (falling within the range of +0.282 a.u. to +0.500 a.u.). In addition, the Mulliken scheme attributes both the positive and negative charge values to the hydrogen atoms, which depends on their localized bonding environment within the studied frameworks. Notably, the hydrogen atoms positioned at N–edges carry stronger positive charges (approximately +0.3 a.u.) than those at B–edges, which hold negative charges (approximately -0.05). It is also important to mention that neutral hydrogen molecules are obtained in this study. The distributions of MEPs for BN nanosheets hosting multiple hydrogen molecules are illustrated in Figure 5 to clarify the rationale behind this improvement. The MEP diagrams exhibit nearly identical map surfaces. This similarity stems from the minimal charge transfer from the BN framework to molecular hydrogens.

Additionally, the computed results indicate that the most positive electrostatic resides near nitrogen atoms, while the negative electrostatic potential is localized near B–edges. These computed findings align with the literature study conducted by Esrafil and Behzadi (2013). With these observations, the results obtained in this study hold great promise in guiding future investigations into single–wall or multi–wall boron nitride nanotube (BNNT) systems.

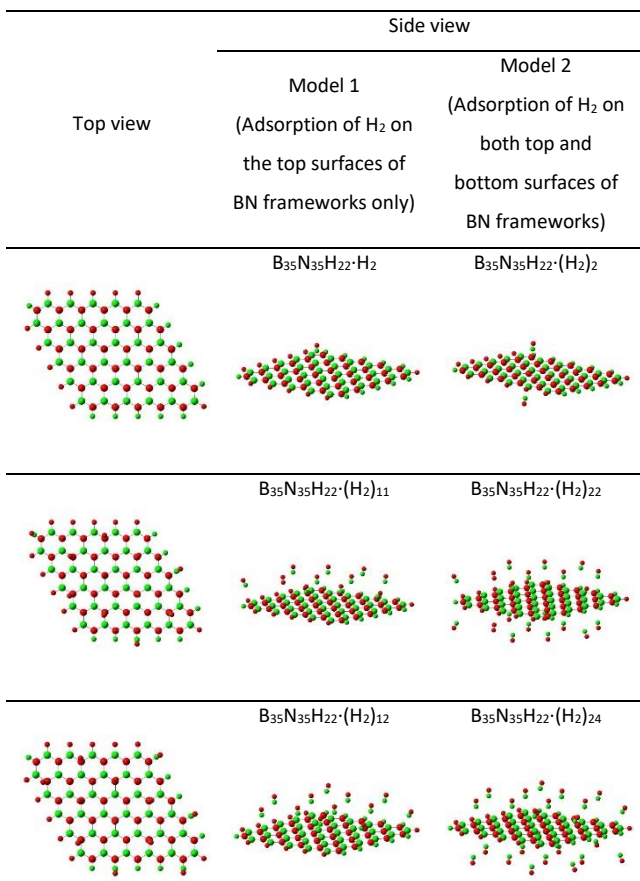


Figure 4. The distributions of Mulliken atomic charges for the various numbers of molecular hydrogens adsorbed on the surfaces of BN sheets.

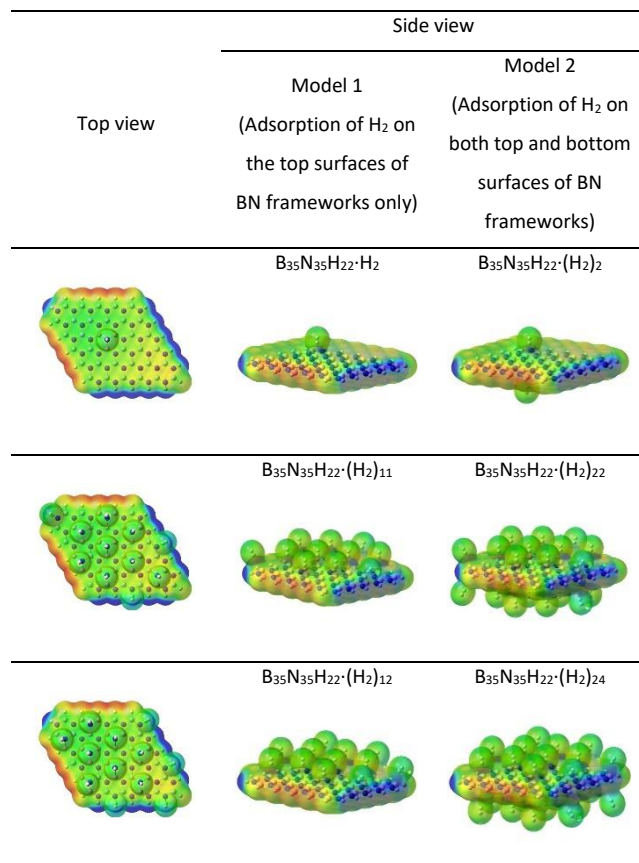


Figure 5. Computed molecular electrostatic potential surface plots for the adsorption of molecular hydrogens on the surfaces of BN nanostructures.

4. Conclusion

This study reports the investigation of BN monolayers as potential H₂ molecular storage through DFT calculations. The molecular hydrogens exhibited favourable adsorption on the top of nitrogen atoms in BN nanosheets. The study performed DFT calculations to comprehend the binding energies and electronic structures of the BN models. The findings indicated that the computed binding energies obtained are approximately 0.01 eV per H₂ molecule. Moreover, the calculated results demonstrate that, for models 1 and 2, the binding energy increases proportionally with the number of molecular hydrogens adsorbed on the BN model's surface. A similar trend is evident in the case of the HOMO-LUMO energy value. The DFT results indicate that increasing the number of molecular hydrogens adsorbed onto the BN framework's surface significantly enhances the HOMO-LUMO gap value, which is approximately 6.0 eV for this study. Surface plots of HOMO and LUMO energies depict the calculated electron densities predominantly concentrated on the N- and B-edges, respectively.

In addition, this study explores the chemical reactivity of the investigated system investigated in this work. Positive and negative electrostatic potentials were identified within the systems. Notably, the most positive region was localized at the N-edge of the studied system, while the hydrogen atoms situated at the B-edge exhibited negative electrostatic potential. The distribution of Mulliken atomic charges illustrates positive charges for boron atoms in the BN models and negative charges for nitrogen atoms. Although the current models fall short of adsorbing molecular hydrogens effectively, the researchers believe that the computational findings lay the groundwork for future development of hydrogen storage materials in the future. Furthermore, it is suggested that Group IV-doped BN can be considered promising research for hydrogen storage study in future investigations.

5. Acknowledgement

The research was supported by the Ministry of Higher Education (MoHE) through the Fundamental Research Grant Scheme FRGS/1/2018/TK10/UTAR/02/7.

6. References

- Anota E. C., Juarez A. R., Castro M. & Cicoletzi H. H. (2013). A density functional theory analysis for the adsorption of the amine group on graphene and boron nitride nanosheets, *Journal of Molecular Modeling* 19: 321–328.
- Ansaloni L. M. S. & Sousa E. M. B. d. (2013). Boron nitride nanostructures: Synthesis, characterization and potential use in cosmetics, *Materials Sciences, and Applications* 4: 22–28.
- Chettri B., Patra P. K., Hieu N. N. & Rai D. P. (2021). Hexagonal boron nitride (h-BN) nanosheet as a potential hydrogen adsorption material: A density functional theory (DFT) study, *Surface and Interfaces* 24: 101043(1–8).
- Denis P. A. & Iribarne F. (2019). Comparative study of the chemical reactivity of graphene and boron nitride sheets, *Computational and Theoretical Chemistry* 1164: 112538(1–7).
- Esfafili M. D. & Behzadi H. (2012). A DFT study on carbon-doping at different sites of (8,0) boron nitride nanotube, *Structural Chemistry* 24(2): 573–581.
- Esfafili M. D. & Behzadi H. (2013). A comparative study on carbon, boron-nitride, boron-phosphide, and silicon-carbide nanotubes based on surface electrostatic potentials and average local ionization energies, *Journal of Materials Chemistry A* 19(6): 2375–2382.
- Frisch, M. J., Trucks, G. W., Schlegel, H. B., Scuseria, G. E., Robb, M. A., Cheeseman, J. R., Scalmani, G., Barone, V., Petersson, G. A., Nakatsuji, H., Li, X., Caricato, M., Marenich, A. V., Bloino, J., Janesko, B. G., Gomperts, R., Mennucci, B., Hratchian, H. P., Ortiz, J. V., Izmaylov, A. F., Sonnenberg, J. L., Williams-Young, D., Ding, F., Lipparini, F., Egidi, F., Goings, J., Peng, B., Petrone, A., Henderson, T., Ranasinghe, D., Zakrzewski, V. G., Gao, J., Rega, N., Zheng, G., Liang, W., Hada, M., Ehara, M., Toyota, K., Fukuda, R., Hasegawa, J., Ishida, M., Nakajima, T., Honda, Y., Kitao, O., Nakai, H., Vreven, T., Throssell, K., Montgomery, J. A., Jr., Peralta, J. E., Ogliaro, F., Bearpark, M. J., Heyd, J. J., Brothers, E. N., Kudin, K. N., Staroverov, V. N., Keith, T. A., Kobayashi, R., Normand, J., Raghavachari, K., Rendell, A. P., Burant, J. C., Iyengar, S. S., Tomasi, J., Cossi, M., Millam, J. M., Klene, M., Adamo, C., Cammi, R., Ochterski, J. W., Martin, R. L., Morokuma, K., Farkas, O., Foresman, J. B. & Fox, D. J., Gaussian 09, Wallingford CT, United State: Gaussian, Inc.
- Gonzalez-Ortiz D., Salameh C., Bechelany M. & Miele P. (2020). Nanostructured boron nitride-based materials: synthesis and applications, *Materials Today Advances* 8: 100107(1–20).
- Izyumskaya N., Demchenko D. O., Das S., Ozgur U., Avrutin V. & Morkoc H. (2017). Recent development of boron nitride towards electronic applications, *Advanced Electronic Materials* 1600485(1–22).
- Javan M. B., Soltani A., Ghasemi A. S., Lemeski E. T., Ghilami N., Balakheyli H. (2017). Ga-doped and antisite double defects enhance the sensitivity of boron nitride nanotubes towards soman and chlorosoman, *Applied Surface Science* 411: 1–10.
- Kannan P. K., Saraswathi R. & Bercamans L. J. (2013). Combustion synthesis of boron nitride by glycine route, *Research Journal of Chemical Sciences* 3(2): 59–64.
- Lale A., Bernard S. & Demirci U. B. (2018). Boron nitride for hydrogen storage, *ChemPlusChem* 83(10): 893–903.

- Mukasyan A. S. (2017). Boron Nitride, Concise Encyclopedia of Self-Propagating High-Temperature Synthesis, pp. 45–47, Amsterdam, Netherlands: Elsevier.
- Oku, T. (2015). Hydrogen storage in boron nitride and carbon nanomaterials, *Energies* 8(1): 319–337.
- Roohi H., Nowroozi A., Ebrahimi A. & Makiabadi B. (2010). Effect of CH₃CO functional group on the molecular and electronic properties of BN43zz nanotube: A computational chemistry study, *Journal of Molecular Structure: THEOCHEM* 952: 36–45.
- Seyed-Talebi S. M. & Neek-Amal M. (2014). The different adsorption mechanism of methane molecule onto a boron nitride and a graphene flakes, *Journal of Applied Physics* 116(15): 153507(1–7).
- Shah-Naqvi S. A. A., Toh P. L., Lim Y. C., Wang S. M., Ang L. S. & Sim L. C. (2022). Computational density functional theory investigation of stability and electronic structures on boron nitride systems doped with/without group IV elements, *Malaysian Journal of Chemistry* 24(1): 85–93.
- Shah-Naqvi S. A. A., Toh P. L., Lim Y. C., Wang S. M., Ang L. S. & Sim L. C. (2021). Computational study of hydrogen molecules adsorption on boron nitride with/without adopted by one of elements from group IV, *IOP Conference Series Earth and Environmental Science* 945(1): 012001(1–12).
- Shuaibu A., Adeyemi O. J. & Usiekpan U. R. (2019). First principle study of structural, elastic and electronic properties of hexagonal boron nitride (Hex-BN) single layer, *American Journal of Condensed Matter Physics* 9(1): 1–5.
- Thomas S., Manju M. S., Ajith K.M., Lee S.U., Zaeem M. A. (2020). Strain-induced work function in h-BN and BCN monolayers, *Physica E: Low-Dimensional Systems and Nanostructures* 123: 114180(1–9).
- Toh P. L. & Wang S. M. (2019). Theoretical investigations of the structural and electronic properties of boron nitride clusters: DFT comparison of several basis sets, *Journal of Physics: Conference Series* 1349: 012137(1–6).
- Zheng F. L., Zhang Y., Zhang J. M. & Xu K. W. (2011). Effect of the dangling bond on the electronic and magnetic properties of BN nanoribbon, *Journal of Physics and Chemistry of Solids* 72(4): 256–262.

NUMERICAL SIMULATION OF ENHANCED OPTICAL FREE SPECTRAL RANGE THROUGH INTEGRATED FANO-MICRORING CONFIGURATION

Mohammad Amirul Hairol Aman^{1a,b}, Ahmad Fakhurrazi Ahmad Noorden^{2a,b*}, Faris Azim Ahmad Fajri^{3a,b}, Muhammad Zamzuri Abdul Kadir^{4a,b}, Wan Hazman Danial^{5c}, Suzairi Daud^{6d}

Abstract: A numerical analysis of the integrated Fano-microring (IFM) racetrack resonator spectrum was performed to investigate the enhancement of the optical system's free spectral range (FSR). The FSR is an important optical property which can contribute to the high sensitivity of optical devices. The IFM refers to the combination of Fano resonance produced in the output spectrum through the interaction of Fabry–Perot resonance and circulation resonance. This work focuses on the study of inducing Fano resonance in the microring resonator to optimize the FSR of the system. The results show that the integration of two resonances can produce a Vernier output spectrum, which significantly enhanced the FSR of the system without any need for additional ring waveguides. This work also compared the IFM resonance with the conventional microring resonance. In this simulation, the optimized FSR obtained by the IFM configuration was 266.55 nm, which is five times higher than the conventional microring configuration.

Keywords: Fano resonance, microring, free spectral range, fabry-perot resonance, numerical simulation

1. Introduction

Optical microring resonators have been applied in various devices and fields, such as sensor technology, including pressure sensors (Seyfari et al., 2020), thermal sensors (Zhu & Lou, 2020), gas sensors (Koushik & Malathi, 2020), and chemical sensors (Bavili et al., 2020). Microring has also been applied as a modulator (Moradi et al., 2021) and an optical switch (Bharti & Rakshit, 2021; Singh et al., 2021) due to its compact size (Biswas et al., 2021), high compatibility (Bogaerts et al., 2012), low cost (Kim et al., 2013), and utilization of evanescence field that makes it immune towards electromagnetic disturbances (Bogaerts et al., 2012). Consequently, performance is essential in the advancement of this technology.

Limit of detection (LOD) is one of the indicators to evaluate the performance of microring configuration in sensing application. LOD can be described as the minimum detectable change (Guider et al., 2015), which is directly related to free spectral range (FSR) (Vollmer & Schwefel, 2014). FSR can be interpreted as the distance between two adjacent peaks (Bogaerts et al., 2012). The relationship of LOD and FSR is inversely proportional, where higher FSR will offer smaller detectable scale (Chao & Guo, 2006). Hence, the FSR significantly shows the performance of the microring. Many efforts have been made to enhance the FSR, such as a double Vernier Panda-ring resonator with the maximum FSR of 90 nm (Seyfari et al., 2021), a microring with multi-Mach–Zehnder interferometers with FSR over 88 nm (Y. Chen & Qiu, 2021), a compact microring resonator using low-loss bends with FSR of 35 nm (Song et al., 2020), and a racetrack microring resonator with Fabry–Perot cavities where the FSR is over 150 nm (Kumar Bag & Varshney, 2021).

By integrating Fano resonance with the microring resonance, the FSR can be improved. The Fano resonance was applied in the microring technology through many methods such as photonic crystal cavity generation (Peng et al., 2018), nanocavities utilization in split-ring resonator (Zhang et al., 2013), double half ring resonator (He et al., 2021), and side coupled ring cavity with a metal nanowall (F. Chen et al., 2019). Fano resonance can be obtained through the interference of a continuous background mode and a discrete resonant mode (Li & Bogaerts, 2017; Zhao et al., 2016). The main attribute of Fano resonance is the asymmetric line shape which is caused by the two-resonance optical

Authors information:

^aCentre for Advanced Optoelectronics Research (CAPTOR), Kulliyah of Science, International Islamic University Malaysia, 25200 Kuantan, Pahang, MALAYSIA. E-mail: amirul.hairol@live.iium.edu.my¹, fakhurrazi@iium.edu.my², azim10miza@gmail.com³, zamzurikadir@iium.edu.my⁴

^bIUM Photonics and Quantum Centre (IPQC), Kulliyah of Science, International Islamic University Malaysia, 25200, Kuantan, Pahang, MALAYSIA. E-mail: amirul.hairol@live.iium.edu.my¹, fakhurrazi@iium.edu.my², azim10miza@gmail.com³, zamzurikadir@iium.edu.my⁴

^cDepartment of Chemistry, Kulliyah of Science, International Islamic University Malaysia, 25200, Kuantan, Pahang, MALAYSIA. E-mail: whazman@iium.edu.my⁵

^dLaser Center, Ibnu Sina Institute for Scientific & Industrial Research, Universiti Teknologi MALAYSIA, 81310, Johor Bahru, Johor, Malaysia. E-mail: suzairidaud@utm.my⁶

*Corresponding Author: fakhurrazi@iium.edu.my

Received: June 20, 2022

Accepted: August 8, 2022

Published: October 31, 2023

interference (Zhao et al., 2016). In this case, the Fano resonance is achieved by merging the circulation resonance from the ring with the Fabry–Perot resonance from the bus waveguide (Yi et al., 2010). Fano resonance also offers the potential to enhance the performance of the microring in terms of FSR, LOD, and sensitivity (Chao & Guo, 2003; Tu et al., 2017; Wang et al., 2017). However, the generated Fabry–Perot resonance, which is essential to produce the Fano resonance, has a small FSR that will affect the overall spectrum (Yi et al., 2010).

In this work, an optimized racetrack microring resonator configuration was proposed to reduce the effect of Fabry–Perot resonance, thus enhancing the FSR. Since the configuration involves a racetrack microring resonator and Fano resonance, the system is called integrated Fano-racetrack microring (IFM) configuration. For this research, two simulations were performed to achieve the maximum FSR: 1) Comparison of the resonance between IFM and conventional racetrack configuration and 2) the optimization process of IFM configuration. The optimization was performed to determine the maximum FSR with various configuration parameters such as ring radius, length of the racetrack, and distance of the reflectors from the center.

2. Model and Theory

The simulation was performed for two types of racetrack microring resonators: (1) the conventional racetrack microring resonator and (2) the racetrack microring resonator with reflectors in the bus waveguide. Figure 1 a) and b) shows both configurations with the labelled propagated electric field. The figure shows that only the IFM configuration was installed with reflectors in the bus waveguide. The reflectors play a major role in the IFM configuration to generate the Fano resonance.

Light is travelled through the input port, E_{in} and propagated in the waveguide. At the coupling region, a fraction of the light is coupled into the ring at E_1 , and another fraction is still propagating in the waveguide. The propagating light in the waveguide is partially reflected due to the presence of the reflector and partially went through the output port, E_{out} . On the other hand, light in the ring is propagated towards the coupling region at E_2 and coupled back into the waveguide. Then, the resonance from the ring is merged with the resonance in the waveguide, thus Fano-like resonance is obtained. It is necessary for the bus reflector to be made of partial reflective materials to generate the Fabry–Perot resonance (Yi et al., 2010). The combination of circulation resonance and Fabry–Perot resonance can create a Fano resonance as the output spectrum.

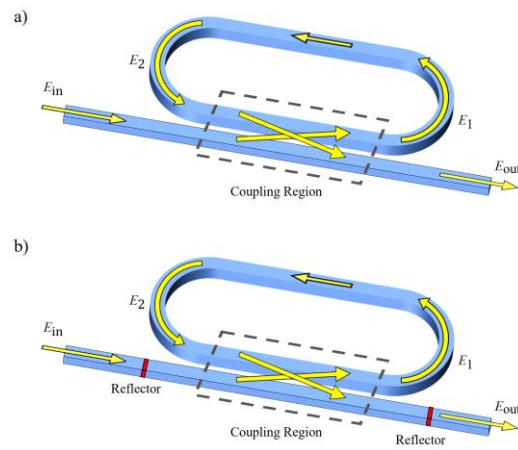


Figure 1. a) The conventional and b) the IFM configuration racetrack configurations.

The mathematical theory of optical coupling was performed for the IFM configuration to construct the numerical programming script. The coupling theory and optical phase shift with the attenuation loss were included in the computation. The transfer matrix for the whole integration system comprises the microring and Fabry–Perot resonances (Gu et al., 2019) can be expressed as follows:

$$\begin{bmatrix} E_{out} \\ E_1 \end{bmatrix} = \frac{1}{i\sqrt{1-r_h^2}} \begin{bmatrix} -1 & -r_h \\ r_h & 1 \end{bmatrix} \cdot \begin{bmatrix} e^{i2\pi n_{eff}L/\lambda} & 0 \\ 0 & e^{-i2\pi n_{eff}L/\lambda} \end{bmatrix} \cdot \begin{bmatrix} t_R & 0 \\ 0 & 1 \end{bmatrix} \cdot \begin{bmatrix} 1 \\ 0 \end{bmatrix} \cdot \frac{1}{i\sqrt{1-r_h^2}} \begin{bmatrix} -1 & -r_h \\ r_h & 1 \end{bmatrix} \cdot \begin{bmatrix} E_{in} \\ E_2 \end{bmatrix} \quad (1)$$

where E_{in} is the input port, E_{out} is the output port, E_1 is the input port to the ring, and E_2 is the output port of the ring. The term n_{eff} is the effective refractive index, which represents both refractive indexes of core and cladding. L represents the distance between the reflector in the waveguide and t_R is the optical transfer function (OTF) of the racetrack microring resonator. The amplitude reflection coefficient (Yi et al., 2010) can be expressed as follows:

$$r_h = \frac{n_{eff}-1}{1-n_{eff}} \quad (2)$$

The OTF of racetrack microring (Bogaerts et al., 2012; Heebner et al., 2008) is given as below:

$$\frac{E_{out}}{E_{in}} = \frac{c - ae^{i2\pi L_R/\lambda}}{1 - cae^{i2\pi L_R/\lambda}} \quad (3)$$

where a is the single-pass amplitude and expressed as follows (Bogaerts et al., 2012; Heebner et al., 2008; Noorden et al., 2020):

$$a = \exp(-\alpha L_R) \quad (4)$$

where α is the attenuation coefficient and L_R is the perimeter of the all-pass microring resonator. c is a self-coupling coefficient which can be expressed as follows (Noorden et al., 2020):

$$c = \sqrt{1 - \kappa} \sqrt{1 - \gamma} \quad (5)$$

where κ is the coupling coefficient (Noorden et al., 2020) and γ is the propagation loss coefficient (Noorden et al., 2020).

In this study, the numerical simulation was conducted using a mathematical computation software named Gnu Octave. The Gnu Octave has a high capability in solving numerical computations and presenting data due to its powerful visualisation tools (GNU Octave, n.d.) The simulated configurations are racetrack microring with reflectors embedded in the waveguide and conventional racetrack microring. The core and substrate materials are silicon (Si) and silicon oxide (SiO₂), respectively. The cladding of the microring is air. Due to the difference in refractive index among the materials, resonance confinement can be achieved. The coupling coefficient was set as constant throughout the research.

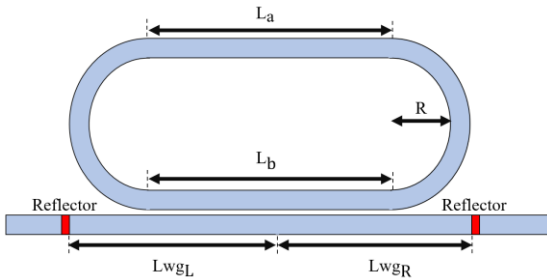


Figure 2. The optimised parameters of the configuration.

The reflectors labelled in Figure 2 are necessary to generate the Fano resonance. The reflector aids in creating interference through Fabry–Perot resonance in the waveguide (Yi et al., 2010). From Figure 2, the perimeter of the system can be calculated as follows:

$$L_R = 2\pi R + L_a + L_b \quad (4)$$

where L_a and L_b are the length of the racetrack microring. L_{wg_L} and L_{wg_R} represent the distance of the reflector from the centre of the waveguide.

Table 1. The range of optimisation for all the parameters based on two configurations.

Parameter	Integrated Fano-Microring	Conventional Microring
R	2 μm – 20 μm	2 μm – 20 μm
L _a	10 μm – 30 μm	10 μm – 30 μm
L _b	10 μm – 30 μm	10 μm – 30 μm
L _{wg_L}	2 μm – 20 μm	-
L _{wg_R}	2 μm – 20 μm	-

The optimisation of both configurations was performed based on the exhaustive search technique, where each configuration was initialised by considering all parameters’ domain as shown in Table 1. For each range of the parameter, 20 values were iterated to observe the FSR. The FSR for each configuration was measured accordingly to analyse the Fano resonance. Both conventional and IFM configurations with the highest FSR were analysed and discussed in the next section. Note that since conventional microring does not have the reflector in the waveguide, only the radius and length of the racetrack were considered.

3. Results and Discussions

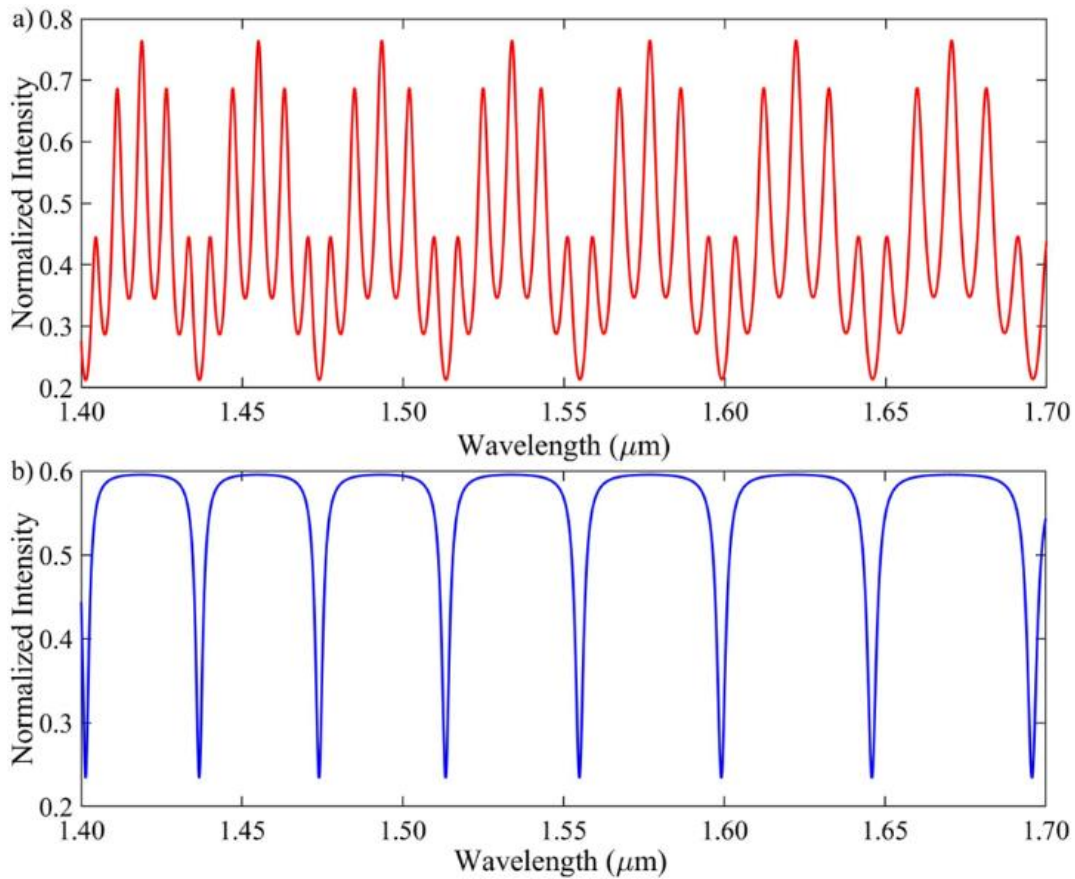


Figure 3. Output numerical simulation of a) IFM spectrum and b) conventional microring spectrum.

Figure 3 depicts the spectrum of IFM comprises numerous peaks compared to the conventional microring. Note that the position of the Lorentzian shape is similar between the two. Besides, the IFM configuration also exhibits a characteristic of Vernier effect where the resonance pattern becomes enveloped in a group (Gomes et al., 2021). The IFM spectrum also shows a Fano-like line shape credited to the reflectors in the waveguide

where a fraction of the resonance still propagates in the waveguide causing the interference of numerous resonances with different phase shifts (Yi et al., 2010). The conventional microring spectrum differs from the IFM spectrum due to the suppression of interstitial peak by Fano resonance (Boeck et al., 2010).

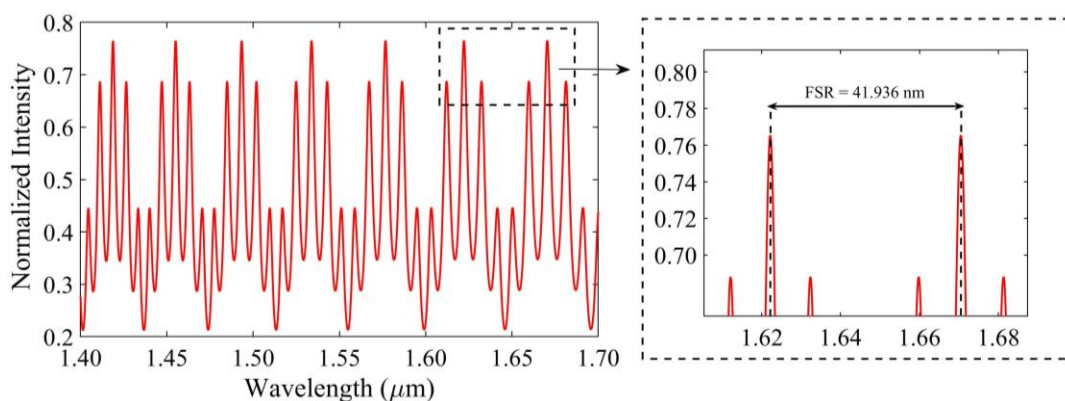


Figure 4. The unoptimised IFM spectrum and the magnified peaks for FSR measurement.

Figure 4 shows the unoptimised spectrum of IFM and the recorded FSR was 41.936 nm. Without optimising the simulation system, the IFM spectrum has a very low FSR, which will reduce

the performance of the microring. This is because, the Fabry-Perot resonance with small FSR merges with the circulation resonance (Yi et al., 2010). The collective small FSR from the

Fabry–Perot resonance affects the microring spectrum by suppressing its peaks and producing a lot of smaller peaks. Subsequently, the FSR, instead of increasing, decreases

tremendously. Therefore, the optimisation process is essential to improve the performance of the microring.

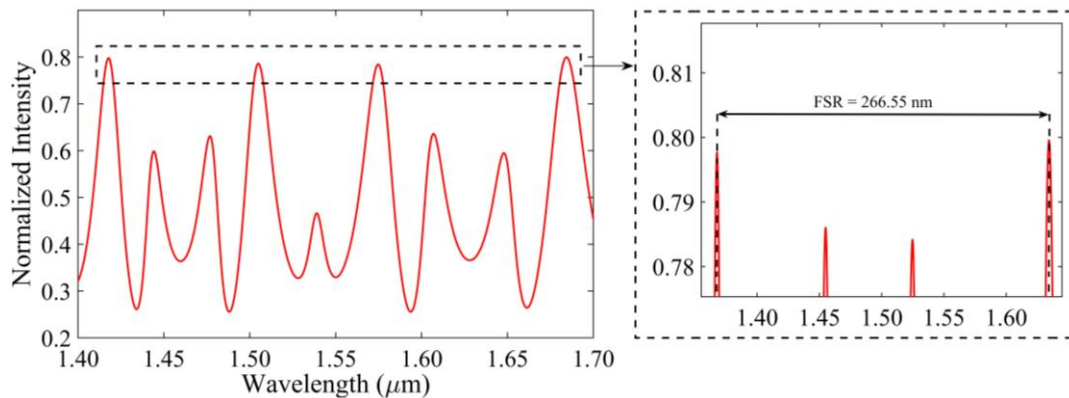


Figure 5. The optimised IFM and the magnified peaks for FSR measurement.

Figure 5 illustrates the optimised IFM spectrum where the measured FSR was 266.55 nm. The FSR of the optimised configuration was five times higher than that of the unoptimised configuration. The parameters of the optimised IFM configuration are tabulated in Table 2.

Table 2. The optimized IFM configuration

Parameter	Value
R	15.26 μm
L_a	30.00 μm
L_b	30.00 μm
L_{WGL}	2.95 μm
L_{WGR}	2.00 μm

The main contributor to the wide FSR of the IFM configuration is the Fano resonance which suppresses the interstitial resonances (Boeck et al., 2010; Schwelb, 2007). Due to the suppression of interstitial peaks in the spectrum, the Vernier effect can be observed, and the Vernier effect helps to extend the FSR of the resonance (Jin et al., 2011; Troia et al., 2014). This is because, the waveguide system of IFM consists of two resonances type: (1) circulation resonance from racetrack waveguide and (2) Fabry–Perot resonance from the reflector at the bus waveguide. In the sensing application, a large FSR benefits the system because it contributes to wider measurement range (C. Chen et al., 2021; Tian et al., 2020). Besides, wide FSR helps the system to distinguish the resonance peak and makes the detection system more accurate especially in all-optical sensing technologies. Even though the FSR is detrimental to the quality factor (QF) (Taufiqurrahman et al., 2020), high FSR is beneficial to achieve high optical sensitivity because the QF does not impose a direct impact on the sensing application. Nevertheless, the simulated system has successfully optimised the FSR of the system based on the IFM waveguide with the reflectors.

4. Conclusion

In conclusion, two simulations were performed to convey the significance of Fano resonance in the application of microring

technology. The first simulation indicates the difference between the conventional racetrack microring resonator with the IFM resonator. With the suppression by the Fano resonance, the vernier effect can be achieved, hence the FSR can be increased significantly. In the second simulation, the system was optimized successfully and a comparison between the unoptimized and optimized Fano resonance was made. The FSR of the optimized Fano resonance was 266.55 nm, which is five times higher than that of the unoptimized. These simulations prove that the IFM spectrum has a huge potential and much room to be improved. Furthermore, the Fano resonance will likely help to improve the sensitivity due to its profile having numerous sharp peaks (Zhao et al., 2016). The sharp peaks may be vital in getting a more significant wavelength shift; hence, the sensitivity of the microring increase.

5. Acknowledgement

This work was supported by CAPTOR and the Department of Physics, International Islamic University Malaysia in term of facilities and financially by the Ministry of Education (Malaysia) through Fundamental Research Grant Scheme (Project No.: FRGS 19-033-0641) (References No.: FRGS/1/2018/TK07/UIAM/02/1).

6. References

- Bavili, N., Balkan, T., Morova, B., Eryürek, M., Uysallı, Y., Kaya, S., & Kiraz, A. (2020). Highly sensitive optical sensor for hydrogen gas based on a polymer microcylinder ring resonator. *Sensors and Actuators B: Chemical*, 310, 127806.
- Bharti, G. K., & Rakshit, J. K. (2021). Design of all-optical logical mode-switching using micro-ring resonator. *Optical Engineering*, 60(3), 035103.
- Biswas, U., Rakshit, J. K., Das, J., Bharti, G. K., Suthar, B., Amphawan, A., & Najjar, M. (2021). Design of an ultra-

- compact and highly-sensitive temperature sensor using photonic crystal based single micro-ring resonator and cascaded micro-ring resonator. *Silicon*, 13(3), 885–892.
- Boeck, R., Jaeger, N. A. F., & Chrostowski, L. (2010). Experimental demonstration of the Vernier effect using series-coupled racetrack resonators. *2010 International Conference on Optical MEMS and Nanophotonics*, 1–2.
- Bogaerts, W., de Heyn, P., van Vaerenbergh, T., de Vos, K., Kumar Selvaraja, S., Claes, T., Dumon, P., Bienstman, P., van Thourhout, D., & Baets, R. (2012). Silicon microring resonators. *Laser & Photonics Reviews*, 6(1), 47–73.
- Chao, C. Y., & Guo, L. J. (2003). Biochemical sensors based on polymer microrings with sharp asymmetrical resonance. *Applied Physics Letters*, 83(8). <https://doi.org/10.1063/1.1605261>
- Chao, C. Y., & Guo, L. J. (2006). Design and optimization of microring resonators in biochemical sensing applications. *Journal of Lightwave Technology*, 24(3), 1395–1402. <https://doi.org/10.1109/JLT.2005.863333>
- Chen, C., Hou, X., & Wang, J. (2021). A Novel Hybrid Plasmonic Resonator with High Quality Factor and Large Free Spectral Range. *IEEE Sensors Journal*, 21(2). <https://doi.org/10.1109/JSEN.2020.3017647>
- Chen, F., Zhang, H., Sun, L., Li, J., & Yu, C. (2019). Temperature tunable Fano resonance based on ring resonator side coupled with a MIM waveguide. *Optics & Laser Technology*, 116, 293–299.
- Chen, Y., & Qiu, Q. (2021). A novel microring resonator based on multi-Mach-Zehnder interferometers. *Optics Communications*, 483. <https://doi.org/10.1016/j.optcom.2020.126643>
- GNU Octave. (n.d.). Retrieved July 14, 2022, from <https://octave.org/>
- Gomes, A. D., Bartelt, H., & Frazão, O. (2021). Optical Vernier Effect: Recent Advances and Developments. In *Laser and Photonics Reviews* (Vol. 15, Issue 7). <https://doi.org/10.1002/lpor.202000588>
- Gu, L., Fang, H., Li, J., Fang, L., Chua, S. J., Zhao, J., & Gan, X. (2019). A compact structure for realizing Lorentzian, Fano, and electromagnetically induced transparency resonance lineshapes in a microring resonator. *Nanophotonics*, 8(5), 841–848.
- Guider, R., Gandolfi, D., Chalyan, T., Pasquardini, L., Samusenko, A., Pederzoli, C., Pucker, G., & Pavesi, L. (2015). Sensitivity and limit of detection of biosensors based on ring resonators. *Sensing and Bio-Sensing Research*, 6, 99–102.
- He, Q., Huo, Y., Guo, Y., Niu, Q., Hao, X., Cui, P., Wang, Y., & Song, M. (2021). Multiple adjustable Fano resonance based on double half ring resonator and its application. *Physica Scripta*, 96(6), 065504.
- Heebner, J., Grover, R., & Ibrahim, T. (2008). *Optical microresonator theory*. Springer.
- Jin, L., Li, M., & He, J. J. (2011). Highly-sensitive silicon-on-insulator sensor based on two cascaded micro-ring resonators with vernier effect. *Optics Communications*, 284(1). <https://doi.org/10.1016/j.optcom.2010.08.035>
- Kim, K. W., Song, J., Kee, J. S., Liu, Q., Lo, G.-Q., & Park, M. K. (2013). Label-free biosensor based on an electrical tracing-assisted silicon microring resonator with a low-cost broadband source. *Biosensors and Bioelectronics*, 46, 15–21.
- Koushik, K. P., & Malathi, S. (2020). Optical micro-ring resonator for detection of carbon dioxide gas. In *Emerging Trends in Photonics, Signal Processing and Communication Engineering* (pp. 157–161). Springer.
- Kumar Bag, S., & Varshney, S. K. (2021). Ultrawide FSR microring racetrack resonator with an integrated Fabry-Perot cavity for refractive index sensing. *Journal of the Optical Society of America B*, 38(5). <https://doi.org/10.1364/josab.416454>
- Li, A., & Bogaerts, W. (2017). An actively controlled silicon ring resonator with a fully tunable Fano resonance. *APL Photonics*, 2(9), 096101.
- Moradi, M., Mohammadi, M., Olyaei, S., & Seifouri, M. (2021). Design and simulation of a fast all-optical modulator based on photonic crystal using ring resonators. *Silicon*, 1–7.
- Noorden, A. F. A., Mohamad, A., Salleh, M. H., Daud, S., Mohamad, S. N., & Ali, J. (2020). Free spectral range analysis of double series microresonator system for all-optical corrosion sensor. *Optical Engineering*, 59(1), 17106.
- Peng, F., Wang, Z., Yuan, G., Guan, L., & Peng, Z. (2018). High-sensitivity refractive index sensing based on Fano resonances in a photonic crystal cavity-coupled microring resonator. *IEEE Photonics Journal*, 10(2), 1–8.
- Schwelb, O. (2007). The nature of spurious mode suppression in extended FSR microring multiplexers. *Optics Communications*, 271(2). <https://doi.org/10.1016/j.optcom.2006.10.053>

- Seyfari, A. K., Bahadoran, M., & Aghili, A. (2020). Ultra-sensitive pressure sensor using double stage racetrack silicon micro resonator. *Optical and Quantum Electronics*, 52(9), 1–16.
- Seyfari, A. K., Bahadoran, M., & Yupapin, P. (2021). Design and modeling of double Panda-microring resonator as multi-band optical filter. *Nano Communication Networks*, 29. <https://doi.org/10.1016/j.nancom.2021.100352>
- Singh, M. P., Hossain, M., Rakshit, J. K., Bharti, G. K., & Roy, J. N. (2021). Proposal for polarization rotation–based ultrafast all optical switch in ring resonator. *Brazilian Journal of Physics*, 51(6), 1763–1774.
- Song, J. H., Kongnyuy, T. D., de Heyn, P., Lardenois, S., Jansen, R., & Rottenberg, X. (2020). Compact Micro-Ring Resonator using Low-Loss Silicon Waveguide Bends. *Conference Proceedings - Lasers and Electro-Optics Society Annual Meeting-LEOS, 2020-May*.
- Taufiqurrahman, S., Dicky, G., Estu, T. T., Daud, P., Mahmudin, D., & Anshori, I. (2020). Free spectral range and quality factor enhancement of multi-path optical ring resonator for sensor application. *AIP Conference Proceedings*, 2256. <https://doi.org/10.1063/5.0014960>
- Tian, C., Zhang, H., Li, W., Huang, X., Liu, J., Huang, A., & Xiao, Z. (2020). Temperature sensor of high-sensitivity based on nested ring resonator by Vernier effect. *Optik*, 204, 164118.
- Troia, B., Khokhar, A. Z., Nedeljkovic, M., Penades, J. S., Passaro, V. M. N., & Mashanovich, G. Z. (2014). Cascade-coupled racetrack resonators based on the Vernier effect in the mid-infrared. *Optics Express*, 22(20), 23990–24003.
- Tu, Z., Gao, D., Zhang, M., & Zhang, D. (2017). High-sensitivity complex refractive index sensing based on Fano resonance in the subwavelength grating waveguide micro-ring resonator. *Optics Express*, 25(17). <https://doi.org/10.1364/oe.25.020911>
- Vollmer, F., & Schwefel, H. G. L. (2014). Taking detection to the limit with optical microcavities: Recent advances presented at the 560. WE Heraeus Seminar. In *The European Physical Journal Special Topics* (Vol. 223, Issue 10, pp. 1907–1916). Springer.
- Wang, G., Dai, T., Jiang, J., Yu, H., Hao, Y., Wang, Y., Li, Y., Jiang, X., & Yang, J. (2017). Slope tunable Fano resonances in asymmetric embedded microring resonators. *Journal of Optics (United Kingdom)*, 19(2). <https://doi.org/10.1088/2040-8986/aa51a1>
- Yi, H., Citrin, D. S., & Zhou, Z. (2010). Highly sensitive silicon microring sensor with sharp asymmetrical resonance. *Optics Express*, 18(3), 2967–2972.
- Zhang, Q., Wen, X., Li, G., Ruan, Q., Wang, J., & Xiong, Q. (2013). Multiple magnetic mode-based Fano resonance in split-ring resonator/disk nanocavities. *Acs Nano*, 7(12), 11071–11078.
- Zhao, G., Zhao, T., Xiao, H., Liu, Z., Liu, G., Yang, J., Ren, Z., Bai, J., & Tian, Y. (2016). Tunable Fano resonances based on microring resonator with feedback coupled waveguide. *Optics Express*, 24(18), 20187–20195.
- Zhu, J., & Lou, J. (2020). High-sensitivity Fano resonance temperature sensor in MIM waveguides coupled with a polydimethylsiloxane-sealed semi-square ring resonator. *Results in Physics*, 18, 103183.

THE EFFECT OF BALL MILLING ON THE MORPHOLOGY OF CUBIC BORON NITRIDE

A R Shashikala^{1a*}, Kothakula Keerthi^{2a}, Ramesh C S^{3b} and B S Sridhar^{4c}

Abstract: Due to its attractive properties, cubic boron nitride (c-BN) finds extensive applications in mechanical and electronic industries. The conversion of micro c-BN to nano c-BN remarkably influences the properties. This study investigates the effect of ball milling on the morphological parameters. Boron nitride was subjected to different hours of ball milling process at different rotation speeds. The crystallite size of the c-BN was measured at different ball milling time intervals, and it is observed that after 100 hours, the crystallite size decreased to nano size. The ball milling was increased to 150-175 hours to get less than 100 nm size particles. The surface morphology and elemental analysis of the samples were done using SEM and EDX studies. EDX confirmed the presence of boron and nitrogen in the sample. SEM images indicated that the agglomerated morphology of c-BN particles with irregular shape. The cubic structure was confirmed from XRD studies. Thermogravimetric analysis (TGA) conducted to determine the samples' thermal stability indicated that weight loss was observed for temperatures up to 700°C. There was no significant weight loss at a higher temperature. Stronger reflectance was observed with increased ball milling time in UV-Visible DSR studies.

Keywords: c-BN, ball-milling, XRD, crystallite size, thermogravimetric analysis, uv-visible DSR

1. Introduction

Boron nitride is an iso-electronic with carbon because boron and nitrogen are present side by side individually to the carbon atom in the periodic table [1]. BN can be synthesized in four polymorphic structures viz hexagonal BN (h-BN), rhombohedral BN (r-BN), wurtzite- BN (w-BN) and cubic BN (c-BN) [2]. h-BN has delocalized pi orbital with sp² hybridization. Hexagonal Boron Nitride exhibits the same crystal structure-like graphite [3]. It finds extensive application as an additive in cosmetic products, used as effective lubricant when added with other alloys, plastics, resins, etc. [4]. A combination of BN with CNTs is prone to increase applications of h-BN in electronic devices and gas storage materials [5].

In r-BN boron and nitrogen are packed with four-membered rings of layers. No four-layer coincidence occurred, but a displacement was seen on every fourth layer and repeated at the first layer. It exhibits sp² hybridization, where three covalent bonds connect each other with their neighboring atoms [6].

Boron and nitrogen atoms in w-BN have 6-membered rings. The rings between layers are in a boat configuration. However, the c-BN layers are in a chair configuration. Recent studies indicate that w-BN is harder than other borides but softer than c-BN [7].

On the other hand, c-BN is extremely hard, close to a diamond's hardness. It exhibits a single crystal phase and sp³ hybridization similar to diamond [2]. As a semiconductor, it shows a wide band gap, has good optical properties, high thermal conductivity and is chemically inert [8-10]. c-BN shows good transmittance with a wide band gap and spectral range from a UV to Visible [11-14]. c-BN can be doped with p- or n-type impurities [15, 16] to improve its band gap and thermal stability. Due to its wide band gap and thermal stability, it finds applications in high-temperature power electronic instruments, unlike diamond [17]. c-BN can be used in cutting tools and optical instruments like UV detectors and emitters [18-20]. It is insoluble at room temperature but is still used as abrasive because it has high-temperature solubility with nickel, iron and its alloys [21].

Nano c-BN can be obtained by a simple top-down process. Ball milling is a top-down process that synthesizes various nanoparticles like metal oxides, zeolites, carbon materials, and metal frameworks [22, 23]. Nanoparticles obtained from the ball milling process have wide applications in fuel cells, electronic devices, drug delivery and catalysis [24]. Ball-milling increases the surface area and changes the chemical functionality and morphology. Ball-milling in the presence of hydrogen, ammonia, or sodium hydroxide leads to forming ex-foliated boron nitride

Authors information:

^aDepartment of Chemistry, Presidency University, Itgalpura, Rajankunte, Yelahanka, Bangalore, INDIA-560064. E-mail: aarudirs@gmail.com¹; kothakulakeerthy@gmail.com²

^bDepartment of Mechanical Engineering, Presidency University, Itgalpura, Rajankunte, Yelahanka, Bangalore, INDIA-560064. E-mail:

csramesh@presidencyuniversity.in³

^cMSRIT, Department of Mechanical Engineering, Bangalore, INDIA-560054. E-mail: sridharbs@msrit.edu⁴

*Corresponding Author: aarudirs@gmail.com

Received: January 11, 2022

Accepted: October 4, 2022

Published: October 31, 2023

with hydroxyl and amino groups on the surface [25-28].

In this work, nano c-BN was prepared by the ball-milling process. We studied the effect of ball-milling time and rotational speed on the morphology, crystal structure, particle size and thermal stability.

2. Materials and Methods

Commercial cubic boron nitride (c-BN) with a particle size of 2 μm was used for the ball milling process. The sample was subjected to different ball-milling time intervals of up to 175 hours and carried out at 50 and 100 rpm.

Ball milling was conducted using the Delta Power Controls Planetary Ball mill with stainless steel balls of 12 grams weight and vials. The impact force jar was stationary and revolved in a planetary orbit. The ball milling was carried out at different rotations per minute (rpm) and at different period without any power interruption.

The samples' elemental analysis was carried out with EDX using the Link Ge Energy Dispersive Spectrometer combined with a Noran Scientific analyzer, Model TN5500, USA, which provides the spatial resolution for compositional analysis and is limited to 1-micrometer diameter on flat specimens.

The Scanning Electron Microscope TESCAN-VEGA3 LMU was used to study the microstructure and surface morphology at different ball milling times and rotational speeds. The XRD analysis of the milled samples was carried out using an X-ray diffractometer, Philips, PW 1140/90, USA, equipped with Ni filter and Cu K radiation [29]. Double beam UV-visible spectrophotometer model UV 2600 with 200 to 800 nm spectral band was used to measure samples reflectance at different ball milling times. The thermogravimetric analysis was studied using the NETZSCH's STA 449 F5 Jupiter Simultaneous Thermal Analyzer TGA/DSR.

3. Results and Discussion

Table 1 depicts the EDX-elemental composition of c-BN after different grinding duration at 50 rpm. Iron appeared as an impurity when the grinding time was increased to 175 hours because of the stainless steel balls used in the ball milling process. The balls were coated with Teflon and subjected to 175 hours of grinding to overcome this. Table 1 shows the elemental composition of the nano c-BN powder at 175 hours of ball milling before and after coating the balls with Teflon. Boron

concentration decreased with increased ball milling time, which may be due to the diffusion of boron into steel balls during ball milling. The diffusion increased at higher rpm, which may be due to increased temperature with increased ball milling speed and diffusion at higher temperatures [30, 31].

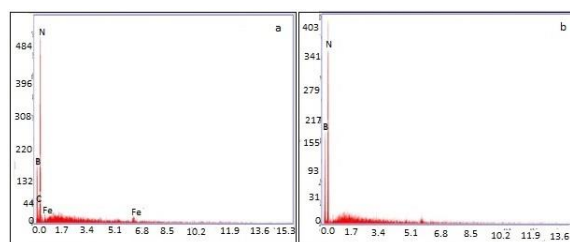


Figure 1. EDAX images of nano c-BN at 175 hours: a) before Teflon coating b) after Teflon coating

Table 1. Elemental composition of the nano c-BN powder at different grinding times at 50 rpm

Time(hrs)	Element	Weight (%)
100	B	50.45
	N	49.55
125	B	48.45
	N	51.04
150	B	48.04
	N	51.66
	B	43.98
175 (before coating the balls with Teflon)	N	54.67
	C	0.41
	Fe	0.26
175 (after coating the balls with Teflon)	B	48.09
	N	51.91

Table 2 shows the presence of iron, chromium, nickel, oxygen, boron, and nitrogen due to using steel balls for grinding. For all further characterization, nano powder obtained at 50 rpm and 175 hours of ball milling with Teflon-coated balls was used as it is free from other impurities.

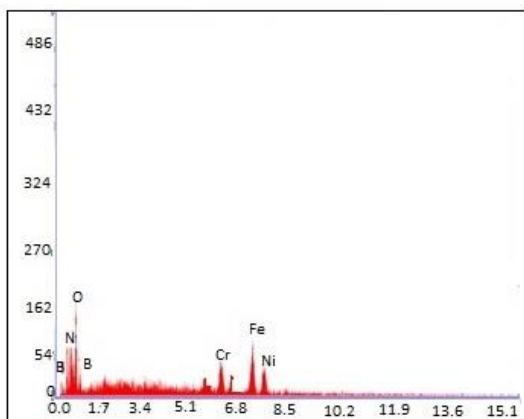


Figure 2. EDAX Image of nano c-BN at 100 rpm

Table 2. Elemental composition of nano c-BN powder at 100 rpm

Time(hrs)	Element	Weight (%)
100	B	46.08
	N	26.23
	Fe	12.68
	Cr	3.65
	O	10.07
	Ni	1.27

Figure 3 shows the XRD images of c-BN at different grinding times. There are four characteristic peaks corresponding to (111), (200), (220) and (311) at 43.6°, 50.9°, 74° and 90°, respectively. The diffraction peaks were only slightly weakened with increased ball milling time due to c-BN's superior hardness. This is similar to the phenomenon reported by Zia and Li [32]. The intensity of (200) peak was decreased to a maximum extent compared to other peaks at 175 hours of ball milling. The c-BN crystallite size decreased with increased ball milling time. Its size decreased from 400 nm at 50 hours of ball milling to 66 nm at 175 hours.

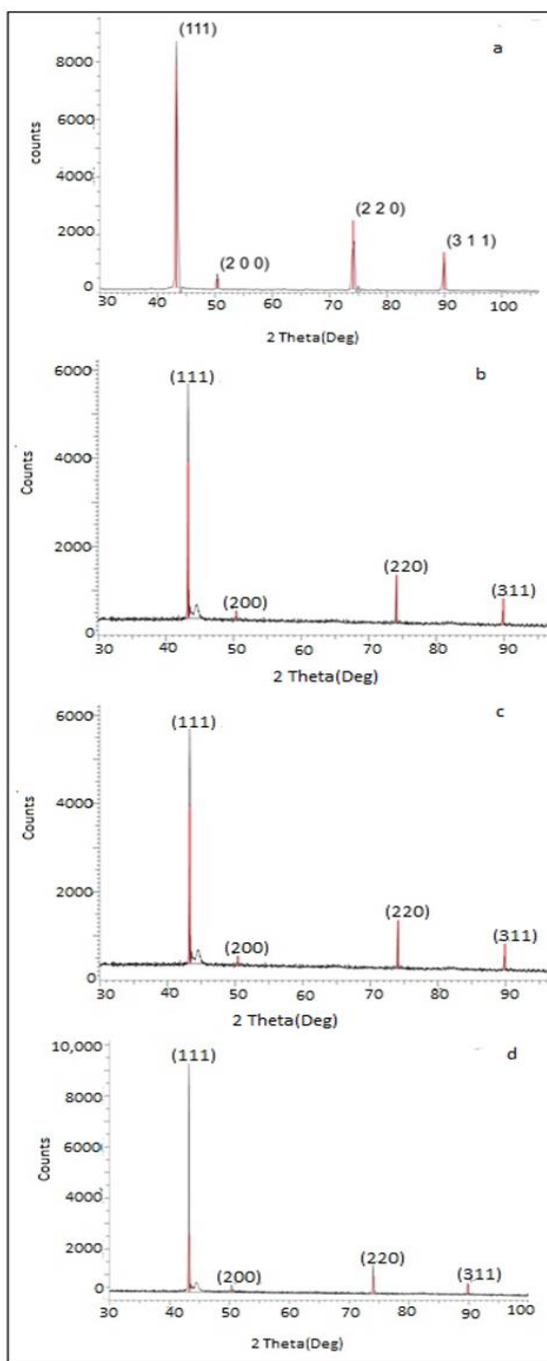


Figure 3. XRD images of c-BN at 50 rpm and different grinding times:

- a)100 hrs.
- b)125 hrs.
- c)150 hrs.
- d)175 hrs.

Figure 4 depicts an XRD image of nano c-BN obtained at 100 hours of ball-milling and 100 rpm speed. The peak intensity decreased and disappeared at 50.9° and 90° with increased speed.

Figure 5 shows the effect of different rotational speeds on the c-BN's crystallite size. Initially, the experiments were conducted at 50 rpm at different grinding times of up to 175 hours. The crystallite size decreased to ~66 nm from 2 μm. The size remained almost constant after 175 hours of ball milling. Experiments were also conducted at 100 rpm. Increasing the rpm decreased the crystallite size; at 100 hours and 50 rpm, the size decreased to less than 60 nm from 125 nm.

Figure 6 displays the scanning electron micrograph of c-BN powder at different ball milling times. The micrographs magnification was kept constant. The specimen was found to have an irregular shape with few agglomerates. Increasing the ball milling time caused the c-BN nanoparticles to have irregular morphologies with sizes that ranged from 57 to 78 nm.

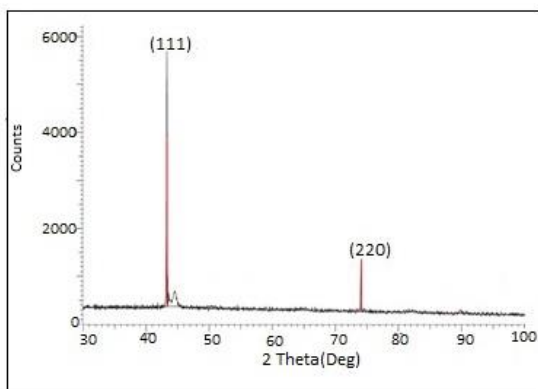


Figure 4. XRD images of c-BN at different grinding times with 100 rpm

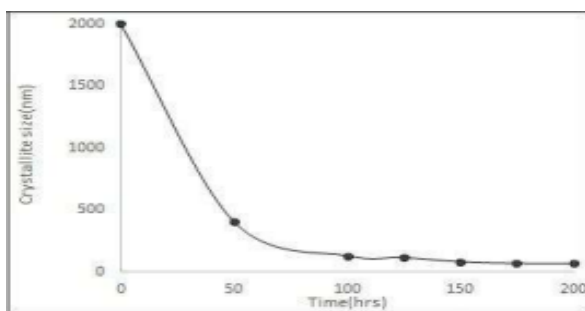


Figure 5. Effect of ball milling on the crystallite size of c-BN at 50 rpm

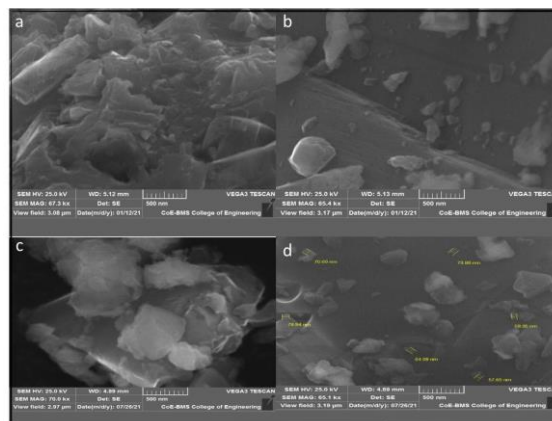


Figure 6. SEM images of c-BN at different ball milling times:

- a) 100 hrs.
- b) 125 hrs.
- c) 150 hrs. and
- d) 175 hrs.

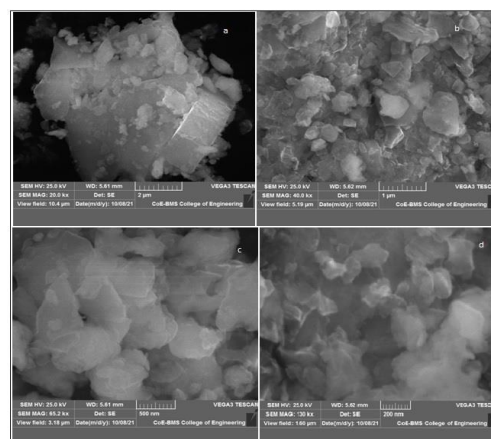


Figure 7. SEM images of c-BN at 100 rpm (100 hrs.) at different magnifications: a) 2μm b) 1μm c) 500nm d) 200 nm.

Figure 7 depicts SEM images of nano c-BN obtained at 100 hours at 100 rpm at different magnifications. At 100 rpm, c-BN consisted of nano-sized amorphous particles with few nodular lumps. The particle size ranged from 60 to 70 nm.

Figure 8 shows the UV-visible DSR spectra of c-BN at different ball milling times. All samples showed UV reflectance in the visible region. The incident light absorption occurred in the 200–800 nm wavelength range. Around 7-12% of reflection is in the longer wavelength region. Overall, reflectance intensity was remarkably enhanced with increased time. Stronger reflectance was observed with increasing ball milling time compared to the micro-sized c-BN.

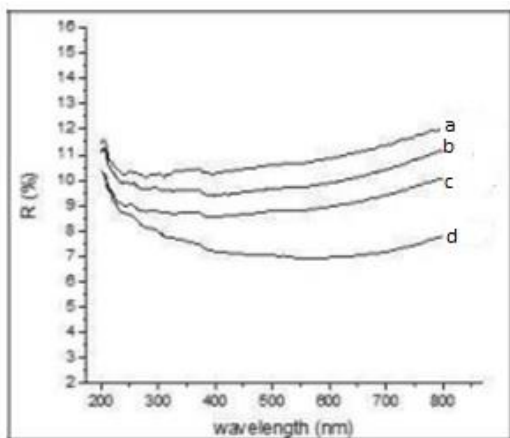


Figure 8. UV-visible DSR spectra of c-BN at different ball milling time:
 a) 0 hrs b) 50 hrs c) 125 hrs d) 175 hrs

The thermal stability test was conducted to study the effect of ball milling time on the degradation temperature of c-BN. Figure 9 shows the Thermogravimetric analysis. The TGA graphs are similar for all samples. The weight loss occurred for all samples at room temperature up to 700°C except for the sample obtained at 175 hours of ball milling. The weight loss may be attributed to the increased surface area of the ball-milled sample. The weight loss is as high as 3% in the 100-hour ball-milled sample. The weight loss slightly decreased as the grinding time increased, as seen in the 150- and 175-hour ball-milled sample. No significant weight loss was observed for all samples after 700°C. After the TGA test, ash was collected for all samples, and the amount of ash formed at higher ball milling time was significantly less than that for 100 hours of ball milling.

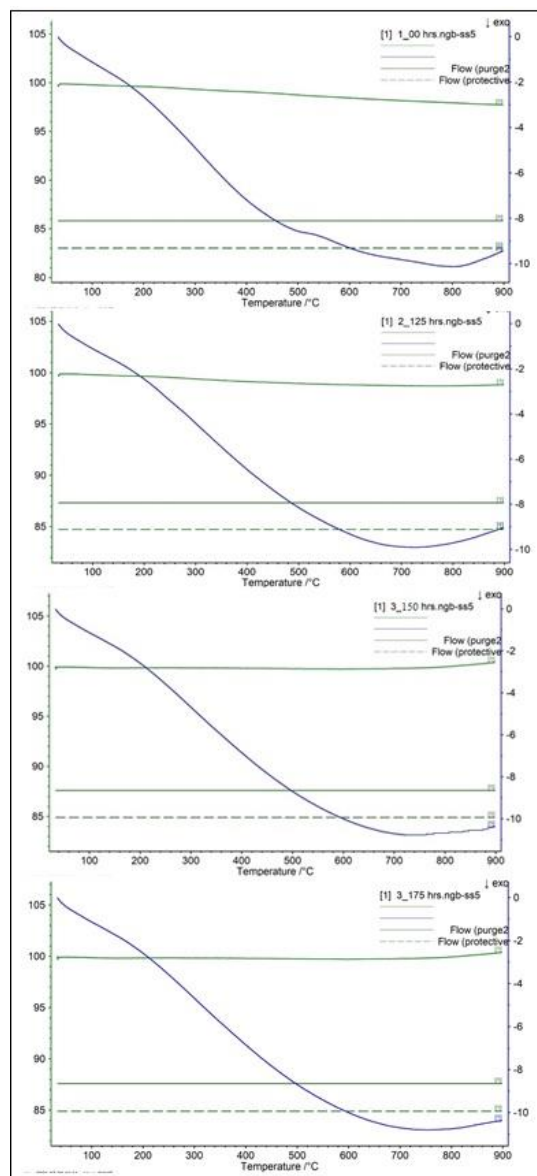


Figure 9. Thermogravimetric analysis of c-BN

4. Conclusion

Nano c-BN was obtained through a simple, eco-friendly ball milling process at different rotational speeds. Effect of ball milling time on morphology and crystallite size was studied. Nano c-BN obtained at 150 to 175 hours of ball milling at 50 rpm were used for the characterization studies. XRD data revealed that increasing ball milling time decreased the peak intensity, and a few peaks disappeared with increased rpm. c-BN nanoparticles were found to have irregular shapes with sizes ranging from 57 to 78 nm. Stronger reflectance was observed with increased ball milling time in the DSR spectra. There was weight loss for all samples at room temperature up to 700°C in the TGA studies. No significant weight loss was observed for all samples after 700°C.

6. References

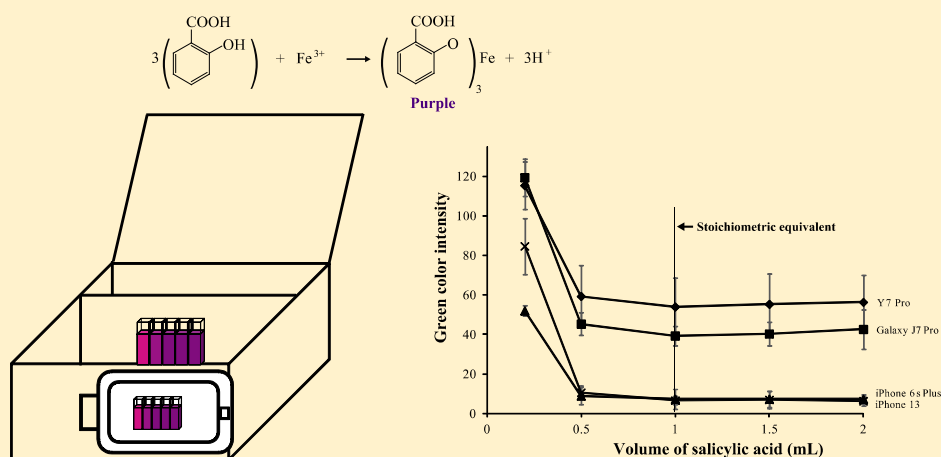
- Arkundato A., Hasan M., Purwandari E., Pramutadi A., & Aziz F., "Temperature dependence diffusion coefficients of iron, boron and iron-boron calculated by molecular dynamics method" *J. Phys.: Conf. Ser.* (2019) 1170. doi:10.1088/1742-6596/1170/1/012008.
- Arkundato A., Su'ud Z., Abdullah M., & Widayani "Inhibition of high corrosion in high temperature stagnant liquid lead: A molecular dynamics study." *AIP Conf Proc* 1244 (2010) 136. doi.org/10.1088/1742-6596/1170/1/012008.
- Arya S. P. S., & D'Amico A., "Preparation, properties and applications of boron nitride thin films". *Thin Solid Films*, 157, (1988), 267–282. doi.org/10.1016/0040-6090(88)90008-9
- Bass J. D., Solovyov A., Pascall A. J., Katz A., & Am J. "Acid-Base Bifunctional and Di-electric Outer-Sphere Effects in Heterogeneous Catalysis: A Comparative Investigation of Model Primary Amine Catalysis". *Chem. Soc.*, 128, (2016), 3737–3747. doi.org/10.1007/s10934-011-9546-x.
- Brazhkin, Vadim V.; Solozhenko, Vladimir L. "Myths about new ultrahard phases: Why materials that are significantly superior to diamond in elastic moduli and hardness are impossible". *J. Appl. Phys.* 13, (2019), 125. doi.org/10.1063/1.5082739.
- Bennett T. D., & Cheetham A. K., "Amorphous Metal-Organic frameworks". *Acc. Chem. Res.* 47, (2014), 1555–1562.
- Davis R. F., "III-V nitrides for electronic and optoelectronic applications". *Proc. IEEE*, 79, (1991), 702. www.lib.ncsu.edu/resolver/1840.2/610
- DeVries C., "Recent advances in grinding". *Research Conference Proceedings*, 25, (1972), 178. doi.org/10.1007/978-1-4615-8300-410.
- Gielisse P. J., Mitra S. S., Plend J. N., Griffis R. D., Mansur L. C., Marshall R. & Pascoe E. A., "Lattice infrared spectra of Boron Nitride and Boron mono phosphide". *Phys. Rev.*, 155, (1967), 1039–1046. doi.org/10.1103/PhysRev.155.1039.
- Ishii T., Sato T., Sekikawa Y., Iwata M., "Growth of whiskers of hexagonal Boron Nitride", *Crystal Growth*, 52, (1981), 285–289. doi.org/10.1016/0022-0248(81)90206-2.
- Kester D. J., & R. Messier., "Mechanism of nucleation and growth of cubic-Boron Nitride thin films". *J. Appl. Phys.*, 72, (1992), 504–513. doi.org/10.1016/S1468-6996(01)00004-3.
- Laurence Vel, Gerard Demazeau and Jean Etourneau "Cubic boron nitride: synthesis, physicochemical properties and applications". *Mater. Sci. Eng. B* (1991) 149–164. doi.org/10.1016/0921-5107(91)90121-B.
- Lee D., Lee B., Park K. H., Ryu H. J., Jeon S., & Hong S. H., "Scalable exfoliation process for highly soluble boron nitride nanoplatelets by hydroxide assisted ball-milling". *Nano Lett.*, 15, (2015), 1238–1244. doi.org/10.1038/srep07288.
- Liu L., Xiong Z., Hu D., Wu G., Liu B., & Chen P., "Solid Exfoliation of Hexagonal Boron Nitride Crystals for the Synthesis of Few-layer Boron Nitride Nanosheets". *Chem. Lett.*, 42, (2013), 1415–1416. doi.org/10.1016/j.carbon.2014.10.008.
- Lu C. J., & Li Z. Q., "Thermodynamic aspects of nano structured Ti₅Si₃ formation during mechanical alloying and its characterization". *J. Alloy. Compd.* 395, (2005) 88. doi.org/10.1007/s12034-012-0298-2.
- Lu M., Bousetta A., Sukach R., Bensaoula A., Waters K., Eipers-Smith K. & Schultz J. A., "Growth of c-BN on Si (100) by neutralized nitrogen ion bombardment". *Appl. Phys. Lett.*, 64, (1994), 1514–1516.
- Mishima O., Era K., Tanaka J., & Yamoka S., "Observation of a hexagonal BN surface layer on the cubic BN film grown by dual ion beam sputter deposition". *Appl. Phys. Lett.*, 53, (1988), 962–964. doi.org/10.1063/1.118402.
- Orellana-Tavara C., Baxter E. F., Tian T., Bennett T. D., Slater N. K. H., Cheetham A. K., & Fairen-Jimenez D., "Amorphous metal-organic frameworks for drug delivery". *Chem. Commun.*, 51, (2015), 13878–13881. doi.org/10.1039/C5CC05237H.

- Pouch J. J., & Alterovitz S. A., "Review of synthesis and properties of cubic boron nitride (c-BN) thin films". Brookfield, Trans Tech Publications. Proc. Mater. Sci. Forum, 54/55, (1990), 313–328. doi.org/10.1016/S0927-796X(97)00009-0.
- Reddy L. M., Srivastava A., & Gowda S. R., et al., "Synthesis of nitrogen-doped graphene films for lithium battery application," ACS Nano, 4, (2010) 6337–6342. doi.org/10.1021/nn101926g.
- Song L., Ci L., Lu H., Sorokin P. B., Jin C., Ni J., Kvashnin A. G., Kvashnin D. G., Lou J., Yakobson B. I. & Ajayan P. M., "Large Scale Growth and Characterization of Atomic Hexagonal Boron Nitride Layers." Nano Letters, 10, (2010), 3209–3215. doi.org/10.4236/jct.2013.46A2001.
- Shashikala, A R.; Mayanna, S M.; Sharma, A. Studies and characterization of electroless Ni–Cr – Palloy coating. Trans IMF, (2007), 85, 6, 320324. doi.org/10.1179/174591907X246483.
- Shashikala, A. R.; Sridhar, B, S. Codeposition of electroless Ni–P/ZnO nano composites and evaluation of corrosion resistance of the coatings. Materials Today: Proceedings, (2021), 45, 4, 3837–3840. doi.org/10.1016/j.matpr.2020.05.447.
- Todd R. H., Allen D. K., & Alting L., "Synthesis and preparation of mono-layer h-BN nano powders by using a combination of CVD method with iso-propanol- assisted exfoliation process". Manufacturing Processes Reference Guide, Industrial Press Inc., 55. N.Y. (1994), 43–48. doi.org/10.1007/s11106-017-9836-1.
- Vel L., Demazeau G., & Etourneau J., "Cubic-boron nitride: synthesis, physicochemical properties and applications". Mater. Sci. Eng. B, 10, (1991), 149–164. doi.org/10.1016/0921-5107(91)90121-B.
- Wada T., & Yamashita N., "Cross-sectional transmission electron microscopy observations of c-BN films deposited in Si by ion- beam-assisted deposition". J. Vac. Sci. Technol. A, 10, (1992), 515–520. doi.org/10.1016/0040-6090(94)90297-6.
- Wang P., Orimo S., Matsushima T., Fujii H., & Majer G., "Synthesis of boron nitride nano fibers and measurement of their hydrogen uptake capacity". Appl. Phys. Lett., 80, (2002), 318–320. doi.org/10.1016/S0008-6223(03)00302-6.
- Wentorf R. H., Jr: "Preparation of semiconducting Cubic Boron Nitride". J. Chem. Phys., 36, (1962), 1990–1991. doi.org/10.1063/1.1732816.
- Xia Z. P., & Li Etourneau Z. Q. "Structural evolution of hexagonal BN and cubic BN during ballmilling" J. Alloy. Compd. 43(2007)170-173. doi.org/10.1016/j.jallcom.2006.06.100.
- Xia Z. P., Li Z. Q., Lu C. J., Zhang B., & Zhou Y., "Structural evolution of Al/BN mixture during mechanical alloying". J. Alloy. Compd. 399, (2005), 139. doi.org/10.1016/j.jallcom.2005.03.087.
- Zhi C. Y., Bando Y., & Tang C. C, et al., "Large scale fabrication of boron nitride nanosheets and their utilization in polymeric composites with improved thermal and mechanical properties," Adv. Mater., 21, (2009) 2889–2893. doi.org/10.1002/adma.200900323.

A SIMPLE 3D TOOLBOX-BASED SMARTPHONE COLORIMETER: THE ABILITY TO DETECT THE STOICHIOMETRIC EQUIVALENT OF A CHEMICAL REACTION

Nuntaporn Moonrungsee^{1a}, Jaron Jakmunee^{2b}, Apaporn Boonmee^{3a}, Juthaporn Kaewloy^{4a}, Waranya Wongkasem^{5a}, and Nipat Peamaroon^{6a*}

Abstract: The simple 3D toolbox is constructed and utilized with a smartphone to detect the stoichiometric equivalent of chemical reactions. The reaction chosen for this purpose involves salicylic acid and iron(III) ions, forming a purple complex. An image of the resultant purple product is captured and analyzed for RGB color intensities. These color intensities are contingent upon the concentration of the colored product, and a consistent color intensity is observed once the reaction reaches its stoichiometric point. Numerous smartphones were tested for image capture and color intensity measurement. It was discovered that all smartphones are suitable, although tuning the white balance mode is necessary to obtain clear images for accurate color intensity measurement. This smartphone-based spectrometer yields results comparable to those obtained from a commercial ultraviolet-visible spectrometer. This endeavor can serve as a blueprint for developing portable devices in chemical analysis using smartphones. Furthermore, the device and methodology developed herein can be effectively replicated in chemistry laboratory classes to impart a practical understanding of stoichiometry and chemical reactions through smartphone-based experimentation.



Keywords: Colorimetry, iron(III) ion, salicylic acid, smartphone, stoichiometric equivalent

Authors information:

^aDepartment of Chemistry, Faculty of Science and Technology, Rambhai Barni Rajabhat University, Chanthaburi 22000, THAILAND. E-mail: nuntaporn.m@rbru.ac.th¹; apaporn.b@rbru.ac.th³; juthaporn.23463@gmail.com⁴; waranyarung13@gmail.com⁵; nipat.p@rbru.ac.th⁶

^bDepartment of Chemistry and Center of Excellence for Innovation in Chemistry and Research Center on Chemistry for Development of Health Promoting Products from Northern Resources, Faculty of Science, Chiang Mai University, Chiang Mai 50200, THAILAND. E-mail: jaron.jakmunee@cmu.ac.th²

*Corresponding Author: nipat.p@rbru.ac.th

Received: July 9, 2022

Accepted: January 23, 2023

Published: October 31, 2023

1. Introduction

Nowadays, a smartphone can be used not only for human communication and entertainment but also for sensing and chemical analysis (Crocombe, 2018). The important feature is the smartphone's camera, which can capture an image and discriminate the color under controlled illuminance (Nixon et al., 2020). Based on the colorimetric method, pictures of standard solutions with different colors were taken and read for RGB color intensities to create a calibration graph for analyzing samples. The advantages of this method are portability, simplicity, low cost, and ease of operation. The achievements of these smartphone-based spectrophotometric methods have been widely reported in various fields, such as agriculture (Jin et al., 2021; Qi et al., 2020), education (Kajornklin et al., 2020; Santos et al., 2020), the environment (Koohkan et al., 2020; Sargazi & Kaykhaii, 2020), food (Peamaroon et al., 2021; Ko et al., 2021), forensic science (Li et al., 2020; Jackson et al., 2020), industry (Moonrungeesee et al., 2020; Shahvar et al., 2020), medical diagnostics (Samacoits et al., 2021; Kap et al., 2021), and pharmaceuticals (Phadungcharoen et al., 2020; Lantam et al., 2020).

The achievements of these smartphone-based spectrophotometers depended on the light-controlled box. The illuminance must be controlled to spread constantly around the samples. The sample blank is also required to be set, following the manner of the spectrophotometric method. In our previous works, many versions of light-controlled boxes have been fabricated using low-cost materials such as plastic and paper sheets for chemical analysis, including phosphorus (Moonrungeesee et al., 2015), iron(III) (Moonrungeesee et al., 2016), tyrosinase inhibitory activity (Moonrungeesee¹ et al., 2018), salicylic acid (Moonrungeesee² et al., 2018), copper(II) (Moonrungeesee et al., 2020), and iodine number (Peamaroon et al., 2021), with a smartphone or a digital camera.

This work constructed the latest version of our designed box using a 3D printer. Another aspect of the smartphone spectrometer as a color measurement device is presented. A simple toolbox incorporated with a smartphone was employed to detect the stoichiometric equivalent of a chemical reaction. This work can serve as a guideline for creating a simple and low-cost smartphone-based spectrometer used for specific purposes.

2. Experimental

2.1 Chemicals and Solutions Preparation

All chemicals were of analytical reagent grade. All solutions were prepared using distilled water. A 3.0 mM iron(III) chloride solution ($\text{FeCl}_3 \cdot 6\text{H}_2\text{O}$, Honeywell International Inc., Switzerland) was freshly prepared by dissolving 0.0203 g of iron(III) chloride in 25.00 mL of water. A 1.5 mM iron(III) chloride solution was prepared by diluting the 3.0 mM iron(III) chloride solution. A 4.5 mM salicylic acid solution ($\text{C}_7\text{H}_6\text{O}_3$, Ajax Finechem, Australia) was prepared by dissolving 0.0156 g of salicylic acid in a small volume of ethanol ($\text{C}_2\text{H}_5\text{OH}$, Ajax Finechem, Australia) and adjusted to the volume of 25.00 mL with water. A 0.1 M chromium(III) nitrate solution ($\text{Cr}(\text{NO}_3)_3 \cdot 9\text{H}_2\text{O}$, Honeywell International Inc., Switzerland) and a 0.1 M ammonium sulphate solution

($(\text{NH}_4)_2\text{SO}_4$, Ajax Finechem, Australia) were prepared by dissolving 1.0004 g and 0.3304 g of solids in 25.00 mL of water, respectively. Finally, a 3.0 mM potassium thiocyanate solution (KSCN, Ajax Finechem, Australia) was prepared by dissolving 0.0073 g of potassium thiocyanate in 25.00 mL of water.

2.2 Device Fabrication and Color Intensity Analysis

A simple 3D toolbox was designed using the Tinkercad program, a free and user-friendly web application. The dimensions of the box were set at 15 cm \times 15 cm \times 9 cm (width \times length \times height), and the cover measured 15 cm \times 15 cm (width \times length). The designed models were then exported to STL format for compatibility with a 3D printer (XYZ Printing, da Vinci 1.0 Pro, Taiwan). The box was constructed using white polylactic acid (PLA) plastic as the printing filament. The box's exterior was covered with a black sticker sheet to create a controlled environment, as shown in **Figure 1(a)**. Illumination inside the box was regulated by a strip of white light-emitting diode (LED) lamps affixed to the inner wall at the back end of the box, as depicted in **Figure 1(b)**. The LED lamps were powered by a 12-volt direct current (DC) power supply. A white acrylic screen with a thickness of 1 mm was positioned 4 cm away from the lamps. Plastic cuvettes with a 1 cm optical path, serving as sample holders (up to 6 cuvettes), were positioned in front of the white acrylic screen. White plastic fins were inserted between the sample cuvettes to prevent color interference. A window measuring 3 cm \times 3 cm on the front of the box allowed for the attachment of a smartphone to capture images of the color products.

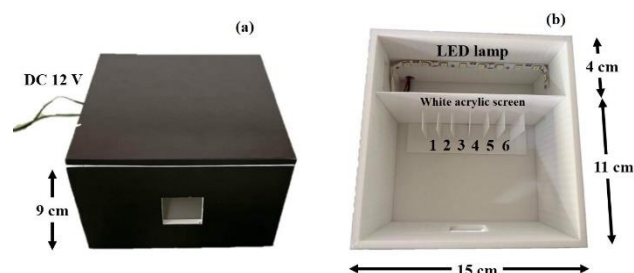


Figure 1. Dimensions and details of a simple 3D toolbox
(a) outside (b) inside

A smartphone equipped with a fixed-focus camera, disabled flash, automatic white balance, and single image mode was positioned in front of the box to capture images of cuvettes containing the colored products resulting from reactions. The cuvettes were placed at the front of the white acrylic screen to minimize shadow effects and ensure optimal image capture. Each captured image was then analyzed using the Color Grab or Color Picker application, both available for free download and compatible with Android and iOS smartphones. These applications allowed the images stored in the smartphone's memory to be imported into the program for analysis. To determine color intensities, a screen touch was used to pinpoint the center of each cuvette, and the intensities of the red (R), green (G), and blue (B) colors were measured. The resulting color intensity values were displayed on the smartphone screen in the

form of three-number series (R, G, B), such as 0, 0, 0, and 255, 255, 255 for black and white colors, respectively.

2.3 Reaction to Form the Colored Products

Three distinct colored products, namely purple, green, and red, were prepared to detect their respective stoichiometric equivalents. To generate the purple product, salicylic acid was reacted with iron(III) ions in a mole ratio of 3:1. The green product, on the other hand, was produced by the reaction between chromium(III) ions and ammonium sulfate in a mole ratio of 1:1. Lastly, the red product was obtained through the reaction between 1 mole of potassium thiocyanate and 1 mole of iron(III) ions. The stoichiometry of these reactions is illustrated in **Figure 2**. To enable accurate measurement using smartphones, the proportions of reactants were adjusted to achieve distinct and vibrant colors. The optimized formulas and comprehensive reaction details are outlined in a step-by-step manner as follows:

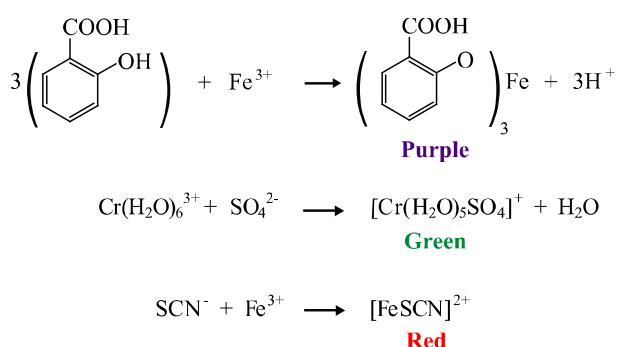


Figure 2. Chemical reaction for producing three colored products (purple, green, and red)

2.3.1 Reaction between Salicylic Acid and Iron(III) Ion

A volume of 1 mL of 1.5 mM iron(III) chloride solution, designated as the limiting reagent, was transferred to five cuvettes. Subsequently, 4.5 mM salicylic acid solution was added to the cuvettes in volumes of 0.2, 0.5, 1.0, 1.5, and 2.0 mL, respectively. Distilled water was added to achieve a final volume of 3 mL in all cuvettes.

2.3.2 Reaction between Chromium(III) Ion and Ammonium Sulphate

A volume of 1 mL of 0.1 M chromium(III) nitrate solution, designated as the limiting reagent, was transferred to five test tubes. Then, 0.1 M ammonium sulphate solution was added to the test tubes in volumes of 0.2, 0.5, 1.0, 1.5, and 2 mL, respectively. Afterward, distilled water was added to reach a final volume of 3 mL in all test tubes. Subsequently, all test tubes were heated in hot water (80-90°C) for 5-10 minutes.

2.3.3 Reaction between Potassium Thiocyanate and Iron(III) Ion

A volume of 1 mL of 3.0 mM iron(III) chloride solution, designated as the limiting reagent, was transferred to five cuvettes. Then, 3.0 mM potassium thiocyanate solution was added to the cuvettes in volumes of 0.2, 0.5, 1.0, 1.5, and 2.0 mL, respectively. Finally, distilled water was added to achieve a final volume of 3 mL in all cuvettes.

The reaction products, which exhibited the colors purple, green, and red, were initially analyzed using an ultraviolet-visible spectrophotometer (Thermo Scientific, model GENESYS 10S, USA) at wavelengths of 530 nm, 595 nm, and 545 nm, respectively. Following this, one of the reactions was chosen for analysis using the smartphone colorimeter. Images of the reaction products placed within the simple 3D toolbox were captured using a smartphone. These images were then analyzed for color intensity using freely available applications (such as Color Grab or Color Picker) installed on the smartphone, allowing for the inspection of stoichiometric equivalents. The intensities of the red, green, and blue (RGB) colors were assessed to determine the optimal color intensity. The point of constant color intensity, signifying the achievement of stoichiometry, was observed.

2.4 Evaluating Suitability of Various Smartphones

Four smartphone brands (Samsung, Vivo, Huawei, and Apple) with ten models were employed to detect stoichiometry using their default camera functions. All ten smartphones were set to fixed-focus camera mode without flash, automatic white balance, and single image mode. These smartphones were positioned in front of the box to capture images through the box window. The specifications of the smartphones utilized are presented in **Table 1**.

Table 1. Specifications of the 10 smartphones used for color measuring device

No.	Brand	Model	Operating system	Camera maximum resolution (megapixels)
1	Samsung	Galaxy J7 Pro	Android	13
2	Samsung	Galaxy A7	Android	24
3	Vivo	V11	Android	16
4	Huawei	Y7 Pro	Android	13
5	Apple	iPhone 6s Plus	iOS	12
6	Apple	iPhone XR	iOS	12
7	Apple	iPhone 12 Pro	iOS	12
8	Apple	iPhone 7	iOS	12
9	Apple	iPhone 12 Pro Max	iOS	12
10	Apple	iPhone 13	iOS	12

3. Results and Discussions

3.1 The Simple Toolbox Performance

The precision of the simple 3D toolbox was assessed by calculating the percentage of relative standard deviation (%RSD = (standard deviation of color intensity/mean of color intensity) × 100) of the measured color intensities. Food coloring solutions (red, green, and blue) at a concentration of 0.001% w/v were added to five cuvettes and measured using three smartphones with iOS and Android operating systems. This test aimed to evaluate the color intensities. The results indicated that the color intensities exhibited similar values across all five cuvettes for each tested color. The %RSD for each color solution was less than 10%, confirming the suitability of this toolbox for color intensity measurements.

3.2 Spectrophotometric Measurement

All the reactions were designed to use a constant volume of 1 mL for the limiting reagent. The other reactant was incrementally added to reach the equivalence point. After this point, a constant color intensity product could be achieved despite excess reactant. The absorbance of the purple, green, and red products was measured. The purple and green products displayed constant absorbance after reaching the equivalence points (**Figure 3(a)-(b)**), while the absorbance of the red product remained higher (**Figure 3(c)**). This could be attributed to the chemical equilibrium that influenced the color of the red product. The reaction between potassium thiocyanate and iron(III) ion could not be completed under our conditions. When comparing the reactions for forming the purple and green products, the reaction between chromium(III) ion and ammonium sulphate was more complex, likely due to the heating step involved. Additionally, the former reaction required a longer time to reach completion. Consequently, the reaction between salicylic acid and iron(III) ion (with iron(III) ion as the limiting reagent) to form the purple product was selected for smartphone-based measurement.

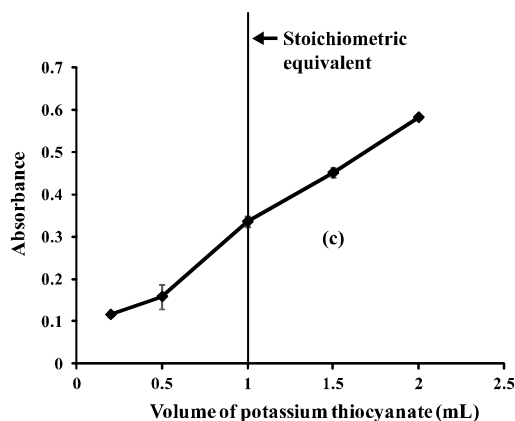
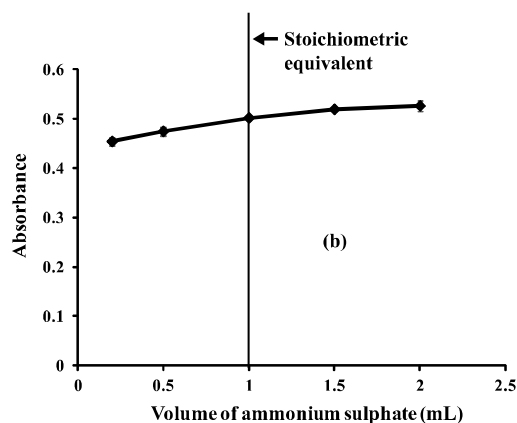
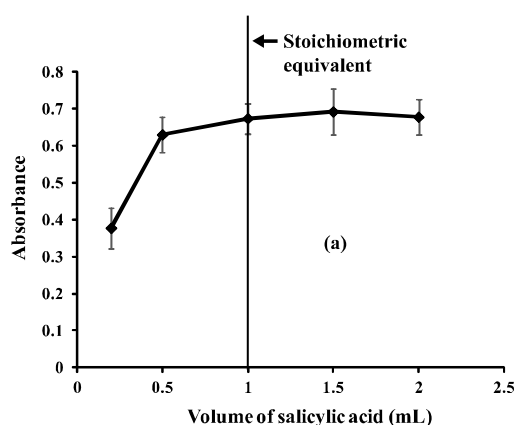


Figure 3. Absorbance of the products from the reaction between (a) salicylic acid (4.5 mM) and iron(III) ion (1.5 mM, 1 mL); (b) ammonium sulphate (0.1 M) and chromium(III) nitrate (0.1 M, 1 mL); (c) potassium thiocyanate (3.0 mM) and iron(III) ion (3.0 mM, 1 mL)

3.3 Smartphone Colorimetric Measurement

3.3.1 RGB Color Intensities

The smartphone (iPhone 6s Plus) captured an image of five cuvettes filled with the purple product. The intensities of the RGB colors for each cuvette were measured and plotted as a function of the volume of salicylic acid, as depicted in **Figure 4**. All colors exhibited a constant intensity after reaching the equivalence point at 1.0 mL of salicylic acid. However, the green color displayed the highest intensity difference between 0.5 and 1.0 mL of salicylic acid compared to the red and blue colors. This indicated that the green color provided better sensitivity than the red and blue colors. As a result, subsequent measurements were conducted using the intensity of the green color.

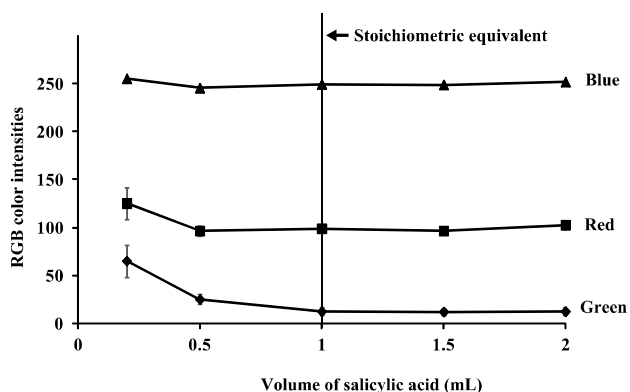


Figure 4. Intensities of RGB colors of the products from the reaction between salicylic acid (4.5 mM) and iron(III) ion (1.5 mM, 1 mL)

3.3.2 Effect of Smartphones Varieties

The image of the five cuvettes containing the purple products was captured using ten different smartphones (Table 1). Figure 5 illustrates that the same image taken with various smartphones displayed different color intensity values due to differences in camera performance. This phenomenon was observed even when smartphones with the same camera resolution were used. Additionally, despite setting the automatic white balance mode on all smartphones, picture clarity and color variations were observed among both iOS and Android smartphones. These variations impacted the color intensities derived from the captured images.

The figure indicates that clear pictures obtained from smartphones such as Y7 Pro, Galaxy A7, Galaxy J7 Pro, iPhone 6s Plus, iPhone 13, and V11 yielded accurate results, showing the true colors of the samples. Following the equivalence point, a constant green color intensity was observed. On the other hand, the remaining smartphones (iPhone XR, iPhone 12 Pro, iPhone 7, and iPhone 12 Pro Max) produced light blue pictures and inaccurate results, with a green color intensity of zero at a volume of 0.5 mL of salicylic acid.

The current market offers a wide variety of smartphones, which presents challenges in maintaining control over this study. Color evaluation using different smartphones results in varying color intensities (Souza et al., 2018). It is necessary to adjust the white balance mode of the smartphone to obtain clear pictures before conducting measurements. Consequently, a fixed green color intensity cannot be universally applied to all smartphones. Determining the optimal RGB color for analysis is essential. For simplified operation, it is recommended to designate and use one smartphone per box for sample analysis.

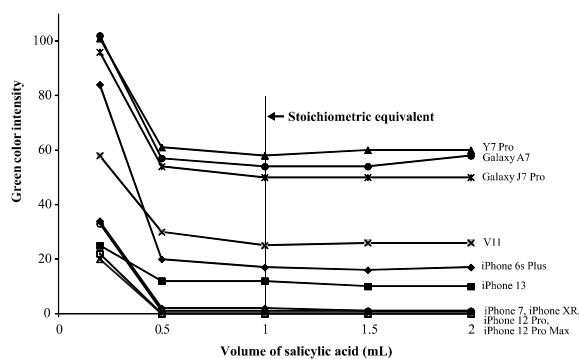


Figure 5. Intensity of green color from the ten smartphones in the range of 0.2-2.0 mL salicylic acid

Four smartphones were selected for the stoichiometric study: two Android devices (Y7 Pro, Galaxy J7 Pro) and two iOS devices (iPhone 6s Plus, iPhone 13). The study was repeated thrice (n=3), and the outcomes are presented in Figure 6. The green color intensity exhibited a consistent pattern following the equivalence point (1.0 mL of salicylic acid). This constant trend persisted even in excess reactant, indicating that the colored product remained unchanged. This consistent behavior of the curve was evident across all four smartphones.

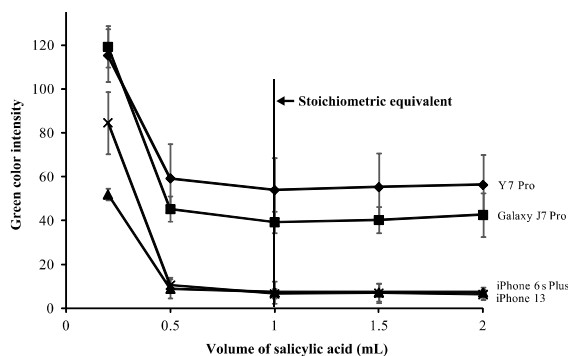


Figure 6. Intensity of green color from the four smartphones in the range of 0.2-2.0 mL salicylic acid.

In conclusion, this study presents a versatile approach that can be applied to monitor a wide range of chemicals, particularly hazardous substances like radioactive elements, pesticides, and heavy metals. The smartphone spectrometer demonstrated excellent performance in detecting colors across the visible light spectrum. In cases where the analyte lacks color or is present in low concentrations, a chemical reaction is employed to produce a colored product. By utilizing a selective color-forming reagent, this method allows for both qualitative and quantitative analysis. The excess reagent reacts with the analyte, forming a colored product whose intensity is linearly proportional to its concentration. For instance, salicylic acid can be determined using excess iron(III) ions as a coloring reagent (Moonrunsee² et al., 2018), and vice versa (Rajendraprasad & Basavaiah, 2016). The remaining unreacted reagent remains stable and

does not interfere when mixed with the colored product. Furthermore, this approach has practical applications in educational settings, as it can be implemented in chemistry laboratory classes to teach concepts related to stoichiometry and chemical reactions using smartphones.

4. Conclusion

To summarize, this work demonstrates the adaptation of a smartphone for measuring RGB intensities of sample solutions within a specially designed light-controlled box referred to as the "simple 3D toolbox". The device successfully detected the stoichiometric equivalent of the reaction between salicylic acid and iron(III) ion. Notably, constant color intensities were observed once the reaction reached its stoichiometry. While all smartphones can be employed, it is important to note that fine-tuning the white balance mode may be necessary to ensure clear and accurate measurements.

5. Acknowledgement

This work was financially supported by the research fund of Rambhai Barni Rajabhat University. The authors would like to thank the Faculty of Science and Technology, Rambhai Barni Rajabhat University, for the partial support.

6. References

- Crocombe R.A. (2018). Portable spectroscopy. *Applied Spectroscopy* 72: 1701-1751. <https://doi.org/10.1177/0003702818809719>
- Jackson K.R., Layne T., Dent D.A., Tsuei A., Li J., Haverstick D.M. & Landers J.P. (2020). A novel loop-mediated isothermal amplification method for identification of four body fluids with smartphone detection. *Forensic Science International: Genetics* 45: 102195. <https://doi.org/10.1016/j.fsigen.2019.102195>
- Jin R., Wang F., Li G., Yan X., Liu M., Chen Y., Zhou W., Gao H., Sun P. & Lu G. (2021). Construction of multienzyme-hydrogel sensor with smartphone detector for on-site monitoring of organophosphorus pesticide. *Sensor and Actuator B: Chemical* 327: 128922. <https://doi.org/10.1016/j.snb.2020.128922>
- Kajornklin P., Jarujamrus P., Phanphon P., Ngerpradab P., Supasorn S., Chairam S. & Amatatongchai M. (2020). Fabricating a low-cost, simple, screen printed paper towel-based experimental device to demonstrate the factors affecting chemical equilibrium and chemical equilibrium constant, K_c . *Journal of Chemical Education* 97: 1984-1991. <https://doi.org/10.1021/acs.jchemed.9b00918>
- Kap O., Kilic V., Hardy J.G. & Horzum N. (2021). Smartphone-based colorimetric detection systems for glucose monitoring in the diagnosis and management of diabetes. *Analyst* 146: 2784-2806. <https://doi.org/10.1039/D0AN02031A>
- Ko C.H., Liu C.C., Chen K.H., Sheu F., Fu L.M. & Chen S.J. (2021). Microfluidic colorimetric analysis system for sodium benzoate detection in foods. *Food Chemistry* 345:128773. <https://doi.org/10.1016/j.foodchem.2020.128773>
- Koohkan R., Kaykhai M., Sasani M. & Paull B. (2020). Fabrication of a smartphone-based spectrophotometer and its application in monitoring concentrations of organic Dyes. *ACS Omega* 5: 31450-31455. <https://doi.org/10.1021/acsomega.0c05123>
- Lantam A., Limbut W., Thiagchanya A. & Phonchai A. (2020). A portable optical colorimetric sensor for the determination of promethazine in lean cocktail and pharmaceutical doses. *Microchemical Journal* 159: 105519. <https://doi.org/10.1016/j.microc.2020.105519>
- Li X., Li J., Ling J., Wang C., Ding Y., Chang Y., Li N., Wang Y. & Cai J. (2020). A smartphone-based bacteria sensor for rapid and portable identification of forensic saliva sample. *Sensor and Actuator B: Chemical* 320: 128303. <https://doi.org/10.1016/j.snb.2020.128303>
- Moonrungsee¹ N., Peamaroon N., Boonmee A., Suwancharoen S. & Jakmunee J. (2018). Evaluation of tyrosinase inhibitory activity in Salak (*Salacca zalacca*) extracts using the digital image-based colorimetric method. *Chemical Paper* 72: 2729-2736. <https://doi.org/10.1007/s11696-018-0528-1>
- Moonrungsee N., Pencharee S. & Jakmunee J. (2015). Colorimetric analyzer based on mobile phone camera for determination of available phosphorus in soil. *Talanta* 136: 204-209. <https://doi.org/10.1016/j.talanta.2015.01.024>
- Moonrungsee N., Pencharee S., Junsomboon J., Jakmunee J. & Peamaroon N. (2020). A simple colorimetric procedure using a smartphone camera for determination of copper in copper supported silica catalysts. *Journal of Analytical Chemistry* 75: 200-207. <https://doi.org/10.1134/S1061934820020136>
- Moonrungsee N., Pencharee S. & Peamaroon N. (2016). Determination of iron in zeolite catalysts by a smartphone camera-based colorimetric analyzer. *Instrumentation Science & Technology* 44: 401-409. <https://doi.org/10.1080/10739149.2015.1137587>

- Moonrungsee² N., Prachain C., Bumrungrakij C., Jakmunee J. & Peamaroon N. (2018). A simple device with a smartphone camera for determination of salicylic acid in foods, drugs and cosmetics (in Thai). *The Journal of KMUTNB* 28: 639-648. <https://doi.org/10.14416/j.kmutnb.2018.03.001>
- Nixon M., Outlaw F. & Leung T.S. (2020). Accurate device-independent colorimetric measurements using smartphones. *PLOS ONE* 15: 1-19. <https://doi.org/10.1371/journal.pone.0230561>
- Peamaroon N., Jakmunee J. & Moonrungsee N. (2021). A simple colorimetric procedure for the determination of iodine value of vegetable oils using a smartphone camera. *Journal of Analysis and Testing* 5: 379-386. <https://doi.org/10.1007/s41664-021-00168-x>
- Phadungcharoen N., Pengwanput N., Nakapan A., Sutitaphan U., Thanomklom P., Jongudomsombut N., Chinsriwongkul A. & Rojanarata T. (2020). Ion pair extraction coupled with digital image colorimetry as a rapid and green platform for pharmaceutical analysis: an example of chlorpromazine hydrochloride tablet assay. *Talanta* 219: 121271. <https://doi.org/10.1016/j.talanta.2020.121271>
- Qi M., Huo J., Li Z., He C., Li D., Wang Y., Vasylieva N., Zhang J. & Hammock B.D. (2020). On-spot quantitative analysis of dicamba in field waters using a lateral flow immunochromatographic strip with smartphone imaging. *Analytical and Bioanalytical Chemistry* 412: 6995-7006. <https://doi.org/10.1007/s00216-020-02833-z>
- Rajendraprasad N. & Basavaiah K. (2016). Modified spectrophotometric methods for determination of iron(III) in leaves and pharmaceuticals using salicylic acid. *Indian Journal of Advances in Chemical Science* 4: 302-307.
- Samacoits A., Nimsamer P., Mayuramart O., Chantaravisoot N., Sitthi-amorn P., Nakhakes C., Luangkamchorn L., Tongcham P., Zahm U., Suphanpayak S., Padungwattanachoke N., Leelarthaphin N., Huayhongthong H., Pisitkun T., Payungporn S. & Hannanta-anan P. (2021). Machine learning-driven and smartphone-based fluorescence detection for CRISPR diagnostic of SARS-CoV-2. *ACS Omega* 6: 2727-2733. <https://doi.org/10.1021/acsomega.0c04929>
- Santos R.C., Cavalcanti J.N.C., Carmo E.C.W., Souza F.C., Soares W.G., Souza C.G., Andrade D.F. & Avila L.A. (2020). Approaching diesel fuel quality in chemistry lab classes: undergraduate student's achievements on determination of biodiesel content in diesel oil applying solvatochromic effect. *Journal of Chemical Education* 97: 4462-4468. <https://doi.org/10.1021/acs.jchemed.0c00773>
- Sargazi M. & Kaykhai M. (2020). Application of a smartphone based spectrophotometer for rapid in-field determination of nitrite and chlorine in environmental water samples. *Spectrochimica Acta Part A: Molecular and Biomolecular Spectroscopy* 227: 117672. <https://doi.org/10.1016/j.saa.2019.117672>
- Shahvar A., Shamsaei D. & Saraji M. (2020). A portable smartphone-based colorimetric sensor for rapid determination of water content in ethanol. *Measurement* 150: 107068. <https://doi.org/10.1016/j.measurement.2019.107068>
- Souza W.S., De Oliveira M.A.S., De Oliveira G.M.F., De Santana D.P. & De Araujo, R.E. (2018). Self-referencing method for relative color intensity analysis using mobile-phone. *Optics and Photonics Journal* 8: 264-275. <https://doi.org/10.4236/opj.2018.87022>

DEBITTERING OF *Borassus flabellifer* MESOCARP USING NARINGINASE: IMPACT ON THE COMPOSITION, PHYSICOCHEMICAL CHARACTERISTICS, AND FUNCTIONAL PROPERTIES

Rodiah M. H^{1a,b*}, Jamilah, B^{2b} Norhayati, H^{3b} and Kharidah M^{4b}

Abstract: This study explores the physicochemical, composition, and functional properties of the *Borassus flabellifer* mesocarp powder following treatment with naringinase. The debittered mesocarp powder (DMP) has good water-holding (9.4 g/g), swelling (7.8 g/g), and wettability (12.3 s) capacities. Naringinase reduced 33.2% of the DMP particle size, causing an increase in surface area. A larger surface area traps more water/oil molecules, contributing to a higher water/oil capacity. However, the solubility, swelling, and wettability of DMP were markedly decreased following naringinase treatment. Nonetheless, although DMP has higher saponin, phenol, tannin, and DPPH activity contents than the control, it has decreased ferrous-reducing activity.

Keywords: Bitterness, dietary fibre, food ingredient and palmyra palm

1. Introduction

Palmyra palm (*Borassus flabellifer* Linn) is known as *kelapa laut* in Malaysia. *B. flabellifer* is from the *Arecaceae* family, subfamily *Borassoideae*, and genus *Borassus* (Nesbit, 2005). The palmyra fruit pulp is commercially used for beverages and food products (Chaurasiya et al., 2014; Vijaya Kumara & Prasad, 2015), with a high demand for the latter. Unfortunately, the fruit pulp bitterness is unfavoured by many. The fruit pulp is a part of the annual production of palmyra fruits and is often used as animal feed or discarded (Jansz et al., 2002). Measures to remove or control the bitterness for broader utilisation of the fruit pulp include the addition of pineapple pulp as a masking agent to conceal the bitterness of palmyra pulp (Thanusan et al., 2018) and the removal of bitterness in the tuber flour by soaking at 53 °C for 1 h (Thivya et al., 2018).

Enzymatic hydrolysis is commonly used to remove bitterness and acquire compounds with increased biological activity (Kumar, 2010). Naringinase has been commonly applied as a debittering agent of citrus fruit juice in the fruit juice industry during processing and aids in improving the stability and properties of the juices (Radhakrishnan et al., 2012). Unfortunately, the removal of bitterness using naringinase was more focused on citrus fruit and berry juices, such as kinnow mandarin juice (Puri, 2001), grape juice (Mishra & Kar, 2003), pummelo (*Citrus grandis*) fruit

juice (Ni et al., 2014), and orange juice (Zhu et al., 2017).

To date, reports on the effects of naringinase to remove bitterness from the mesocarp of *B. flabellifer* are scarce. Jansz et al. (1994) successfully attempted to debitter palmyra fruit pulp using naringinase (a mixture of β -glycosidase and β -rhamnosidase), resulting in a beverage with a pleasant mango cordial-like flavour, colour, and texture. A similar attempt was conducted by Ariyasena et al. (2001) to hydrolyse palmyra pulp using naringinase with reduced flabelliferin content without changing its nutritive values. However, the amount of reduced flabelliferin was not reported because the research only used thin-layer chromatography for estimation (only R_f value was reported).

It is beneficial that removing the bitter compound could control the bitterness of the final product without wastage or adversely affecting other desirable properties of the end product. According to Debenthini et al. (2014), the sensory scores of samples treated at various temperatures were significantly different ($p < 0.05$) from the control based on the bitter taste. The bitterness of the palmyra pulp was eliminated after a 1-h treatment at 60, 80, and 100 °C. Another group demonstrated improved bulk density and increased fibre, starch, and protein contents of the debittered flour of palmyra young shoot using the aqueous extraction technique (Thivya et al., 2018). It is hypothesised that the action of naringinase may influence the chemical and physical properties of the *B. flabellifer* mesocarp powder. Hence, this work investigates the physicochemical, composition, and functional characteristics of debittered *B. flabellifer* mesocarp powders after naringinase treatment.

Authors information:

^aUniversiti Selangor, Faculty of Engineering and Life Sciences, Department of Science and Biotechnology, Bestari Jaya Campus, Jalan Timur Tambahan, 45600 Bestari Jaya, Selangor, MALAYSIA. E-mail: rodiah@unisel.edu.my^{1*}

^b Universiti Putra Malaysia, Faculty of Food Science and Technology, 43400 Serdang, Selangor, MALAYSIA. E-mail: jamilah@upm.edu.my²; aryatihussain@upm.edu.my³; kharidah@upm.edu.my⁴

*Corresponding Author: rodiah@unisel.edu.my

Received: August 17, 2022

Accepted: February 7, 2023

Published: October 31, 2023

2. Materials & Methods

2.1 Materials

The main materials used in this investigation were as follows: mesocarp of *B. flabellifer*, gallic acid, Trolox, 2,2-diphenyl-1-picrylhydrazyl (DPPH), naringin, and naringinase (EC- 9068-31-9) with the activity of 10,000 units/g.

2.2 Sample Preparation for Debittering of *B. flabellifer*

The mesocarp of the immature *B. flabellifer* fruit was cut into smaller pieces, oven-dried (EW-00299-WK, Cole-Parmer, USA) at 50 °C for 24 h and ground (FZ-240, Zhong Xing, Malaysia) before naringinase treatment for the removal of bitterness. The sample was treated using 2.0 g/L of naringinase for 5 h at pH 5.0 and 55 °C. The mixture was then neutralised to pH 7.0 by adding 0.1 M sodium hydroxide (NaOH). The solid sample was collected by filtration through a strainer, and the filtrate was discarded. The sample was washed three times to remove the excess neutralising agent, re-filtered, and oven-dried (EW-00299-WK, Cole-Parmer, USA) at 50 °C for 24 h. The dried sample was ground for 5 min and sieved through a 0.5 mm sieve to obtain the debittered mesocarp powder (DMP). The mesocarp sample without the naringinase treatment was also prepared and used as a control.

2.3 Physicochemical Analysis

2.3.1 Proximate Analysis

The proximate composition of the DMP and control samples were analysed using the AOAC (2000) method. Other analyses involved were the moisture content (the oven method), crude protein (Kjeldahl method), crude fat (Soxhlet method), and dietary fibre (using the enzymatic-gravimetric method), as described by AOAC (2005).

2.4 Functional Properties of DMP and Control Sample

2.4.1 Solubility and Swelling Power

The solubility and swelling power of DMP and control samples were determined according to Osundahunsi et al. (2003). About 0.35 g of powder sample was mixed with distilled water (12.5 mL) before heating at 60 °C in a water bath for 30 min, with constant shaking. Following centrifugation at 3500 × g for 20 min, the supernatant was decanted into a pre-weighed evaporating dish and dried for 20 min at 100 °C. The solubility was acquired from the difference in the evaporating dish weight, and the weight of the residue after centrifugation was divided over the initial sample weight (dry weight basis) to determine the swelling power.

2.4.2 The Oil-holding and Water-holding Capacities

The oil-holding capacity (OHC) and water-holding capacity (WHC) were measured by mixing 1 g of BMF powder and 20 g of oil (or distilled water) by rigorous vortexing, with 10 min rest periods between each mixing before centrifugation at 3000 × g for 30 min. The remaining materials were weighed after decanting the free oil, and OHC was calculated as g of oil held per g of sample, whereas the WHC was deduced as g of water held per g of sample (Robertson et al., 2000).

2.4.3 The Wettability

The wettability was determined according to Belscak-Cvitanovic et al. (2010), i.e., the time required for 3 g of powder deposited on distilled water surfaces to fully submerge in 100 mL of distilled water at 27 °C.

2.5 Physical Analysis

The total soluble solids and pH were ascertained using a refractometer (Mettler Toledo, Schwerzenbach, Switzerland) and a pH meter (HI 221, Hanna, India). The colour of the DMP and control samples were analysed using a chromameter (00328Q, Konica Minolta, Japan), where L* denotes lightness from 0 (black) to 100 (white), a* and b* for redness (+a) to greenness (-a), and yellowness (+b) to blueness (-b; Reddy et al., 2015).

The particle size of each sample was measured using the Mastersizer S (Malvern Instruments Ltd, UK), according to Kelly et al. (2015). The median diameter, i.e., $d_{(v0.5)}$, was chosen to characterise the particle size of the powders. The bulk density was determined according to Samec et al. (2016). Sample powder was poured vertically into a 50-mL measuring cylinder through a cone. The measuring cylinder was subjected to 10 taps before the excess powder on the measuring cylinder was gently scraped off with a steel ruler, and the filled measuring cylinder was weighed.

2.6 Determination of Sugar Composition

The sugar composition of the DMP and control samples were determined according to AOAC (1993) and Puwastien et al. (2011). Sugar content was identified and quantified using HPLC (Agilent 1200 Series, USA). Glucose, fructose, mannose, sucrose, and galactose (Sigma-Aldrich, USA) were utilised as the standard sugars. A weight/weight percentage (g/100 g) of each sugar on the sample was calculated after duplicate injections of the samples.

2.7 Determination of Lignocellulosic Composition

Acid-insoluble lignin and holocellulose were determined based on the T222 om-88 standard method of TAPPI (Berlin et al., 2006). Meanwhile, cellulose and hemicellulose were measured according to Sabiha-Hanim et al. (2011) with modifications on the chemical concentration used. The composition of hemicellulose in the sample was estimated by the holocellulose and cellulose level differences.

2.8 Extraction of Bioactive Compounds

Bioactive compounds were extracted by microwave-assisted extraction technique (ME71K, Samsung, Korea), according to Asma et al. (2016). About 10 g of mesocarp powder was mixed with 200 mL 0.1 M NaOH in a Falcon tube, heated in the microwave at 300 W for 2 min and cooled to room temperature before filtering using a filter paper with a diameter of 150 mm (CHM, Germany). The filtrates were stored at 4 °C for further analysis. A similar procedure was performed for the control sample.

2.9 Phytochemical Analysis

Filtrates from the extraction were screened for their bioactive compounds, such as alkaloids, saponins, flavonoids, steroids, cardiac glycosides, tannins, terpenoids, anthraquinone, and flabelliferin (Obadoni & Ochuko, 2002; Obidoa et al., 2010; Aiyegroro & Okoh, 2010). Samples exhibiting positive results from the screening analysis were subjected to quantification.

2.10 Quantification of Phytochemical Content

2.10.1 Total Phenolic Content Determination

The Folin-Ciocalteu reaction method was utilised to determine the total phenolic content in the extract (Aiyegroro & Okoh, 2010). The standard gallic acid (0–125 µg/mL) was treated similarly to 200 µL of the sample, and the result was expressed as mg of GAE/g sample.

2.10.2 Tannin Determination

The method by Eleazu et al. (2012) was employed to evaluate tannin content in the extract. The tannic acid standard curve (0–500 ppm) was used to measure the samples' tannin content, represented as mg of tannic acid equivalence (TAE) per 100 g of dried sample.

2.10.3 Saponin Content Determination

Saponin content was determined by the percentage of the sample according to Obadoni and Ochuko (2001).

2.10.4 Crude Flabelliferin Determination

The extraction of crude flabelliferin from the mesocarp was adopted from Wickramasekara and Jansz (2003). A mixture of 80 mL of 10% methanol and 20 g of the sample was left at 30 °C for 16 h. The mixture was concentrated at 60 °C in a rotary evaporator after filtering through a filter paper (Whatman No1, U.S.A). The flabelliferin was twice extracted with 50 mL of ethyl acetate before being filtered with a 0.45-µm nylon syringe filter.

The extract was analysed for flabelliferin using the Davis colourimetric method (Puri et al., 2005). This study used naringin as the standard, as flabelliferin is not commercially available. Naringin comprises a sugar complex of α-L-rhamnosides and β-D-glucose, similar to flabelliferin. Naringin was dissolved in warm deionised water to prepare the standard concentration (100–500 ppm). Then, 0.1 mL of the standard solution was added to 5 mL of 90% diethylene glycol, followed by 0.1 mL of 4 N NaOH. The mixture was kept at 30 °C for 15 min. The resultant yellow colour was measured spectrophotometrically at 420 nm. The blank was prepared by treating distilled water similar to the standard procedure. For the sample, 0.1 mL of extract was added instead of the standard solution to measure the concentration of flabelliferin.

2.11 Antioxidant Activities

2.11.1 Determination of DPPH Radical Scavenging Assay

The free radical scavenging capacity, denoting the antioxidant capacity of the powder samples, was estimated spectrophotometrically using the stable radical DPPH (2,2-diphenyl-1-picrylhydrazyl) based on Chu et al. (2000). Standard Trolox from 100 to 500 µM/mL was prepared, and the results were expressed as mol of Trolox equivalent DPPH radical scavenging activity per g of sample.

2.11.2 Ferric Reducing Antioxidant Power (FRAP)

The antioxidant capacity was assessed using the ferric reducing antioxidant power (FRAP) assay described by Langley-Evans (2000), with some modifications. The ferrous sulphate (0.1–1 mM) dilution series was used to obtain the FRAP results, and the antioxidant activity was quantified as mM ferrous per g of sample.

2.12 Statistical Analysis

All samples were prepared and tested in triplicate, and the mean and standard deviations were obtained. The data were analysed with Minitab for Windows version 16 (Minitab Inc., Sydney, New South Wales, Australia) using an independent t-test and analysis of variance (ANOVA), and the differences were considered significant at $p < 0.05$. The associations between variables were determined using Pearson correlation coefficients, and differences at $p < 0.05$ were considered significant.

3. Results and Discussion

3.1 Chemical and Physical Analysis

3.1.1 Proximate Composition

DMP exhibits a reduced pattern in all proximate compositions (Table 1). Protein and fat declined 3.5 and 2.5 times after naringinase treatment, while moisture and ash decreased by 1.1-fold and 1.9-fold to the control. Kelly et al. (2015) reported that moisture level might influence the main functional properties, such as stickiness, wettability, bulk density, and powder flowability. Pectinase and naringinase increase the yield of pummelo juice and eliminate bitterness (naringin, limonin, and nomilin; Ni et al., 2014). Enzymatic debittering processes would likely affect nutrients due to the specification of the enzyme towards bitter compounds. The present results will likely have a similar impact on the proximate composition.

Table 1. Phytochemical composition of the debittered mesocarp and the control sample from *B. flabellifer*

Composition (%)	<i>Borassus flabellifer</i>	
	Debittered Mesocarp Powder (DMP)	Control
Proximate (%)		
Protein	1.19±0.04 ^b	4.20 ±0.47 ^a
Fat	0.61±0.03 ^b	1.52 ±0.50 ^a
Moisture	9.35±0.16	10.35±0.22 ^a
Ash	1.88±0.35 ^b	3.66±0.12 ^a
Dietary Fibre (g/100g)		
Total dietary fibre (TDF)	84.420±0.01 ^a	65.970±0.820 ^b
Insoluble dietary fibre (IDF)	79.99 ±0.05 ^a	61.84±1.16 ^b
Soluble dietary fibre (SDF)	4.43 ±0.09 ^a	4.13±0.35 ^a
Ratio IDF/SDF	18.06	14.97
Total soluble solids (%)	0.77±0.06 ^b	2.13±0.06 ^a
pH	5.16±0.01 ^a	3.58±0.08 ^a
Colour		
L*	72.80±0.56 ^a	66.00±0.10 ^b
a*	3.03±0.21 ^a	2.70±0.10 ^b
b*	16.40±0.52 ^a	15.33±0.06 ^b
Particle size (µm)	279.83±8.17 ^b	418.89±23.2 ^a
Bulk density (kg/m ³)	173.91±4.27 ^b	324.83±0.82 ^a
Lignocellulosic (%)		
Holocellulose	88.10±7.43 ^a	52.52±0.78 ^b
Cellulose	53.76±8.22 ^a	29.03±0.75 ^b
Hemicellulose	34.33±3.73 ^a	23.50±0.02 ^b
Lignin	12.99±0.18 ^a	10.29±0.45 ^b

Results as means from triplicates. a-b Different superscript between debittered mesocarp and control denote significant differences (Independent t-test, $p < 0.05$).

3.1.2 Total, Soluble, and Insoluble Dietary Fibre

The total DMP dietary fibre increased 1.3-fold higher than the control (Table 1). The insoluble and soluble dietary fibre of DMP increased significantly ($p < 0.05$) by up to 27.8% and 10.5% after naringinase treatment (Table 1). From the microscope image (image is not shown), the enzymatic treatment caused the fibre-like structure to be broken down into smaller strands, increasing the overall surface area for enzyme penetration and improving enzyme accessibility. Elleuch et al. (2011) reported that enzymatic treatment could alter the proportion of soluble to insoluble fibres, e.g., cell wall treatment with xylanase increased the amount of soluble dietary fibres. The insoluble fibre in DMP is significantly ($p < 0.05$) higher than soluble fibre, with an IDF/SDF ratio of 18.06 (an increase of 17.1% after the naringinase treatment). IDF is the

dominant fibre fraction (about 84.4% of TDF). Thus, DMP may affect insoluble fibre consumption as IDF exerts pronounced effects on intestinal regulation and stool volume (Chau & Uang, 2003). Since IDF absorbs water and expands bolus size, consumption of IDF produces a feeling of satiety. Additionally, it increases the size and weight of the faecal bolus, promoting better digestion and preventing conditions like constipation and colon cancer (Ku & Mun, 2008). Insoluble fibres improve product density and minimise shrinkage, stabilise the food system, and are used as an agent to enhance food appeal and texture (Al-Sheraji et al., 2011).

Thermal processing could alter the amount of total dietary fibre, the ratio of insoluble to soluble fibres, and physicochemical properties (Elleuch et al., 2011). Naringinase treatment in the study was conducted at 55 °C for 5 h before deactivation at 90 °C for 5 min. The temperature employed could be a contributing factor to the outcomes. High temperature and pressure can cause the breakdown of macromolecule covalent bonds, disrupting their physical structures and changing their functional properties (Kim et al., 2006; Singh et al., 2007).

3.1.3 Total Soluble Solids, pH, and Sugar Composition

The DMP is less acidic, with less total soluble solids (TSS) than the control (Table 1). TSS is related to the sugar content, and this study found that TSS in DMP was reduced by 63.8% following naringinase treatment, the possible reason for sugar not being detected in the sample. The HPLC analysis revealed that the DMP lacks sugar due to the absence of peaks in the chromatogram. This could be due to the undetectable sugar composition or the absence altogether. Besides, the washing process of DMP before drying could have removed the soluble sugar. In this study, DMP was rinsed three times after the naringinase treatment before drying to eliminate any flabelliferin and naringinase residues, hence the result. De Moraes et al. (2013) confirmed that a washing process before fibre drying from fruit by-products caused sugar removal.

3.1.4 Colour

The chromaticity coordinate attributes (L*, a*, and b*) of DMP showed higher values than the control, indicating that the DMP sample is lighter and possesses more red and yellow hues than the control (Table 1). In food drying, colour is one of the vital quality parameters that could lead to darkening (reduced L* and increased a*; Garau et al., 2007; Lario et al., 2004). It could be due to the high temperature (90 °C) and the duration (8.3 h) of the drying process, which causes the Maillard reaction (non-enzymatic browning reaction). However, DMP did not turn darker in this study, as the L values increased by 9.34% after the naringinase treatment. Washing the sample before drying could prevent the fibre darkening due to sugar removal (De Moraes et al., 2013). A similar phenomenon was observed when dietary fibre lemon powder from lemon (*Citrus limon* cv. Fino) by-product was washed before drying (Fuentes, 2004). The washing process prevented the fibre from browning due to sugar elimination.

3.1.5 Particle Size

The particle size of the mesocarp sample is reduced by 33.2% after naringinase treatment (Table 1). Naringinase could have probably worked on the mesocarp by degrading the fibre strands. The increase in surface area and the rupture of fibre matrix pores could result from reduced particle size, which would also alter the hydration properties (i.e., solubility; Peerajit et al., 2012).

3.1.6 Bulk Density

The DMP has a 173.91 kg/m³ bulk density, 1.9 times lower than the control (Table 2), exhibiting the small amount of packaging materials required. Furthermore, the bulk density and wettability property exhibit a strong negative correlation ($r = -0.923$), i.e., water can easily penetrate the powder surface. The higher bulk density materials indicated lower surface area and lower ability to bind to lipid components (Garcia-Amezquita & Serna-Saldi, 2015).

3.1.7 Lignocellulosic Composition

The composition of holocellulose, cellulose, hemicellulose, and lignin of the DMP increases (Figure 1). Naringinase treatment degrades lignin structure, simultaneously allowing the cellulose in the mesocarp fibres to be exposed to enzyme action, represented by increased cellulose and hemicellulose (46.0% and 31.6%). This is likely due to the breakdown of lignin by naringinase, which disrupted the cellulosic crystalline structure of DMP. Lignocellulosic biomass denotes plant biomass with lignin as the recalcitrant outer layer, strongly bound to the complex carbohydrate polymers (cellulose and hemicellulose; Nur Liyana Izyan et al., 2014). The presence of cellulose in the substrate may affect the enzymatic hydrolysis of pretreated lignocellulosic biomass, which is accessible to cellulolytic enzymes or the cellulose surface area of the enzyme (Chandra et al., 2009).

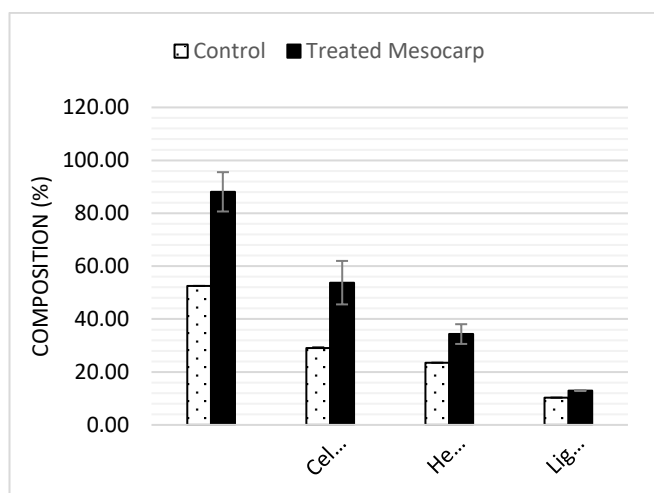


Figure 1. Lignocellulosic Composition of the DMP and Control Sample

3.2 Functional Properties

3.2.1 Solubility and Swelling Properties

The solubility of the DMP, performed at 30 and 60 °C, ranged from 4.31% to 4.55% (Table 2). The naringinase treatment affected the solubility of DMP, i.e., reduction by 2-fold and nearly 5-fold, when tested at 30 and 60 °C. The solubility of DMP was lower than dried egg white, buttermilk solids, and non-fat dried milk (18.0%–34.6%; Wong & Kitts, 2003). The solubility property has a strong negative correlation ($r = -0.907$) to the crude fibre content of DMP powder. Kumar et al. (2010) and Selani et al. (2014) also noted a decrease in solubility with increased carrot and pineapple pomace fibre.

The DMP had a swelling capacity value of 7.75 g/g (Table 2), significantly ($p < 0.05$) lower than the control. The swelling capacity of DMP is lower than the apple (12.8 g/g), orange pomace (8.13 g/g; O’Shea et al., 2015), and fibre powder of pink guava by-product (10.9–15.0 g/g; Ibrahim, 2009) but slightly higher and comparable to the dietary fibre powder of citrus by-products (6.11–9.19 g/g; Figuerola et al., 2005). The swelling capacity indicates the extent of the swelling of the fibre upon water absorption due to the amount of soluble dietary fibre (SDF), particularly pectin (López-Vargas et al., 2013). Wuttipalakovorn et al. (2009) demonstrated that the reduced particle size of dietary fibre (63–150 µm) from lime residues resulted in the reduced water retention ability (9.72–11.74 g water/g dry basis) and swelling capacity (10.12–11.86 mL water/g dry basis) of the fibre powder.

Table 2. Functional properties of the debittered mesocarp and the control from *B. flabellifer*

Properties	Debittered mesocarp Powder	Control
Water Holding Capacity (g/g)	9.38±0.39 ^a	7.11±0.29 ^b
Oil Holding Capacity (g/g)	5.76±0.55 ^a	3.33±0.08 ^b
Solubility (%) (Treatment at 30 °C)	4.31±0.24 ^b	8.76±0.99 ^a
Solubility (%) (Treatment at 60 °C)	4.55±0.27 ^b	21.84±2.20 ^a
Swelling Power (g/g d.w.)	7.75±0.86 ^b	9.15±0.11 ^a
Wettability (s)	12.28±0.21 ^b	44.33±1.53 ^a

Results as means from triplicates. ^{a-b} Different superscripts between debittered mesocarp and control denote significant differences (Independent t-test, $p < 0.05$).

3.2.2 The Water-Holding Capacity (WHC) and Oil Holding Capacity (OHC)

In this investigation, the WHC and OHC of DMP increased after the removal of bitterness via naringinase treatment. Correlation

analysis displayed a robust positive correlation ($r = 0.948$) between WHC and OHC. In another research, Yi et al. (2014) determined the physicochemical properties of dietary fibre of citrus juice by-products after treatment with α -amylase. The enzyme-treated samples showed higher functional properties such as increased water retention (13.31 mL water/g powder), swelling (8.55 mL/g powder), and oil-holding capacity (8.37 g oil/g powder). This study showed a strong negative correlation ($r = -0.811$) between the particle size and WHC. It indicates that the hydration property of DMP was increased with decreased particle size. According to Raghavendra et al. (2006), the hydration characteristics of coconut fibre increased when the particle size decreased from 1127 to 550 μm .

The WHC of the DMP increased by 24.3% (Table 2), possibly due to the higher content of IDF in the DMP. Zhou et al. (2012) reported that the WHC of Tartary buckwheat (*Fagopyrum tataricum Gaertn*) bran dietary fibre flour was increased to 2.22 g/g after enzymatic treatment with amylase and cellulase due to increased SDF/IDF (0.62%/43.33%) and the decreased size of dietary fibre particles (61.6 nm). Water uptake kinetics were significantly affected by structural characteristics and the chemical composition of fibre, including its component water affinity (Figuerola et al., 2005). The capillary action of water in the fibre is due to its high surface tension. Moreover, different molecular fibre components can interact with water through hydrogen bonding or dipole formation (Martínez et al., 2012). In addition, Chau and Uang (2003) reported that the difference in WHC between the samples is attributed to the number and nature of the water-binding site differences, chemical content, and structure of each sample.

Meanwhile, the OHC of the DMP has increased by 24.25% following naringinase treatment (Table 2). Karaman et al. (2017) revealed that grapefruit seed dietary fibre treated with hesperinidase and naringinase showed enhanced OHC values (3.44 and 4.19 g oil/g fibre). In food applications, the capacity of a sample to retain oil can be crucial, i.e., to prevent fat loss upon cooking (Tosh & Yada, 2010). Meanwhile, from the nutritional aspect, the increased excretion due to the ability to absorb or bind bile acids is associated with reduced plasma cholesterol (Tungland & Meyer, 2002). In addition, high OHC allows high-fat food products and emulsions to stabilise (Elleuch et al., 2011). Hence, DMP may be a potential ingredient for dressings and condiments (such as sauce, ketchup, and mayonnaise) to better emulsion structure and stability. Correlation analysis displayed a robust positive correlation ($r = 0.948$) between WHC and OHC.

3.2.3 Wettability

In this study, wettability has increased significantly (3.6-fold, $p > 0.05$) after the naringinase treatment. Very low lipid content prompts the excellent wettability value of the DMP powder (Table 2), which could be supported by the correlation analysis between the fat content and wettability properties, showing a moderate positive correlation for DMP ($r = 0.327$). This finding supported

the findings by Benkovic et al. (2015), where the agglomeration of lower wettability values (6.83 to 60.52 s) of cocoa powder with a high-fat content (16–18 g/100 g) was observed due to the susceptibility of high-fat powder to lipid oxidation, which was less wettable and flowable compared to those with lower free fat levels (Vignolles et al., 2007).

3.4 Phytochemical Composition

Table 3 shows that only saponin, tannins, phenol, and flabelliferin are present in DMP. Saponin has increased by 2.4-fold after the naringinase treatment. Saponin is an antioxidant capable of binding to and stopping cholesterol from being absorbed, allowing the body to easily eliminate excess cholesterol. The consumption of saponins is recommended due to their hypocholesterolemic activity, aid in proper immune function, and are important as chemopreventive agents (Abioye, 2018; Emojorho & Akubor, 2016). In contrast, Emojorho and Akubor (2016) reported that the saponin concentration in orange seed flour was gradually reduced following bitterness removal when boiled. In this study, the mesocarp sample was boiled for 5 min at 90 °C to deactivate the naringinase activity upon completion of the treatment. The release of saponin from the DMP was not affected by the thermal effect, possibly due to the shorter exposure to the heat.

Table 3. Phytochemical composition and antioxidant activities of the debittered mesocarp and control of *B. flabellifer*

Compounds and antioxidant activities	Debittered Mesocarp Powder (DMP)	Control
Compounds		
Alkaloids (%)	ND	ND
Saponins (%)	41.06±5.21 ^a	16.75± 1.44 ^b
Flavonoids (QE/g)	ND	ND
Steroid (ng/ ml)	ND	ND
Cardiac glycosides (%)	ND	ND
Phenol (GAE/g)	6.080±0.001 ^a	3.230±0.001 ^b
Tannins (TE/g)	3.260±0.020 ^a	0.007±0.005 ^b
Terpenoids (LE/g)	ND	ND
Anthraquinone (%)	ND	ND
Flabelliferin (mg/L)	153.57±2.08 ^b	240.57±23.03 ^a
Antioxidant activity		
FRAP (mM Fe ²⁺ /g)	126.38±0.03 ^b	157.05±0.08 ^a
DPPH (mM TE/g)	35.93±0.02 ^a	29.90±0.056 ^b

Results as means from triplicates. ^{a-b} Different superscripts between debittered mesocarp and control denote significant differences ($p < 0.05$). ND: Not detected.

The total phenolic compound (TPC) of DMP was increased almost 2-fold compared to the control. The enhanced TPC may be caused by the release of bound phenolic chemicals from their polymeric or glycosidic precursors (Variyar et al., 2004). A strong negative association was observed between the TPC and DPPH levels. Polymeric phenolic component degradation to simple phenols could cause increased antioxidant activity, increasing

their solubility and capability to interact with DPPH (Kondapalli et al., 2014). The diverse bioactivity of the phenolic compounds, such as antiviral, anti-allergy, anti-mutagenic, and anti-inflammatory properties (Peng et al., 2010), provides an extra benefit to the DMP.

In another debittering process, the phenolic and saponin contents of debittered flour significantly decreased from 320 to 131.651 mg/g and 2.04 to 0.106 mg/g when young shoot palmyra flour was soaked in water at 65 °C for 1 h compared to the raw flour (Thivya et al., 2020). The decreased bioactive compounds in the debittered flour could be attributable to the leaching of soluble phenolics and saponin into water or the chemical oxidation caused by the heat treatment. Similar findings have been documented for the reduced fennel bulb polyphenols after boiling treatment (Rawson et al., 2013). The heating process caused the breakdown of the structure and converted it into a more water-soluble form (Thivya et al., 2020). As previously reported, naringinase action at 55 °C might not be strong enough to leach out the saponin and phenolic contents. However, the deactivation of naringinase activity at 95 °C for 5 min might influence the result.

Likewise, the total tannin content in DMP is higher than in the control. Tannin structure has a significant impact on the qualities of emulsions; the best possibilities are tannins with relatively high molecular weights, which have undergone oxidation processes. Tannins are preferred as stabilisers as they have primary antioxidant capacities, although several natural surfactant agents are currently available (Figuroa-Espinoza et al., 2015).

About 36.2% of residual flabelliferin remained in DMP after the naringinase treatment (unpublished). Despite its contribution to the bitter taste, flabelliferins possess several benefits. The fresh palmyra fruit pulp (PFP) that contained flabelliferins and fibre as the main chemical components caused lower postprandial blood glucose levels in mice due to its hypoglycaemic components (Thabrew & Jansz, 2004). Likewise, Uluwaduge et al. (2005) proved that flabelliferin II might prevent intestinal glucose uptake in mice. It was also reported that the significant inhibitory effects on the absorption of intestinal glucose in mice are mediated by the fraction of flabelliferin (flabelliferin-II) rather than the fibre in PFP (Uluwaduge et al., 2008).

3.5 Antioxidant Activities

The DPPH levels of the DMP increased by 1.2-fold higher than the control (Table 3). As reported earlier, the particle size of DMP was reduced after treatment with naringinase. Likely, the smaller size of the fragment is closely related to the size-reduced fibre strand, increasing the DPPH value. Likewise, the superfine dietary fibre of wheat bran had increased antioxidant activities following superfine grinding, including total phenolic content, chelating activity, and reducing power (Zhu et al., 2012).

However, the DMP has a significantly ($p < 0.05$) lower reducing power than the control (Table 3). These results are congruent with Muñiz et al. (2011), who reported that the highest total phenolic content (1227 mg GAE/L) and the lower reducing power (6.3–14.0 mM FeSO₄) were detected in grapefruit juice following naringinase treatment. The correlation of the particle size with DPPH and FRAP values yielded a moderate negative correlation ($r = -0.676$) and a strong positive correlation ($r = 0.980$, Table 3).

4. Conclusion

A decline in all chemical compositions of DMP was observed except the dietary fibre. The solubility, swelling, bulk density, and wettability of DMP were markedly decreased, whereas water and oil holding capacities were significantly increased. The low fat content in DMP directly affected solubility, WHC, OHC, and wettability properties because it is less susceptible to lipid oxidation, more wettable, and flowable. The naringinase action increased the lignocellulosic content (mainly the cellulose and hemicellulose) and improved the colour property. DMP also had an enhanced content of saponin, phenol, tannin, and DPPH activity than the control, but the reduced activity of ferrous reducing power. In conclusion, DMP has the potential as a functional ingredient to increase fibre in products that require hydration, low calories, and high fibre, such as noodles, energy bars, and breakfast cereal. DMP with an enhanced content of saponin, phenol, tannin and DPPH activity is also useful for pharmaceutical industries. The results of this study can trigger more investigation into the broader application of *B. flabellifer* in various functional food products.

5. Acknowledgement

The authors are grateful to Universiti Putra Malaysia, Universiti Selangor, and the Malaysian Ministry of Higher Education for their facilities and support.

6. References

- Abioye, V. F., Akande, E. A., & Aluko, B. O. (2014). Effects of different local debittering methods on some chemical components and antioxidants in Bitter leaf (*Vernonia amygdalina*). *International Journal of Research in chemistry and environment*, 4(1), 96-101.
- Aiyegroro, O.A., & Okoh, A.I. (2010). Preliminary phytochemical screening and in vitro antioxidant activities of aqueous extract of *Helichrysum longifolium* DC. *BMC complementary and Alternative Medicine*, 10: 21
- Al-Sheraji, S. H., Ismail, A., Manap, M. Y., Mustafa, S., Yusof, R. M., & Hassan, F. A. (2011). Functional properties and

- characterization of dietary fiber from *Mangifera pajang* Kort. fruit pulp. *Journal of Agricultural and Food Chemistry*, 59(8), 3980-3985.
- AOAC International – Association of Analytical Communities. (2000). Official methods of analysis of AOAC international (17th ed.). Gaithersburg, MD, USA: AOAC International.
- AOAC. (2005). In W. Horwitz, & G.W. Latimer (Eds.), Official methods of analysis of AOAC International 18th ed, p. 2200. Gaithersburg: AOAC.
- Ariyasena, D. D., Jansz, E. R., Abeysekera, A. M. (2001). Some studies directed at increasing the potential use of palmyrah (*Borassus flabellifer* L) fruit pulp. *Journal of Science of Food and Agricultural*, 81: 1347-1352.
- Asma, F.Z., Rodiah, M.H., & Aziah, M.Y. 2016. Microwave-assisted extraction of natural colorant extracted from mesocarp and exocarp of *Cocos nucifera* (coconut palm). *European Journal of Biotechnology and Bioscience*, 4(4):1-5.
- Berlin, A., Gilkes, N., Kurabi, A., Bura, R., Tu, M., Kilburn, D., & Saddler, J. (2005). Weak lignin-binding enzymes. *Applied Biochemistry and Biotechnology*, 121(1), 163-170.
- Belscak-Cvitanovic, A., Benkovic, M., Komes, D., Bauman, I., Horzic, D., Dujmic, F., & Matijasec, M. (2010). Physical properties and bioactive constituents of powdered mixtures and drinks prepared with cocoa and various sweeteners. *Journal of Agricultural and Food Chemistry*, 58(12), 7187-7195.
- Benković, M., Tušek, A. J., Belščak-Cvitanović, A., Lenart, A., Domian, E., Komes, D., & Bauman, I. (2015). Artificial neural network modelling of changes in physical and chemical properties of cocoa powder mixtures during agglomeration. *LWT-Food Science and Technology*, 64(1), 140-148.
- Chandra, R. P., Ewanick, S. M., Chung, P. A., Au-Yeung, K., Del Rio, L., Mabee, W., & Saddler, J. N. (2009). Comparison of methods to assess the enzyme accessibility and hydrolysis of pretreated lignocellulosic substrates. *Biotechnology letters*, 31(8), 1217-1222.
- Chau, C. F., & Huang, Y. L. (2003). Comparison of the chemical composition and physicochemical properties of different fibers prepared from the peel of *Citrus sinensis* L. Cv. Liucheng. *Journal of Agricultural and Food Chemistry*, 51(9), 2615-2618.
- Chaurasiya, A. K., Chakraborty, I., & Saha, J. (2014). Value addition of Palmyra palm and studies on the storage life. *Journal of food science and technology*, 51(4), 768-773.
- Chu, Y. H., Chang, C. L., & Hsu, H. F. (2000). Flavonoid content of several vegetables and their antioxidant activity. *Journal of the Science of Food and Agriculture*, 80(5), 561-566.
- De Moraes Crizel, T., Jablonski, A., de Oliveira Rios, A., Rech, R., & Flôres, S. H. (2013). Dietary fiber from orange byproducts as a potential fat replacer. *LWT-Food Science and Technology*, 53(1), 9-14.
- Debenthini, S., Brasathe, J., & Sarananda, K. H. (2014, December). Antioxidant Properties of Palmyrah (*Borassus flabellifer* L.) Fruit Pulp and Effect of Heat Treatment on Bitterness. In Proceedings of the Faculty of Agriculture Undergraduate Research Symposium.
- Elleuch, M., Bedigian, D., Roiseux, O., Besbes, S., & Blecker, C. (2011). Dietary fibre and fibre-rich by-products of food processing : Characterisation , technological functionality and commercial applications : A review. *Food Chemistry*, 124(2), 411–421.
- Eleazu, C.O., Eleazu, K.C., Awa, E & Chukwuma, S.C. 2012. Comparative study of the phytochemical composition of the leaves of five Nigerian medicinal plants. *Journal of Biotechnology and Pharmaceutical Research*, 3(2):42-46.
- Emojorho, E. E., & Akubor, P. I. (2016). Effect of Debittering Methods on the Minerals, and Phytochemical Properties of Orange (*Citrus Sinensis*) Seeds Flour. *IOSR Journal of Environmental Science, Toxicology and Food Technology*, 10(9), 134-139.
- Figueroa F., Hurtado M.L., Estévez A.M., Chiffelle I. & Asenjo F. (2005). Fibre concentrates from apple pomace and citrus peel as potential fibre sources for food enrichment. *Food Chemistry*, 91(3), 395-401.
- Figueroa-Espinoza, M. C., Zafimahova, A., Alvarado, P. G. M., Dubreucq, E., & Poncet-Legrand, C. (2015). Grape seed and apple tannins: Emulsifying and antioxidant properties. *Food chemistry*, 178, 38-44.
- Fuentes-alventosa, J. M., Rodríguez-gutiérrez, G., Jaramillo-carmona, S., & Espejo-calvo, J. A. (2009). Effect of extraction method on chemical composition and functional characteristics of high dietary fibre powders obtained from asparagus by-products. *Food Chemistry*, 113(2), 665–671.
- Garau, M. C., Simal, S., Rosselló, C., & Femenia, A. (2007). Effect of air drying temperature on physico-chemical properties of dietary fiber and antioxidant capacity of orange (*Citrus aurantium* cv. *Canoneta*) by-products. *Food Chemistry*, 104, 1014–1024

- García Herrera, P., Sánchez-Mata, M. C., & Cámara, M. 2010. Nutritional characterization of tomato fiber as a useful ingredient for food industry. *Innovative Food Science and Emerging Technology*, 11(4):707–711.
- Ibrahim, A. H. (2009). Physico-chemical and Health-promoting Properties of Dietary Fibre Powder from Pink Guava By-products (Doctoral dissertation, Universiti Putra Malaysia).
- Jansz, E. R., Nikawela, J. K., & Gooneratne, J. (1994). Studies on the bitter principle and debittering of Palmyrah fruit pulp. *Journal of the Science and Food Agricultural* 65:185-189.
- Jansz, E. R., Wickremasekara, N., & Sumuduni, K. A. V. (2002). A review of the chemistry and biochemistry of seed shoot flour and fruit pulp of the palmyrah palm (*Borassus flabellifer* L). *Journal of the National Science Foundation of Sri Lanka*, 30(1-2).
- Karaman, E., Yilmaz, E., & Tuncel, N. B. (2017). Physicochemical, microstructural and functional characterization of dietary fibers extracted from lemon, orange and grapefruit seeds press meals. *Bioactive carbohydrates and dietary fibre*, 11, 9-17.
- Kelly, G. M., Mahony, J. A. O., Kelly, A. L., Huppertz, T., Kennedy, D., & Callaghan, D. J. O. (2015). Influence of protein concentration on surface composition and physico-chemical properties of spray-dried milk protein concentrate powders. *International Dairy Journal*, 51, 34–40.
- Kim, J. H., Tanhehco, E. J., & Ng, P. K. W. (2006). Effect of extrusion conditions on resistant starch formation from pastry wheat flour. *Food chemistry*, 99(4), 718-723.
- Kondapalli, N., Sadineni, V., Variyar, P. S., Sharma, A., & Obulam, V. S. R. (2014). Impact of γ -irradiation on antioxidant capacity of mango (*Mangifera indica* L.) wine from eight Indian cultivars and the protection of mango wine against DNA damage caused by irradiation. *Process Biochemistry*, 49(11), 1819-1830.
- Ku, C. S., & Mun, S. P. (2008). Optimization of the extraction of anthocyanin from Bokbunja (*Rubus coreanus* Miq.) marc produced during traditional wine processing and characterization of the extracts. *Bioresource Technology*, 99(17), 8325-8330.
- Kumar, V. V. (2010). Comparative studies on inducers in the production of naringinase from *Aspergillus niger* MTCC 1344. *African Journal of Biotechnology*, 9(45), 7683-7686.
- Kumar, R., Rajarajeshwari, N., & Narayana Swamy, V. B. (2012). Isolation and evaluation of *Borassus flabellifer* mucilage as a natural suspending agent. *International Journal of PharmTech Research*, 4(4), 1614–1630.
- Langley-Evans, S. C. 2000. Antioxidant potential of green and black tea Lario, Y., Sendra, E., Garcia-Pérez, J., Fuentes, C., Sayas-Barberá, E., 185
- Lecumberri, E., Mateos, R., Izquierdo-Pulido, M., Rupérez, P., Goya, L., & Bravo, L. (2007). Dietary fibre composition, antioxidant capacity and physico-chemical properties of a fibre-rich product from cocoa (*Theobroma cacao* L.). *Food chemistry*, 104(3), 948-954.
- López-Vargas, J. H., Fernández-López, J., Pérez-Álvarez, J. A., & Viuda-Martos, M. 2013. Chemical, physico-chemical, technological, antibacterial and antioxidant properties of dietary fiber powder obtained from yellow passion fruit (*Passiflora edulis* var. *flavicarpa*) co-products. *Food Research International*, 51(2), 756–763.
- Martínez, R., Torres, P., Meneses, M. A., Figueroa, J. G., Pérez-Álvarez, J. A., & Viuda-Martos, M. (2012). Chemical, technological and in vitro antioxidant properties of cocoa (*Theobroma cacao* L.) co-products. *Food Research International*, 49(1), 39-45.
- Mishra N & Chandra R. (2012). Development of functional biscuit from soy flour and rice bran. *International Journal of Agricultural and Food Science*, 2, 14-20.
- Muñiz, P., Ortega, N., & Busto, M. D. (2011). Effect of enzymatic debittering on antioxidant capacity and protective role against oxidative stress of grapefruit juice in comparison with adsorption on exchange resin. *Food Chemistry*, 125(1), 158–163.
- Nesbitt, M. (2005). The Cultural history of plants. Taylor & George Francis. 173.
- Ni, H., Yang, Y. F., Chen, F., Ji, H. F., Yang, H., Ling, W., & Cai, H. N. (2014). Pectinase and naringinase help to improve juice production and quality from pummelo (*Citrus grandis*) fruit. *Food Science and Biotechnology*, 23(3), 739-746.
- Nur Liyana Izyan, Z. (2014). Tensile and thermal properties of oil palm empty fruit bunch regenerated cellulose biocomposite films using ionic liquid (Doctoral dissertation, Universiti Malaysia Perlis (UniMAP)).
- Obadoni, B. O., & Ochuko, P. O. 2001. Phytochemical studies and comparative efficacy of the crude extracts of some homeostatic plants in Edo and Delta States of Nigeria. *Global Journal of Pure and Applied Sciences*, 86: 2003-2008.

- O'Shea, N., Ktenioudaki, A., Smyth, T.P., McLoughlin, P., Doran, L., Auty, M.A.E., Arendt, E., Gallagher, E. 2015. Physicochemical assessment of two fruit by-products as functional ingredients: Apple and orange pomace, *Journal of Food Engineering*, 153, 89-95.
- Osundahunsi O. F., Fagbemi T. N., Kesselman E. & Shimoni E. (2003). Comparison of the physicochemical properties and pasting characteristics of flour and starch from red and white sweet potato cultivars. *Journal of Agricultural and Food Chemistry*, 51(8), 2232-2236.
- Peerajit, P., Chiewchan, N., & Devahastin, S. (2012). Effects of pretreatment methods on health-related functional properties of high dietary fibre powder from lime residues. *Food Chemistry*, 132(4), 1891–1898.
- Peng, X., Ma, J., Cheng, K. W., Jiang, Y., Chen, F., & Wang, M. (2010). The effects of grape seed extract fortification on the antioxidant activity and quality attributes of bread. *Food Chemistry*, 119(1), 49-53.
- Puri, M., Seth, M., Marwaha, S. S., & Kothari, R. M. (2001). Debittering of kinnow mandarin juice by covalently bound naringinase on hen egg white. *Food Biotechnology*, 15(1), 13-23.
- Puri, M., Banerjee, A., & Banerjee, U. C. (2005). Optimization of process parameters for the production of naringinase by *Aspergillus niger* MTCC 1344. *Process Biochemistry*, 40(1), 195-201.
- Puwastien P., Siong, T. E., Kantasubrata, J., Craven, G., Feliciano, R. R., & Judprasong, K. (2011). ASEAN Manual of Food Analysis 2011. Thailand: Institute of Nutrition, Mahidol University.
- Radhakrishnan, I., Sampath, S. & Satishkumar, T. (2012). Optimization of medium composition for improving naringinase activity using response surface methodology. *International Journal of Biotechnology and Research*, 2: 29-36.
- Raghavendra, S. N., Swamy, S. R., Rastogi, N. K., Raghavarao, K. S. M. S., Kumar, S., & Tharanathan, R. N. (2006). Grinding characteristics and hydration properties of coconut residue: A source of dietary fiber. *Journal of Food Engineering*, 72(3), 281-286.
- Rawson, A., Hossain, M. B., Patras, A., Tuohy, M., & Brunton, N. (2013). Effect of boiling and roasting on the polyacetylene and polyphenol content of fennel (*Foeniculum vulgare*) bulb. *Food Research International*, 50(2), 513-518.
- Reddy, C. K., Suriya, M., Vidya, P. V., Vijina, K., & Haripriya, S. (2015). Effect of γ -irradiation on structure and physico-chemical properties of *Amorphophallus paeoniifolius* starch. *International Journal of Biological Macromolecules*, 79, 309-315.
- Robertson, J. A., de Monredon, F. D., Dysseler, P., Guillon, F., Amado, R., & Thibault, J.-F. (2000). Hydration properties of dietary fibre and resistant starch: a European collaborative study. *Lebensmittel-Wissenschaft und Technologie*, 33, 72–79
- Sabiha-Hanim, S., Noor, M. A. M., & Rosma, A. 2011. Effect of autohydrolysis and enzymatic treatment on oil palm (*Elaeis guineensis* Jacq.) frond fibres for xylose and xylooligosaccharides production. *Bioresource Technology*, 102(2):1234–1239.
- Šamec, D., Maretić, M., Lugarić, I., Mešić, A., Salopek-Sondi, B., & Duralija, B. (2016). Assessment of the differences in the physical, chemical and phytochemical properties of four strawberry cultivars using principal component analysis. *Food Chemistry*, 194, 828-834.
- Selani, M. M., Brazaca, S. G. C., dos Santos Dias, C. T., Ratnayake, W. S., Flores, R. A., & Bianchini, A. (2014). Characterisation and potential application of pineapple pomace in an extruded product for fibre enhancement. *Food chemistry*, 163, 23-30.
- Singh, S., Gamlath, S., & Wakeling, L. (2007). Nutritional aspects of food extrusion: a review. *International Journal of Food Science & Technology*, 42(8), 916-929.
- Thabrew, M. I. & Jansz, E. R. (2004). Nutritive importance of palmyrah products. *Recent Research Development. Environmental Biology*. 1: 43-60.
- Thanusan, S., Tharmaratnam, G., & Priyantha, K. D. P. (2018). Physicochemical Evaluation in the Development of Palmyrah and Pineapple Mixed Fruit Toffee. *Annals. Food Science and Technology*, 19 (2). 244-249
- Thivya, P., Durgadevi, M., & Jaganmohan, R. (2018). Effect of debittering on the physical and chemical properties of palmyrah young shoots flour. *International Journal of Agriculture, Environment and Biotechnology*, 11(4), 609-614.
- Thivya, P., Durgadevi, M., Rawson, A., Vadakkepuppara Ramachandran Nair, S., & Rangarajan, J. (2020). Exploring the feasibility of bitterness reduction in palmyrah young shoot for its effective utilization. *Journal of Food Process Engineering*, 43(3), e13315.
- Tosh, S. M., & Yada, S. (2010). Dietary fibres in pulse seeds and fractions: Characterization, functional attributes, and applications. *Food Research International*, 43(2), 450-460.

- Tungland B. C. & Meyer D. (2002). Nondigestible oligo- and polysaccharides (dietary fibre): their physiology and role in human health and food. *Comprehensive Reviews in Food Science and Food Safety*, 1(3), 90-109
- Uluwaduge, D. I & Thillainathan, K. (2019). Palmyrah research in Sri Lanka: a way forward, ed. E.R. Jansz, pp. 11-51. Sri Lanka: University of Jaffna
- Variyar, P. S., Limaye, A., & Sharma, A. (2004). Radiation-induced enhancement of antioxidant contents of soybean (*Glycine max* Merrill). *Journal of Agricultural and Food Chemistry*, 52, 3385–3388.
- Vignolles, M. L., Jeantet, R., Lopez, C., & Schuck, P. (2007). Free fat, surface fat and dairy powders: interactions between process and product. *A review. Le Lait*, 87(3), 187-236.
- Vijaya kumara B, V. P., & Prasad KR, M. G. (2015). Physico-Chemical Properties of Palmyrah fruit Pulp (*Borassus flabellifer* L). *Journal of Nutrition & Food Sciences*, 05(05).
- Wickramasekara, N. T., & Jansz, E. R. (2003). The range of steroidal saponins of palmyrah flour: could they contribute to toxic effect on consumers. *Journal of Science EUSL*, 3(1), 11-18.
- Wong, P. Y. Y., & Kitts, D. D. (2003). A comparison of the buttermilk solids functional properties to nonfat dried milk, soy protein isolate, dried egg white, and egg yolk powders. *Journal of Dairy Science*, 86(3), 746-754.
- Wuttipalakov, P., Srichumpuang, W., & Chiewchan, N. (2009). Effects of pretreatment and drying on composition and bitterness of high-dietary-fiber powder from lime residues. *Drying Technology*, 27(1), 133-142.
- Yi, T., Huang, X., Pan, S., & Wang, L. (2014). Physicochemical and functional properties of micronized jincheng orange by-products (*Citrus sinensis* Osbeck) dietary fiber and its application as a fat replacer in yogurt. *International Journal of Food Sciences and Nutrition*, 65(5), 565-572.
- Zhou, X. L., Qian, Y. F., Zhou, Y. M., & Zhang, R. (2012). Effect of enzymatic extraction treatment on physicochemical properties, microstructure and nutrient composition of tartary buckwheat bran: A new source of antioxidant dietary fiber. In *Advanced Materials Research* (Vol. 396, pp. 2052-2059). Trans Tech Publications Ltd.
- Zhu, Y., Dong, Y., Qian, X., Cui, F., Guo, Q., Zhou, X., & Xiong, Z. (2012). Effect of superfine grinding on antidiabetic activity of bitter melon powder. *International Journal of Molecular Sciences*, 13(11), 14203-14218.
- Zhu, Yunping, Jia, H., Xi, M., Li, J., Yang, L., & Li, X. (2017). Characterization of a naringinase from *Aspergillus oryzae* 11250 and its application in the debitterization of orange juice. *Process Biochemistry*, 62, 114–121.

SYNTHESIS, PHYSICOCHEMICAL ELUCIDATION AND BIOLOGICAL SCREENING STUDY OF NEW LIGAND DERIVED FROM 5,6-O-ISO PROPYLIDENE-L-ASCORBIC ACID AND ITS METAL(II) COMPLEXES

Fawzi Yahya Wadday^{1a}, Lekaa Khalid Abdul Karem^{2b}, Duha Mohammed Mortatha^{3c}

Abstract: A simple chemistry method approach was used to synthesise new ligand derivative from L-ascorbic acid and its complexes. All of them were water-soluble and are used quite extensively in the medical and pharmaceutical fields. This study synthesised the new ligand derivative from L-ascorbic acid-base using the following steps: A 5,6-O-isopropylidene-L-ascorbic acid was prepared by reacting dry acetone with L-ascorbic acid followed by reacting it with trichloroacetic acid to yield [chloro(carboxylic)methylidene]-5,6-O-isopropylidene-L-ascorbic acid in the second stage. In the third stage, the derivative was reacted with (methyl(6-methyl-2-pyridylmethyl)amine) to create a new ligand (ONMILA). This novel ligand was identified using a number of techniques, namely mass spectroscopy, ¹H, ¹³C-Nuclear magnetic resonance, Fourier Transform Infrared (FT-IR), and Ultraviolet-visible (UV-Vis) spectra. It was observed that several complexes formed between the ligand and divalent metal ions (Co, Ni, Cu, Zn, Cd). Based on Micro Elemental Analysis, the mole ratio was (1:1) (M:L). Magnetic susceptibility, elemental analysis (C.H.N.O) procedures, molar conductivity tests, and proportion of metal ions calculations were used to describe the complexes. The findings showed the novel ligand had a mono, negative charge and behaved like a tridentate ligand type (N.N.O.). Therefore, the octahedral formula is suggested for all compounds. Only one spot was observed on thin layer chromatography (T.L.C.) for ligand (L) and complexes, indicating that the reaction completed and delivered only a single product. These chemicals have been connected to both Gram-negative and Gram-positive bacteria. The results suggested that antibacterial activity in metal complexes is higher than in the free ligand.

Keywords: L-ascorbic acid, ligand, techniques, metal complexes, antibacterial activity

1. Introduction

L-enantiomer of ascorbic acid without scurvy is a condition caused by vitamin C deficiency (Zümreoglu-Karan, 2006). The human body requires a robust immune system and therefore, a vitamin-rich daily diet is recommended. Vitamins with critical biological properties are abundant in natural foods, particularly vegetables and fruits, which are rich in cinnamon, vitamin C, and hesperidin and well-known for their health benefits (Bellavite & Donzelli 2020). L-ascorbic acid is a type of vitamin C which has water-soluble antioxidants and a protective function. Although most mammals can produce ascorbate, they cannot produce vitamin C (Chatterjee, 1973). L-ascorbic acid is a biological antioxidant (Loke et al., 2006) that protects the cell from damaging radicals, especially those generated during incomplete O₂ oxidation (Padayatty et al., 2003). In both chemistry and biology, L-ascorbic acid is a critical chemical and its complexes are significant in both (Hanukoglu, 2006). Although ascorbic acid has

many antimicrobial effects, some of its oxidative products are toxic (Hollis et al., 1985). According to Fodor (1983), L-ascorbic acid molecule has four hydroxyl groups which participate in conventional esterification. It is possible to use L-ascorbic acid (L-asc.) or Vitamin C and its derivatives in various biological and industrial uses (John & James, 2009). It has several donors, atoms, O(1), O(2), O(3), O(5), and O(6), that are usually involved in metal-ligand bonding (Tajmir-Riahi, 1990). The functional groups -OH, -COOH, -SH, -NH₂ in derivatives of L-asc. have been found to coordinate with metal ions and form complexes [10]. These vitamin-metal complexes are essential in development of medication and nutrition (Wasi, 1987) while metal complexes are crucial for the pharmaceutical and agricultural industries. A living system relies heavily on trace amounts of metal elements and these transition metal ions ensure that different enzymes function correctly (Hariprasath et al., 2010). The current study examined these metal complexes for their antiseptic action alongside various bacterial strains. Their antibacterial activity was found to be effective against all the strains. The study also attempted to establish and validate a new apparent synthesis and description of an L-ascorbic acid derivative ligand (L).

Authors information:

^aKufa University, Faculty of Science, Chemistry Department, Najaf, IRAQ. E-mail: fawzi.almuwashi@uokufa.edu.iq¹

^bBaghdad University, College of Education for Pure Sciences, Ibn/Al-Haitham Chemistry Department, IRAQ. E-mail: likaa.k.a@ihcoedu.uobaghdad.edu.iq²

^cKufa University, Faculty of Pharmacy, Department of Pharmaceutical and Industrial Pharmacy, Najaf-IRAQ. E-mail: duham.najaf@uokufa.edu.iq³

*Corresponding Author: fawzi.almuwashi@uokufa.edu.iq

Received: September 27, 2022

Accepted: December 24, 2022

Published: October 31, 2023

2. Experimental

2.1 Instrumentation

Shimadzu FT-IR spectrophotometer ranging 4000-400 cm^{-1} , Shimadzu UV-Vis. spectrophotometer with 200-1100 nm, Stuart electrothermal equipment, model SMP30 W.T.W. in OLAP cond 720 digital conductivity meter, Bruker D.R.X. (500-MHz, DMSO-d_6) spectrometer, mass spectrometer 5975 quadrupole. Elemental analyser Euro Vectro-3000A, Atomic absorption spectrophotometer Analytic Jena (A.A350), Magnetic Susceptibility Balance Mode (MSB-MKI). 854 Schwach Autoclave, Gallen Kamp Sterilizer, Memmert Incubator.

2.2 Materials

L-ascorbic acid, Trichloro acetic acid, Potassium hydroxide, Methyl(6-methyl-2-pyridylmethyl) amine, Metal chloride " $\text{CoCl}_2 \cdot 6\text{H}_2\text{O}$, $\text{NiCl}_2 \cdot 6\text{H}_2\text{O}$, $\text{CuCl}_2 \cdot 2\text{H}_2\text{O}$, ZnCl_2 , $\text{CdCl}_2 \cdot \text{H}_2\text{O}$ ", Mueller Hinton agar, dry acetone, N-Hexane, Dimethylsulfoxide, Dimethylformamide, HCl gas, Ethanol, Distilled water. "All chemicals used were of the highest purity. B.D.H., Fluka, and Merck were used without further purification.

2.3 Synthesis of The New Ligand (L)

2.3.1 Synthesis of 5,6-O-iso propylidene-l-ascorbic acid:

A 250 mL flask containing 0.528 grams (0.003 moles) of L-ascorbic acid powder along with 50 mL of dry distillers acetone was given a rapid bubble bath of dry hydrogen chloride and stirred for 20 minutes. The supernate was decanted after 20 mL of n-hexane was added followed by additional stirring and then chilling (ice-water). After each addition, the precipitate was rinsed with (100 mL) of the acetone-hexane combination (3:7) (v/v) followed by stirring, cooling in cold water, and then extracting the supernate. This process was repeated four times. The final precipitate was subjected to drying under decreased pressure, which resulted in the production of a white crystalline residue with a melting temperature of 216 $^{\circ}\text{C}$. This yielded 70.51 grams R_f (0.69) in benzene:ethanol (8:2) (v/v) solvent solution.

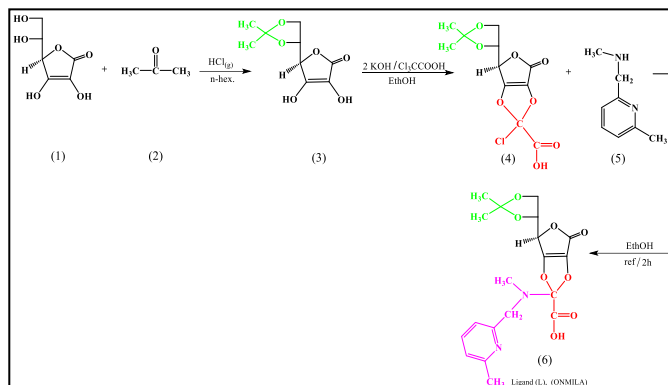
2.3.2 Synthesis of [Chloro(Carboxylic)Methylidene]-5,6-Isopropylidene-L-Ascorbic Acid:

5,6-O-isopropylidene-L-ascorbic acid (0.432 g, 0.002 mole) was dissolved in (25 mL) ethanol. A potassium hydroxide solution (0.112 g, 0.002 moles) in ethanol (20 mL) was later added and stirred for 30 minutes. Next, trichloro acetic acid (0.163 g, 0.001 mole) in ethanol (15 mL) solution was added and left for one hour. The product was filtered. Recrystallisation from 25mL (20 mL ethanol + 5 mL water) yielded 73.5% of pale brown solid crystalline residue with a melting point of 209 $^{\circ}\text{C}$. (benzene: methanol) R_f 0.57 in (5:5).

2.3.3 Synthesis of The Ligand (L), [O, O-2,3-(N-Carboxylicmethylidene)-N-Methyl-1-(6-Methylpyridyl]-5,6-Isopropylidene-L-Ascorbic Acid:

0.306 g (1 mmole) of methylidene-(chloro(carboxylic)-5,6-iso propylidene-L-ascorbic acid was diluted in 20 mL ethanol. Using methyl (6-methyl-2-pyridylmethyl)amine, the solution was

dropped wide (0.14 mL, 0.001 mole) and refluxed for two hours. A deep dark precipitate mass formed after some time at room temperature, and which was subsequently separated from the solution. Recrystallising the resulting mass in ethanol yielded a brown crystalline substance with a melting point of (127 $^{\circ}\text{C}$) and a yield of 80.47 percent. R_f (0.48) in a solvent solution of benzene and ethanol (8:2) (v/v). The diagram below (Scheme 1) describes the reaction.



Scheme 1. Synthesis route of a new ligand (ONMILA) derivative.

2.3.4 Synthesis of Metal Complexes

1 mmol metal chloride 0.238 g $\text{CoCl}_2 \cdot 6\text{H}_2\text{O}$, 0.237 g $\text{NiCl}_2 \cdot 6\text{H}_2\text{O}$, 0.170 g $\text{CuCl}_2 \cdot 2\text{H}_2\text{O}$, 0.136 g ZnCl_2 , 0.183 g $\text{CdCl}_2 \cdot \text{H}_2\text{O}$ in 10 mL ethanol solution was added to a mixture of ligand (0.406 g, 1 mmol) in 10 mL ethanol. After agitating the solutions for an hour, the complexes were gently precipitated by evaporation. Figure 9 describes the process of recrystallising the complexes from heated ethanol. Water, methanol, ethanol dimethylsulfoxide, and dimethylformamide are all effective for dissolving isolated complexes which are colourful solids that are stable in air but insoluble in normal organic solvents. Table 1 describes the physical characteristics and provides analytical data for ONMILA and its complexes.

2.4 Biological Activity

The agar-well diffusion technique was applied in the testing of synthesised ligand and complexes against *Staphylococcus aureus* and *Streptococcus pyogenes* which are Gram (+), *E-coli* and *Klebsiella pneumonia*, Gram (-). All of the compounds were found to be effective against the bacteria (Al-Khafagy, 2016; Valarmathy et al., 2020). Muller Hinton Agar was used as the medium for the cultivation of the microorganisms to be tested. Dimethyl sulfoxide (DMSO), was used as a solvent in a single concentration of 1×10^{-3} M to make the chemical solutions; this was aimed at studying its biological activity. The plates were kept in an incubator at 37 $^{\circ}\text{C}$ for a whole day. The compounds' antibacterial activity was evaluated with regard to the size of the inhibition zone they produced against the particular strain of bacteria tested. The growth inhibition zone for each sample was determined by utilising the mean value obtained from three separate repetitions in order to reach a conclusion.

3. Results and Discussion

3.1 Physical Characteristics and Elemental Examination

Table 1 shows physical features and results of elemental analysis (C.H.N.O) examination and the organized compounds' metal substances.

Table 1. Physical properties and analytical statistics of ONMILA and its complexes

Empirical formula	Colour	M.wt	M.P °C	Yield %	R _f	Element Analysis				Found (calcul.) Metal %
						Found (calcul.) %				
						C	H	N	O	
ONMILA= C ₁₉ H ₂₂ O ₈ N ₂	Deep brown	406.38	127	80.47	0.48	56.15 (55.93)	5.45 (5.31)	6.89 (6.94)	31.49 (31.7)	—
[Co(L)Cl ₂ (H ₂ O)]H ₂ O	Reddish-Brown	572.25	151	74.71	0.43	39.87 (39.49)	4.57 (4.59)	4.88 (4.67)	27.95 (27.81)	10.29 (9.74)
[Ni(L)Cl ₂ (H ₂ O)]3H ₂ O	Olive	608.04	145	70.13	0.41	37.53 (37.46)	4.97 (4.9)	4.6 (4.72)	31.57 (31.74)	9.65 (9.05)
[Cu(L)Cl ₂ (H ₂ O)]H ₂ O	Deep green	576.86	187	82.36	0.37	39.55 (39.71)	4.54 (4.42)	4.85 (4.54)	27.73 (27.9)	11.01 (11.24)
[Zn(L)Cl(H ₂ O) ₂]Cl.3H ₂ O	ale brown	632.74	191 °D	73.2	0.40	36.06 (35.45)	5.09 (5.23)	4.42 (4.69)	29.43 (29.49)	10.33 (10.17)
[Cd(L)Cl(H ₂ O) ₂]Cl.2H ₂ O	Deep beige	661.76	173 °D	65.68	0.35	34.48 (33.9)	4.56 (4.47)	4.23 (4.29)	29.01 (29.25)	16.98 (16.42)

3.2 N.M.R Spectra for the ONMILA Ligand

¹H-NMR spectrum in Figure 1 (500 MHz in DMSO-d₆) showed numerous signals. A carboxylic-OH low signal strength was seen at δ 11.85 ppm (s, 1H). The Pyridine ring showed multiplet signals at δ 7.7-7.21 (m, 3H) (Lee & McCarthy, 2019). A doublet peak at δ 5.25, δ 5.22 (d, 1H) was due to CH-4 lactone ring. The signals at δ 4.84, δ 4.73 (m, 2H) were assigned to CH-5, and the signals at δ 3.79 (s, 2H) and δ 3.71 (t, 2H) were attributed to pyridine-CH₂ and CH₂-6 l-ascorbic acid moieties, while that at δ 2.73 (s, 3H), 2.45 (s, 3H) were due to CH₃- pyridine and CH₃-N of 2-aminomethyl moieties. A single peak at δ 1.51 (s, 6H) ppm was attributed to (CH₃)₂ of 5,6-O-iso propylidene (Al-Noor et al., 2021).

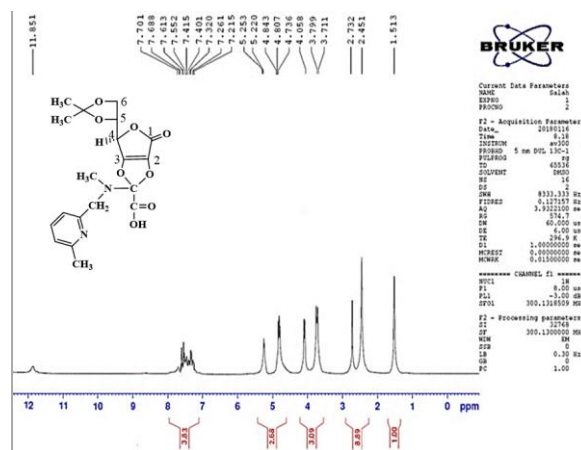


Figure 1. ¹H-NMR spectrum of ONMILA.

There was a carboxylic acid peak at 176.04 ppm in the ¹³C-NMR spectrum as shown in Figure 2, with lactones ring carbon and pyridine (C=N) signal also present. Carbons (C-2 and C-3) were responsible for the two peaks at (137.22 and 142.71) ppm. There is a possibility that the "double bond that was conjugated from (C-1 to C-3)" shifted the (C-3) signal upfield (Lee & McCarthy, 2019) while the signals in the range of (136,26-120.6) "ppm were dispensed to C=C" pyridine ring carbon atoms. The signals at (66.03) due to C10-N of 2-methylpyridine, and the peak at (55.95) were assigned to C9-N amino-methyl moieties, while the signals in the range of (73.6-66.03) ppm were assigned to (C5-C4) and (C5-C-6). C-C carbon atoms C-7 and C-8 were responsible for the signals at 33.81, 29.23, and 27.13 ppm respectively (Lee & McCarthy, 2019; Al-Noor et al., 2021).

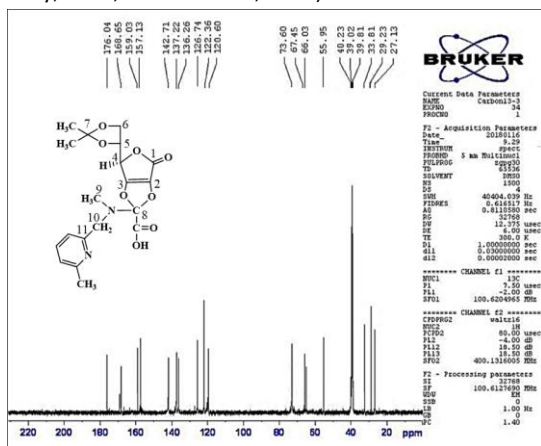


Figure 2. ¹³C-NMR spectrum of ONMILA.

3.3 Mass Spectrum for ONMILA

It was discovered that the molecular ion top at (m/z = 406.2) in the ligand's mass spectrum as described in Figure 3 corresponded with (C₁₉H₂₂N₂O₈) (Ahmed et al., 2015; Gao, (2021). Scheme 2 summarises the pieces and their relative abundance.

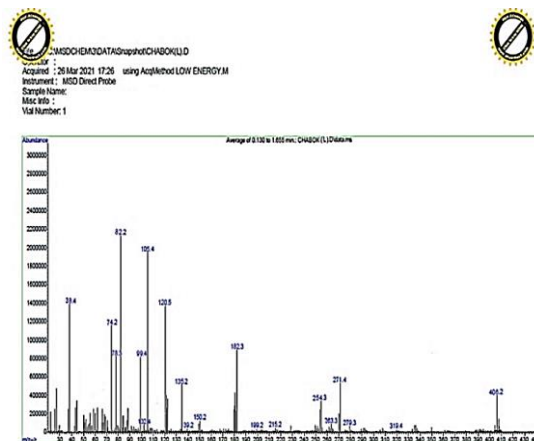
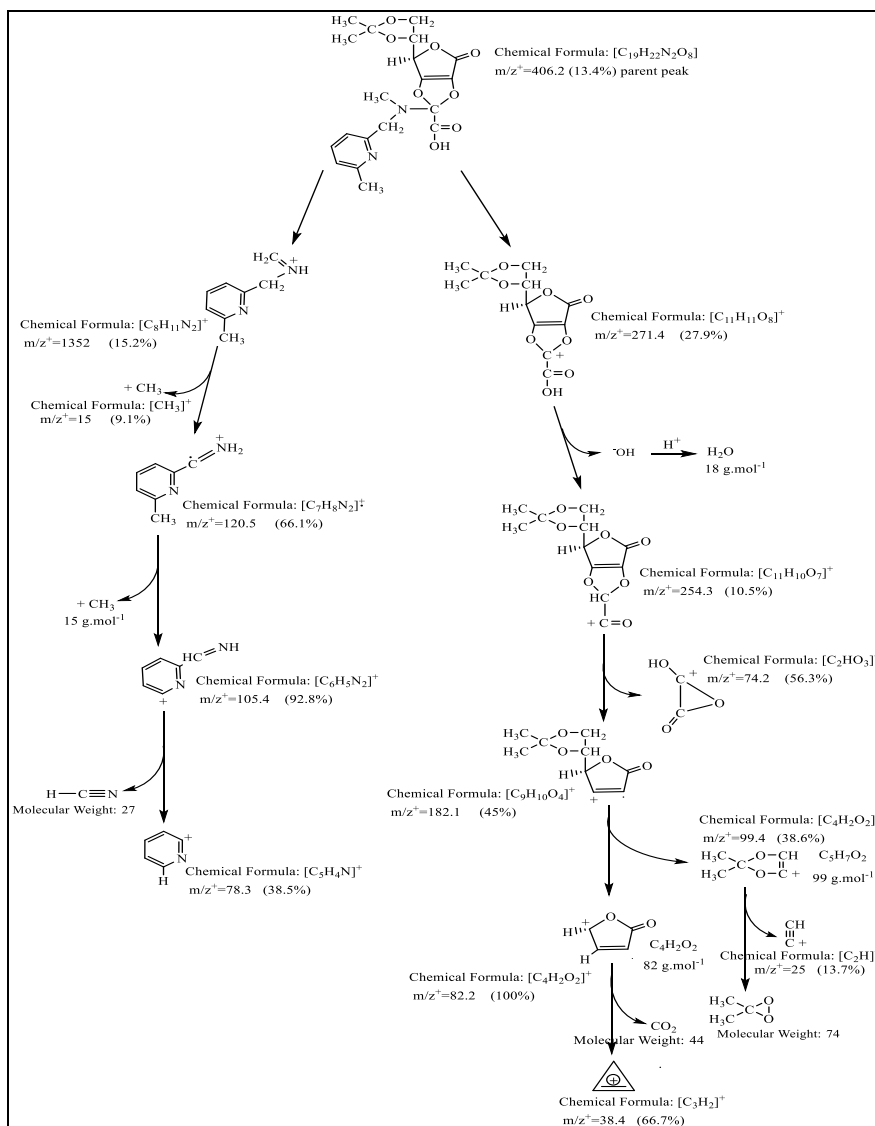


Figure 3. Mass spectrum of ONMILA.



Scheme 2. The fragmentation of ONMILA.

3.4 Infrared Spectra of ONMILA and its Complexes

A comparison of ONMILA (FT-IR) spectrum and its metal complexes (nickel complex, for example) is shown in Figure 4 and Figure 5. Table 2 summarises the major I.R. bands and their potential assignments. The frequency of the essential wide band at 3429 cm^{-1} , which may be attributed to the OH-carboxylic acid in the free ligand, did not change for any complexes in the range of 3435-3416 cm^{-1} (Waddai et al., 2015). A band that was produced at 1627 cm^{-1} and was ascribed to the (C=N) stretching vibration of pyridine-N was linked with $\nu(C=N)$ altered in shape and moved to a lower frequency in all complexes in the range of 1611-1595 cm^{-1} (El-Sonbati et al., 2016; Naji, 2014). Broad bands at 3419, 3435, 3416, 3432, and 3422 cm^{-1} due to (O-H) stretching in conjunction with OH-carboxyl stretching and bands

at (807, 861, 855, 869, and 874) cm^{-1} in Co(II), Cu(II), Ni(II), Zn(II), and Cd(II) complexes respectively attributable to coordination water were found in all complexes (Waddai et al., 2015; Al-Farhan et al., 2021). The stretching vibration to the (C=O) ring of lactones was found at (1710) cm^{-1} , with a slight frequency shift in the range (1695-1723) cm^{-1} due to it not being involved in the coordination (Waddai et al., 2015; Radisavljević & Petrović, 2020). The stretching band (C=O)-carboxyl was found at (1685) cm^{-1} with a shape change and lower frequency in the range (1668-1653) cm^{-1} caused by a complex framework with the metal ions (Lawal et al., 2017). New weak bands displayed in all metal complexes spectra in the low-frequency range at (518-483) cm^{-1} and (477-446) cm^{-1} proved to bond (Kareem et al.; Raman & Sobha, 2010).

Table 2. Characteristics of FT-IR absorption bands of ONMILA and its complexes.

Empirical formula	ν OH Carbox., Hydrat.	ν C=O lactone	ν C=O Carbox.	ν C=N ν C=C	ν C-N pyridine	δ H ₂ O aqua	ν M-N	ν M-O
(L) ONMILA	3429,b	1710,m	1685,sh	1627,s	1155,m	-	-	-
[Co(L)Cl ₂ (H ₂ O)]H ₂ O	3419,b	1719,m	1653,s	1598,s	1118,m	807,w	518,w	454,w
[Ni(L)Cl ₂ (H ₂ O)]3H ₂ O	3435,b	1698,s	1668,m	1605,m	1125,w	861,w	483,w	446,w
[Cu(L)Cl ₂ (H ₂ O)]H ₂ O	3416,b	1714,m	1659,s	1611,s	1132,m	855,w	511,w	477,w
[Zn(L)Cl(H ₂ O) ₂]Cl.3H ₂ O	3432,b	1723,s	1666,s	1609,m	1121,w	869,w	487,w	461,w
[Cd(L)Cl(H ₂ O) ₂]Cl.2H ₂ O	3422,b	1695,s	1660,m	1605,m	1129,m	874,w	501,w	470,w

s= sharp, m= medium, w= weak, b= broad, sh=shoulder

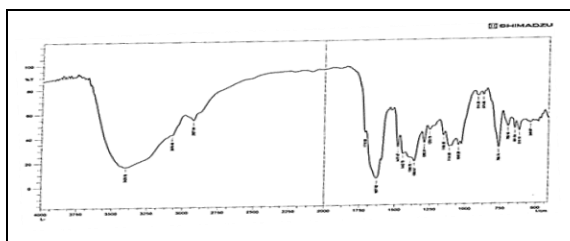


Figure 4. FT-IR spectrum of ONMILA.

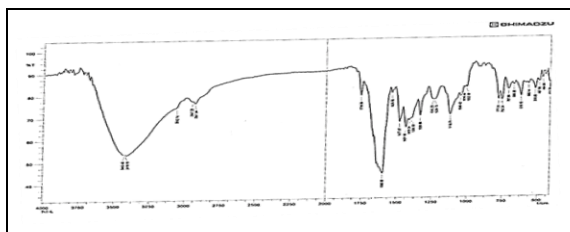


Figure 5. FT-IR spectrum of Ni(II) complex with ONMILA.

3.5 Electronic spectra

Table 3 lists the electronic absorption bands. Uv-Visible spectrum of ONMILA revealed three absorptions as shown in Figure 6 - two at (261 nm, 38341 cm⁻¹) and the other at (334 nm, 29940 cm⁻¹) due to the $\pi-\pi^*$, and one at (411 nm, 24330 cm⁻¹) attributable to the $n-\pi^*$ transition (Ahmed et al., 2015). Two bands that emerged at 825 nm, 12121 cm⁻¹ in Figure 7 electronic spectra for the Co-complex in ethanol solution were ascribed to the ${}^4T_{1g} \rightarrow {}^4A_{2g}$ (ν_2) and ${}^4T_{1g} \rightarrow {}^4T_{1g(p)}$ (ν_3) transitions of octahedral geometry (Ahmed et al., 2015). Using the diagram of Tanaba-Sugano for the d⁷ arrangement of octahedral geometry, the $B_{complex}$ (607.14) value as well as the position of ν_1 (9621 cm⁻¹) were computed using the ratio of (ν_3)/(ν_2) (1.35). (Nisah et al., 2021). The covalent nature is shown by the value of β (0.62). Three bands can be seen in the visible part of the Ni(II) complex's spectrum at (425 nm, 23512 cm⁻¹) ${}^3A_{2g} \rightarrow {}^3T_{1g(p)}$ (ν_3), (702 nm, 14226cm⁻¹) ${}^3A_{2g} \rightarrow {}^3T_{1g(f)}$ (ν_2), the final one at (9183 cm⁻¹) ${}^3A_{2g} \rightarrow {}^3T_{2g(f)}$ (ν_1). On the Tanaba-Sugano diagram, the ratio of ν_2/ν_1 1.54, was used for the d⁸ octahedral complexes (Ahmed et al., 2016), $B_{complex}$ (694.7), and β (0.67). Broadband at (760 nm, 13157 cm⁻¹) in the Cu(II) complex spectrum was due to the ${}^2E_g \rightarrow {}^2T_{2g}$ transition, which is related to the Jahn-Teller distortion

of the octahedral geometry (O'Toole et al., 2019). There was no visible bands in the Cd(II) and Zn(II) complexes spectra as described in Figures 8, 9; instead, there were only bands associated with charge transfer transitions (348 nm, 28735 cm⁻¹) Zn(II) (321 nm, 31152 cm⁻¹) When contrasted were free ligand, there was a presence of two bands at (237 nm, 42194 cm⁻¹) and at (263 nm, 38022 cm⁻¹) (Mutlu et al., 2020).

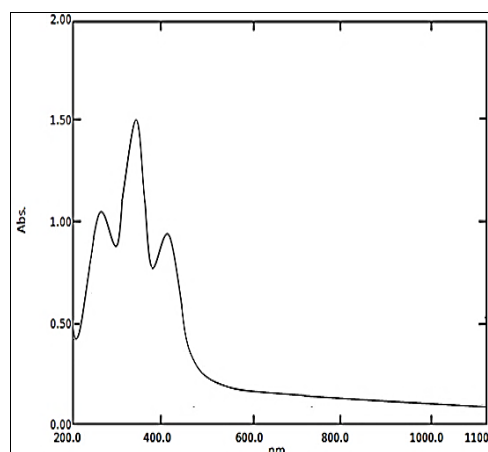


Figure 6. Electronic spectrum of ONMILA.

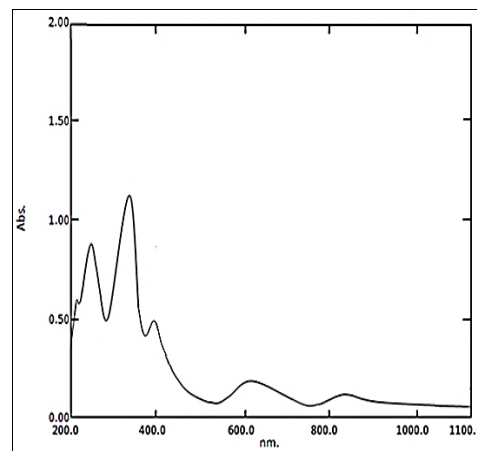


Figure 7. Electronic spectrum of ONMILA-Co(II) complex.

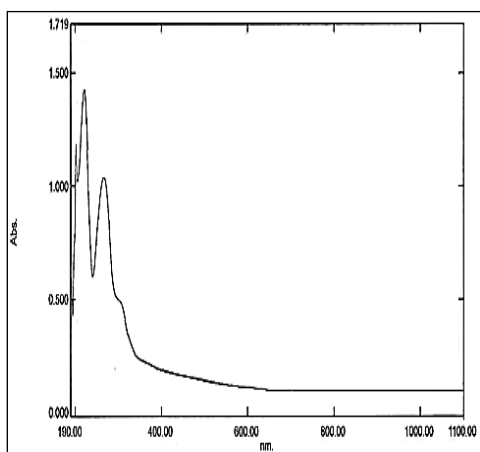


Figure 8. Electronic spectrum of ONMILA-Zn(II) Complex

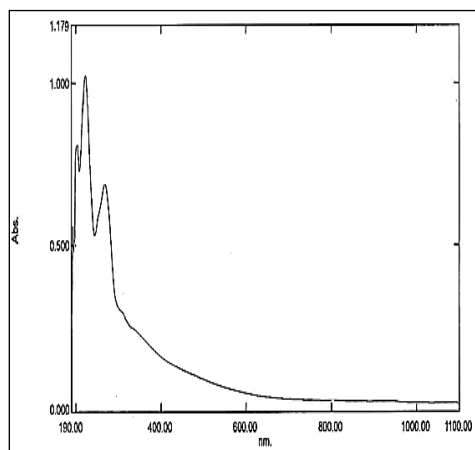


Figure 9. Electronic spectrum of ONMILA-Cd(II) Zn(II) complex.

3.6 Magnetic measurements

The magnetic moment's values possessed by the complexes were used in order to ascertain the coordination of the metal ion. Due to the inherent orbital angular momentum, there is always a big orbital contribution in the ground state, and the effective magnetic moment at ambient temperature was between (4.7 and 5.2 B.M.). The magnetic moment magnitude of the present complex, which was 4.83 B.M., suggested that the Co(II) complex in its high-spin form has the structure of an octahedron (Ahmed et al., 2016). The orbital contribution magnitude is what determines the greater range of values of magnetic moment (2.9-3.4 B.M.) for the complex of a high-spin Ni(II). The magnetic moment obtained in this investigation, 3.16, was in the expected range like octahedral Ni(II) ions (Ahmed et al., 2016). The Cu(II) complex magnetic moment was 1.76 B.M., and it was rather near to the spin value expected for one unpaired electron at 1.73 B.M.. As a result, the Cu(II) complex has the structure of an octahedron (Mutlu et al., 2020; Padmaningrum et al., 2022). According to Sanchez-Lara et al., 2021, the diamagnetic magnetic moments values of the metal complexes Zn(II) and Cd(II) are equal to those of the (d¹⁰) configuration. Table 3 lists the magnetic moments that have been measured.

3.7 Conductivity measurements

All soluble complexes were dissolved in ethanol solvent (1x10⁻³ M) at room temperature and they showed molar conductivity values of (38.07 – 12.95) S.cm². mol⁻¹. The complexes of Co(II), Cu(II) and Ni(II) had low conductivity and a non-ionic structure (Ahmed et al., 2016) while the conductivity tests of Cd(II) and Zn(II) revealed them as electrolytes (Yoe & Jones, 1944). Table 3 shows the conductivity values.

Table 3. Electronic spectra of ONMILA and its metal complexes, measurements of Racah parameter B', nephelauxetic parameter β, magnetic and conductivity values.

Compound	Band position nm	Band position cm ⁻¹	Assignments	B' cm ⁻¹	β	Λ.M S.cm ² .mol ⁻¹	μ _{eff} B.M	Proposed Structure
ONMILA (L)	261	38341	π→π*	—	—	—	—	—
	334	29940						
	411	24330						
L-Co(II)	610	16393	⁴ T _{1g} → ⁴ T _{1g} (p)	607.14	0.62	15.31	4.83	Octahedral Sp ³ d ²
	825	12121	⁴ T _{1g} → ⁴ A _{2g}					
L-Ni(II)	425	23512	³ A _{2g} → ³ T _{1g} (p)	694.7	0.67	12.95	3.16	Octahedral Sp ³ d ²
	702	14226	³ A _{2g} → ³ T _{1g} (F)					
	1088	9183	³ A _{2g} → ³ T _{2g} (F)					
L-Cu(II)	760	13157	² E _g → ² T _{2g}	—	—	16.02	1.76	Octahedral Sp ³ d ²
L-Zn(II)	348	28735	M-L.C.T	—	—	37.84	Dia.	Octahedral Sp ³ d ²
L-Cd(II)	321	31152	M-L C.T	—	—	39.07	Dia.	Octahedral Sp ³ d ²

C.T. = Ligand Field Charge Transfer

3.8 Proposed Molecular Structures of Prepared Complexes

Earlier studies (Ahmed *et al.*, 2016; Mutlu *et al.*, 2020; Nisah *et al.*, 2021; Padmaningrum *et al.*, 2022) have examined the coordination sites available in the ligand and how they are related to various metal ions. The spectroscopic and analytical results based on the molar ratio, elemental analysis metal contents, magnetic measurements and the molar electrical conductivity measurements, as well as the results of the ¹H-NMR spectrum, the ¹³C-NMR spectrum, the UV-Vis spectra and the infrared (FT-IR) spectra all indicated the complexes had octahedral geometry where the ligand behaved as tridentate coordination process. The oxygen of the carbonyl group and two nitrogen atoms of the 6-methyl-2-pyridylmethyl amine bound the ligand to metal ions in addition to water as aqua and chloro ion resulting in six donated atoms to the metal ions, Figures (10 and 11) describe the geometrical aspects of these compounds. There is a 1:1 mole ratio of M to L in these structures.

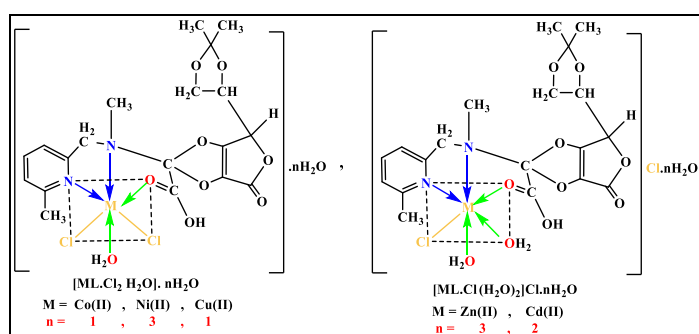


Figure 10. The suggested structure of metals ion complexes with ONMILA.

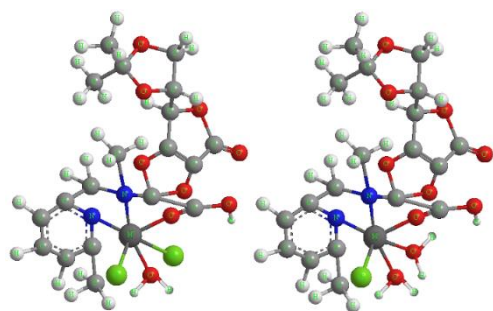


Figure 11. The proposed molecular 3D structure of ONMILA complexes.

3.9 Biological activity

The *in-vitro* growth inhibitory ligand activities and their complexes on Gram (+) bacteria, such as *Staphylococcus aureus* and *Streptococcus pyogenes* and Gram (-) bacteria, namely *Klebsiella pneumonia* and *E-coli*, were investigated using the spotted diffusion method. All of the substances exhibited a significant level of antibacterial activity when tested against the organisms in question. The *Streptococcus pyogenes* and *Staphylococcus aureus* were sensitive to the ligand and its complexes indicating that the biological activity of the complexes ranged from moderate to high. The Cd(II) complex showed higher

antibacterial activity, either *E. coli* or *K. pneumonia*. There was only a slight amount of activity with the ligand and the complexes of Co(II), Cu(II) and Ni(II) while Cu(II) and Zn(II) showed moderate activity. However, the Cd(II) complex showed higher antibacterial activity from either *E. coli* or *K. pneumonia*. The cause of this resistance is the bacteria that live in the colon. These bacteria exist as a single bacillus and have a thick shell that completely encases their cell. The high lipid content of this coating helps to prevent them from entering the cell, in contrast to the bacteria *Staphylococcus aureus* and *Streptococcus pyogenes* which lack this characteristic. They will have a reduced ability to withstand the effects of chemical and antibiotic chemicals that penetrate the inside of the bacterial cell (Shiekhzadeh *et al.*, 2020; Abu-Dief *et al.*, 2020). As a direct consequence of this, the chemical agents that were investigated had a more powerful inhibiting effect. Since the metal ions included inside metal complexes were lipophilic, metal complexes have a higher activity level than free ligands (Omotade *et al.*, 2020). There is also the possibility that these complexes contain antibacterial capabilities which would stop the multiplication of microbes by blocking the active sites of the organisms (Xue *et al.*, 2020). The impermeability of the microorganisms' cells or alterations in the ribosomes of the microbial cells determine the effectiveness of different complexes against the germs that have been tested (Abdel-Rahman *et al.*, 2016). According to Overtone's theory and chelation as described by Tweedy (1964), the metal ion polarity is significantly decreased during the chelation process because of overlaps of the ligand orbital and the slight sharing of the metal ion positive with donor groups. Additionally, the π -electron delocalisation is magnified throughout the chelate sphere resulting in an increase in the lipophilicity of the complex. Through the process of chelation, the core metal atom becomes more lipophilic, which makes it possible for it to traverse the lipid layer of the cell membrane (Pang *et al.*, 2019). Variations in the antibacterial activity are caused by the properties of metal ions as well as the cell membranes of the microorganisms. According to (Hameed *et al.*, 2021), cell wall function inhibition, cell membrane and nucleic acid generation are the four different modes of action that may be attributed to antibacterial medications. These data are presented in Table 4, and the graphical representation of the statistics may be seen in Figure 12.

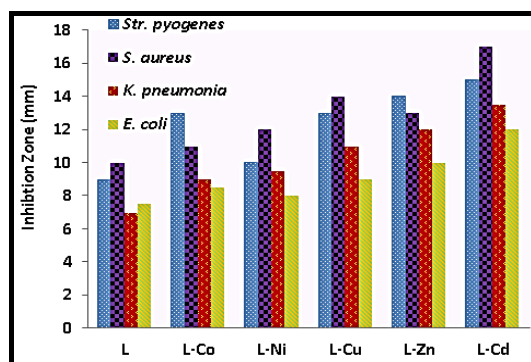


Figure 12. Statistical representation of antibacterial activity for ONMILA and its complexes.

Table 4. Inhibition area (mm) of the bacterial sensitivity (zone inhibition) to the compounds.

Compound	Pathogenic Bacteria			
	<i>Str. pyogenes</i> G(+)	<i>S. aureus</i> G(+)	<i>K. pneumoniae</i> G(-)	<i>E. coli</i> G(-)
Ligand (L)	++	++	+	+
[Co(L)Cl ₂ (H ₂ O)]H ₂ O	+++	++	+	+
[Ni(L)Cl ₂ (H ₂ O)]3H ₂ O	++	+++	+	+
[Cu(L)Cl ₂ (H ₂ O)]H ₂ O	+++	+++	++	+
[Zn(L)Cl(H ₂ O) ₂]Cl.3H ₂ O	++	+++	++	++
[Cd(L)Cl(H ₂ O) ₂]Cl.2H ₂ O	+++	+++	+++	++

Not: (6-9) mm = + (A bit active), (9-12) mm = ++ (Moderate active),

(12-17) mm = +++ (High level of activity)

4. Conclusion

Spectroscopic analyses, such as elemental analysis, metal content, mass spectrum, ¹H, ¹³C-NMR, I.R., and UV-Vis, were used in this research to examine metal ions complexes of the new ligand. Conductivity measurements and magnetic susceptibility testing supported the octahedral geometry of all complexes. There was a 1:1 mole ratio of M to L in these structures. The biological activity of each chemical pointed to its antibacterial properties.

5. Acknowledgement

The author expresses his gratitude to the staff of Department of Chemistry, Faculty of Science, Kufa University for their support which resulted in the completion of this research paper. A big thank you is also due to Dr Lekaa Khalid and lecture Duha Mohammed for their research assistance.

6. References

- Abdel-Rahman L H., Abu-Dief A M., Ismael M., Mohamed M A., Hashem N A. (2016). Synthesis, structure elucidation, biological screening, molecular modeling and DNA binding of some Cu (II) chelates incorporating imines derived from amino acids, *Journal of Molecular Structure*, 1103: 232-244.
- Abu Dief A M, Abdel Rahman L H., Abdel Mawgoud A H. (2020). A robust in vitro anticancer, antioxidant and antimicrobial agents based on new metal-azomethine chelates incorporating Ag (I), Pd (II) and VO (II) cations: Probing the aspects of DNA interaction, *Applied Organometallic Chemistry*, 34, no. 2, e5373: 1-20.
- Ahmed A. H., Hassan A. H., Gumaa A. B., Mohamed H., Eraky A M. (2016). Nickel (II)-oxaloyldihydrazone complexes: Characterization, indirect band gap energy and antimicrobial evaluation, *Cogent Chemistry*, 2, no. 1: 1142820: 1-14.
- Ahmed N., Riaz M., Ahmed A., Bhagat M. (2015). Synthesis, characterisation, and biological evaluation of Zn (II) complex with tridentate (NNO Donor) schiff base ligand, *International Journal of Inorganic Chemistry*, 2015: 1-5.
- Al-Farhan B S., Basha M T., Abdel Rahman L H., El-Saghier A M., El-Ezz D A., Marzouk A., Shehata M R., Abdalla E. M. (2021). Synthesis, DFT Calculations, Antiproliferative, Bactericidal Activity and Molecular Docking of Novel Mixed-Ligand Salen/8-Hydroxyquinoline Metal Complexes, *Molecules*, 26, no. 16: 4725.
- Al-Khafagy A. (2016). Synthesis, characterization and biological study of some new metal-azo chelate complexes, *Journal of Chemical and Pharmaceutical Research*, 8, no. 8: 296-302.
- Al-Noor T H., Mohapatra R K., Azam M., AbdulKarem L K., Mohapatra P K., Ibrahim A A., Parhi P K., Dash G C., El-ajaily M., Al-Resayes S I., Raval M K., Pintilie L. (2021). Mixed-ligand complexes of ampicillin derived Schiff base ligand and Nicotinamide: Synthesis, physico-chemical studies, DFT calculation, antibacterial study and molecular docking analysis, *Journal of Molecular Structure*, 1229: 129832.
- Bellavite P., Donzelli A. (2020). Hesperidin and SARS-CoV-2: New Light on the Healthy Function of Citrus Fruits, *Antioxidants*, 9, 742: 1-18.
- Chatterjee I. (1973). "Evolution and the biosynthesis of ascorbic acid, *Science*, 182, no. 4118: 1271-1272.
- El-Sonbati A., El-Bindary A., Mohamed G., Morgan S M., Hassan W., Elkholy A. (2016). Geometrical structures, thermal properties and antimicrobial activity studies of azodye complexes, *Journal of Molecular Liquids*, 218: 16-34.

- Fodor G., Arnold R., Mohacsi T., Karle I., Flippen-Anderson J. (1983). A new role for L-ascorbic acid: Michael donor to α , β -unsaturated carbonyl compounds, *Tetrahedron*, 39, no. 13: 2137-2145.
- Gao K., Mi H. (2021). Application of Membrane-Inlet Mass Spectrometry to Measurements of Photosynthetic Processes, *Research Methods of Environmental Physiology in Aquatic Sciences*, Springer: 187–192.
- Hameed G F., Wadday F Y., Farhan M A A., Hussain S A. (2021). Synthesis, Spectroscopic characterization and bactericidal valuation of some metal (II) complexes with new Tridentate Heterocyclic Azo Ligand Type (NNO) Donor, *Egyptian Journal of Chemistry*, 64, no.3:10-11.
- Hanukoglu I. (2006). Antioxidant protective mechanisms against reactive oxygen species (ROS) generated by mitochondrial P450 systems in steroidogenic cells, *Drug metabolism reviews*, 38, no. 1-2: 171-196.
- Hariprasath K., Deepthi B., Babu I., Venkatesh S P., Sharfudeen S., Soumya V. (2010). Metal complexes in drug research-a review, *Journal of Chemical and Pharmaceutical Research*, 2, no. 4: 496-499.
- Hollis L S., Amundsen A R., Stern E W. (1985). Synthesis, structure and antitumor properties of platinum complexes of vitamin C, *Journal of the American Chemical Society*, 107, no. 1: 274-276.
- John N., James C. (2009). Scientific opinion of the panel on food additive and nutrient sources added to food on a request from the commission on calcium ascorbate, magnesium ascorbate and zinc ascorbate added for nutritional purposes in food supplements, *The European Food Safety Authority Journal*, 994: 1-22.
- Kareem M J., Al-Hamdani A A., Al Zoubi Y K., Mohammed S G. (2021). Synthesis, characterization, and determination antioxidant activities for new Schiff base complexes derived from 2-(1H-indol-3-yl)-ethylamine and metal ion complexes, *Journal of molecular Structure*, 1231, 129669: 1-18.
- Lawal M., Obaleye J A., Bamigboye M. O., Nnabuike G G., Ayinla S O., Rajee, A O., Babamale H. F., Ajibola A A. (2017). Mixed metal complexes of isoniazid and ascorbic acid: chelation, characterization and antimicrobial activities, *Nigerian Journal of Chemical Research*, 22, no. 1: 20-28.
- Loke W M., Proudfoot J M., McKinley A J., Croft K D. (2006). Augmentation of monocyte intracellular ascorbate in vitro protects cells from oxidative damage and inflammatory responses, *Biochemical and biophysical research communications*, 345, no. 3: 1039-1043.
- Mutlu Gençkal H., Erkisa M., Alper P., Sahin S., Ulukaya E., Ari F. (2020). Mixed ligand complexes of Co (II), Ni (II) and Cu (II) with quercetin and diimine ligands: Synthesis, characterization, anti-cancer and anti-oxidant activity, *JBIC Journal of Biological Inorganic Chemistry*, 25, no. 1: 161-177.
- Naji S H. (2014). Synthesis, Spectroscopic and biological studies of some metal complexes with 2,4-dinitro-2'-amino hydrazo benzene Al- Mustansiriyah *Journal of Science*, 25, No.2: 73-88.
- Nisah K., Ramli M., Idroes R., Safitri E. (2021). Study of linearity and stability of Pb (II)-1, 10-phenanthroline complex with the presence of Fe (II) dan Mg (II) matrix ions using UV-Vis spectrophotometry, in *IOP Conference Series: Materials Science and Engineering*, 1087, 012052, no. 1: IOP Publishing: 1-7.
- O'Toole N., Lecourt C., Suffren Y., Hauser A., Khrouz L., Jeanneau E., Brioude A., Luneau D, Desroches C. (2019). Photogeneration of manganese (III) from luminescent manganese (II) complexes with thiacalixarene ligands: Synthesis, structures and photophysical properties, *European Journal of Inorganic Chemistry*, 2019, no. 1: 73-78.
- Omotade E., Oviawe A., Elemike E. (2020). Synthesis, Characterization And Antimicrobial Activity Of Mixed Ligand Complexes of Benzyliminothiosemicarbazide And L-Phenylalanine With Divalent Fe, Co and Ni, *Journal of Chemical Society of Nigeria*, 45, no. 2: 282 - 289.
- Padayatty S J., Katz A., Wang Y., Eck P., Kwon O., Lee J., Chen S., Corpe C., Dutta A., Dutta S K., Levine M. (2003). Vitamin C as an antioxidant: evaluation of its role in disease prevention, *Journal of the American college of Nutrition*, 22, no. 1: 18-35.
- Padmaningrum R. T., Louise I S Y., Yunita I., Sugiyarto K H. (2022). Infrared Spectral And Magnetic Properties Of Basic Copper(II) Nitrate Produced By Slow Titration Method, *Malaysian Journal Of Science*, 41(1): 106-116.
- Pang Z., Raudonis R., Glick B R., Lin T J., Cheng Z. (2019). Antibiotic resistance in *Pseudomonas aeruginosa*: mechanisms and alternative therapeutic strategies, *Biotechnology advances*, 37, no. 1: 177-192.
- Radisavljević S., Petrović B. (2020). Gold (III) complexes: An overview on their kinetics, interactions with DNA/BSA, cytotoxic activity, and computational calculations, *Frontiers in chemistry*, 8, 379: 1-8.
- Raman N., Sobha S. (2010). Synthesis, characterization, DNA interaction and antimicrobial screening of isatin-based polypyridyl mixed ligand Cu (II) and Zn (II) complexes, *Journal of the Serbian Chemical Society*, 75, no. 6: 773-788.

- Sánchez-Lara E., García-García A., González-Vergara E., Cepeda J., Rodríguez-Diéguez A. (2021). Magneto-structural correlations of cyclo-tetranavanadates functionalized with mixed-ligand copper (ii) complexes, *New Journal of Chemistry*, 45, no. 11: 5081-5092.
- Shiekhzadeh A., Sohrabi N., Moghadam M E., Oftadeh M. (2020). Kinetic and thermodynamic investigation of human serum albumin interaction with anticancer glycine derivative of platinum complex by using spectroscopic methods and molecular docking, *Applied Biochemistry and Biotechnology*, 190, no. 2: 506-528.
- Tweedy B. (1964). Plant extracts with metal ions as potential antimicrobial agents, *Phytopathology*, 55: 910-914.
- Valarmathy G., Subbalakshmi R., Sumathi R., Renganathan R. (2020). Synthesis of Schiff base ligand from N-substituted benzenesulfonamide and its complexes: Spectral, thermal, electrochemical behavior, fluorescence quenching, in vitro-biological and in-vitro cytotoxic studies, *Journal of Molecular Structure*, 1199: 127029.
- Waddai F Y., Musa F H., Fidhel H A. (2015). Synthesis And Characterization Of Some Metal Complexes With Bis [O, O-2, 3; O, O-5, 6-(N, N-Dicarboxylic Methylidene)-N-2-Methylenepyridyl]-L-Ascorbic Acid, *European Chemical Bulletin*, 4, no. 2: 74-79.
- Wasi N., Singh H., Gajanana A., Raichowdhary A. (1987). Synthesis of metal complexes of antimalarial drugs and in vitro evaluation of their activity against plasmodium falciparum, *Inorganica chimica acta*, 135, no. 2: 133-137.
- Xue L W., Zhang H J., Wang P P. (2020). Synthesis, crystal structures, and antimicrobial activity of copper(II) complexes derived from N'-(1-(pyridin-2-yl)ethylidene)isonicotinohydrazide, *Inorganic and Nano-Metal Chemistry*, 50, no. 8: 637-643.
- Yoe J. H., Jones A L. (1944). Colorimetric determination of iron with disodium-1, 2-dihydroxybenzene-3, 5-disulfonate, *Industrial and Engineering Chemistry Analytical Edition*, 16, no. 2: 111-115.
- Zümreoglu-Karan B. (2006). The coordination chemistry of Vitamin C: An overview, *Coordination Chemistry Reviews*, 250, no. 17-18: 2295-2307.

A NUMERICAL STUDY OF JOULE HEATING EFFECT IN ELECTRODEPOSITION PROCESS-CASE OF COPPER ELECTRODEPOSITION

Watheq Naser Hussein^{1a*}, Mohammed Ali Alshuraifi^{2a}, Bashar Abid Hamza^{3a}, and Raheem Aziz Hussein^{4b}

Abstract: The electrochemical process in the presence of heat dissipation effect (Joule heating effect) is highly detected in practical electroplating solutions such as 0.6 M CuSO₄+0.5 M H₂SO₄ electrolyte, where currents passing through the cathode-anode-electrolyte increase temperature in the electrolyte and electrodes. Due to the complex nature of such systems and the diversity of physics describing it, a theoretical approach of appearance for natural convection on vertical and horizontal sides of a cathode in the presence and absence of Joule effect under unsteady state condition was observed using Comsol Multiphysics. It was found that the onset of natural convection on a vertical side depends on the Joule effect, and the time (t_n) for appearance is longer on the edges than in other areas. The horizontal side of a cathode assists the appearance of natural convection in the presence and absence of the Joule effect. The Rayleigh (Ra) number has larger values on the vertical side than the horizontal side due to the effect of surface concentration distribution C_s. A Sherwood, Sh-Ra mathematical relation such that $Sh=0.03Ra^{0.86}$ was proposed where natural convection had no pronounced effect on the deposition process. It was found that the Joule heating effect negatively affects the electrodeposition process by reducing the local current values.

Keywords: Natural convection, buoyancy, comsol, rayleigh

1. Introduction

Electrochemical deposition reduces metal ions of more than one metal (alloy) on a well-prepared conducting surface substrate to protect against corrosion or obtain some useful properties (Lowenheim, 1977). Accordingly, the electrodeposition process is a type of surface engineering activity.

Many factors affect the electrodeposition process, such as substrate morphology type, electrochemical properties, thermodynamic properties, and kinetic factors. Other factors affecting the solution-substrate interface include pH and temperature (Kanani, 2005; Lowenheim, 1977). In general, temperature can play several roles. The first is its effect on the solution through solubility, evaporation of the bath solution, stability of the solution constituents etc. The second effect is confined to the surface-solution interface, where increasing temperature increases the rate and efficiency of the electrodeposition process and reduces energy consumption (Gonçalves et al., 2021). The third relates to the electrodeposit properties, where previous studies suggest that increasing the temperature to 60°C increases surface roughness or dendrite formation (Gonçalves et al., 2021; Jeon et al., 2022). Kwon et al. (2017) found that increasing temperature reduces the hardness of some deposits and increases the grain size.

It is known that an electrochemical process is a rate process, meaning that the oxidation or the anodic process and the reduction of ions are sensitive to the surface temperature and mass transfer effect (Al-Duaij et al., 2017; Paunovic, 2006). Many electrochemical depositions take place at approximately constant temperatures of about 30°C. In electrodeposition, the works (pieces, load or cathode to be electrodeposited) is a batch process. As soon as a quantity of pieces is treated-electrodeposited, another quantity is served for the process in a sequence. Depending on the requirements, this could be done within a work shift or more. Large electrical current values are used depending on the work area (the current density is determined by dividing the total current by the total load area, which is commonly used in the electrodeposition field). Since the current path from the bus bar to the solution is variable, there will be a potential drop accompanied by a heating dissipating mechanism or Joule heating effect. Joule heating or Ohm's law (Diogo et al., 2013) is a phenomenon that accompanies the passing of a current in a conductor and is proportional to the conductor's resistance value.

Figure 1 shows the resistivity values for some electrodes used in electrochemistry (Diogo et al., 2013). Zinc, steel, and cadmium deposition with lower conductivity values than copper and aluminium are widely used in many electroplating systems. Therefore, Joule heating is expected to have more effect for the same current value, eventually increasing solution and deposit layer or surface temperature.

Authors information:

^aEnergy Engineering, Babylon University, Babylon, IRAQ.
E-mail: met.watheq.naser@uobabylon.edu.iq¹;
met.bashir.abid@uobabylon.edu.iq³

^bChemistry, Wasit University, Alkut, IRAQ. E-mail:
raheem_aziz2002@yahoo.com⁴

*Corresponding

Author:

met.watheq.naser@uobabylon.edu.iq

Received: December 1, 2022

Accepted: February 21, 2023

Published: October 31, 2023

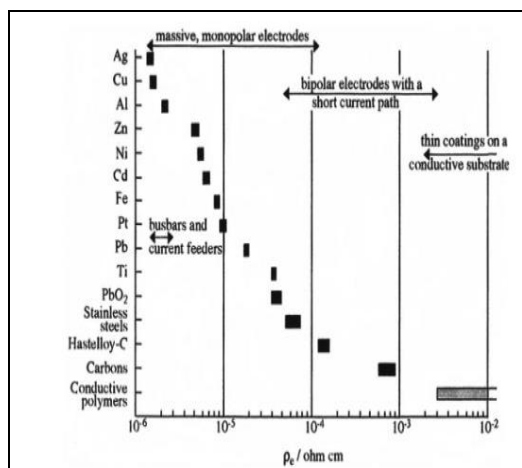


Figure 1. Resistivity of some electrodes (Diogo et al., 2013)

The process involves heat transfer between the electrodes or works and the solution, meaning the surface temperature is higher than the solution wherever the current is passing. Increasing the cathode surface’s temperature in the presence of dissolved species affects concentration distribution. Due to the density effect, the ions are intensified near the bottom of the solution, imparting a poverty zone in the upper layers of the solution. Therefore, the current distribution is affected, especially when the kinetics are concentration-dependent. Density variation within the solution induces free convection. This variation is either due to localized heating or the distribution of dissolved species. Natural convection depends on the object geometry and temperature difference between the hot surface and the colder fluid (Selman et al., 1971; Amir et al., 2019).

Only a few studies consider the Joule heating effect on the electrodeposition process. Only the Laplace equation with heat transfer by conduction was solved without referring to the convection effect (Barvinski, 2006). According to our knowledge, this is far from the industrial problem consideration regarding electrodeposition solutions. Schröter et al. (2002) showed that temperature gradient has a pronounced effect on convection near electrodes. Other concepts were used for other purposes (Hwang et al., 2019; Li et al., 2017). Other studies investigated conditions totally different from this study's focus and did not deal with complicated conditions (Selman et al., 1971; Amir et al., 2019; Kawai et al., 2009).

Natural convection appears due to the non-uniform density of the solution due to concentration or temperature differences. Therefore, in this study, a numerical approach was conducted to detect the Joule heating effect on the onset of natural convection via the concentration of the active species under an unsteady state process. The deposits' morphology, adherence, and porosity were not the subject of this study because these properties require experimental work and inspection. Unsteady state process best fits industrial applications, where the surface and solution temperature are variable as time proceeds, and

increasing solution temperature is accompanied by some risks. The cooling process to maintain the temperature within the desired range using a cooling coil or jacket adds complexities to the economic considerations.

This study assumed that: 1) the work received a constant value of current or current density (galvanostat); 2) the energy dissipation as heat (Joule effect) takes place only in the stagnant solution in absence of cooling process (i.e., insulated walls of the cell); 3) the evolution of deposit layer has no significant role in affecting the electrode’s surface temperature (thin layer); 4) the anodes have a larger area than the cathode, therefore, their joule heat effects are negligible; 5) Cu⁺² is electrodeposited on cathode as the main reduction reaction; 6) H⁺ also is reduced on cathode; 7) the initial temperature of the solution is 303 K.

2. Numerical Simulation

The electrochemical system in this study is very complex. There are several ions with different diffusivities, concentrations and charge numbers. A system might not be adequately studied, and experimental work for obtaining the relevant variables is difficult due to interactions between diffusion and electro-migration flux, where both have the same direction. Moreover, there are more than two ions with different properties. This attribution conforms with (Volgin et al., 2009).

In this study, the Joule effect is used with applied current density on one side, and the other side is grounded. The general form handles and represents heat transfer (Holm and Jack, 2010).

$$\nabla(K\nabla T) + q = \rho c_p \frac{\partial T}{\partial t} \tag{1}$$

For a constant thermal conductivity (within the range of temperatures estimated in this study and for ease of solution convergence), the following equation is used:

$$-\frac{q}{K} = -\frac{\rho c_p}{k} \frac{\partial T}{\partial t} + \nabla(\nabla T) \tag{2}$$

We consider the copper plating process (composed mainly of 0.6 M CuSO₄+0.5 M H₂SO₄) (Huang et al., 2019; Hussein, 2018) with an applied current density of 2 A/m². The cathode dimension is 15x40 cm, as shown in Figure 2. Electrolyte conductivity was approximated to 55 S/m. Unsteady state, laminar, and weakly incompressible flow were considered. Hence, the following forms of the Navier–Stokes and continuity equations are applicable:

$$\rho \frac{\partial U}{\partial t} + \rho(U \cdot \nabla)U = -\nabla P + \nabla \cdot (\rho I + k) + F + \rho g \tag{3}$$

$$\rho \nabla \cdot (U) = 0 \tag{4}$$

$$k = \mu(\nabla U + (\nabla U)^T) \tag{5}$$

The mass balance for the involved species can be represented by

$$\frac{\partial C_i}{\partial t} + \nabla J_i + U \nabla C_i = R_i \quad (6)$$

$$J_i = -D \nabla C_i + Z_i \mu_{m,i} F C_i \nabla \theta_i \quad (7)$$

Since the solution was composed of 0.6 M CuSO₄+0.5 M H₂SO₄ with a dissociation degree of 0.31 for HSO₄ (Sakr et al., 2013), the initial concentrations, *c*₀, for C⁺², H⁺, SO₄⁻², and HSO₄⁻ are 0.6, 0.65, 0.75 and 0.35, respectively. The flux at the electrode surface is (Kawai et al., 2009):

$$-D_1 \frac{\partial C_1}{\partial x} = \frac{j}{ZF} (1 - t_1 - t_2) \quad (8)$$

The transference number is given by

$$t_i = \frac{C_{i0} Z_i \mu_i}{\sum_{i=1} C_{i0} Z_i \mu_i} \quad (9)$$

Electroneutrality is also applicable inside the solution:

$$\sum C_i Z_i = 0 \quad (10)$$

With zero velocity and no concentration effect, Equation 7 is reduced to

$$\nabla^2 \theta = 0 \quad (11)$$

Equation 11 with appropriate boundary conditions can give the primary and secondary current distribution. The effect of mass transfer on current distribution is represented by tertiary current distribution:

$$j = j_0 C / C_b \cdot \exp(-\eta / b_c) \quad (12)$$

The flux of the deposition process for Cu⁺² ion at the cathode is given by

$$D \frac{\partial C_{Cu+2}}{\partial \xi} = C_{Cu+2} / C_b \cdot \exp(-\eta / b_c) / ZF \quad (13)$$

where ξ is the normal direction to the surface.

Equation 12 is a modified Tafel equation used to estimate the mass transfer effect on current distribution. Using appropriate boundary conditions with the given values (Kawai et al., 2009), in addition to the Joule effect, Equations 3-12 also give velocity, temperature, and concentration distribution. It is assumed that the current value used in this study is less than the limiting current value.

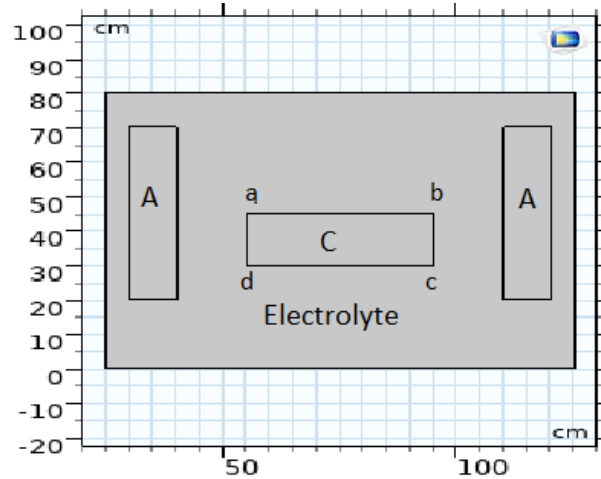


Figure 2. Configuration of the cell: A is the anode, and C is the cathode

Due to temperature variation within the solution, the relation of solution density to concentration can be represented by the linear expression in terms of solute concentration.

$$\frac{\rho_s - \rho_b}{\rho_b} = \sum_i^n \alpha_i (C_i - C_{ib}) \quad (14)$$

where α_i is the densification coefficient (Kawai et al., 2009; Sakr et al., 2013) in m³/mol=0.14*10⁻³, 2.68*10⁻⁵, 0 for Cu⁺² and H⁺, respectively and =0 for SO₄⁻² and HSO₄⁻.

The numerical simulation is approached using COMSOL 6 using time-dependent non-linear solver, element number of 9215. The parameters such as exchange current density and initial concentration can be found in (Hussein, 2018).

3. Results and Discussions

Many variables were used in this study, such as temperature distribution in the cell, solution velocity due to electrochemical process and temperature variation, concentration distribution for each active ion, diffusion layer, and temperature dependency. Considering all of them was tedious and needed much work that could be covered in more than one article. Therefore, a few limitations were introduced as necessary.

First, natural convection's appearance must be detected for both cases, with and without the Joule effect, as shown in Figure 3.

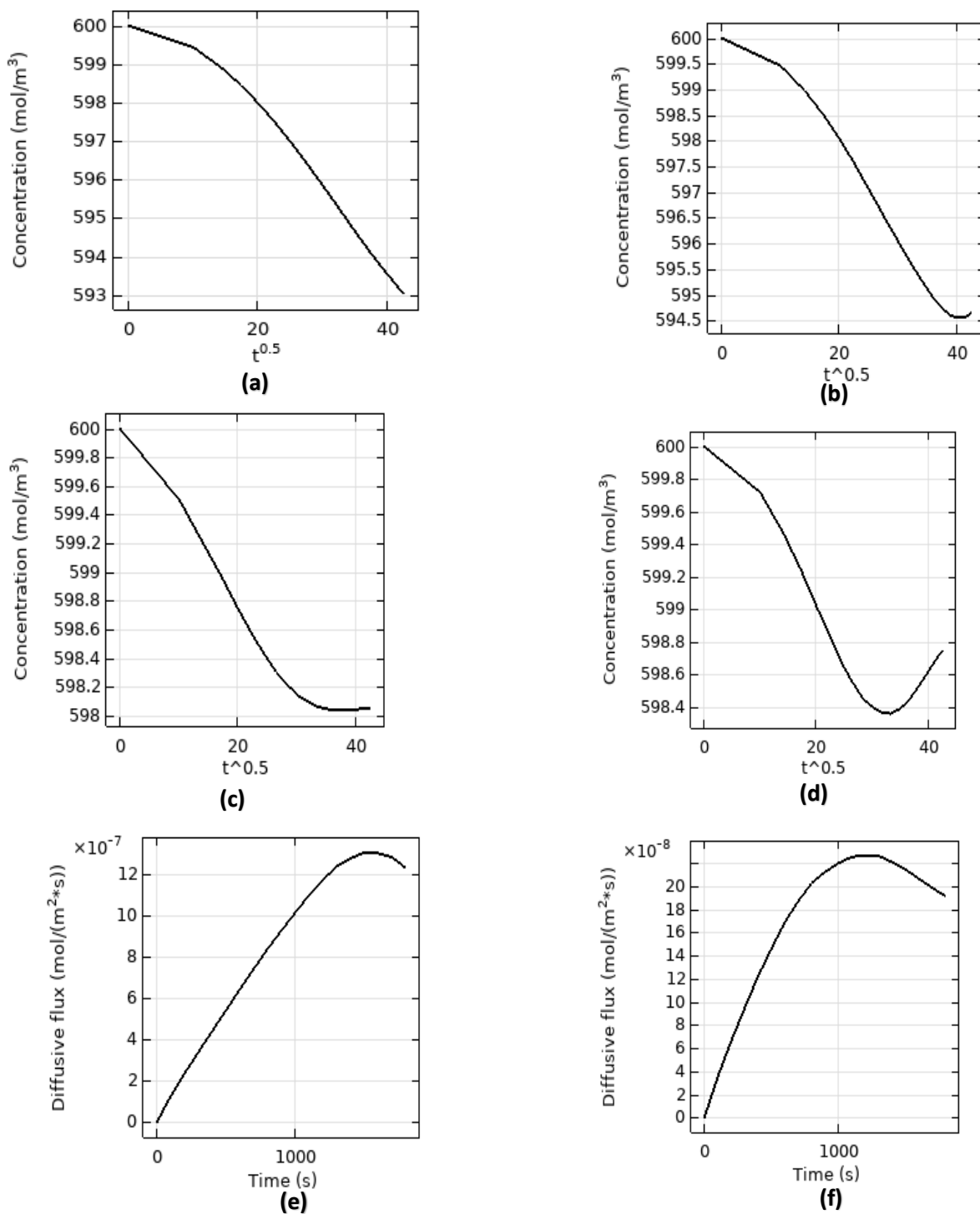


Figure 3. The onset of natural convection and diffusion flux: (a) without Joule effect at the midway of ad (b) with Joule effect at the midway of ad (c) without Joule effect at the midway of cd (d). with Joule effect at the midway of cd (e) diffusive flux at the midpoint of ad (f) diffusive flux at the midpoint of cd

Figure 3a and Table 1 show that natural convection is absent without Joule effect on the vertical surface along ad. The onset of natural convection on ad needs a longer time to appear near the edges of the electrode compared to Figure 3b and Table 1. In the early stages, the diffusion and migration mass transfer prevailed (Figures 3d-3e), and the Cu⁺² ions reduction is proportional to t^{0.5},

according to the Sand equation (Xuegeng et al., 2008). As time proceeds to a certain value, a deviation from linear to a quasi-steady state or equilibrium state of surface concentration is seen. At this stage, the buoyant force or natural convection becomes dominant. At the edges of the electrodes, the local current density intensified to a larger value than other points, and the

main component is the migration current. Accordingly, the edges needed a longer time for buoyancy to appear. In the case of the Joule effect, a higher temperature on the cathode surfaces created a graduated zone of temperature formation at the thermal boundary layer, assisting the appearance of buoyant forces, especially at the vertical electrode where the hot fluid motion was upwards against gravity. This behaviour coincided with the finding of (Xuegeng et al., 2008). The value differences are due to different cell configurations, process time, solution composition and temperature.

The onset of buoyant forces with and without the Joule effect on the horizontal cd surface was detected (Figures 3c and 3d) and could be attributed to increasing Archimedes force. The Archimedes force exceeded the viscous force at time t_n , leading to instability of the solution motion, where the force intensified in the vicinity of the surface ad. As the local current value increased, the time for the onset of buoyant force t_n also increased due to the reasons explained above. Table 1 gives the t_n values at a few positions of ad and cd.

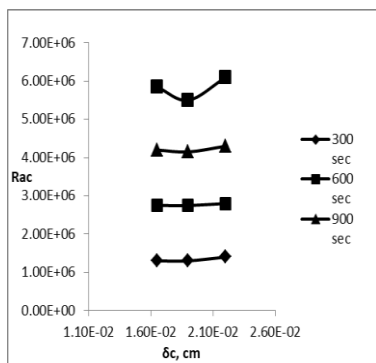
Table 1. Time of natural convection onset at selected positions

Surface	Position on electrode (cm)	Value of t_n (sec) ^{0.5} ($\delta_n, 10^{-5}m$)	
		With Joule effect	without
ad	5	37 (22)	-----
	7.5	31.5 (19)	-----
	10	33 (16.5)	-----
	20	37 (13)	35 (12)
cd	10	36 (15)	34 (13)
	5	39 (21)	33 (19)

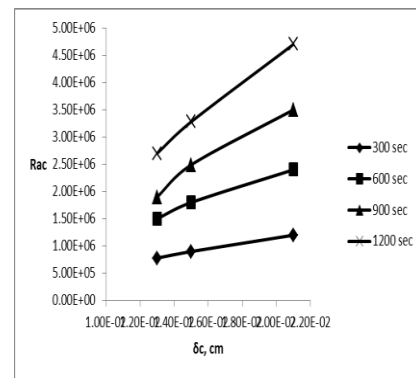
The critical Rayleigh number defined as the onset of natural convection, Ra_c is given by

$$Ra_c = g\delta_n(\rho_s - \rho_b) / \mu D \quad (15)$$

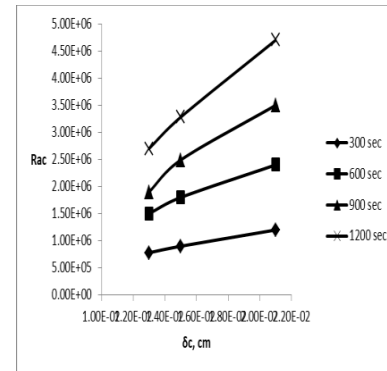
Here, ρ_s and ρ_b are the density values on the cathode surface and at the bulk, respectively, δ_n is diffusion layer thickness at time t_n .



(a)



(b)

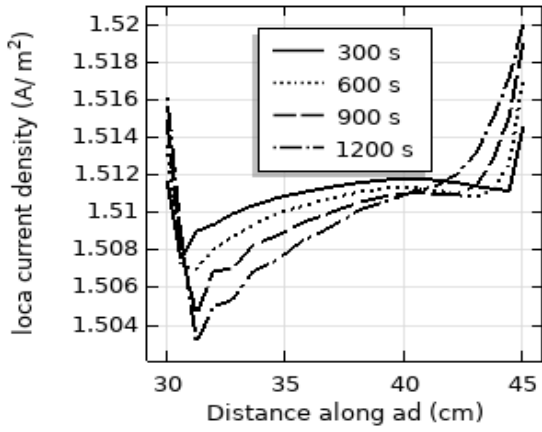


(c)

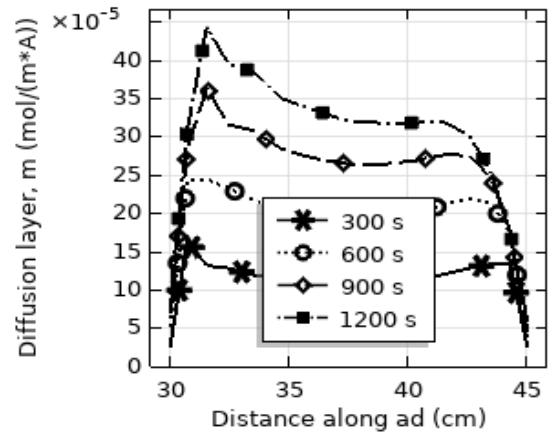
Figure 4. Relation of critical Rayleigh vs. critical diffusion layer at different time intervals:

(a) ad with Joule effect (b) cd with Joule effect (c) cd without Joule effect

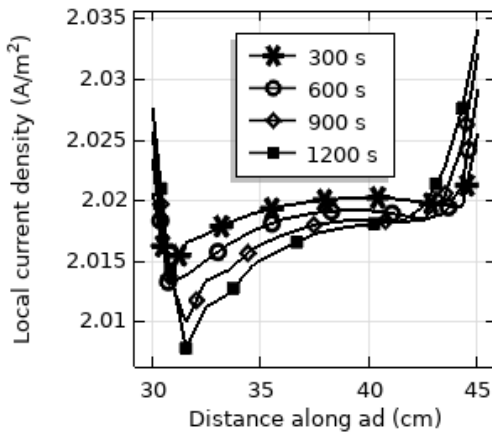
Figure 4 shows that the Ra_c values are generally higher in the absence of the Joule effect on the horizontal surface cd (Figure 4 c), which can be attributed to the larger values of surface concentration. The Ra_c values are approximately stabilized along the diffusion layer on the ad surface (Figure 4a). At the same time, Ra_c increased with increasing diffusion layer and was proportional to increasing time on the cd surface. Ra_c enhancement is generally clearly pronounced in the absence of the Joule effect, attributed to the lower surface concentration (higher local current, Figure 5). According to Table 1, the diffusion layer formed adjacent to cd is lower in the absence of the Joule effect than in its presence (see also Figure 6). Figure 5 shows approximately the same shape as the results obtained by Kawai et al. (2009) and Xue Geng et al. (2008).



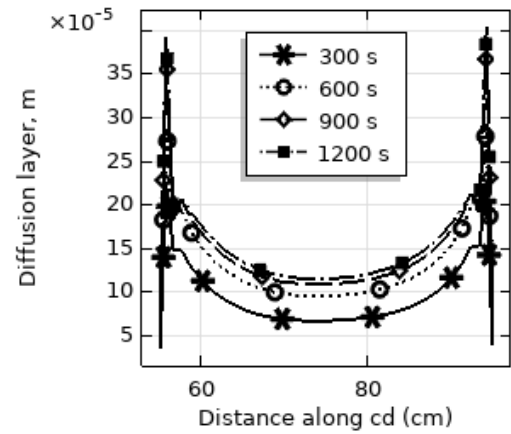
(a)



(b)



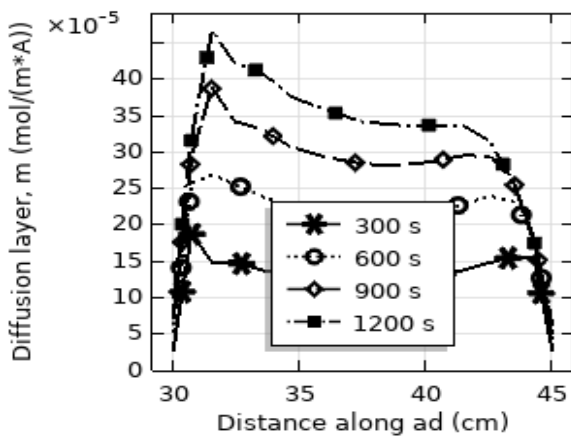
(b)



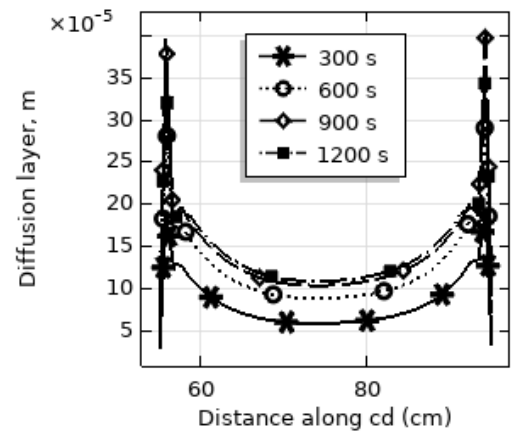
(c)

Figure 5. Distribution of local current on the ad: (a) in the presence of the Joule effect (b) in the absence of the Joule effect

Figure 6 shows the boundary layer evolution on ad and cd in the presence and absence of the Joule effect.



(a)



(d)

Figure 6. Evolution of diffusion layer δ : (a) with the Joule effect along ad starting from the bottom (b) without the Joule effect starting from the bottom along the same surface (c) with Joule effect along cd surface (d) without Joule effect along the same surface

Figure 6a shows that the diffusion layer values are uniformly distributed along the surface and with increasing thickness as time proceeds due to the Cu²⁺ depletion. Figure 6b shows the same shape in the absence of the Joule effect, except that it is slightly lower than in Figure 6a. Figures 6c and 6d show the same trend for surface cd except for the thickness of the diffusion layer, where the Joule effect is slightly higher. This can be attributed to the larger amount of diffusive flux in the presence of the Joule effect or the temperature effect on the surface concentration distribution of Cu²⁺ ions and the resultant effect of viscous extension.

Rayleigh can be correlated to Sherwood number through analogy concepts (Sang-Hyuk and Deok-Woon, 2006), where the attained relation from Figure 7 is $Sh=0.03Ra^{0.86}$ for ad and cd, where

$$Sh = \frac{K.L}{D} \tag{16}$$

$$K = \frac{(1-t)j}{nF(C_b - C_s)} \tag{17}$$

Other relations can be found in (Duchanoy et al., 2000; Xue Geng et al., 2008).

Generally, Rayleigh has a higher value on the vertical side ad than cd with enhanced mass transfer value. This observation confirms the findings mentioned above.

The convective force increased along ad and cd surfaces as an exponential function while the diffusive flux decreased (Figures 3e-3f). Figure 8 shows the velocity field after 1000 sec, representing approximately the onset of buoyant forces (Table 1), where the vortices are gathered near the vertical surface from the bottom. The vortices increase as the time passes 1200 sec and so on.

Finally, Figure 9 shows the surface temperature plot, where the surface temperature facing the anode increases as time proceeds due to the Joule effect and has larger values than other areas.

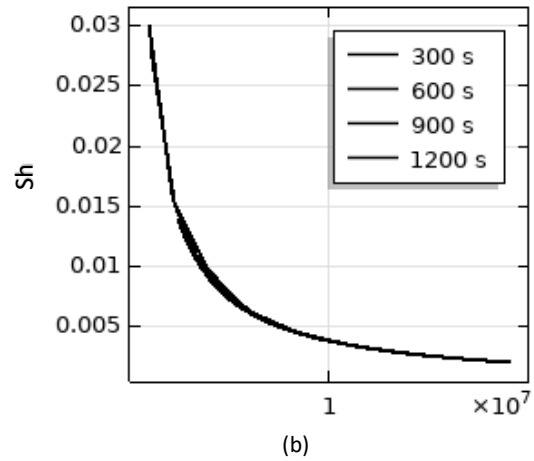
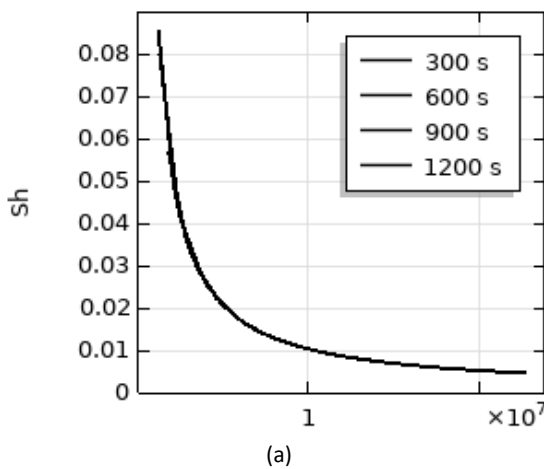


Figure 7. Sherwood-Rayleigh relationship: (a) ad surface (b) cd surface

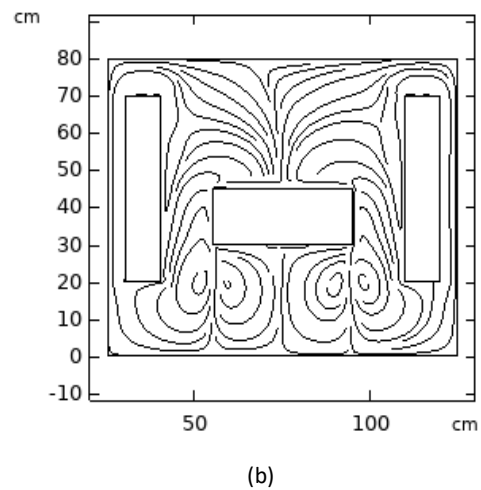
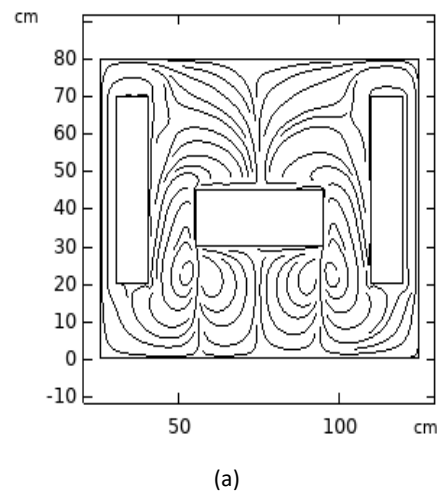


Figure 8. Velocity field after (a) 1000 sec (b) 1200 sec

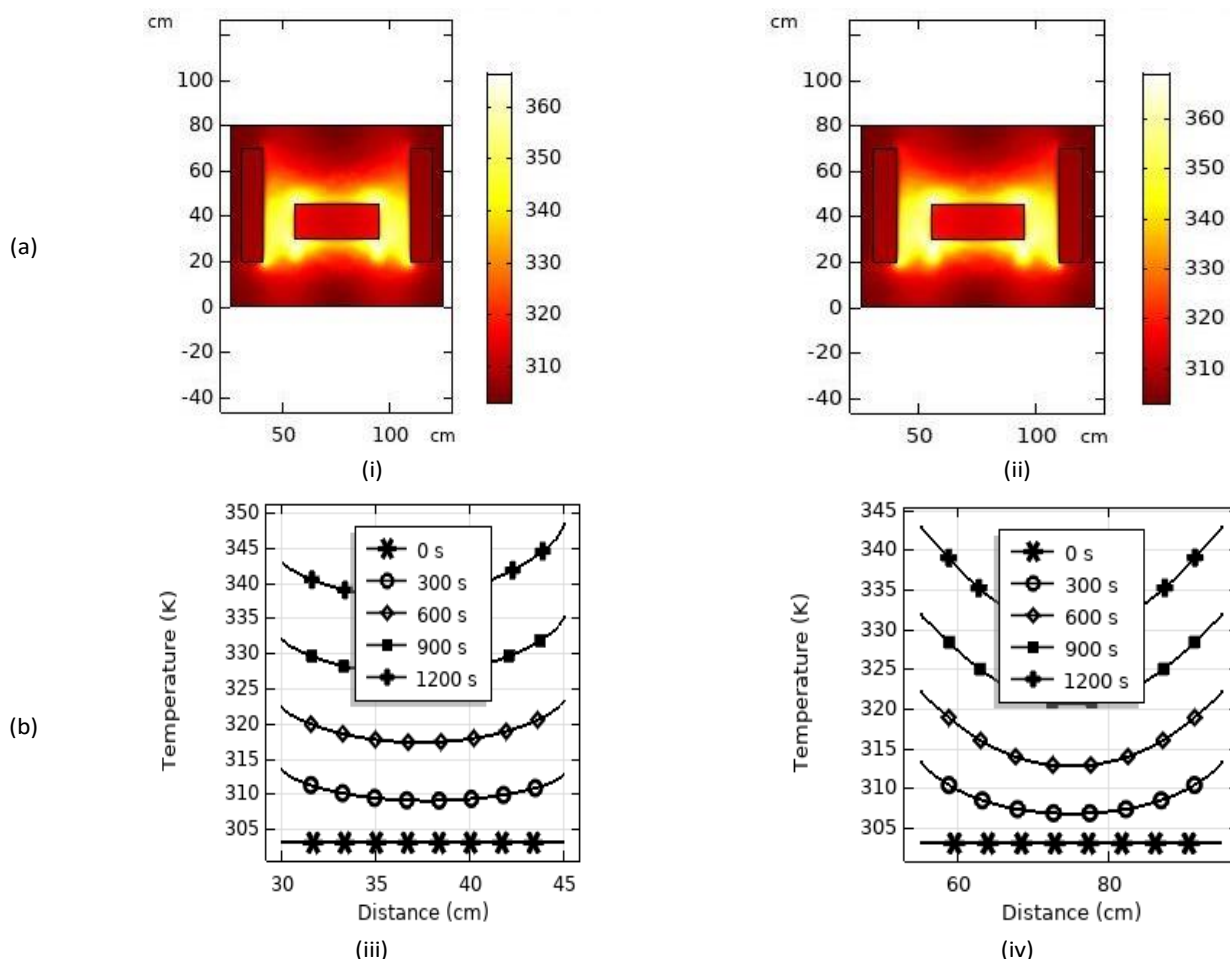


Figure 9. (a) Surface temperature plot: (i) after 1000 sec (ii) after 1200 sec
 (b) Temperature plot: (iii) on ad (iv) on cd

5. Conclusion

In this study, based on the given working conditions:

1. The appearance of natural convection was detected on the vertical side in the presence of the Joule effect, while there is no such appearance in its absence.
2. On the lower side of the horizontal electrode, natural convection appeared both with and without the Joule effect.
3. Ra has larger values on the ad surface than horizontal cd.
4. The Sherwood relation with Ra is of an exponential form on both surfaces, ad and cd.
5. Natural convection took longer to appear on the parts receiving higher currents.
6. The solution temperature raised due to the Joule effect; it was smaller than on the cathode surface, in particular, the one facing the anode.
7. The onset of natural convection had a small effect on the electrodeposition process.
8. The Joule effect reduced the speed of the electrodeposition process due to lower current at the specified surface.

6. References

Ahmadkhanhiha Donya, Ericso Fredrik, Zanella Caterina (2020) Optimizing Heat Treatment for Electroplated NiP and NiP/SiC, *Coatings*, 10: 1179.

Amir, Karimdoost Yasur, Mohsen, zadi, Hossein Hatemi (2019) Numerical Study of Natural Convection in a Square Enclosure Filled by Nanofluid with a Baffle in the Presence of Magnetic Field,, *Iran. J. Chem. Chem. Eng* 38: 209-220.

C. Duchanoy, F. Lopicque, C.F. Oduoza, A.A. Wragg(2000) Mass transfer and free convection associated with electrodeposition at long narrow upward facing tracks, *Electrochimica Acta*, 46: 433441.

Diogo M. F. Santos, César A. C.(2013) Hydrogen Production By alkaline water electrolysis, *Sequeira Quim Nova*. 36: 1176-1193.

F.A. Lowenheim (1977). *Electroplating*. McGraw-Hill, First Edition, 1977.

- G. A. C. Gonçalves, P. M. S. Campos, T. C. Veloso, V. R. Capelossi (2021) Influence of current density and temperature in the zinc electroplating process at sulfate-based acid solution: study on process efficiency and coating morphology
- Holman, P. Jack (2010) Heat Transfer. 9th ed. Published by McGraw-Hill Companies, Inc.
- Hussein Watheq Naser (2018) A geometrical configuration and its effect on the performance of an electrochemical cell under free convection, *Journal of Engineering Science and Technology*, 13:3432-3444.
- I.M. Sakr, W.A. El-Askary, A. Balabel, K. Ibrahim (2013) Numerical Study on natural and forced convection in Electrochemical Cells, *CFD Letters*, 5:120-131.
- Jeon Joonyeob, Yoon Gil Ho, Vegge Tegs, Chang Jin Hyun (2022) Phase-Field Investigation of Lithium Electrodeposition at Different Applied Overpotentials and Operating Temperatures, *Appl. Mater. Interfaces*, 14: 15275–15286.
- Jinjun Li, Xiaofei Lu, Feng Wu, Wei Cheng, Weidong Zhang, Shaoli Qin, Zhen Wang, Zhixiong You (2017) Electroplated Palladium Catalysts on FeCrAlloy for Joule-Heat-Ignited Catalytic Elimination of Ethylene in Air, *Ind and Eng. Chem. Res*, 56: 12520–12528.
- K. Sang-Hyuk, M. Deok-Woon, C. Bum-Jin (2006) Application of Electroplating Method For Heat Transfer Studies Using Analogy Concept, *Nuclear Engineering Technology*, 38: 251-258.
- Kanani Nasser (2005). *Electroplating: Basic Principles, Processes and Practice*. Elsevier Science, 1st Edition.
- Kwon, Hong-Beom, Kim, Kyong Tae, Ahn, Hye-Rin, Kim, Yong-Jun (2017) Electrodeposition and Characterization of Nanocrystalline Ni–B with Low Boron Content for MEMS Applications, *Sensors and Materials*, 29: 225-234.
- M. Schröter, K. Kassner, I. Rehberg, J. Claret, F. Sagues (2002) Influence of ohmic heating on the flow field in thin-layer electrodeposition, *Physical Review* 66:1-6.
- M. Huang, G. Marinaro, X. Yang, Fritzsche, B.Z. Lei, M. Uhlemann, K. Eckert, G. Mutschke (2019) Influence of ohmic heating on the flow field in thin-layer electrodeposition, *Journal of Electroanalytical Chemistry* 842: 203-217.
- Milan Paunovic, Mordechai Schlesinger (2006) *Fundamentals of Electrochemical Deposition*, 2nd edition, John Wiley & Sons, INC.
- O.K. Al-Duaij, M.M. Abou-Krishna, M.I. Attia (2017) Influence of the Deposition Temperature on the Electrodeposition Mechanism of Zn-Co-Fe Alloy, *Int. J. Electrochem. Sci.* 12: 11972 – 11986
- P. Barvinschi (2006) Numerical simulation of ohmic heating in idealized, *Journal of Optoelectronics and Advanced Materials*, 8:271-279.
- S. Kawai, Y. Fukunaka, S. Kida (2009) Numerical Calculation of Transient Current Density Distribution along Vertical Plane Electrode in CuSO₄ – H₂SO₄ Electrolyte Solution, *Journal of the Electrochemical Society*, 157: F99.
- Selman, Jan Robert, Newman, John (1971) Desalting by Means of Porous Carbon Electrodes, *Journal of Electrochemical Society* 118: 510.
- V.M. Volgin, A.V. Zhukov, G.N. Zhukova, A.D. Davydov (2009) Onset of natural convection in the electrochemical cell with horizontal electrodes under non-steady-state conditions: A numerical study, *Russian Journal of Electrochemistry*, 8: 1005.
- Y. Xuegeng, E. Kerstin, H. Armin, U. Margitta (2008) The concentration field during transient natural convection between vertical electrodes in a small-aspect-ratio cell, *Journal of Electroanalytical Chemistry*, 613: 97-107.

NEUTRON INDUCED ^{55}Mn REACTION IN THE ENERGY RANGE 0.001MeV TO 40MeV

A. K. M. Rezaur Rahman^{1a*}, Taslim Hoque Happy^{2a}, Mustofa Khalid Ovi^{3a}, Abdul Awal^{4b}, Mark Anthony Bromuela^{5a}, MD. Jubayer Rahman Akhand^{6c}, Shyamal Ranjan Chakraborty^{7a}, and A. K. M. Moinul Haque Meaze^{8a}

Abstract: Neutron induced ^{55}Mn reactions were evaluated in the energy range 0.001 MeV to 40 MeV using TALYS 1.95 computer code. During this evaluation, local and global parameterisations of Koning and Delaroche were used in nuclear optical model. Comparisons were made with experimental data, collected from EXFOR and other sources. Some optical model parameters (OMP) were needed to be adjusted for better agreement between theoretical calculations and experimental findings. Various evaluated libraries such as ENDF, JENDL etc. were checked and compared with our evaluation. TALYS evaluation showed better agreement when parameters were adjusted.

Keywords: Neutron cross section, manganese, optical model, TALYS, nuclear data evaluation

1. Introduction

Application of developed nuclear science that has and will have an important impact on society – nuclear energy, medicine, security, material characterisation, geological exploration, radiation safety and protection and the promise of fusion energy (Plompen et al. 2020). Accurate nuclear cross section data that need to be provided to predict the tritium breeding capability, assess the shielding efficiency, estimate the nuclear power generated in the system, and produce activation and radiation damaged data for the irradiated materials/components (Fischer et al. 2018). The new evaluated nuclear data plays an efficient role in nuclear technology (Rahman & Awal 2020; Rahman et al. 2019; Lorenz & Schmidt, 1986). Evaluation of nuclear data is a continuous process and the evaluation of cross-section data is very important for those who have experimental difficulty and are hopeless for measuring the cross-section data (Rahman & Zubair 2020a; Rahman 2012a). So, the cross-section evaluation for materials has special importance in systematic use of neutron induced reaction cross-section. (Rahman 2012b). In nuclear data evaluations, theoretical calculation is essential and the evaluated data from the theoretical calculation plays an important role on their applications to fusion reactor neutronics. Precise data on cross sections are needed for comprehensive computer modeling for future experiments. Success of many nuclear research

programs depends on the quality of nuclear database (Rahman & Zubair 2020b; Reshid 2013; Shibata 1989).

Manganese is a very hard, brittle, grey-white transitional metal that has only one stable isotope ^{55}Mn with 100% abundance. It is a nutritional inorganic trace element required for a variety of physiological processes including development, antioxidant defenses, reproduction and neuronal function (Horning et al. 2015; Kwakye 2015). It is a key component of aluminium copper alloys which is widely used in accelerator technology, fission and fusion devices as structural materials, dosimeter materials, control module etc. Manganese is also essential for anti-tumor immune responses (Lv et al. 2020). At present, 85% to 90% stainless steel contains around 2% of manganese. Many radioactive isotopes are produced from $n+^{55}\text{Mn}$ reactions like ^{54}Mn , ^{56}Mn , ^{55}Mn , ^{51}Cr . Cancer can be obstructed by summing some manganese supplements in daily diet. Manganese has also displayed ability in controlling the balance of sugar in human blood by normalizing insulin synthesis and secretion and can prevent diabetes (Kaziet al. 2008). Al-Mn alloys are possibly the most important of the non-age hardenable alloys of aluminium and generally contain between 0.25 to 1.25% Mn (Zamin 1981). Cu–Al–Mn alloys are well-known types of shape memory alloys introduced to technological use (Canbay et al. 2014).

Accurate neutron capture cross-sections of ^{55}Mn are important for reactor design in view of its use as an alloy structural material. Cross-section data provide important information of various kinds of actions and these data can be used for different types of researches. Data evaluation of ^{55}Mn is very essential for the design of nuclear device and many features are

Authors information:

^aDepartment of Physics, University of Chittagong, Chittagong, BANGLADESH.

E-mail: rezaur.physics@cu.ac.bd¹;
taslimhoque529@gmail.com²;
mustafakhalid.soaf@gmail.com³;
mabromuela.88@gmail.com⁵; shyamal@cu.ac.bd⁷;
meaze@cu.ac.bd⁸

^bObninsk Institute for Nuclear Power Engineering of MEPhI, RUSSIA. E-mail: abdulawal1993@gmail.com⁴

^cBangladesh Military Academy, Chittagong, BANGLADESH. E-mail: jubayer27@gmail.com⁶

*Corresponding Author: rezaur.physics@cu.ac.bd

Received: December 10, 2021

Accepted: July 17, 2022

Published: October 31, 2023

currently placed on it for using fusion reactor neutronics (Shibata 1989). ^{55}Mn is used as an alloy of structural material in which accurate capture cross-section is necessary for the future of reactors. Reliable estimation of the activation levels of manganese is needed to support critical safety analyses (Barough et al. 2017). In nuclear data evaluations, theoretical calculation is essential and the evaluated data from the theoretical calculation play an important role on their applications to fusion reactor neutronics.

Experimental nuclear data are stored in the EXFOR database. Collection of nuclear data from nuclear models is subject to uncertainties, coming from the imperfect knowledge of model parameters or the models themselves. These two sources need to be combined. An isotopic evaluation results in a probability distribution for the observables of a (usually) neutron induced reaction on that isotope. The most probable solution is the evaluation of nuclear data, while the full probability distribution is often missing. Nevertheless, this is often the case for many of the world libraries, the evaluated file is the evaluators' "best shot" (Koning 2015).

In our current research, we aim to analyze the nature of nuclear reaction for $n+^{55}\text{Mn}$ in the energy range 0.001MeV to 40 MeV. The experimental values from EXFOR data file of INDC of IAEA and evaluated values from various data libraries are to be used for evaluation purpose. Reaction channels and production routes are also analyzed. Discrepancies will be mitigated by adjusting the parameters of necessary nuclear model(s).

2. Theoretical Model and Evaluation Tool

TALYS is the modern nuclear data evaluation code system (Koning 2015). It is a software for the simulation of nuclear reactions and a versatile tool to analyze basic microscopic experiments. This code is used to generate nuclear data for all open channels in the fast neutron energy region, that is, beyond the resonance region. In situations where experimental data are unavailable, TALYS is used for the prediction and extrapolation of data (Koning & Rochman, 2012). The objective of TALYS is to provide a complete simulation of nuclear reactions in the 1 KeV-200MeV energy range, through an optimal combination of reliable nuclear models, flexibility and user-friendliness.

Optical model returns a prediction for the basic observable, namely the elastic angular distribution as well as polarization, the reaction and total cross section and for low energies, the s , p -wave strength functions and the potential scattering radius R' . When enough experimental scattering data of a certain nucleus are available, a so called local OMP can be constructed. TALYS retrieves all the parameters v_1 , v_2 , etc. of these local OMP automatically from the nuclear structure and model parameter database. The global neutron OMP, validated for $0.001 \leq E \leq 200\text{MeV}$ and $24 \leq A \leq 209$.

Pre-equilibrium emission takes place after the first stage of the reaction but long before statistical equilibrium of the compound nucleus is attained. It is imagined that the incident particle step-by-step creates more complex states in the compound system and gradually loses its memory of the initial energy and direction. Pre-equilibrium processes cover a sizable part of the reaction cross section for incident energies between 10 and (at least) 200MeV. Pre-equilibrium reactions have been modeled both classically and quantum-mechanically and both are included in TALYS.

Various models for direct reactions are included in the program: DWBA for spherical nuclides, coupled-channels for deformed nuclides, the weak-coupling model for odd nuclei, and also a giant resonance contribution to the continuum. In all cases, TALYS drives the ECIS-06 code to perform the calculations. The results are presented as discrete state cross sections and angular distributions, or as contributions to the continuum.

During this calculation, local and global parameterisations of Koning and Delaroche were used (Koning & Delaroche 2003). The parameter set are given below, where, the units are in fm:

$$r_v = 1.3039 - 0.4054 A^{-1/3} \quad (1)$$

$$a_v = 0.6778 - 1.487 \times 10^{-4} A \quad (2)$$

$$r_D = 1.3424 - 0.01585 A^{1/3} \quad (3)$$

$$a_D = 0.5446 - 1.656 \times 10^{-4} A \quad (4)$$

$$r_{SO} = 1.1854 - 0.647 A^{-1/3} \quad (5)$$

$$a_{SO} = 0.59 \quad (6)$$

3. Results and Discussions

Based on our evaluation, the reaction grid for $n + {}^{55}\text{Mn}$ is shown in Fig. 1. Different reaction channels, residual production and production routes of residual production are tabulated in Table 1.

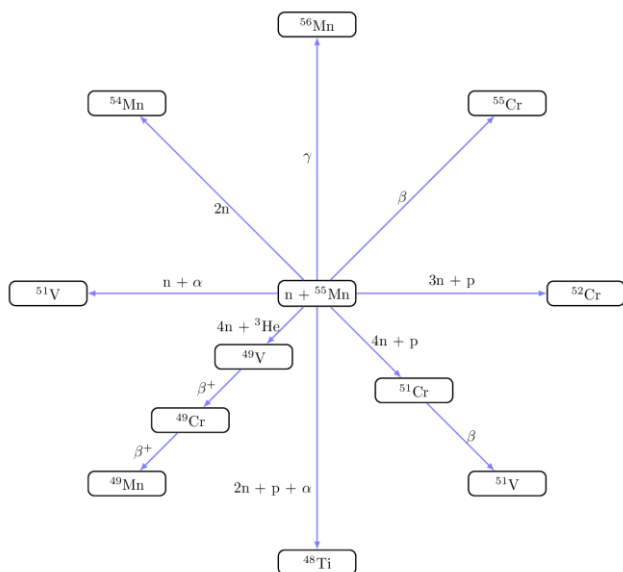


Figure 1. Main reaction grid for $n + {}^{55}\text{Mn}$ reaction.

Table 1. Table for residue particle product, reaction channels, and most probable routes according to this work.

Sl. No.	Reaction Channel	Half-life of Residue Particle	Residue Particle Production Routes	Most Probable Route
1	${}^{55}\text{Mn} (n, g)$ ${}^{56}\text{Mn}$	2.5789 hr	(n, g)	(n, g)
2	${}^{55}\text{Mn} (n, \text{inl})$ ${}^{55}\text{Mn}$	Stable	(n, inl)	(n, inl)
3	${}^{55}\text{Mn} (n, 2n)$ ${}^{54}\text{Mn}$	312.12 d	(n, 2n)	(n, 2n)
4	${}^{55}\text{Mn} (n, p)$ ${}^{55}\text{Cr}$	3.4967 min	(n, p)	(n, p)
5	${}^{55}\text{Mn} (n, d)$ ${}^{54}\text{Cr}$	Stable	(n, d) (n, np)	(n, np)
6	${}^{55}\text{Mn} (n, t)$ ${}^{53}\text{Cr}$	Stable	(n, t) (n, nd) (n, 2np)	(n, 2np)
7	${}^{55}\text{Mn} (n, 3\text{He})$ ${}^{53}\text{V}$	1.6 min	(n, he3) (n, pd) (n, n2p)	(n, n2p)
8	${}^{55}\text{Mn} (n, \alpha)$ ${}^{52}\text{V}$	3.7433 min	(n, α)	(n, α)

In the grid, only main reactions are considered. There are lots of isotopes of manganese, among them only ${}^{55}\text{Mn}$ is the stable isotope with 100% abundance and the others are radioisotopes, like: ${}^{46}\text{Mn}$, ${}^{47}\text{Mn}$, ${}^{48}\text{Mn}$, ${}^{49}\text{Mn}$, ${}^{50}\text{Mn}$, ${}^{51}\text{Mn}$, ${}^{52}\text{Mn}$, ${}^{54}\text{Mn}$, ${}^{56}\text{Mn}$, ${}^{57}\text{Mn}$. These radioactive isotopes emit β (β^+ , β^-) particles with the half-life of 36.2ms to 312.12 days. From $n + {}^{55}\text{Mn}$ reaction many isotopes are produced, the most significant isotopes we considered here, ${}^{54}\text{Mn}$, ${}^{56}\text{Mn}$, ${}^{55}\text{Mn}$, ${}^{51}\text{Cr}$, ${}^{52}\text{Cr}$, ${}^{49}\text{V}$, ${}^{51}\text{V}$, and ${}^{48}\text{Ti}$.

All sorts of reaction processes happened in $n + {}^{55}\text{Mn}$ reaction are shown in Fig. 2. It is seen that the cross-section data of non-elastic, elastic, shape-elastic and reaction cross-section value are quite closer to the total cross-section data; with some fluctuation, they have significant cross-section data in both low and high energies.

The cross-section value of compound non-elastic cross-section for $n + {}^{55}\text{Mn}$ is too low at the higher energy range. It has been seen that, between the energy ranges 1 MeV to 10 MeV, cross-section values of compound non-elastic cross-section are increasing slowly to the higher energy range, but it is damping about the energy range 15 MeV (about 900 mb). The cross-section values of the compound elastic cross-section for $n + {}^{55}\text{Mn}$ are reduced to zero in the energy range between 10 MeV to 15 MeV, while its lower energy range contains momentous cross-section data. Direct reaction process starts after 0.2 MeV and reaches maxima around 2 MeV (about 116 mb). Then it reduces slowly. Pre-equilibrium reaction begins at 3 MeV. For Pre-equilibrium, cross section rises rapidly, immediately after the straight point. Pre-equilibrium process rapidly ascends toward its flat maxima (about 700 mb) around 30 MeV.

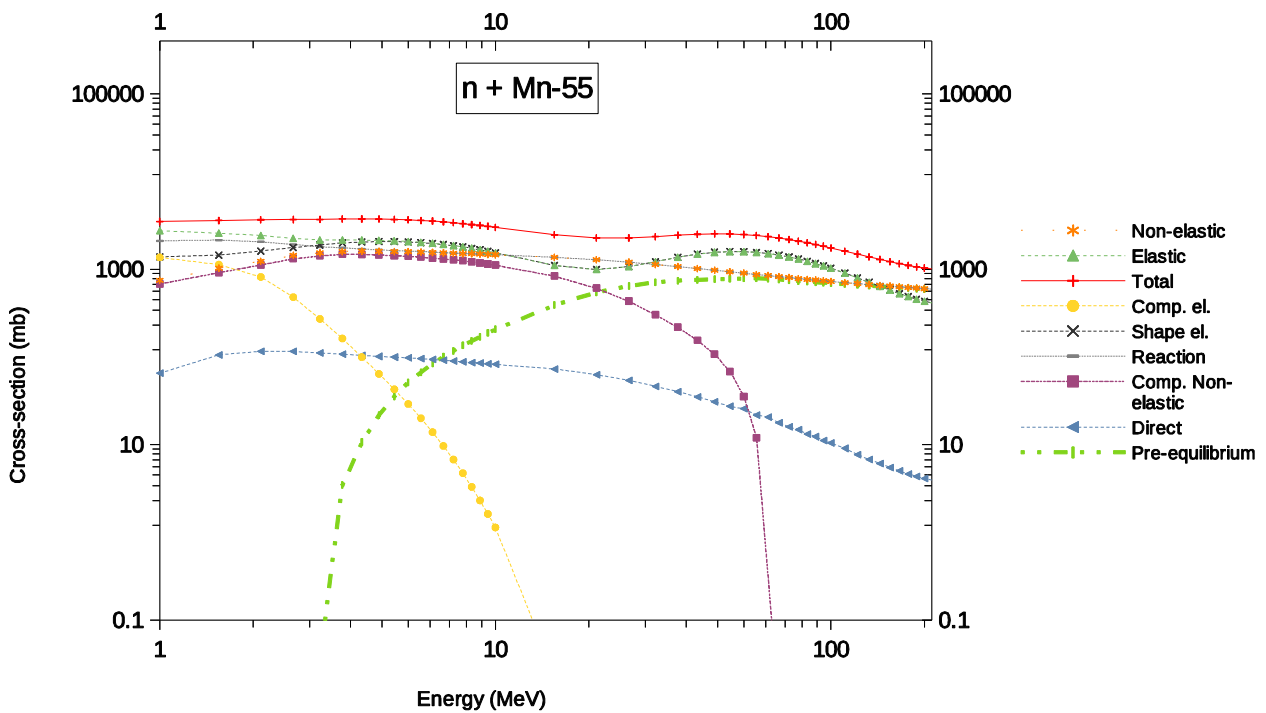


Figure 2. Various scattering and reaction cross-section from n + ⁵⁵Mn reaction.

The default model used by TALYS is the two-component exciton model with collision probabilities based on the effective squared matrix element. To fit experimental data, the model parameters can be adjusted via adjustable parameters through different keywords. The *rvadjust* is a multiplier to adjust the OMP parameter r_v which has default value 1.0 for all nuclei. We changed its value to 1.0502 for ⁵⁵Mn for better agreement with experimental values. Multiplier to adjust the OMP parameter a_v is *avadjust* which has default value 1.0. We have changed its value 0.8199 for better agreement with experimental values. These changes are tabulated in Table 2.

Table 2. Table for showing OMP values

Calculation Type	<i>Rvadjust</i>	<i>Avadjust</i>
Default	1.0	1.0
Adjusted	1.0502	0.8199

For adjusting our parameters to the desired values above, multiple reruns on TALYS were made with new and better values as to fit with the experimental plots. The values were chosen as prescribed by Eqns. (1-2). All other parameter values were kept default in TALYS. The values were given up to four decimal figures for accuracy which we deemed fitting sufficiently such experimental plots.

3.1 Total Scattering Cross-Section

From Fig. 3, we compared our calculated values of total scattering cross-section for $n+^{55}\text{Mn}$ reaction with the experimental and evaluated values which were collected from EXFOR and ENDF. Fig. 3 shows that both the experimental and evaluated data show several fluctuations in structure below 0.1 MeV. From this present work we can observe that after 2MeV, our calculated values of total Scattering cross-section have a good agreement to the cross-section data of different sources and we can also see that there is much resonance at lower energy range region. Calculated data with default parameters do not match

with experimental values at 0.01MeV. At 0.01MeV, the total scattering cross section is up to 25000 mb (Cote et al 1964). According to calculated values with default parameters, the total scattering cross section is around 30000mb. So, adjustment is made. After adjustment, our calculated values pass through the experimental data at 0.01 MeV – 0.3MeV region. But, the fluctuation in this region could not be well produced. There is no experimental and evaluated cross-section values from 0.3MeV to 2MeV as far as we have searched.

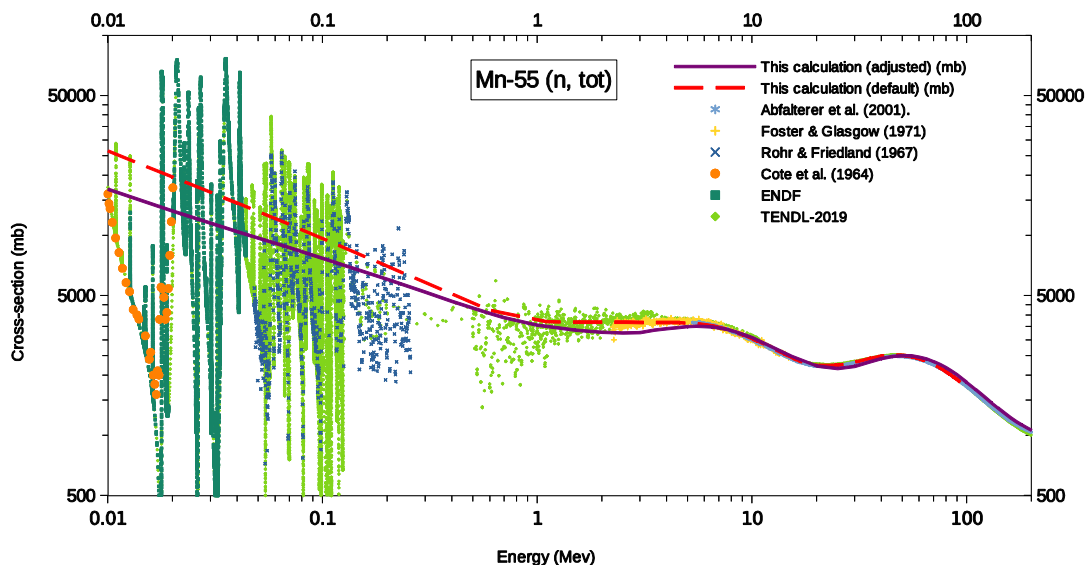


Figure 3. The comparison graph between experimental data, evaluated data and calculated values of total cross-section for $n + ^{55}\text{Mn}$ reaction.

3.2 Neutron Elastic Scattering Cross-Section

Neutron elastic scattering cross sections for ⁵⁵Mn are calculated from 0.01MeV, and comparison is made between the experimental and evaluated data. Fig. 4 shows the comparison with experimental values and with evaluated values from ENDF. At very low neutron energy (0.01 MeV) our calculated data with default parameters do not match with experimental values. So we adjusted parameters. At 0.1 MeV, the elastic cross section is more than 6000 mb. But its values decline rapidly with energy. At low energy region (0.2 MeV-0.6MeV) calculation with default parameters shows a little bit higher cross sections. The calculation

with parameter adjustment makes the agreement better with experimental values in that region. The pattern of the experimental and theoretical curves agrees with each other and the calculated value passes through the evaluated and experimental data at 1MeV-100MeV region. From this present work, it has been noticed that there are high resonances in the lower energy range and our calculated values have quite good similarity to the experimental values at the higher energy range and pass through the resonance region.

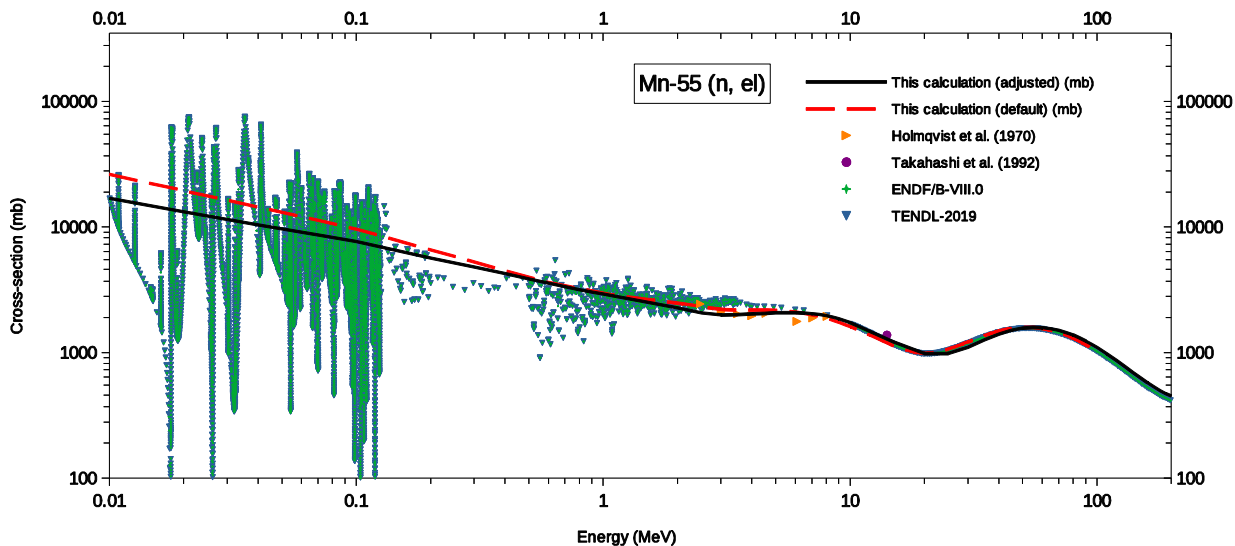


Figure 4. The elastic scattering cross-section for n + ⁵⁵Mn reaction.

3.3 Total Neutron Production Cross-Section

From Fig. 5, we have compared our present work for calculated total neutron production of $n+^{55}\text{Mn}$ reaction with the experimental and evaluated values which are collected from different sources. In the energy region 0.1MeV-1 MeV calculated data with default parameters do not match with evaluated and experimental values. But the calculated curve with adjusted parameters passes through the evaluated and experimental data. From this present work it has been observed that the experimental and evaluated values of total neutron production

cross-section have good agreement with our calculated values with adjusted parameters at lower energy range, except the experimental values of Fujita et al. (1972) and Thomson (1963). There is no experimental and evaluated values at higher energy range as far as we searched. At 10MeV, the total neutron production cross-section is more than 1250 mb. At 10MeV – 20 MeV, its value inclines with energy. There is a flat valley in the curve at 50MeV-100MeV region according to our calculated values.

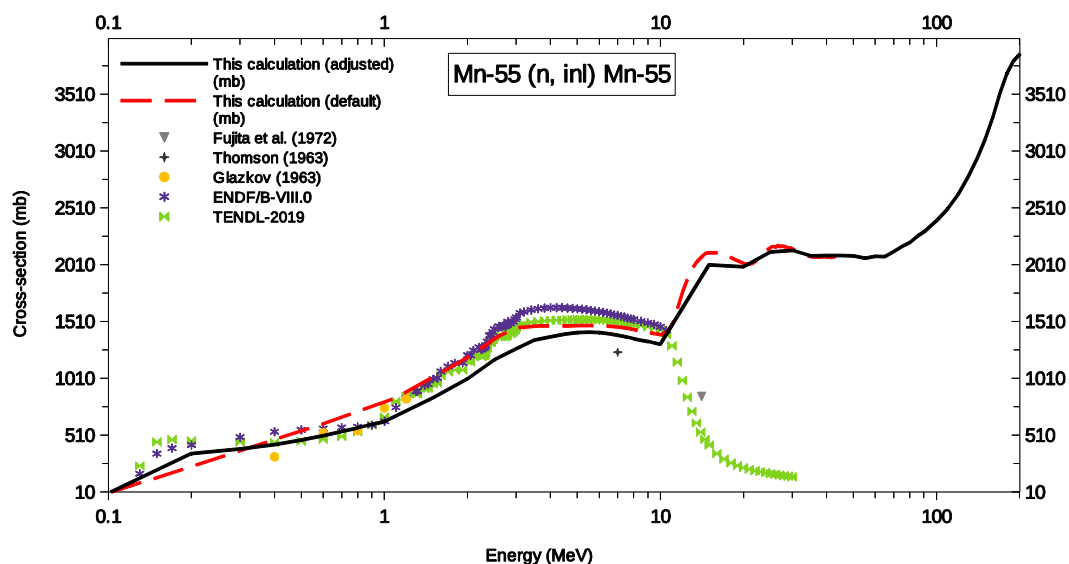


Figure 5. The comparison graph between experimental data, evaluated data and calculated data value of total neutron production cross-section for $n + ^{55}\text{Mn}$ reaction.

3.4 Total Proton Production Cross-Section

From Fig. 6, we compared our calculated values of total proton production for $n + {}^{55}\text{Mn}$ reaction with the experimental and evaluated values which are collected from different experimental and evaluated sources. From this present work, it has been seen that our calculated values are almost similar to the experimental and evaluated values. We did not find any cross-

section value at higher energy range as far as we searched as well as at the lower energy range, most of the experimental values were found between 6 MeV to 15 MeV. We can see that at the lower energy range our calculated values have good agreement with evaluated and experimental values we collected for the total proton production for $n + {}^{55}\text{Mn}$ reaction.

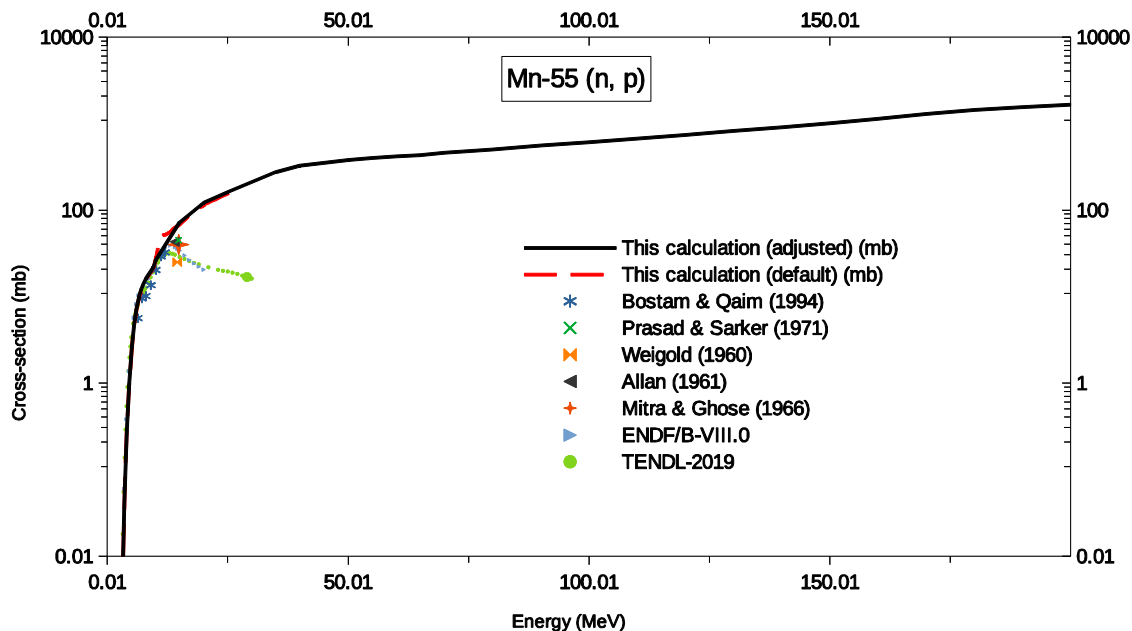


Figure 6. Comparison graph of total proton production from $n+{}^{55}\text{Mn}$ reaction.

By adjusting the parameters, we have increased the value of the real potential (r_v) and decreased the diffuseness parameter (a_v) for probability of interaction decrease. As a result, the excitation function with adjusted parameters comes closer to the experimental values.

4. Conclusion

We know, cross-section data of ${}^{55}\text{Mn}$ are used for reactor or nuclear device designing, safety analysis or different types of research. We compared our evaluated cross-section values with different experimental and evaluated data values from different sources. The present evaluation with default parameters agrees well with evaluated and experimental data except for 0.01 – 10 MeV region. For better agreement, hence, geometrical and diffuseness parameters of optical model are adjusted so that more accurate data can be used for application if experimental data are unavailable.

Our evaluation shows that among all scattering and reaction cross-sections for $n+{}^{55}\text{Mn}$ reaction, the cross-section data of non-elastic, elastic-scattering, shape-elastic scattering and reaction cross-section are nearly equal to the total cross-section data values with some fluctuation and they have effective cross-section data in both low and high energy ranges too. Our calculated total and elastic cross section values with adjusted

parameters agree well with experimental values in the overall investigated energy range. Experimental and evaluated cross-section data at lower energy range have good agreement with our calculated cross-section data with adjusted parameters of total neutron production for $n+{}^{55}\text{Mn}$. At the lower energy range, our calculated values of total proton production data with adjusted parameters for $n+{}^{55}\text{Mn}$ reaction are also in good agreement with evaluated and experimental cross-section values.

6. References

- Abfalterer, W. P., Bateman, F. B., Dietrich, F. S., Finlay, R. W., Haight, R. C., & Morgan, G. L. (2001). Measurement of neutron total cross sections up to 560 MeV. *Physical Review C*, 63(4), 44608. <https://doi.org/10.1103/PhysRevC.63.044608>
- Allan, D. L. (1961). An experimental test of the statistical theory of nuclear reactions. *Nuclear Physics*, 24, 274–299. [https://doi.org/10.1016/0029-5582\(61\)90380-7](https://doi.org/10.1016/0029-5582(61)90380-7)
- Barough, M. S., Bharud, V. D., Patil, B. J., Attar, F. M. D., Bhoraskar, V. N., & Dhole, S. D. (2017). Measurement and Estimation of Cross Sections for ${}^{55}\text{Mn}(n, \gamma){}^{56}\text{Mn}$ and ${}^{65}\text{Cu}(n, \gamma){}^{66}\text{Cu}$ Reactions Using Accelerator-Based Neutron Source. *Nuclear Science and Engineering*,

- 187(3), 302–311.
<https://doi.org/10.1080/00295639.2017.1323505>
- Bostan, M., & Qaim, S. M. (1994). Excitation functions of threshold reactions on ^{45}Sc and ^{55}Mn induced by 6 to 13 MeV neutrons. *Physical Review C*, *49*(1), 266–271.
<https://doi.org/10.1103/PhysRevC.49.266>
- Canbay, C. A., Ozgen, S., & Genc, Z. K. (2014). Thermal and microstructural investigation of Cu–Al–Mn–Mg shape memory alloys. *Applied Physics A*, *117*(2), 767–771.
<https://doi.org/10.1007/s00339-014-8643-5>
- Coté, R. E., Bollinger, L. M., & Thomas, G. E. (1964). Total Neutron Cross Section of Manganese. *Physical Review*, *134*(5B), B1047–B1051.
<https://doi.org/10.1103/PhysRev.134.B1047>
- Fischer, U., Angelone, M., Avrigeanu, M., Avrigeanu, V., Bachmann, C., Dzysiuk, N., Fleming, M., Konobeev, A., Kodeli, I., Koning, A., Leeb, H., Leichtle, D., Ogando, F., Pereslavtsev, P., Rochman, D., Sauvan, P., & Simakov, S. (2018). The role of nuclear data for fusion nuclear technology. *Fusion Engineering and Design*, *136*.
<https://doi.org/10.1016/j.fusengdes.2018.01.036>
- Foster, D. G., & Glasgow, D. W. (1971). Neutron Total Cross Sections, 2.5–15 MeV. I. Experimental. *Physical Review C*, *3*(2), 576–603. <https://doi.org/10.1103/PhysRevC.3.576>
- Fujita, I., Sonoda, M., Katase, A., Wakuta, Y., Tawara, H., Hyakutake, M., & Iwatani, K. (1972). Inelastic Scattering of 14MeV Neutrons by Medium Weight Nuclei. *Journal of Nuclear Science and Technology*, *9*(5), 301–309.
<https://doi.org/10.1080/18811248.1972.9734846>
- Glazkov, N. P. (1963). Cross sections of the inelastic scattering of neutrons with energies of 0.4–1.2 MeV on medium and light nuclei. *Soviet Atomic Energy*, *15*(5), 1173–1176. <https://doi.org/10.1007/BF01115942>
- Holmqvist, B., Wiedling, T., Benzi, V., & Zuffi, L. (1970). Analysis of fast neutron elastic scattering from tantalum using a non-spherical optical potential. *Nuclear Physics A*, *150*(1), 105–113.
[https://doi.org/https://doi.org/10.1016/0375-9474\(70\)90460-4](https://doi.org/https://doi.org/10.1016/0375-9474(70)90460-4)
- Horning, K. J., Caito, S. W., Tipps, K. G., Bowman, A. B., & Aschner, M. (2015). Manganese Is Essential for Neuronal Health. *Annual review of nutrition*, *35*, 71–108. <https://doi.org/10.1146/annurev-nutr-071714-034419>
- Kazi, T. G., Afridi, H. I., Kazi, N., Jamali, M. K., Arain, M. B., Jalbani, N., & Kandhro, G. A. (2008). Copper, chromium, manganese, iron, nickel, and zinc levels in biological samples of diabetes mellitus patients. *Biological trace element research*, *122*(1), 1–18.
<https://doi.org/10.1007/s12011-007-8062-y>
- Koning, A. J. (2015). Bayesian Monte Carlo method for nuclear data evaluation. *The European Physical Journal A*, *51*(12), 184.
<https://doi.org/10.1140/epja/i2015-15184-x>
- Koning, A. J., & Delaroche, J. P. (2003). Local and global nucleon optical models from 1 keV to 200 MeV. *Nuclear Physics A*, *713*(3), 231–310.
[https://doi.org/https://doi.org/10.1016/S0375-9474\(02\)01321-0](https://doi.org/https://doi.org/10.1016/S0375-9474(02)01321-0)
- Koning, A. J., & Rochman, D. (2012). Modern Nuclear Data Evaluation with the TALYS Code System. *Nuclear Data Sheets*, *113*(12), 2841–2934.
<https://doi.org/https://doi.org/10.1016/j.nds.2012.11.002>
- Kwakye, G. F., Paoliello, M. M., Mukhopadhyay, S., Bowman, A. B., & Aschner, M. (2015). Manganese-Induced Parkinsonism and Parkinson's Disease: Shared and Distinguishable Features. *International journal of environmental research and public health*, *12*(7), 7519–7540. <https://doi.org/10.3390/ijerph120707519>
- Lorenz, A., & Schmidt, J. J. (1986). Nuclear data: Serving basic needs of science and technology. *IAEA Bulletin*, *28*(4)17-20.
<https://www.iaea.org/sites/default/files/28405081720.pdf>
- Lv, M., Chen, M., Zhang, R., Zhang, W., Wang, C., Zhang, Y., Wei, X., Guan, Y., Liu, J., Feng, K., Jing, M., Wang, X., Liu, Y.-C., Mei, Q., Han, W., & Jiang, Z. (2020). Manganese is critical for antitumor immune responses via cGAS-STING and improves the efficacy of clinical immunotherapy. *Cell Research*, *30*(11), 966–979. <https://doi.org/10.1038/s41422-020-00395-4>
- Mitra, B., & Ghose, A. M. (1966). (n, p) cross sections of some low Z nuclei for 14.8 MeV neutrons. *Nuclear Physics*, *83*(1), 157–165.
[https://doi.org/https://doi.org/10.1016/0029-5582\(66\)90346-4](https://doi.org/https://doi.org/10.1016/0029-5582(66)90346-4)
- Plompen, A. J. M., Cabellos, O., De Saint Jean, C., Fleming, M., Algora, A., Angelone, M., Archier, P., Bauge, E., Bersillon, O., Blokhin, A., Cantargi, F., Chebboubi, A., Diez, C., Duarte, H., Dupont, E., Dyrda, J., Erasmus, B.,

- Fiorito, L., Fischer, U., ... Žerovnik, G. (2020). The joint evaluated fission and fusion nuclear data library, JEFF-3.3. *European Physical Journal A*, 56(7). <https://doi.org/10.1140/epja/s10050-020-00141-9>
- Prasad, R., & Sarkar, D. C. (1971). Measured (n, p) reaction cross-sections and their predicted values at 14.8 MeV. *Il Nuovo Cimento A (1965-1970)*, 3(4), 467–478. <https://doi.org/10.1007/BF02823319>
- Rahman, A. K. M. R. (2012a). Neutron cross-sections for ⁵⁵Mn in the energy range from 0.2 to 22 MeV. *Turkish Journal of Physics*. <https://doi.org/10.3906/fiz-1107-3>
- Rahman, A. K. M. R. (2012b). Neutron interaction cross-sections for ²⁷Al in the energy range from 0.2 to 22 MeV using optical model program. *Science Journal Ubon Ratchathni University, Thailand*, 2.
- Rahman, A. K. M. R., & Awal, A. (2020). Production of ¹⁴⁹Tb, ¹⁵²Tb, ¹⁵⁵Tb and ¹⁶¹Tb from gadolinium using different light-particle beams. *Journal of Radioanalytical and Nuclear Chemistry*, 323(2), 731–740. <https://doi.org/10.1007/s10967-019-06973-0>
- Rahman, A. K. M. R., Meaze, A. K. M. M., Chakraborty, S. R., & Mohsin, M. (2019). Evaluations of n + ²⁷Al reaction in the energy range 0.1–200 MeV. *Indian Journal of Physics*, 94. <https://doi.org/10.1007/s12648-019-01555-y>
- Rahman, A. K. M. R., & Zubair, M. A. (2020a). Excitation functions of ⁵⁸Ni(n, charged particle) from threshold to 20 MeV using NLD models. *Indian Journal of Physics*, 95. <https://doi.org/10.1007/s12648-020-01808-1>
- Rahman, A. K. M. R., & Zubair, M. A. (2020b). Cross sections of ⁵⁶Fe(n, p)⁵⁶Mn, ⁵⁵Mn(n, p)⁵⁵Cr, ⁵²Cr(n, p)⁵²V, ⁵⁶Fe(n, α)⁵³Cr, ⁵⁵Mn(n, α)⁵²V and ⁵²Cr(n, α)⁴⁹Ti reactions using phenomenological level density models from threshold to 20 MeV. *Applied Radiation and Isotopes*, 166, 109429. <https://doi.org/https://doi.org/10.1016/j.apradiso.2020.109429>
- Reshid, T. S. (2013). Calculation of Excitation Function of Some Structural Fusion Material for (n, p) Reactions up to 25 MeV. *Journal of Fusion Energy*, 32(2), 164–170. <https://doi.org/10.1007/s10894-012-9541-5>
- Rohr, G., & Friedland, E. (1967). A study of neutron resonances of vanadium and manganese. *Nuclear Physics A*, 104(1), 1–16. [https://doi.org/10.1016/0375-9474\(67\)90753-1](https://doi.org/10.1016/0375-9474(67)90753-1)
- Shibata, K. (1989). Calculation of Neutron-Induced Reaction Cross Sections of Manganese-55. *Journal of Nuclear Science and Technology*, 26(10), 955–965. <https://doi.org/10.1080/18811248.1989.9734411>
- Takahashi, A., Sasaki, Y., Maekawa, F., & Sugimoto, H. (1989). Measurement and analysis of double differential neutron emission cross sections at En = 14.1 MeV for ⁹³Nb and ¹⁸¹Ta (INDC(JPN)–118/L). International Atomic Energy Agency (IAEA).
- Thomson, D. B. (1963). Nuclear Level Densities and Reaction Mechanisms from Inelastic Neutron Scattering. *Physical Review*, 129(4), 1649–1667. <https://doi.org/10.1103/PhysRev.129.1649>
- Weigold, E. (1960). Cross Sections for the Interaction of 14-5 MeV Neutrons with Manganese and Cobalt. *Australian Journal of Physics*, 13(2), 186–188. <https://doi.org/10.1071/PH600186>
- Zamin, M. (1981). The Role of Mn in the Corrosion Behavior of Al-Mn Alloys. *Corrosion*, 37(11), 627–632. <https://doi.org/10.5006/1.3577549>

POINT CLOUD SIMPLIFICATION METHOD BASED ON IMPROVED FUZZY C-MEANS WITH AUTOMATIC NUMBER OF CLUSTERS

Siti Nur Athirah Adibah Maiddin^{1a} and Normi Abdul Hadi^{2a*}

Abstract: The essence of the point cloud is to express geometric information about objects by getting discrete coordinates on their surfaces. However, with a million points, this data may record redundant details in which it is needless to be kept for the model's analysis. In addition, there is also a limitation where the processors cannot process the large-size datasets. The point cloud simplification algorithm was developed to solve the stated obstacles in data processing. Numerous algorithms have been published to produce the best methods for data reduction process. Since the simplification process might eliminate essential features of the data, this study introduces the features preservation process to keep the important points before the simplification. This study employed the Fuzzy C-Means (FCM) algorithms for the simplification stage due to their simplicity and ability to generate an accurate result. Regardless, the FCM still suffers from drawbacks, where their initial cluster centres are prone to fall into local optima. This study improved the FCM by employing the Score and Minimum Distance (SMD) to determine the number of clusters and cluster centres. The SMD is enhanced by changing the Gaussian to Cosine kernel function to increase the accuracy. This new technique is named SMD(C)-IFCM. The method was then applied to the 3D point cloud of a box, cup, and Stanford bunny. The performance of the developed method was compared with the original SMD-FCM and SMD-IFCM for the percentage of the simplified data, error evaluation, and processing time. The result and analysis showed that the developed method had the best score, which was six (6) out of nine (9) measurements, compared to the other two methods with scores of one (1) and two (2) respectively. This score suggests that the developed algorithm successfully reduced the error evaluation and the processing time to generate the output.

Keywords: Point cloud simplification, fuzzy C-means, automatic number of cluster, and preservation strong features

1. Introduction

A point cloud can be described as a collection of data points arranged in space. A three-dimensional (3D) structure or object might be represented by points, each with its Cartesian coordinate, which illustrates each point position (Wang & Kim, 2019). The source of point clouds can be from a 3D scanner or a photogrammetry software, and other devices.

Point clouds are used for various applications, including creating 3D Computer-Aided Design (CAD) models for manufactured components, metrology and quality inspection, and a variety of visualisation, animation, rendering, and mass customisation. In order to ensure that the result is reliable for later applications, the process of point cloud simulation must be precise (Hadi & Alias, 2019). However, by creating thousands of point clouds for each data set, the procedure of point cloud analysis might face some interference. Moreover, storage space and the processing time in analysing the point clouds are likely to be vast and prolonged, and a standard processor such as a laptop will reach its memory bottleneck. Removing random data from the dataset may eliminate the essential features of the data and

give misleading information. It is crucial to preserve the features of an object since it gives measurements that specify the characteristics of an object (S. A. Halim et al., 2021).

On that account, the technique of point cloud simplification was introduced to eliminate duplicate data points and reserve the essential and meaningful point position (Mahdaoui & Sbai, 2020). Based on the literature, simplification algorithm can be done using two approaches of creating polygonal networks on the point cloud data or using geometric details. However, several studies focused on the second approach as setting up polygonal networks can be extremely expensive in calculation and storage. The clustering process can be a handy approach in differentiating the necessary spots in the point cloud data sets.

Accordingly, several clustering approaches have been published to simplify the point clouds while guaranteeing that the results will be accurate. One of the methods in data clustering that many researchers utilised was the Fuzzy C Means (FCM) algorithm, because it was proven to give satisfactory results. However, FCM still encountered drawbacks as their initial cluster centre was unstable, making it easy to fall into local optimal (Alomoush et al., 2021; Krishna & Bhaskari, 2016; Yang et al.,

Authors information:

^aFaculty of Computer and Mathematical Sciences, Universiti Teknologi MARA, 40170 Shah Alam, Selangor, MALAYSIA. E-mail: tyrahdybah@gmail.com¹; normi@fskm.uitm.edu.my²

*Corresponding Author: normi@fskm.uitm.edu.my

Received: June 23, 2022

Accepted: January 25, 2023

Published: October 31, 2023

2020). Considering that, the clustering results can be inaccurate. Therefore, improvement steps need to be done in the FCM to make the clustering process more trustworthy.

Another stumbling block discovered in the FCM is that most of the existing methods used random cluster numbers and did not preserve the essential features, significantly influencing the simplification results. Thus, this can make the algorithm remove a wrong point cloud instead, and consequently, the output of the simplified point clouds could be unreliable.

Therefore, this study improves the simplification method by generating an automatic number of clusters by utilising the Score and Minimum Distance of the Point Clouds (SMD). The SMD model by He et al. (2019) became the chosen method since it is an established technique in scoring each point cloud based on the density function in getting an optimal number of clusters. Rating the point clouds is the best conceptual method in generating the number of clusters. In addition, the method is also considered the theory of minimum distance as the cluster centres should not be close to each other to avoid unnecessary cluster creation.

Moreover, the original SMD is improved by changing the Gaussian Kernel Function to Cosine Kernel Function, which has a higher accuracy, and the feature-preservation process is done before the simplification. This improvement can reduce errors from the wrong clustering process caused by a random number of clusters. Consequently, the output of a simplified algorithm can be more reliable as this process only retains an important point position. The formulation of the cluster number can make the whole process done automatically. The following are the study's main contributions:

- 1) The number of cluster centres can be generated automatically without needing a user to decide beforehand. The SMD model is embedded into the algorithm, which will give the number of clusters and initial cluster centres that can overcome the drawbacks of FCM.
- 2) The algorithm also includes the techniques of preserving strong feature information of the point cloud, before being divided through the FCM. Consequently, the output of the simplification is the reduced point cloud data with the features reserved.
- 3) The discussion analysis has shown that the algorithm is effective to some extent.

The flow of this paper is organized by section. Section 2 reviews some works on the point cloud simplification and the FCM. The steps taken in the developed algorithm are illustrated in Section 3. The following section is where the result and discussion of the three datasets occurred. Lastly, the summary of this study and the suggested further direction can be found in Section 5.

2. Literature Review

A considerable amount of literature has been published on point cloud simplification. Among these papers, Xuan et al. (2018) described that point cloud simplification is a process that needs to be done to remove the redundant points while retaining the main geometric features of the object. Scanning the surface of a physical object using a 3D technology could produce a massive number of point clouds (Halim et al., 2017; Leal et al., 2017).

Thus, to reduce the storage and computing problems, the point cloud simplification process plays an important role. In short, point cloud simplification can be defined as a process to eliminate duplicate data points while selecting important and meaningful 3D points (Mahdaoui & Sbai, 2020). In general, Wu et al. (2021) stated that there are two categories of point cloud simplification methods: (i) mesh-based, and (ii) mesh-free. The authors explained that mesh-based methods were constructed to set up polygonal networks on the point cloud data and cut down the point connectivity information. Meanwhile, the mesh-free approaches seek to assess the local neighbour information of cloud points and resample important spots among original point cloud data using geometric information. However, mesh-based methods are suffering from extreme complexity of computational issues since these approaches require geometric and topological computation (Ji et al., 2019; Wu et al., 2021). For that reason, the main focus of this research is to simplify the point cloud data using mesh-free methods or, more precisely, clustering algorithms.

Most previous studies defined clustering as a process of dividing a set of data into clusters so that images in the same cluster are as similar as possible, while images from other clusters are as distinct as possible (Askari, 2021; Zhang et al., 2020). Mahdaoui & Sbai, (2020) described clustering as statistical dissection techniques used to categorise raw data into homogeneous groups. According to Askari (2021), clustering methods are classified into many types such as cluster-centric algorithms, K-means, and FCM, which determine the centres of groupings of data points using distance to measure similarity and dissimilarity. Density-based clustering could also mark adjacent data points with a particular concentration into a single cluster based on pre-set density and neighbourhood criteria.

Nevertheless, Askari (2021) also stated that FCM is preferred by many researchers as the method used in data clustering. This view is supported by Zhang et al. (2020), who said that FCM developed from fuzzy logic is one of the most outstanding clustering methods due to its simplicity and efficacy. Despite that, the FCM still suffers from certain drawbacks that the researchers are still interested in solving. The literature review by Askari (2021) stated that the FCM is extremely sensitive to noise, outliers, and cluster size. The authors explained that there was no specific calculation to filter out the noise and outliers from necessary points since all data points equally contribute to the estimation of cluster centres which affects the actual structures of the point cloud objects.

The FCM could be bad in clustering due to the random initial cluster centres. Therefore, several modifications have been made to the FCM algorithm by combining it with other models, such as Gravitational Search Algorithm (GSA) (Yang et al., 2020), Particle Swarm Optimization (PSO) algorithm (Siringoringo & Jamaluddin, 2019), and Artificial Bee Colony algorithm (Alomoush et al., 2021).

As stated before, the FCM is the most well-known method among researchers. However, there is a lack of literature that tries to generate an optimal number of clusters for fuzzy clustering in the point cloud simplification process. Nearly all studies used an arbitrary number of clusters that had to be decided by the researchers beforehand (Leal et al., 2017). Therefore, this study has developed a method to estimate an automatic number of clusters by adopting the Score and Minimum Distance of the Point Clouds (SMD) technique by He et al. (2019).

3. Methodology

Figure 1 below illustrates the point simplification algorithm used in this study:

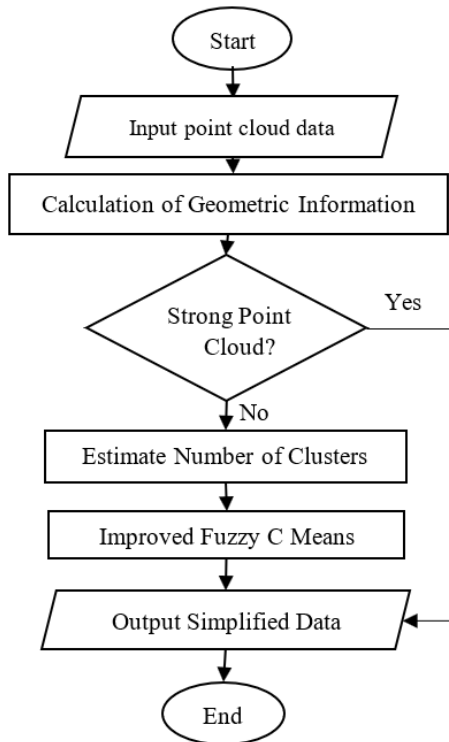


Figure 1. Flowchart of the developed point cloud simplification algorithm.

3.1 Input Point Cloud Datasets

This study uses three different datasets for experimental verification purposes: (i) box, (ii) cup, and (iii) Stanford bunny obtained from the PointCleanNet database.

3.2 Calculation of Geometric Information

Preserving point cloud features requires the spatial coordinate value of the point cloud and the geometric information, which are normal vector and point curvature. However, Yang et al. (2020) added angle entropy and point cloud density as an additional information.

3.2.1 Point Cloud Normal Vector and Curvature Estimation

The Normal vector is calculated using the Principal Component Analysis (PCA). PCA is built by the covariance matrix using the neighbourhood information.

Equations (1) and (2) below illustrate the formula used for kNN and PCA models for a given point $p(x, y, z)$, respectively.

$$d = \sqrt{(x_a - x_b)^2 + (y_a - y_b)^2 + (z_a - z_b)^2} \tag{1}$$

$$C^{3 \times 3} = \sum_{i=1}^k (p_i - \bar{p})(p_i - \bar{p})^T \tag{2}$$

where k is the neighbourhood size, d is the Euclidean distance between point (x_a, y_a, z_a) and (x_b, y_b, z_b) which are the three-dimensional coordinates of point a and point b , and \bar{p} is the mean value of the point p .

Then, it is suggested to adjust the normal consistency to equation (3) owing to the unpredictability of the point cloud's normal vector direction.

$$\bar{y}' = \begin{cases} \bar{y}\bar{y}(l - p_i) & \text{if } \bar{y} \geq 0 \\ -\bar{y}\bar{y}(l - p_i) & \text{if } \bar{y} < 0 \end{cases} \tag{3}$$

where \bar{y} and \bar{y}' is the original and adjusted normal vector in the form of (h, m, n) , respectively, and l is the location of the view.

The formula for the curvature σ_i of point p_i is given as,

$$\sigma_i = \frac{\tau_0}{\tau_0 + \tau_1 + \tau_2} \tag{4}$$

where $\tau_0, \tau_1,$ and τ_2 are the eigenvalues from equation (2) that satisfy $\tau_0 \leq \tau_1 \leq \tau_2$.

3.2.2 Point Cloud Angle Entropy

Another method to describe the local geometric characteristics of the subject is to estimate the angles between the normal vectors of its neighboring points which known as angle entropy. According to Xuan et al. (2018), angle entropy can be used to decide which point needs to be reserved, and which does not. A high value indicates that the point is situated in an area where the concave and convex clearly differ, and the removal of the point would result in a change to the local geometry. As a result, the point is crucial in expressing the specific geometric feature in the area and must be kept. Contrarily, a low value indicates that the point is in a flat area, where it can be replaced by its neighbours and removed.

Thus, angle entropy En_i for each point cloud is estimated based on its neighbourhood as follows,

$$En_i = -\frac{\bar{\theta}_i}{\bar{\theta}_i + \sum_{j=1}^k \bar{\theta}_j} \log_2 \frac{\bar{\theta}_i}{\bar{\theta}_i + \sum_{j=1}^k \bar{\theta}_j} - \sum_{j=1}^k \frac{\bar{\theta}_j}{\bar{\theta}_i + \sum_{j=1}^k \bar{\theta}_j} \log_2 \frac{\bar{\theta}_j}{\bar{\theta}_i + \sum_{j=1}^k \bar{\theta}_j} \tag{5}$$

$$\bar{\theta}_i = \frac{1}{k} \sum_{j=1}^k \arccos \left(\frac{\bar{y}_i \cdot \bar{y}_j}{|\bar{y}_i| |\bar{y}_j|} \right)$$

where \bar{y}_i is the normal vector of p_i , $\bar{\theta}_i$ is the angle of p_i , and $\bar{\theta}_j$ is the angle of point p_j .

3.3 Preservation of Point Cloud Strong Features

Strong features are essential to retain the unique nature of the cloud model data. Thus, this study adopts the statistical principle together with point cloud curvature as the strong features preservation evaluation parameter (Hadi et al., 2021). Firstly, estimate the average curvature $\bar{\sigma}$ of all point clouds and standard deviation σ_{std} using equation (6). Then, it is followed by a simplification model by Yang et al. (2020), where the curvature threshold σ_0 will be computed. If $\sigma_i > \sigma_0$, point p_i is classified as a strong feature and will be preserved from the clustering process.

$$\bar{\sigma} = \frac{1}{n} \sum_{i=1}^n \sigma_i$$

$$\sigma_{std} = \sqrt{\frac{\sum_{i=1}^n (\bar{\sigma} - \sigma_i)^2}{n}} \tag{6}$$

$$\sigma_0 = \bar{\sigma} + \beta \times \sigma_{std}$$

where n is the total point cloud, and β is a constant from 1 to 5.

3.4 Number of Clusters

This subsection discusses an automatic method for the number of clusters. The analysis was based on a conceptual model by He et al. (2020) called the Score and Minimum Distance of the Centre Point (SMD). This model consists of four steps as below:

STEP 1: Choose the dimension that has the largest discreteness.

A dimension with the largest degree of dispersion could reflect the actual distribution of the data, which means that the overlap in this dimension is more significant. Thus, equation (8) was used to compare the level of dispersion in a dimension called the discreteness function, and equation (7) was used to normalise the data beforehand. Then, a dimension was said to have a tremendous discreteness when the discreteness function was the lowest among all other dimensions. The chosen dimension was sent to the next step to get the density values based on the kernel function.

$$x' = \frac{x - \min}{\max - \min} \tag{7}$$

$$F = \sum_{i=1}^{n-1} |x_{i+1} - x_i| \tag{8}$$

Where x' is the normalised data, and F is the discreteness function.

STEP 2: Calculation of density using kernel estimation and obtained $kmax$.

Triangular Kernel function, Epanechnikov Kernel function, Gaussian Kernel function, and Tricube Kernel function are among the types of kernel functions used to estimate the density values. He et al. (2020) adopted the Gaussian Kernel density function as their method so that the density curve would be smooth. However, Wang & Kim (2019a) mentioned that the time complexity of calculating the local density using the Gaussian kernel function was indefinitely long. Moreover, the Gaussian kernel function is inefficient for large-scale datasets. Hence, this study chose the Cosine kernel function to ensure that the result is accurate with the datasets of various shapes and scales.

Once the dimension with the largest discreteness was extracted, the density values would be evaluated using equation (9). Afterwards, $kmax$ were obtained by choosing the smallest value among \sqrt{n} and the number of extreme values for density

$$f(x) = \frac{1}{nh} \sum_{i=1}^n K \left(\frac{x - x_i}{h} \right) \tag{9}$$

$$K(u) = \frac{\pi}{4} \cos \left(\frac{\pi}{2} u \right)$$

where $f(x)$ is the density distribution function, K is the Cosine Kernel function, $h = 1.059\sigma n^{-\frac{1}{5}}$ is the window width, and σ is the variance of the random variable.

STEP 3: Determining the candidate's set of cluster centre

The first step in this process was to sort the data points, c_i in descending order based on their score, as in equation (10).

$$score(c_i) = \min_{\substack{density(c_j) > density(c_i), c_i, c_j \in P \\ density(c_j)}} distance(c_i, c_j) \cdot density(c_i) \quad (10)$$

where $density(c_i)$ is the density of point c_i , $distance(c_i, c_j)$ is the distance between point c_i and point c_j .

Then, the sorted points were cut into the size of the $kmax$ to get the candidate's set of centre points. The process continued by judging the score change between all candidates by score variation. He et al. (2020) defined score variation as the method to find the number of clusters when the last great score change occurred, decided using Equation (11). A new value of $kmax$ is obtained when $Gradrop(k)$ is greater or equal to 2. The centre points were said to change significantly at this stage, and all the centre points in the same class will be removed.

$$CGrade(k) = Grade(k) - Grade(k + 1)$$

$$AverCGrade = \frac{\sum_{i=1}^{n-1} CGrade(k)}{n - 1}$$

$$CGrade(k) > AverCGrade \quad (11)$$

$$Gradrop(k) = \frac{CGrade(k)}{\max_{k < i < Kmax} CGrade(i)}$$

$CGrade(k)$ is the score change value, $Grade(k)$ is the sorted points based on Equation (10) in descending order, $AverCGrade(k)$ is the average of the top $Kmax$ score changes, and $Gradrop(k)$ is the degree of the score change.

STEP 4: Generating the final number of clusters.

The last step in estimating the automatic number of clusters would be to investigate the change of the minimum distance between the central points so that the cluster points are not close to each other. He et al. (2020) developed equation (12) to judge the minimum distance, and the cluster centre was selected when $Disdrop(c_k, c_{k+1}) \geq a, a \geq 2$. This is because this condition portrays that no more small distance between the two centre points occurred. Then, the final number of clusters was decided by the size of the points before the last great change in the minimum distance between the centre points.

$$Disdrop(C_k, C_{k+1}) = \frac{\min_{c_i \in C_k, c_j \in C_k \text{ and } i \neq j} distance(c_i, c_j)}{\min_{c_i \in C_{k+1}, c_j \in C_{k+1} \text{ and } i \neq j} distance(c_i, c_j)} \quad (12)$$

3.5 Improved Fuzzy C-Means (IFCM)

Some alterations need to be done to the established FCM so that it can overcome the drawbacks of this algorithm. This study modified the cluster centre based on the density estimation instead of the random membership matrix. The improved method is named Improved Fuzzy C Means (IFCM). The flow of IFCM is as follows:

STEP 1: Generate random initialisation of the cluster centre $V = \{v_1, v_2, \dots, v_c\}$, together with membership matrix $F = [f_{ki}]_{c \times n}$, that follows the condition of FCM.

$$f_{ki} \in [0,1], \sum_{k=1}^c f_{ki} = 1, 0 < \sum_{k=1}^c f_{ki} < n$$

$$\forall i = 1, 2, \dots, n, \forall k = 1, 2, \dots, c \quad (13)$$

Where c is the total number of clusters that was computed previously.

STEP 2: Update the membership matrix using the cluster centre generated in equation (14). Zhang et al. (2020) suggested using the fuzzy index, $m \geq 1$. However, after a further investigation, a trend was noticed between the fuzzy index and cluster centre, by which the overlapping among cluster centre occurred significantly when the fuzzy index is increasing. For that reason, this study used a fixed value for the fuzzy index, which was $m = 1.15$ to avoid all cluster centres falling into the centre of the models.

$$f_{ij} = \frac{1}{\sum_{k=1}^c \left(\frac{d_{ij}}{d_{kj}}\right)^{\frac{2}{m-1}}} \quad (14)$$

Where $d_{ij} = \|p_i - c_j\|$, and $d_{kj} = \|p_k - c_j\|$.

STEP 3: Determine if the calculation procedure satisfies the threshold requirements. The computation procedure is complete, and the clustering result is computed when the number of iterations reaches the total number of iterations. Return to Step 2 if the termination condition is not satisfied.

3.6 Output Simplified Data

The point cloud data in different regions were simplified to complete the simplification process of point cloud based on the angle entropy in each region. Then, all the retained points from the simplification process will be combined with strong features preserved earlier to be the simplified dataset.

4. Results and Discussions

This section discusses the result computed based on an algorithm in the previous section. Four main characteristics were analysed: (i) number of clusters, (ii) size of simplified data, (iii) error evaluation, and (iv) processing time.

4.1 Analysis of the Preservation of the Strong Features

Based on the literature review, some researchers did not consider preservation of strong point clouds as one of the processes in their algorithm. Therefore, this subsection investigates the effect of preserving the critical points for each model based on the total simplified data, error evaluation, and figure comparison. The algorithm for this inspection was performed on the fixed number of clusters set to 10 and applied the established Fuzzy C-Means (FCM) clustering algorithm. The original data sets for all three models consist of 100,000 points. However, due to the processor capacity, 100,000 will be reduced to 5,000 points. The summary for this analysis is shown in Table 1.

Table 1. Analysis of Data Simplification with Strong Point Cloud Preservation.

Reservation of Strong Feature?	Number of Strong Points	Number of Clusters	Total Simplified Data	Error Evaluation	
				Maximum	Mean
BOX					
YES	711	10	2832	13.741	2.8378
NO	-	10	2469	13.7821	3.3582
STANFORD BUNNY					
YES	808	10	2659	3.9483	0.6471
NO	-	10	2216	3.9526	0.7713
CUP					
YES	725	10	3361	1.811	0.4867
NO	-	10	3111	1.811	0.5698

This result shows that the features preservation process gives the total number of final data somewhat higher than the unpreserved algorithm. Another aspect that stands out in the table is the error evaluation result. As for the maximum error, there is no comparable difference between the two algorithms. Regardless of that, it can be said that the algorithm with preservation of unique features effectively reduced the error for box and Stanford bunny. Mean errors show a significant contradiction for all three models. Thus, it is guaranteed that the features preservation step can minimise the error occurring in the point cloud simplification algorithm.

The following figures illustrate the distribution of the simplified data with the preserved points in red. Other colours in the figures show different clusters.

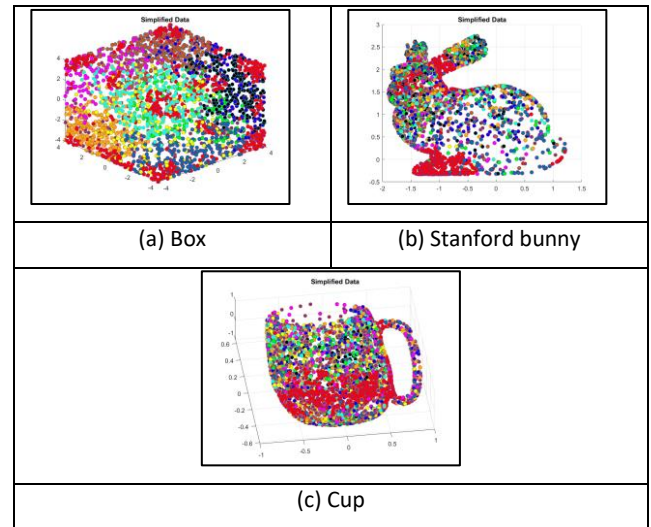


Figure 2. Analysis of strong features preservation on three different datasets.

Figure 2 shows the simplified models with preserved features in red colour. For the box, obviously, the strong elements are the edges. Unlike the box, the Stanford bunny has more round edges, and the method preserves points mainly at the bunny's face and legs. Similarly, the cup's strong features are located at its bottom part.

4.2 Analysis of the Developed Algorithm

This subsection discusses the outcome of the fully developed algorithm. The first modification of this study introduced a method to generate an automatic number of clusters. This modification was established by embedding the Score and Minimum Distance of the Centre Point (SMD) to rate the point clouds. The original Kernel Density Function by Wang and Kim (2019a) that used Gaussian Kernel Function was changed to the Cosine Kernel Function to increase the accuracy. At this point, the technique was named SMD-FCM because the SMD method is only used to get the number of clusters, and the cluster centres still depends on the random membership matrix.

The second modification is the cluster centre that was refined based on the score of the point clouds instead of the random membership matrix. This new technique is called the Improved Fuzzy C-Means (IFCM). The new algorithm with kernel and membership matrix modification is SMD(C)-IFCM. Table 2 shows the differences between these three algorithms.

Table 2. Differences among SMD-FCM, SMD-IFCM, SMD(C)-IFCM.

	SMD-FCM	SMD-IFCM	SMD(C)-IFCM (developed algorithm)
Kernel Density Function	Gaussian Kernel Function	Gaussian Kernel Function	Cosine Kernel Function
Cluster Centre	Based on membership matrix	Based on score of the point clouds	Based on score of the point clouds

The discussion for these three algorithms focuses on the number of cluster centres, total simplified data, error evaluation, and processing time in computing the algorithm. The results of the developed techniques are reported in Table 3.

Table 3. Results of Simplified Algorithm for SMD_FCM, SMD-IFCM, and SMD(C)-IFCM.

	Number of Strong Points	Number of Clusters	Total Simplified Data	Error Evaluation		Time Taken (s)
				Maximum	Mean	
BOX						
SMD-FCM	711	13	2860 (57.2%)	13.7821	3.9170	1756.044
SMD-IFCM	711	13	2866 (57.32%)	13.7821	3.9246	1840.031
SMD(C)-IFCM	711	14	2831 (56.62%)	13.7821	<u>3.8726</u>	<u>1606.853</u>
STANFORD BUNNY						
SMD-FCM	808	17	2666 (53.32%)	3.9522	0.9210	802.928
SMD-IFCM	808	17	2649 (52.98%)	3.9526	<u>0.9138</u>	1253.575
SMD(C)-IFCM	808	10	2678 (53.56%)	3.9526	0.9247	<u>775.776</u>
CUP						
SMD-FCM	725	5	3201 (64.01%)	1.811	0.5834	<u>682.029</u>
SMD-IFCM	725	5	3250 (65%)	1.811	0.5931	795.361
SMD(C)-IFCM	725	8	3174 (63.48%)	1.811	<u>0.5783</u>	717.929

The result shows that a change in Kernel Function affects the simplified result in which the total number of clusters can be different. The datasets are prone to be reduced more in the model with more clusters. For box and cup, the error evaluation between SMD-FCM and SMD-IFCM indicates that the Cosine Kernel Function produces a better result when applied to the IFCM technique. However, the SMD(C)-IFCM performed

inadequately for the Stanford bunny, and it may be related to other parameters involved in the whole process, such as the kNN value. The overall performance showed that the SMD(C)-IFCM scored six (6) out of nine (9) measurements, where the SMD-FCM and SMD-IFCM scored one (1) and two (2) respectively. Note that the maximum error was not considered in the measurement since it showed an insignificant difference between the methods.

Figures 3 to 5 display the simplified data and the cluster centres accordingly.

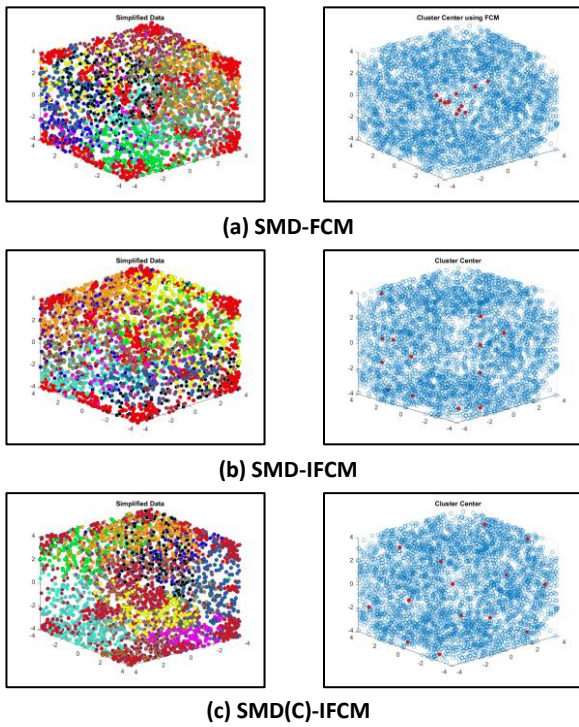


Figure 3. Analysis of simplified data and cluster centre for the box using three different methods.

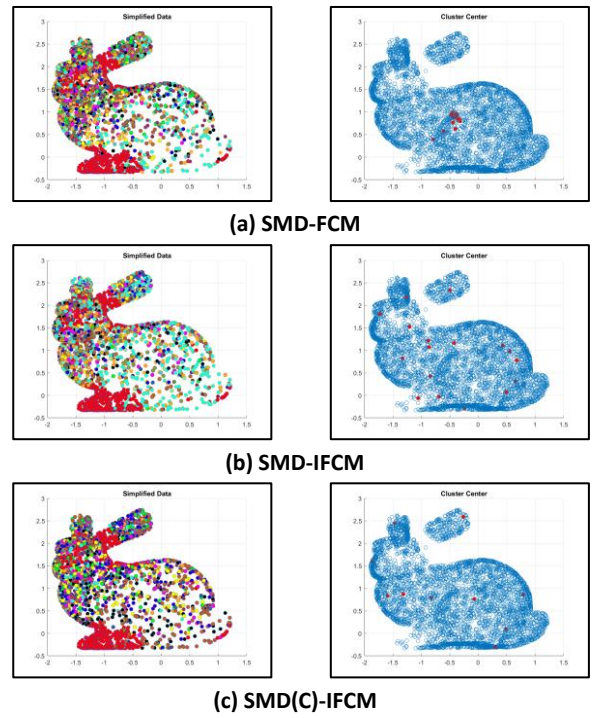


Figure 4. Analysis of simplified data and cluster centre for the Stanford bunny.

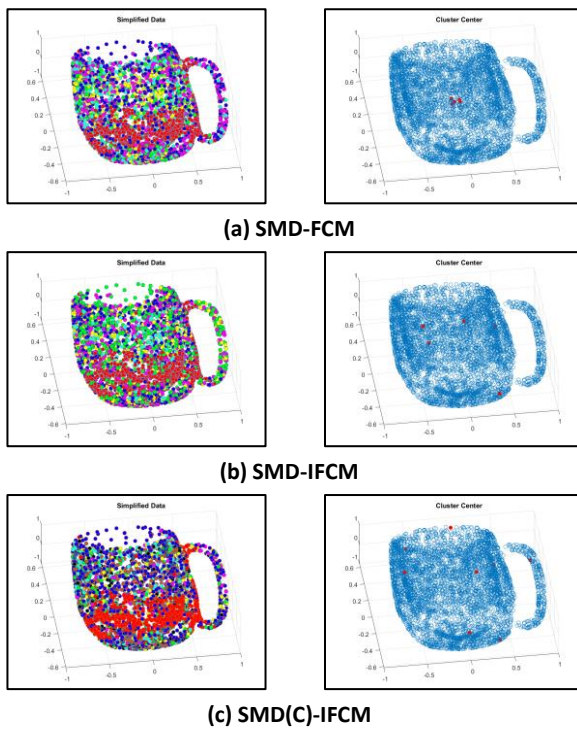


Figure 5. Analysis of simplified data and cluster centre for the cup.

In Figures 3 to 5, (a) is the resulted datasets and cluster centre using SMD-FCM, (b) is the resulted point clouds and cluster centre using SMD-IFCM, and (c) is the simplified model and cluster centre using the new model developed in this study which is the SMD(C)-IFCM. For SMD-FCM, the cluster centres for all datasets have gravitated to the model's centre, which shows the drawback of FCM. Meanwhile, for the SMD-IFCM, the distribution of cluster centres improved and got better with the SMD(C)-IFCM.

5. Conclusion

This study has developed the point cloud simplification algorithm named SMD(C)-IFCM with features preservation. The main characteristic of SMD(C)-IFCM is that it generates an automatic number of clusters according to the Cosine Kernel Function as the density estimator. Furthermore, the cluster centre for this algorithm is based on the score of the point clouds instead of a random membership matrix.

This study was carried out by analysing the results of the developed algorithm with the two other algorithms: (i) SMD-FCM, and (ii) SMD-IFCM. The analysis shows that the number of clusters mainly influences the total points after the simplification process. It can be observed that more data will be removed with a larger number of clusters. The results show that SMD-FCM had the weakest performance with one (1) score. This was due to the cluster centre in the methods of FCM being unstable and falling into the local optima. SMD-IFCM showed a better performance with a score of two (2). SMD(C)-IFCM had the best performance with a score of six (6). In this method, the cluster centres were distributed fairly. Furthermore, the number of cluster centres

were automatically calculated, and the significant features were preserved before the simplification.

For improvements, future studies should focus on kNN as this parameter has a huge impact on the preservation process.

6. Acknowledgement

This research is supported by FRGS-RACER (600-IRMI/FRGS-RACER 5/3 (053/2019) and RACER/1/2019/STG06/UITM//4).

7. References

- Alomoush, W., Alrosan, A., Almomani, A., Alissa, K., Khashan, O. A., & Al-Nawasrah, A. (2021). Spatial information of fuzzy clustering based mean best artificial bee colony algorithm for phantom brain image segmentation. *International Journal of Electrical and Computer Engineering*, *11*(5). <https://doi.org/10.11591/ijece.v11i5.pp4050-4058>
- Askari, S. (2021). Fuzzy C-Means clustering algorithm for data with unequal cluster sizes and contaminated with noise and outliers: Review and development. *Expert Systems with Applications*, *165*. <https://doi.org/10.1016/j.eswa.2020.113856>
- Hadi, N. A., & Alias, N. (2019). 3-Dimensional Human Head Reconstruction Using Cubic Spline Surface on CPU-GPU Platform. *Proceedings of the 2019 4th International Conference on Intelligent Information Technology*, 16–20. <https://doi.org/10.1145/3321454.3321476>
- Hadi, N. A., Halim, S. A., & Alias, N. (2021). Statistical filtering on 3D cloud data points on the CPU-GPU platform. *Journal of Physics: Conference Series*, *1770*(1). <https://doi.org/10.1088/1742-6596/1770/1/012006>
- Halim, M. S. A., Hadi, N. A., Sulaiman, H., & Halim, S. A. (2017). An Algorithm for Beta-Spline Surface Reconstruction from Multi Slice CT Scan Images using MATLAB pmode. *IEEE Symposium on Computer Applications & Industrial Electronics (ISCAIE)*, 1–6. <https://doi.org/10.1109/ISCAIE.2017.8074939>
- Halim, S. A., Hadi, N. A., & Mat Lazim, N. S. (2021). Segmentation and features extraction of Malaysian herbs leaves. *Journal of Physics: Conference Series*, *1770*(1), 1–7. <https://doi.org/10.1088/1742-6596/1770/1/012005>
- He, Z., Jia, Z., & Zhang, X. (2019). A fast method for estimating the number of clusters based on score and the minimum distance of the center point. *Information*, *11*(16), 1–14.
- He, Z., Jia, Z., & Zhang, X. (2020). A fast method for estimating the number of clusters based on score and the minimum

- distance of the center point. *Information (Switzerland)*, 11(1). <https://doi.org/10.3390/info11010016>
- Ji, C., Li, Y., Fan, J., & Lan, S. (2019). A novel simplification method for 3d geometric point cloud based on the importance of point. *IEEE Access*, 7. <https://doi.org/10.1109/ACCESS.2019.2939684>
- Krishna, P. G., & Bhaskari, D. L. (2016). Fuzzy C-means and fuzzy TLBO for fuzzy clustering. *Advances in Intelligent Systems and Computing*, 379. https://doi.org/10.1007/978-81-322-2517-1_46
- Leal, N., Leal, E., & German, S. T. (2017). A linear programming approach for 3D point cloud simplification. *IAENG International Journal of Computer Science*, 44(1).
- Mahdaoui, A., & Sbai, E. H. (2020). 3D point cloud simplification based on k-nearest neighbor and clustering. *Advances in Multimedia*, 2020.
- Siringoringo, R., & Jamaluddin, J. (2019). Initializing the Fuzzy C-Means Cluster Center with Particle Swarm Optimization for Sentiment Clustering. *Journal of Physics: Conference Series*, 1361(1). <https://doi.org/10.1088/1742-6596/1361/1/012002>
- Wang, Q., & Kim, M.-K. (2019). Applications of 3D point cloud data in the construction industry: A fifteen-year review from 2004 to 2018. *Advanced Engineering Informatics*, 39, 306–319.
- Wu, Z., Zeng, Y., Li, D. S., Liu, J., & Feng, L. (2021). High-volume point cloud data simplification based on decomposed graph filtering. *Automation in Construction*, 129. <https://doi.org/10.1016/j.autcon.2021.103815>
- Xuan, W., Hua, X., Chen, X., Zou, J., & He, X. (2018). A New Progressive Simplification Method for Point Cloud Using Local Entropy of Normal Angle. *Journal of the Indian Society of Remote Sensing*, 46(4). <https://doi.org/10.1007/s12524-017-0730-6>
- Yang, Y., Li, M., & Ma, X. (2020). A Point Cloud Simplification Method Based on Modified Fuzzy C-Means Clustering Algorithm with Feature Information Reserved. *Mathematical Problems in Engineering*, 2020. <https://doi.org/10.1155/2020/5713137>
- Zhang, L., Luo, M., Liu, J., Li, Z., & Zheng, Q. (2020). Diverse fuzzy c-means for image clustering. *Pattern Recognition Letters*, 130. <https://doi.org/10.1016/j.patrec.2018.07.004>

QUARTERLY VARIATION IN TROPOSPHERIC SURFACE REFRACTIVITY IN ILORIN, NIGERIAM.S Otto^{1a}, O.J Abimbola^{2a}, O.A Falaiye^{3b}, F.U.Muhammad^{4a}, A.A Sule^{5a}

Abstract: Refractivity impacts radio communication systems that are above the atmosphere. It is thus necessary to understand variations in refractivity to improve the effectiveness of cellular networks and navigation and surveillance systems. The purpose of this study is to measure seasonal changes in tropospheric surface refractivity in Ilorin, Kwara, Nigeria. During the dry (first quarter) and rainy (third quarter) seasons from 2000 to 2002, refractivity was calculated using meteorological data obtained from the Nigerian Meteorological Agency, Ilorin. Average surface refractivity of 243.34 N-units was recorded in the third quarter (July–September) of 2000; it was 212.86 N-units in the first quarter (January–March). Refractivity was measured at 240.25 N-units and 212.73 N-units in the third and first quarters of 2001, respectively. Finally, refractivity was measured at 242.83 N-units and 216.51 N-units in the third and first quarters of 2002, respectively. These results show that tropospheric surface refractivity differs in the dry and rainy seasons; higher surface refractivity was observed during the rainy season than during the dry season over a three-year period. This is attributed primarily to water content in the atmosphere (troposphere), which is higher during the rainy season than the dry season.

Keywords: Refractivity, atmosphere, troposphere, meteorological parameters

1. Introduction

Variations in meteorological parameters, particularly in the troposphere, can change the composition of the atmosphere, which has a profound effect on the propagation of electromagnetic waves in the atmosphere (specifically in the troposphere) (Korak, 2003). Variations in meteorological parameters such as temperature, pressure, and relative humidity impact the index of refraction of the air within this layer. Solar radiation influences all meteorological parameters, either directly or indirectly, causing typical daily or yearly trends. To measure these trends, it is necessary to calculate the mean values of multiple measurements taken over a specific period (Bean & Horn, 1959). However, the daily cycles of some meteorological parameters are quite easy to measure.

Variations in meteorological parameters such as clouds and rain have a stronger impact on radio wave propagation in the lower atmosphere, particularly in the troposphere (Hall, 1979). In the tropics, these variables vary every quarter hour, as well as hourly, daily, and seasonally. Radio communication (terrestrial and satellite) systems must account for variations in refractivity. Radio refractivity, which is impacted by these three parameters (temperature, pressure, and relative humidity), affects the

propagation of radio waves at various frequencies, such as ultra-high frequencies and microwave frequencies. Radio refractivity is influenced by the meteorological variables of temperature, pressure, and relative humidity (Bean & Horn, 1959). Distribution studies of refractivity can help address the challenges that arise due to unexpected path loss and uncharacteristic propagation of radio waves, which obstruct radio signal performance in cellular networks and in surveillance and navigation systems (Ukhurebor & Nwankwo, 2020).

Many researchers have made significant contributions to this field, including Ukhurebor and Nwankwo (2020), who used an inexpensive, portable, self-implemented meteorological monitoring device to estimate the refractivity gradient from basic climate variables in Iyamho-Auchi, Edo State, South-South Region of Nigeria over a one-year period (2018). They concluded that refractivity gradient values are higher during months with lower relative humidity. Abimbola et al. (2021) estimated radio refractivity from a decade of satellite meteorological data for West Africa and discovered a seasonal pattern in refraction variation across the West African region, with super-refraction dominating the coastal area during the wet season and sub-refraction dominating during the dry season. In 2017, Ukhurebor et al. (2018) used a portable weather monitoring system to estimate atmospheric refractivity over Auchi town (Edo State), Nigeria, and found that air temperature impacts refractivity more than relative humidity or atmospheric pressure. Edet et al. (2017) investigated monthly variations in radio refractivity in Calabar, Nigeria, in 2016 and found that radio refractivity patterns varied

Authors information:

^aDepartment of Physics, Federal University of Lafia, NIGERIA. E-mail: o.muhammed@science.fulafia.edu.ng¹; abimbola.oladiran@science.fulafia.edu.ng²; faisal.usman@science.fulafia.edu.ng⁴; ahmedsule0104@gmail.com⁵

^bDepartment of Physics, University of Ilorin, NIGERIA. E-mail: sesantayo2001@yahoo.com³

*Corresponding

o.muhammed@science.fulafia.edu.ng

Author:

Received: February 16, 2022

Accepted: October 13, 2022

Published: October 31, 2023

only slightly due to Calabar’s nearly uniform weather conditions (i.e., a small observed increase in tropospheric temperature and humidity). Ikeh and Okeke (2016) found that, over a two-year period, surface refractivity over Awka, South East Nigeria, varied most during the rainy season and least during the dry season. Bawa et al. (2015) examined average hourly variations in radio refractivity in several Nigerian cities: Yola (9° 11' N, 12° 30' E), Anyigba (7° 45' N, 6° 45' E), Lagos (6° 27' N, 5° 12' E), and Port-Harcourt (40° 48' N, 7° E). This study found that average hourly variations in refractivity during the dry season are due primarily to variations in humidity, while refractivity varies during the rainy season due to changes in both dry (pressure) and wet components (humidity). Ali et al. (2011) also examined seasonal variations in radio refractivity, using measurements taken at a height of 10 km over Minna (9° 37' N, 6° 30' E). They found that the atmosphere over Minna was super-refractive during the wet season and sub-refractive during the dry season. Adediji et al. (2013) computed radio refractivity using measurements of atmospheric parameters taken by weather stations in Akure, Nigeria (2007–2011) (Davies 6162 wireless vantage Pro2 specs), at different altitudes. They found that, at all levels, water vapour pressure impacts radio refractivity more than any other parameter. Igwe and Adimula (2009) used the University of Ilorin Atmospheric observatory to obtain data from the radiometric network of the Baseline Surface Radiation Network (BSRN) and computed surface-level monthly variations in the radio refractive index over Ilorin (8° 32' N, 4° 34' E) over a period of five years (2000–2004). Okoro and Agbo (2012) investigated the effect of diurnal variations in meteorological parameters on tropospheric radio refractivity during the dry and rainy seasons in Minna in 2008. They found that variations in meteorological parameters, such as humidity and temperature, in the lower troposphere caused radio refractivity to vary throughout the day; this impact was more significant during the rainy season than the dry season. Agbo et al. (2013) evaluated atmospheric refractivity on disturbed and quiet days in Abuja during the dry and rainy seasons and found that refractivity is impacted by changes in weather variables. Other similar studies include Willoughby et al. (2002), Adeyemi (2004), Falodun (2006), Adedeji (2008), Ekpe et al. (2010), Igwe et al. (2011), Daniel et al. (2015), Falaiye et al. (2016), and Ukhurebor and Azi (2019). However, none of the reviewed studies have computed quarterly surface refractivity in Ilorin, Kwara State, North-Central Nigeria, despite this region’s unique climate (tropical savanna).

Because changes in the index of refraction play such a large role in radio wave propagation in the troposphere, it is convenient to use refractivity (N) when modelling atmospheric variation in the index of refraction (Bean, 1966; Thayer, 1974). Refractivity (N) is related to the index of refraction, n, as shown in Eq. 1:

$$N = (n - 1) \times 10^6 \tag{1}$$

Refractivity is also related to meteorological parameters (Willoughby et al., 2002):

$$N = \frac{77.6}{T} \left(P + 4810 \frac{e}{T} \right) = 77.6 \frac{P}{T} + \left(3.732 \times 10^5 \frac{e}{T^2} \right) \tag{2}$$

where T = Absolute temperature in Kelvin, P = Barometric pressure in millibars, e = Partial pressure of water vapor in millibars, and e_s = Saturated vapor pressure in millibars.

$$e_s = 6.11 \times \exp(x) \tag{3}$$

$$x = \frac{17.2694(T - 273.15)}{T - 35.85} \tag{4}$$

$$e = \frac{RH}{100} e_s \tag{5}$$

The present paper aims to measure and compare quarterly variations in refractivity in Ilorin, Nigeria, and to measure the relationships of these variations with the aforementioned meteorological parameters.

2. Methodology

Ilorin (4.542 °E, 8.497 °N; altitude 303 m), the research location of the present study, is the capital city of Kwara State, Nigeria. It has a population of about 777,667 and a Köppen climate classification of Aw, tropical savanna. The average climatic data for Ilorin is as follows: temperature: 32.5 °C; total annual rainfall: 1,185 mm; average annual rainy days: 88; average relative humidity: 51.1%. Figure 1 shows Ilorin on a map of Nigeria. The data used in this study were recorded over a period of three years and provided by the Nigerian Meteorological Agency (NIMET). The station uses a dry bulb thermometer to measure temperature, a barometer to measure atmospheric pressure, and a hygrometer to measure relative humidity.

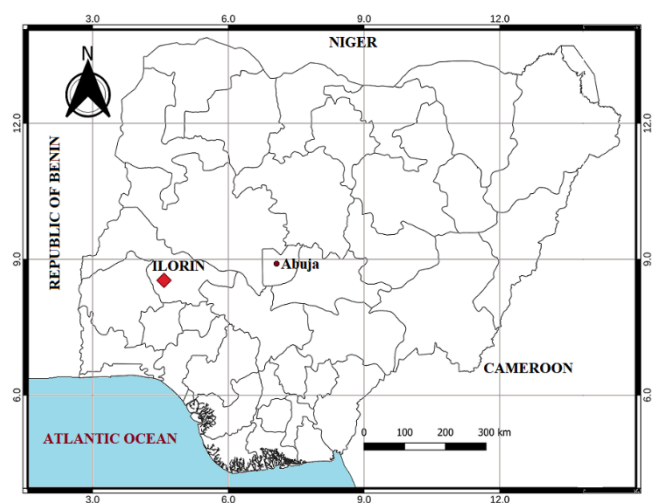


Figure 1. Research location (Ilorin) on a map of Nigeria.

To compute the seasonal surface refractivity, the quarterly values of each of the three meteorological parameters (temperature, pressure, and relative humidity) from 2000 to 2002 were determined by averaging the values for the same three months of each of the three measured years. The first quarter includes the average values for January to March, the second quarter includes those from April to June, the third quarter includes those from July to September, and the fourth quarter includes those from October to December. All temperature, pressure, and relative humidity measurements were entered separately into a Microsoft Excel document and then input into the formula shown in Eq. 2. Graphs were also plotted to compare quarterly variations in surface refractivity from 2000 to 2002.

3. Results and Discussions

Quarterly variations in tropospheric surface refractivity were computed based on meteorological data. The extreme dry season is the first quarter (January–March), while the moderately rainy season is the second quarter (April–June), the extreme rainy season is the third quarter (July–September), and the moderately dry season is the fourth quarter (October–December) in Ilorin. During the extreme rainy season (the third quarter), average surface refractivity was 243.34 N-units. During the extreme dry season (the first quarter), it was lower, only 212.86 N-units, as shown in Figure 2. This is due to higher atmospheric water content during the extreme rainy season. The standard deviation (SD) in surface refractivity for each quarter was also calculated; the third quarter has the highest surface refractivity (243.34 N-units) and the lowest SD (4.86) (first quarter: 212.86 N-units, SD = 8.22; second quarter: 227.02 N-units, SD = 9.00; fourth quarter: 223.26 N-units, SD = 12.72).

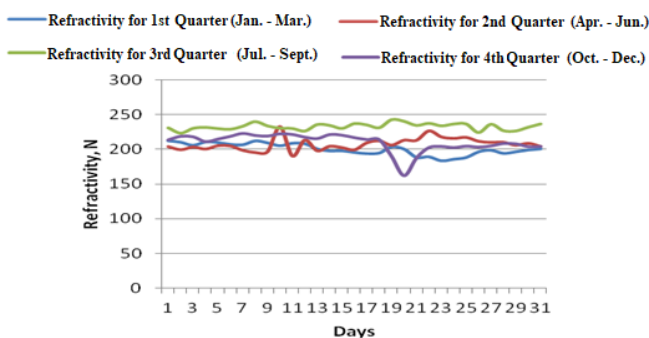


Figure 2. Quarterly refractivity for all quarters of 2000.

Figures 3 and 4 show that, during the first and third quarters, seasonal surface refractivity responds more to changes in relative humidity than in other parameters.

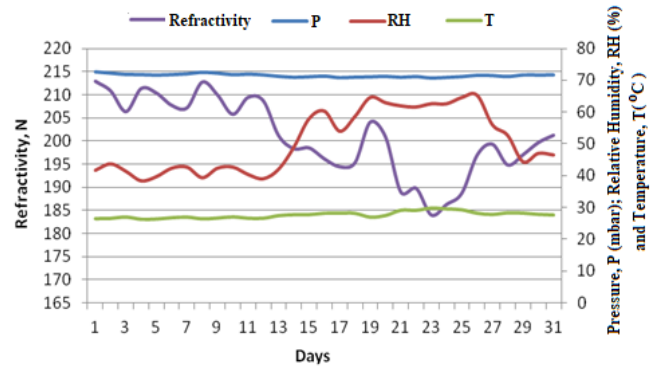


Figure 3. First-quarter (dry season) seasonal refractivity in 2000.

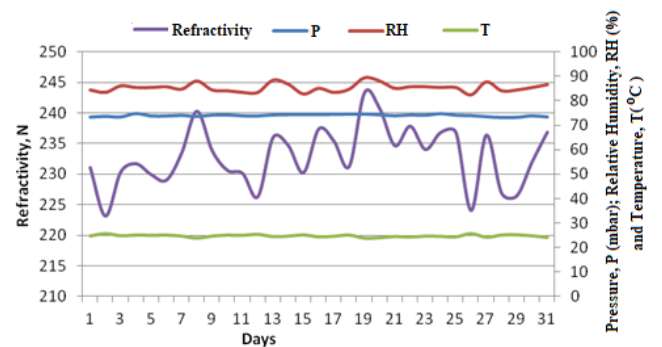


Figure 4. Third-quarter (rainy season) seasonal refractivity in 2000.

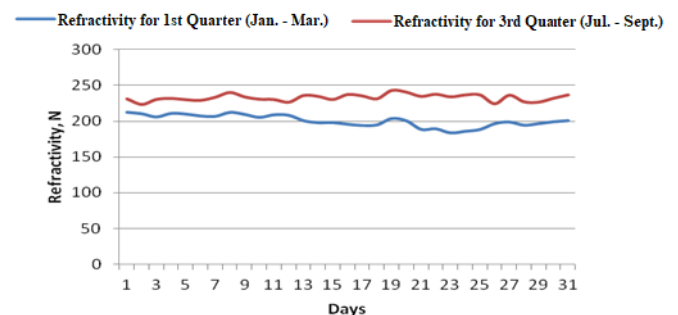


Figure 5. Quarterly refractivity for the first and third quarters of 2000.

Figure 6 shows that in 2000, surface refractivity was higher during the extreme rainy season (third quarter; 240.25 N-units) than during the extreme dry season (first quarter; 212.73 N-units). This is due to the higher atmospheric water content during the extreme rainy season. The third quarter has the highest surface refractivity (240.25 N-units) and the lowest SD (3.39) (first quarter: 212.73 N-units, SD = 7.26; second quarter: 224.78 N-units, SD = 5.96; fourth quarter: 244.36 N-units, SD = 9.70).

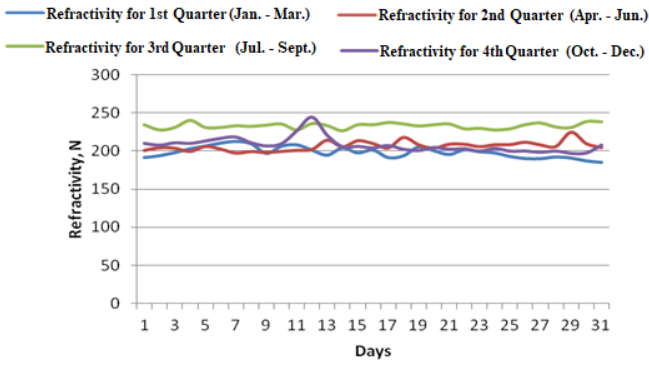


Figure 6. Quarterly refractivity for all quarters of 2001.

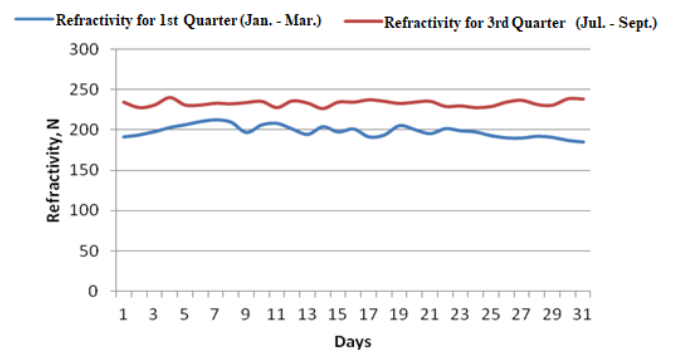


Figure 9. Quarterly refractivity for the first and third quarters of 2001.

As shown in Figure 10, surface refractivity during the extreme rainy season of 2001 was 242.83 N-units, higher than refractivity during the extreme dry season (216.51 N-units). In 2001, the third quarter had the highest surface refractivity (242.83 N-units) and the lowest SD (4.20) (first quarter: 216.51 N-units, SD = 9.25; second quarter: 222.91 N-units, SD = 7.82; fourth quarter: 223.56 N-units, SD = 5.27).

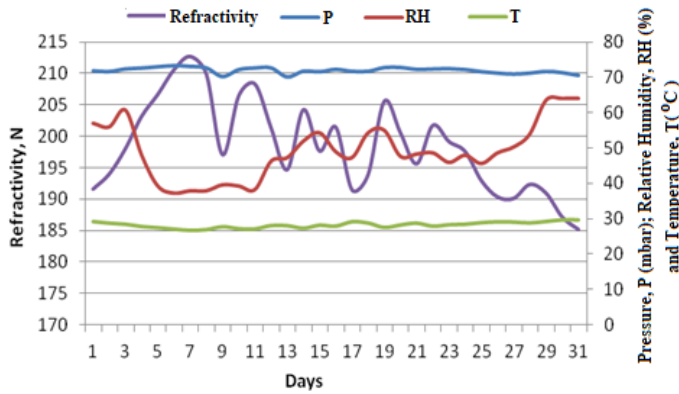


Figure 7. First-quarter (dry season) seasonal refractivity in 2001.

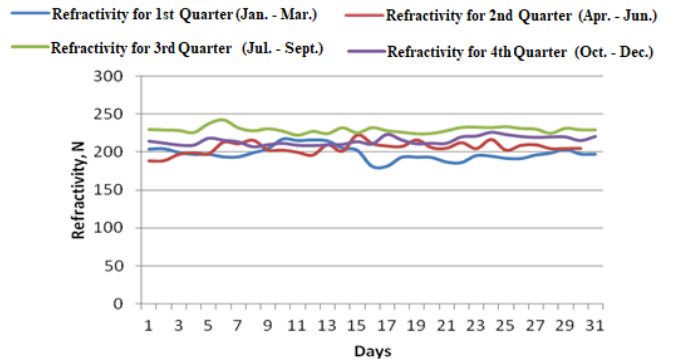


Figure 10. Quarterly refractivity for all quarters of 2002.

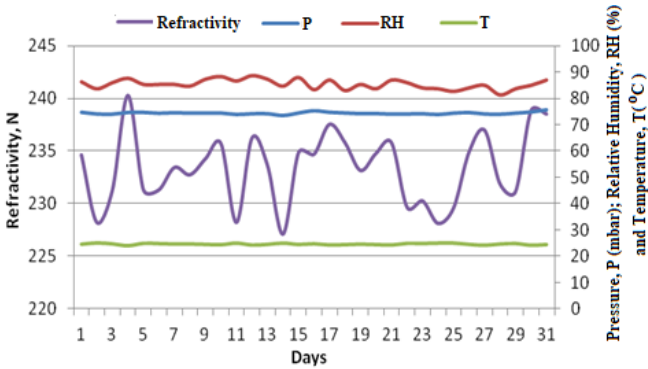


Figure 8. Third-quarter (rainy season) seasonal refractivity in 2001.

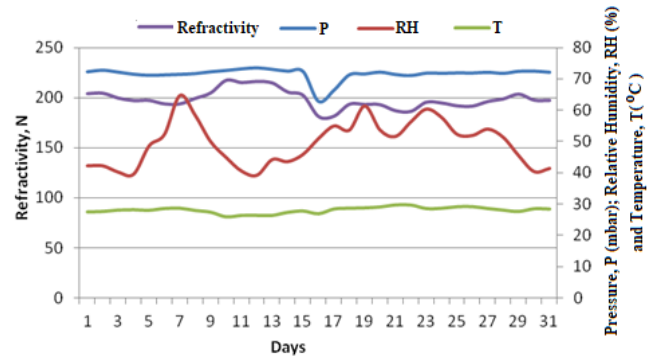


Figure 11. First-quarter (dry season) seasonal refractivity in 2002.

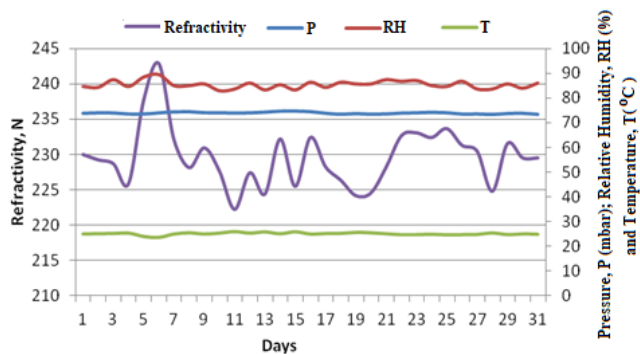


Figure 12. Third-quarter (rainy season) seasonal refractivity in 2002.

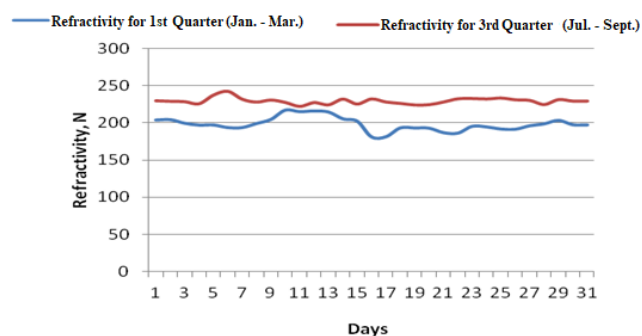


Figure 13. Quarterly seasonal refractivity for the first and third quarters of 2002.

Table 1. Correlation coefficients of the weather parameters for the dry and wet seasons in Ilorin over a period of three years.

VARIATION	YEAR	PRESSURE, P (millibars)	RELATIVE HUMIDITY, RH (%)	TEMPERATURE, T (°C)
First quarter (dry season) refractivity	2000	0.84	-0.81	-0.99
	2001	0.76	-0.72	-0.97
	2002	0.68	-0.59	-0.78
Third quarter (rainy season) refractivity	2000	0.42	0.76	-0.96
	2001	0.62	0.42	-0.95
	2002	0.14	0.64	-0.95

As shown in Table 1, in 2000, dry season refractivity in Ilorin correlated with pressure (correlation coefficient: 0.84 at the 5% significant level). This indicates that these factors increase together. Thus, based on pressure, it can be predicted that refractivity in Ilorin during the dry season is 84%. Relative humidity and temperature have very high negative correlation coefficients with surface refractivity (-0.81 and -0.99), indicating that these factors have an inverse relationship with surface refractivity during the dry season.

In contrast, during the rainy season in Ilorin, refractivity has a small or insignificant correlation with pressure, but it has a positive correlation coefficient with relative humidity and a very high negative correlation coefficient with temperature. This suggests that, during the rainy season, daily surface refractivity in Ilorin increases due to other parameters (an increase in relative humidity leads to a decrease in temperature), while pressure has no or little impact on tropospheric surface refractivity in Ilorin during the rainy season. More research is needed to confirm these findings.

Quarterly tropospheric surface radio refractivity (N) in 2000 can be predicted based on relative humidity (RH) and temperature (T) using multiple regression equations:

$$N = 420.39 - 0.07RH - 7.80T \text{ (dry season)} \tag{6}$$

$$N = 480.28 - 0.02RH - 9.95T \text{ (rainy season)} \tag{7}$$

Radio refractivity (N) in 2000 can be predicted based on three parameters (pressure [P], relative humidity [RH], and temperature [T]) using the following equations:

$$N = 178.69 - 0.005RH - 6.99T + 3.02P \text{ (dry season)} \tag{8}$$

$$N = 230.66 + 0.02RH - 9.36T + 3.12P \text{ (rainy season)} \tag{9}$$

5. Conclusion

This study has used meteorological parameters recorded in Ilorin from 2000 to 2002 to investigate quarterly variations in tropospheric surface refractivity. The results show that surface refractivity was high during the extreme rainy season (third quarter, July–September) and low during the extreme dry season (first quarter, January–March) during the study period (2000–2002). It can be stated unequivocally that tropospheric surface refractivity varies seasonally (dry and rainy); it is higher during the rainy season and lower during the dry season. Furthermore, during the rainy season, refractivity correlates positively with relative humidity and negatively with temperature, while during the dry season, refractivity correlates negatively with both temperature and relative humidity.

Future studies should use data from a broader spatial region, such as satellite data, which could enable a vertical study of refractivity in Ilorin. This will provide a better picture of the spatio-temporal variation in radio refractivity, which will support decisions about systems that use radio signals.

5. Acknowledgement

We would like to thank the Nigerian Meteorological Agency (NIMET) in Ilorin for allowing us to use their data. In addition, the success of this study is due to teamwork, so we would like to express our heartfelt appreciation to everyone who has helped during any phase of the study.

6. References

- Abimbola, O. J., Bada, E., Falaiye, A. O., Sukam, Y. M., & Muhammad, S. (2021). Estimation of radio refractivity from a decade of satellite-derived meteorological data for West Africa. *Scientific African*, 14. <https://doi.org/10.1016/j.sciaf.2021.e01054>.
- Adediji, A. T., & Ajewole, M. O. (2008). Vertical profile of radio refractivity gradient in Akure, Southwest Nigeria. *Progress in Electromagnetic Research C*, 4, 157–168.
- Adediji, A. T., Ajewole, M. O., Ojo, J. S., Ashidi, A. G., Ismail, M., & Mandeep, J. S. (2013). Influence of some meteorological factors on tropospheric radio refractivity over a tropical location in Nigeria. *Journal of Atmospheric and Solar-Terrestrial Physics*, 125–127.
- Adeyemi, B. (2004). Tropospheric radio refractivity over three radiosonde stations in Nigeria. *Ife Journal of Science*, 6(2), 167–176.
- Agbo, G. A., Okoro, O. N., & Amechi, A. O. (2013). Atmospheric refractivity over Abuja, Nigeria. *International Research Journal of Pure and Applied Physics*, 1(1), 37–45.
- Ali, S., Malik, S. A., Alimgeer, K. S., Khan, K. S., & Ali, R. L. (2011). Statistical estimation of tropospheric radio refractivity derived from ten years meteorological data. *Journal of Atmospheric and Solar-Terrestrial Physics*, 77, 96–103.
- Bawa, M., Ayantunji, B. G., Mai-Unguwa, H., Galadanchi, G. S. M., & Shamsuddeen, I. M. (2015). Study of average hourly variations of radio refractivity variations across some selected cities in Nigeria. *IOSR Journal of Applied Physics (IOSRJAP)*, 7(6), 37–43.
- Bean, B. R., & Horn, J. D. (1959). Radio refractive index of climate near the ground. *Journal of Research of the National Bureau of Standards, Section D: Radio Propagation*, 63D(3).
- Bean, B. R. (1966). *Radio meteorology*. New York, USA.
- Daniel E. O., Amajama, J., & Mfon, O. C. (2015). Observing the radio refractivity pattern variation during the dry season in Calabar, Nigeria. *International Journal of Scientific Research Engineering and Technology (IJSRET)*, 4.
- Edet, C. O., Eno, E. E., & Ettah, E. B. (2017). Monthly variation of radio refractivity in Calabar, Nigeria. *International Journal of Scientific Research Engineering and Technology (IJSRET)*, 6(4), 315–317.
- Ekpe, O. E., Agbo, G. A., Ayantunji, B. G., Yusuf, N., & Onugwu, A. C. (2010). Variation of tropospheric surface refractivity at Nsukka in the southeastern Nigeria. *Nigeria Journal of Space Research*, 7, 42–48.
- Falaiye, O. A., Abimbola, O. J., & Akinyanyu, D. J. (2016). Spacio-temporal variation of radio refractivity in Lafia, Nasarawa State using CM SAF ATOVS satellite data. *Fulafia Journal of Science and Technology*, 2(1), 111–119.
- Falodun, S. E., & Ajewole, M. O. (2006). Radio refractive index in the lowest region (100 m) of the troposphere in Akure. *South-Western Journal of Atmospheric and Solar-Terrestrial Physics*, 68, 236–243.
- Hall, M. P. (1979). Effects of the troposphere on radio communication. *Institute of Electrical Engineers*, 1–22.
- Hughes, K. A. (1998). *Radio propagation data from tropical regions: A brief review of a seminar on radio propagation in tropical regions*. [Unpublished notes from a lecture presented at the Centre for Theoretical Physics.]
- Igwe, K. C., Adimula, I. A., Falaiye, O. A., & Oyedum, O. D. (2011). Radio refractive index variations with related

- weather parameters at surface level in Ilorin, North Central Nigeria. *IUP Journal of Physics*, 4(3), 57–66.
- Igwe, K. C., & Adimula, I. A. (2009). Variations of surface radio refractivity and radio refractive index gradients in the Sub-Sahel. *Nigerian Journal of Space Research*, 6, 135–144.
- Ikeh, U. C., & Okeke, C. C. (2016). The study of surface radio refractivity in Awka, South Eastern Nigeria. *Journal of Geography, Environment and Earth Science International*, 6(2), 3–7.
- Korak Shaha, P. (2003). *The physics of the earth and its atmosphere*. John Wiley & Sons.
- Okoro, O. N., & Agbo, G. A. (2012). The effect of variation of meteorological parameters on the tropospheric radio refractivity for Minna. *Global Journal of Science Frontier Research Physics and Space Science*, 12(2), 4–6.
- Thayer, G. D. (1974). An improved equation for radio refractive index of air. *Radio Science*, 9(10), 803–807.
- Ukhurebor, K. E., & Nwankwo, W. (2020). Estimation of the refractivity gradient from measured essential climate variables in Iyamho-Auchi, Edo State, South-South Region of Nigeria. *Indonesian Journal of Electrical Engineering and Computer Science*, 19(1), 276–284.
- Ukhurebor, K. E., & Azi, S. O. (2019). Review of methodology to obtain parameters for radio wave propagation at low latitudes from meteorological data: New results for Auchi area in Edo State, Nigeria. *Journal of King Saud University of Science*, 31(4), 1445–1451. <https://doi.org/10.1016/j.jksus.2018.03.010>
- Ukhurebor, K. E., Azi, S. O., Abiodun, I. C., & Ojiemudia, S. E. (2018). Influence of weather variables on atmospheric refractivity over Auchi Town, Edo State, Nigeria. *Journal of Applied Science and Environment Management*, 22(4), 471–475.
- Willoughby, A. A., Aro, T. O., & Owotabi, I. E. (2002). Seasonal variations of radio refractivity gradients in Nigeria. *Journal of Atmospheric and Solar–Terrestrial Physics*, 64, 417–425.

SPATIAL DISTRIBUTION OF MALARIA AND LAND COVER PATTERNS IN OSONI LAND, RIVERS STATE, NIGERIA

Sylvia E. Egbom^{1a*}, Florence O. Nduka^{2b}, Sidney O. Nzeako^{3b}, Chigozie C. Ikechukwu^{4c}, Joseph I. Nwachukwu^{5d}, Chinonye O. Ezenwaka^{6e}, Charity O. Ihejirika^{7a}, Martin C. Opara^{8a}, Emilia O. Anyanwu^{9a}, Blessing O. Agoh^{10f}, Justin N. Okorondu^{11d} and Grace C. Egwuogu^{12a}

Abstract: The distribution of malaria is characterised by microgeographic variations determined by a range of factors, including the local environment. A study on the spatial distribution of malaria and land cover patterns was carried out by sampling Primary Health Centres in Ogoni Land. Nine Primary Healthcare Centres (PHCs) were selected across four local government areas (LGA) using Systematic Grid Point Sampling. Human blood samples were obtained from 318 consented individuals, and questionnaires were administered to obtain demographic data. *Plasmodium* species were identified through microscopy using thick and thin blood films. A geodatabase was created and imported into ArcGIS 10.7 to produce a thematic map of the study area. A cloud-free Landsat-8 Operational Land Imager (OLI) was employed for land cover analysis. Both supervised and unsupervised classifications of land cover were performed to generate the land cover classes. Pearson correlation was carried out to determine the significance between malaria distribution and land cover. Of the 318 individuals, 169 were infected with an overall prevalence of 53.1%. Only *P. falciparum* was identified and malaria distribution showed spatial variations. Across the PHCs sampled, the highest point prevalence was recorded in Model Primary Health Centre Koroma in Tai LGA whereas the lowest was recorded in MPHOC Okwale in Khana LGA. Cumulatively, Kwawa PHC recorded the highest malaria prevalence whereas MPHOC Bunu in Tai recorded the lowest prevalence. The highest prevalence was recorded in Khana LGA while the lowest was recorded in Eleme LGA. Land cover analysis revealed that Ogoni Land has a total land cover mass of 982.97km². Sparse vegetation dominated the study area (471.06km²) while dense vegetation covers a total mass of 213.1km². Bivariate analysis showed a significant correlation between malaria prevalence and dense vegetation ($p < 0.05$, 0.952). Dense vegetation played a significant role in malaria transmission in Ogoni Land. The study concludes that the presence of dense vegetation is associated with high malaria prevalence in the study area.

Keywords: Malaria distribution, land cover, gis, remote sensing, pearson correlation

Authors information:

^aEnvironmental Health Science Department, Federal University of Technology, Owerri, NIGERIA. E-mail: sylviaegbom@gmail.com¹; nachiihejirika@yahoo.com⁷; come9092@gmail.com⁸; okunamirioluchi@gmail.com⁹; graceegwuogu@gmail.com¹²

^bAnimal and Environmental Biology Department, University of Port Harcourt, Choba, Port Harcourt, NIGERIA. E-mail: florence.nduka@uniport.edu.ng²; sidney.nzeako@uniport.edu.ng³

^cDepartment of Geology, Federal University of Technology, Owerri, NIGERIA. E-mail: gisgrandmaster@gmail.com⁴

^dEnvironmental Management Department, Federal University of Technology, Owerri, NIGERIA. E-mail: joseph.nwachukwu@futo.edu.ng⁵; justin.okorondu@gmail.com¹¹

^eBiology Department, Federal University Otuoke, Bayelsa, NIGERIA. E-mail: ezenwakaco@fuotuoke.edu.ng⁶

^fBiology Department, College of Education, Warri, NIGERIA. E-mail: blessingchristian2013@gmail.com¹⁰

*Corresponding Author: sylviaegbom@gmail.com

1. Introduction

Malaria is a parasitic disease caused by parasites of the genus *Plasmodium* (Sato, 2021) and is transmitted naturally through the bite of the female *Anopheles* mosquitoes (Bassey and Izah, 2017). In Sub-Saharan Africa, significant deaths occur annually (Bassey and Izah, 2017) due to the disease. Malaria is environmentally driven (Onyiri, 2015) and is one of the most common public health issues across Nigeria (Ayanlade *et al.*, 2013). Nigeria is in tropical Africa where the best combination of adequate rainfall, humidity and temperature are characteristic, thereby providing favourable breeding conditions for malaria vectors. Malaria is holo-endemic in rural Nigeria and meso-endemic in urban areas with stable and intense transmission (Nmadu *et al.*, 2015).

The distribution of malaria is characterised by microgeographic variations, regularly amongst nearby villages, households, or homes (Coleman *et al.*, 2009). The local heterogeneity in malaria distribution is determined by a range of

Received: September 8, 2022

Accepted: January 25, 2023

Published: October 31, 2023

factors, including human factors (Ngom and Siegmund, 2015), environmental factors (Abiodun *et al.*, 2016) etc. Environmental factors can influence the profusion and continued existence of both the parasites and vectors transmitting them and are therefore said to be responsible for over 70% risk (Ye *et al.*, 2007). Precise malaria and land use data are required to monitor disease risk in a changing environment. Global changes in land cover have been monitored, and data resulting from remote sensing is becoming more accessible. These data have been supplemented with new technologies that allow for the mapping of regions of interest. Since proper vector control necessitates a good understanding of the ecology of breeding, resting habitats and behaviour of the various species of mosquito (Okogun, 2005), the advent of a tool with such functionality and great efficiency is of paramount importance (Pam *et al.*, 2017) in malaria studies. A more valuable approach to analysing the distribution patterns of malaria disease is achieved by the application of geospatial technology (Adeola *et al.*, 2015).

Mapping malaria for effective control and elimination has become valuable since the recognition and adoption of GIS as a tool (Hay and Snow, 2006). Malaria prevalence and incidence

mapping is the most basic application of GIS and has been used to visualise and classify the spatial distribution patterns of malaria over a distinct geographical location (Feng *et al.*, 2018, Weiss *et al.*, 2019). Mapping and other geostatistical applications are used to link relationships between the spatial distribution of malaria and other variables like weather and climate (Kakmeni *et al.*, 2018; Okunlola and Oyeyemi, 2019), vector breeding sites (Palaniyandi *et al.*, 2016; Ndiaye *et al.*, 2020) and land use (Ayo *et al.*, 2017; Paul *et al.*, 2018). This research aimed to evaluate the prevalence and spatial distribution of malaria in Ogoni Land, Rivers State, Nigeria using the GIS tool. The specific objectives are to determine the prevalence of malaria, produce prevalence maps of malaria and evaluate the impact of land cover on malaria prevalence in the study area.

2. Method

2.1 Study Area

Ogoni Land is in Rivers State on the coast of the Gulf of Guinea, east of the city of Port Harcourt. It extends across the local government areas (LGAs) of Khana, Gokana, Eleme and Tai. The map of the study area is shown in Figure 1. The study was conducted in nine primary health care (PHC) centres.

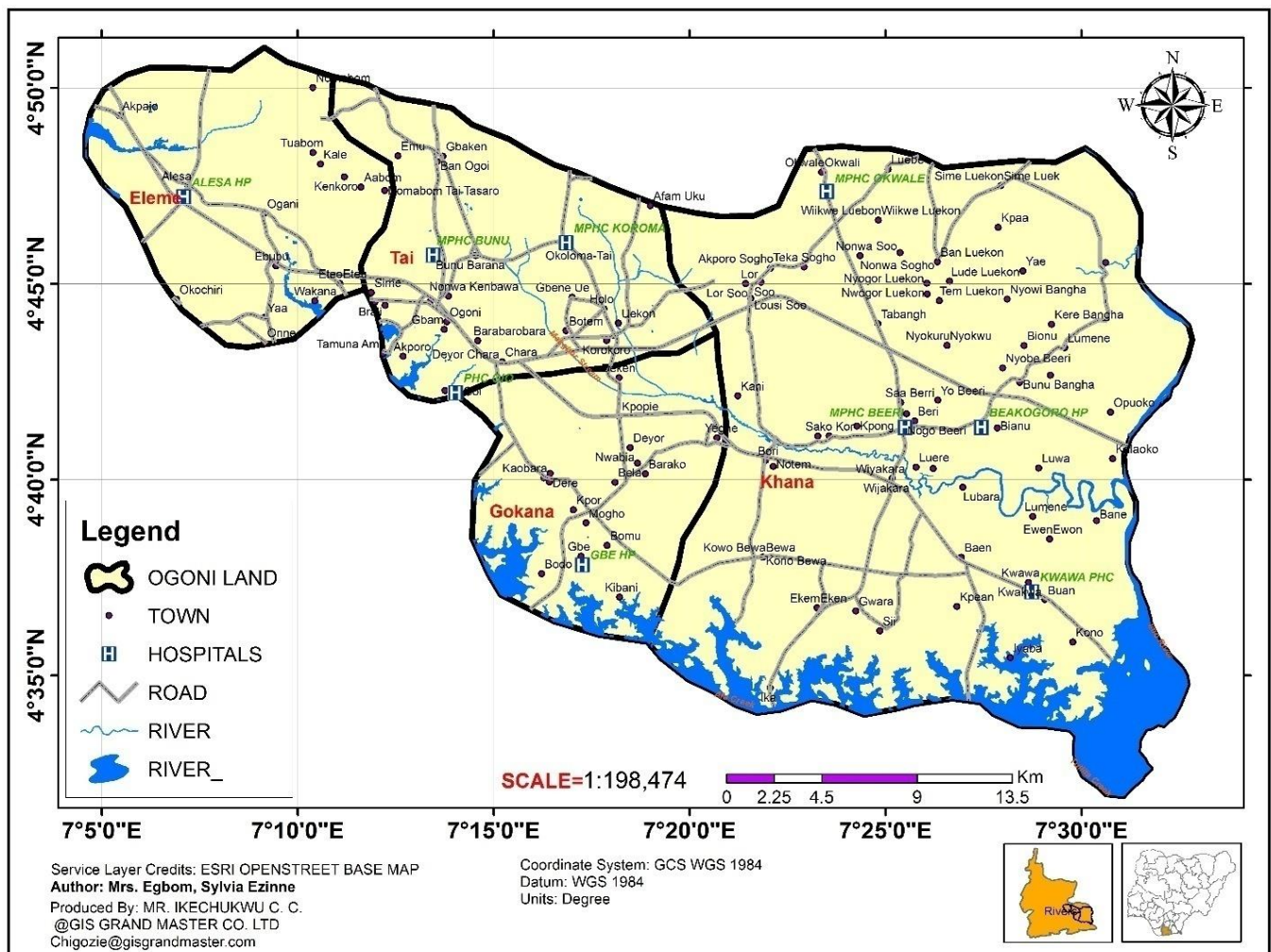


Figure 1. Location Map of Ogoni Land

2.2 Research design and data collection

The geographic coordinates of all the PHCs in Ogoni Land were obtained using a handheld Garmin eTrex 30x Global Positioning System (GPS). A cross-sectional hospital-based study was conducted at nine selected PHCs using a systematic grid-point sampling method (Oluwole *et al.*, 2018). Blood samples were obtained through venipuncture from a total of 318 individuals using a stratified random sampling technique. This study involved 318 patients (irrespective of gender or age) seeking medical care in the selected PHCs. Ethical clearance to undertake this research was obtained from the University of Port Harcourt Health Research Ethics Committee (UPH/CEREMAD/REC/MM77/020) and Rivers State Ministry of Health (MH/PRS/391/VOL.2/438). Verbal consent was obtained from the participants and caregivers who enrolled for the study. A cloud-free Landsat-8 Operational Land Imager (OLI) was downloaded from the United States Geological Survey (USGS) Earth Explorer website. Landsat scene downloaded for the study area has path 188 and row 057 World Reference System (WRS).

2.3 Data Analysis

Data collected from the field were cleaned and datasets were developed. All data were entered into Microsoft Excel Version and analysed using IBM SPSS Version 26. Data obtained were presented in tables. Additionally, geographic coordinates and malaria prevalence data were computed into Microsoft Excel 2016 and imported into the GIS database. Spatial queries were performed using Boolean Operation in the ArcGIS environment. The Environmental System Research Institute (ESRI) ArcGIS 10.7 software was used to compute the spatial and aspatial datasets collected from the field to further display, analyse, query and model information from the results generated in the GIS software. Point prevalence and thematic maps of the study area were produced. LandSat_8 (OLI/TIRS) band 6, band 5 and band 2 were used to generate the composite band using an agricultural renderer. The composite band was used to perform unsupervised image classification. The data was further used to delineate training samples for supervised image classification into five (5)

classes: waterbodies, bare soil, built-up regions, sparse vegetation and dense vegetation. The extent of these classes was extracted using the Calculate Geometry Attributes tool. The various areas occupied by the 4 LGAs were extracted and exported as an Excel file for correlation analysis. *Pearson correlation was carried out to determine the significance between malaria prevalence and land cover classes.*

3. Results

3.1 Prevalence of malaria at the various Primary Health Care facilities

Out of the 318 individuals examined, 169 (51.3%) were infected (Table 1). The highest prevalence (75%) was recorded at Model Primary Healthcare Centre Koroma in Tai LGA, followed by Kwawa PHC (62%) and Beakogoro HP (59.09%). MPHOC Okwale recorded the lowest prevalence of 39.54%. However, no significant statistical relationship was found between malaria and facilities ($p > 0.05$).

Table 1. Prevalence of malaria at the various PHCs

LGA	PHC	No examined	No infected (%)	Point Prevalence (%)	Overall prevalence (%)
Khana	Kwawa PHC	50	31	62	9.748
Khana	MPHC Beeri	39	17	43.59	5.346
Khana	Beakogoro HP	44	26	59.09	8.176
Khana	MPHC Okwale	43	17	39.54	5.346
Gokana	Gbe HP	40	22	55	6.918
Eleme	Alesa HP	23	12	52.17	3.774
Tai	MPHC Bunu	21	10	47.62	3.145
Tai	MPHC Koroma	16	12	75	3.774
Tai	PHC Gio	42	22	52.38	6.918
	Total	318	169		

($\chi^2 = 10.228$; $P = 0.249$)

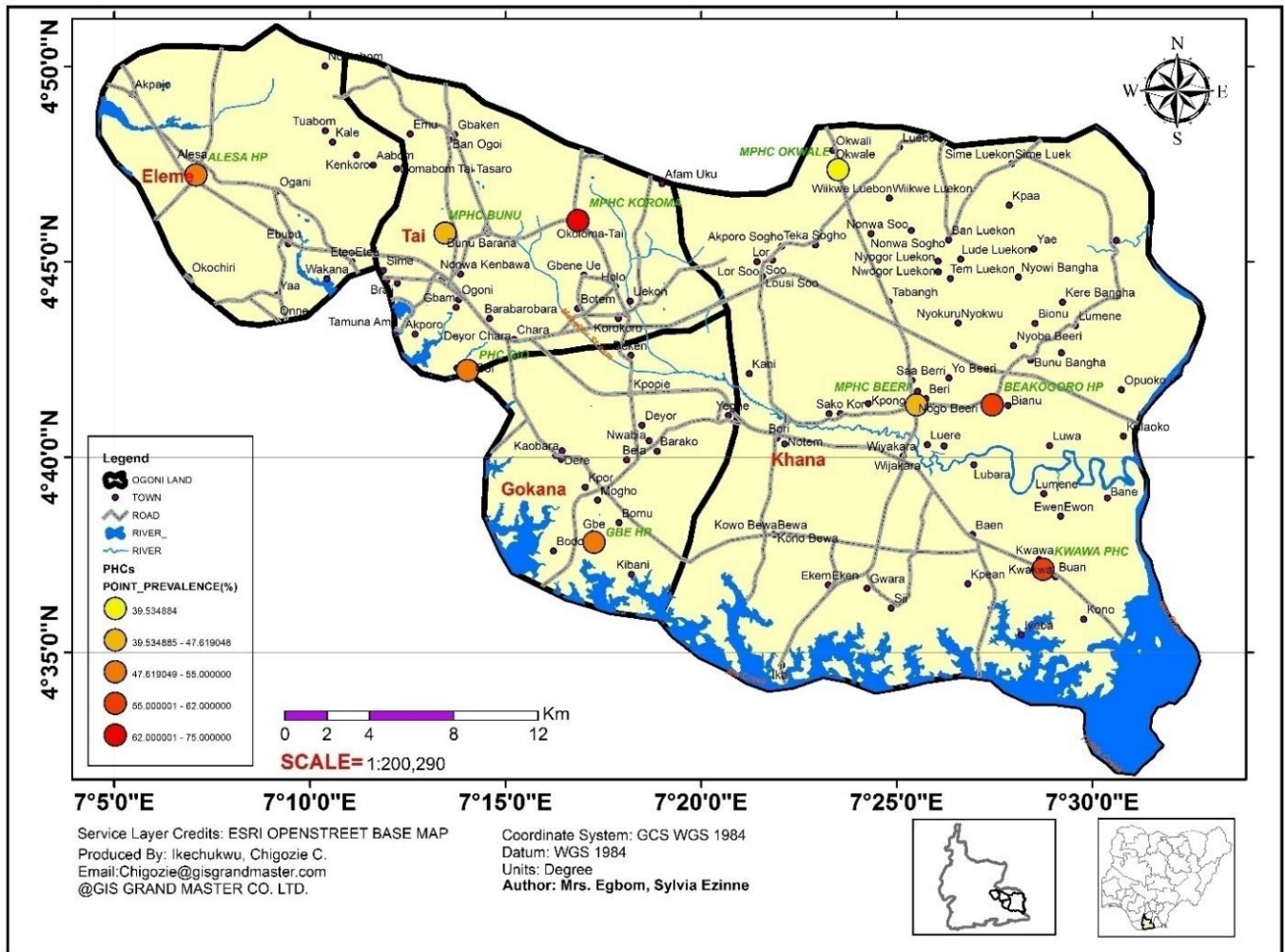


Figure 2. Point prevalence map of malaria in the study area

3.2 Prevalence of Malaria across the LGAs

Table 2 presents the prevalence of malaria across the LGAs in Ogoni Land during the study period. Khana LGA recorded the highest overall prevalence of 28.6% while Eleme LGA recorded the lowest prevalence of 3.8%. No significant statistical relationship was found between malaria and LGA ($p > 0.05$).

Table 2. Prevalence of malaria across the LGAs in Ogoni land

LGA	No examined(%)	No infected	Overall prevalence (%)
Khana	176(55.3)	91	28.6
Gokana	40(12.6)	22	6.9
Eleme	23(7.2)	12	3.8
Tai	79(24.8)	44	13.8
Total	318	169	53.1

$\chi^2 = 0.417; P = 0.937$

The prevalence map of malaria distribution in Ogoni Land during the study is shown in Figure 3.

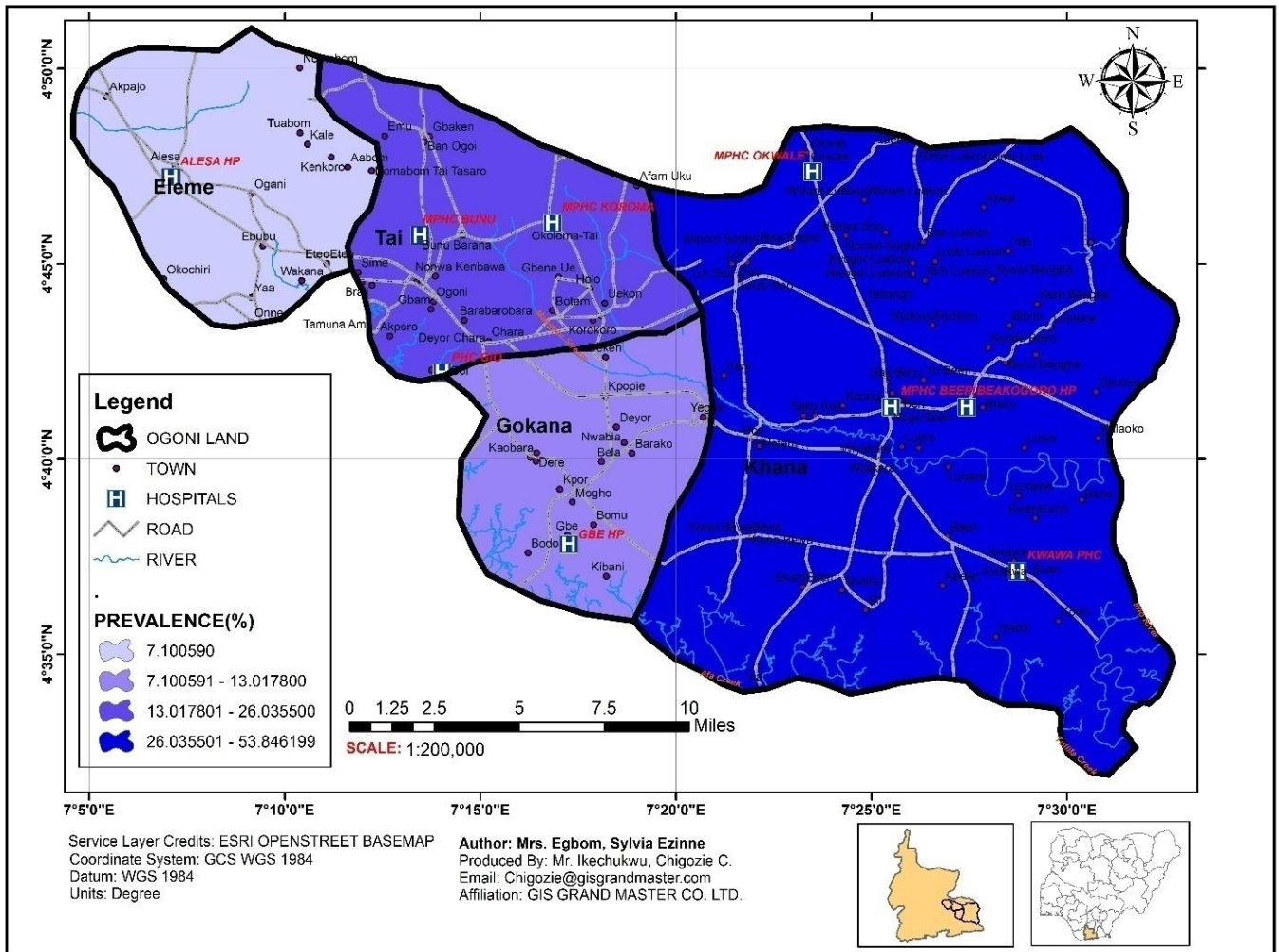


Figure 3. Map of malaria prevalence in Ogoni Land during the study

3.3 Land Cover Analysis of Ogoni Land

Table 3 illustrates the land cover analysis of the study area and Figure 4 shows the land cover map. Land cover analysis revealed that the area of Ogoni Land is 982.97km², which is composed of waterbodies, bare soil, sparse vegetation, dense vegetation and built-up regions with an area of 33.18km², 208.27km², 471.06km², 213.1km² and 57.33km² respectively. The sparse vegetation dominates the study area with 471.06km², followed by dense

vegetation with 213.1km². Khana LGA covers the largest area of 560.36km², whereas Gokana LGA covers the least with 125.94km². The impact of land cover on malaria prevalence during the study period was assessed using correlation analysis. Dense vegetation demonstrated a highly positive significant correlation with malaria (p=0.048, R²=0.952). Meanwhile, sparse vegetation showed an insignificant positive correlation with malaria (p=0.154, R²=0.846).

Table 3. Land cover analysis of Ogoniland

LGA	Waterbody (km ²)	Bare soil (km ²)	Sparse vegetation (km ²)	Dense vegetation (km ²)	Built up regions (km ²)	Total (km ²)
Khana	22.04	56.59	303.34	168.97	9.40	560.36
Gokana	8.48	45.74	44.85	18.35	8.51	125.94
Eleme	1.75	9.94	89.23	4.10	33.06	138.08
Tai	0.91	96.00	33.64	21.68	6.36	158.59
Total	33.18	208.27	471.06	213.1	57.33	982.97

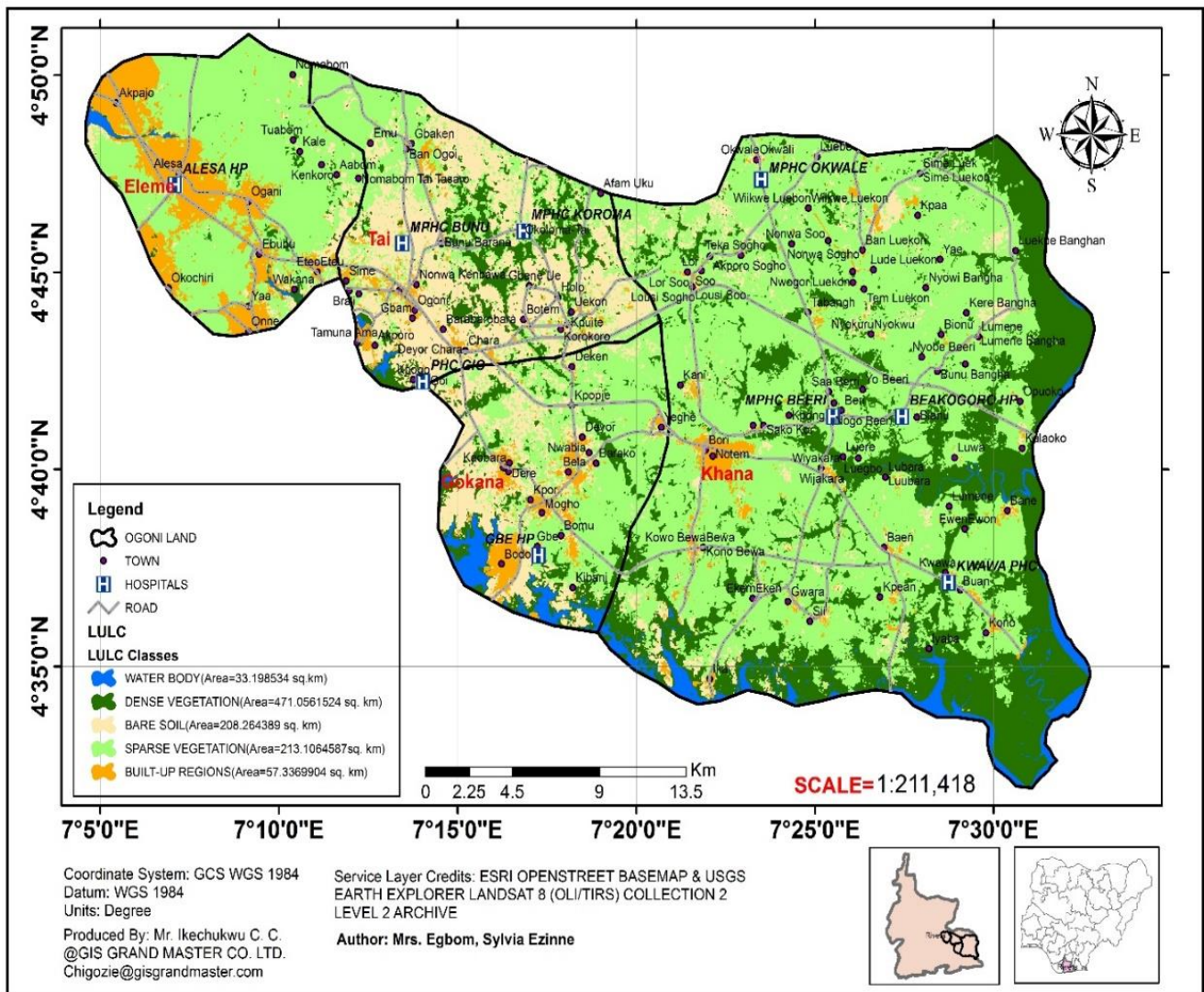


Figure 4. Land cover map of Ogoni Land

4. Discussion

An overall malaria prevalence of 51.3% was reported in the study area. This finding agrees with the numbers reported in Rivers State by Egbom and Nzeako (2017), Egbom *et al.* (2021) and Egbom *et al.* (2022), which were 52.5%, 57.4% and 56.3%, respectively. Additionally, the number was higher than that of previous reports in other parts of the State. Wogu and Nduka (2016) and Wogu *et al.* (2017) recorded a prevalence of 32% and 43.1%, respectively in Port Harcourt. However, the observed prevalence in different study areas in the State was lower than the numbers reported by Wokem *et al.* (2017) and Augustine-D’Israel and Abah (2018), which were 87% and 78%, respectively. The lower malaria prevalence obtained in this research when compared with the higher prevalence reported by Wokem *et al.* (2017) and Augustine- D’Israel and Abah (2018) could be ascribed to the increased level of awareness about malaria and its intervention strategies among the population. However, the prevalence is still high.

P. falciparum was the only species of malaria parasite recorded in this study. This finding agrees with the reports from Abah *et al.* (2017), Wogu and Onosakponome (2021), Egbom *et al.* (2021) and Egbom *et al.* (2022) who observed only *P. falciparum*. In contrast, Nzeako *et al.* (2013) reported the presence of *Plasmodium vivax* along with *P.falciparum*. The authors argued that the presence of *P. vivax* in the Delta region could be due to the presence of non-African people since the region is a hub for the petroleum industry that attracts many expatriates.

The study demonstrated spatial variations in the geographic distribution of malaria in Ogoni Land. Remote sensing of the environment in Ogoni Land used in this study provides valuable information for explaining the geographic variations of malaria. The highest prevalence was recorded in Khana LGA which has the largest area of dense vegetation. Bivariate analysis revealed that

the disease patterns showed a positive correlation with dense vegetation, which may account for the observed spatial variations.

It can be concluded that spatial variation in malaria prevalence observed in the study is influenced by varying land cover classes, with a high prevalence linked with the presence of dense vegetation. The findings in this study agree with the previous reports by Adlaoui *et al.* (2011), Machault *et al.* (2012), Kabaria *et al.* (2016), Olalubi *et al.* (2020) and Awosolu *et al.* (2021) who reported a positive relationship between malaria prevalence and vegetation. However, the findings contradict the previous findings by Paul *et al.* (2018), who found no statistically significant correlation between malaria and land use patterns. The findings also disagree with Kigozi *et al.*, (2016) who reported a negative relationship between vegetation and malaria prevalence. Additionally, studies done by Adimi *et al.* (2010), Zinszer *et al.* (2012) and Ricotta *et al.* (2014) have associated vegetation with malaria incidence.

Mosquito survival and foraging are key elements in the general epidemiology of malaria (Ricotta *et al.* 2014). Vegetation provides outdoor resting locations for malaria vectors (Bassene *et al.*, 2020). Plant sugars also provide sufficient energy for male mosquitoes to efficiently fertilize females thus guaranteeing species perpetuity (Stone *et al.*, 2009). Research has shown that some plants provide mosquitoes with readily available meals thereby increasing their life span and decreasing contact with humans (Nikbakhtzadeh *et al.*, 2014). Therefore, vegetation plays a prominent role in the survival of mosquito vectors in their innate environment.

5. Conclusion

This study has provided prevalence statistics and spatial distribution maps of malaria in the study area. The findings confirm that malaria remains a public health burden in the study area. The observed malaria distribution patterns in this study are influenced by land cover classes with a significant positive correlation between dense vegetation and malaria prevalence. The hybrid of GIS and remote sensing has established a link between malaria and land cover, thereby explaining the observed spatial distribution patterns. These findings will aid in the deployment of appropriate malaria interventions to places most in need and in the development of an environmental management approach for malaria control to address the menace at local scales.

6. References

- Abah A.E., Awi-Waadu G. D. B., Nduka F.O. and Richard A. (2017). Malaria infection and socioeconomic status of some residents of Port Harcourt metropolis, Rivers State, Nigeria. *Journal of Applied Sciences and Environmental Management*; **21** (2): 299-304.
- Abiodun, G.J., Maharaj, R., Witbooi, P. and Okosun, K.O. (2016). Modelling the influence of temperature and rainfall on the population dynamics of *Anopheles arabiensis*. *Malaria Journal*, **15**:364.
- Adeola, A.M., Botai, J.O., Olwoch, J.M., de W Rautenbach, H.C.J., Kalumba, A.M., Tsela, P.L., Adisa, M.O., Wasswa, N.F., Mmtoni, P. and Ssentongo, A. (2015). Application of geographical information system and remote sensing in malaria research and control in South Africa: a review. *Southern African Journal of Infectious Diseases*, **30**:4: 114-121 DOI: 10.1080/23120053.2015.1106765
- Adimi, F., Soebiyanto, R.P., Safi, N. and Kiang, R. (2010). Towards malaria risk prediction in Afghanistan using remote sensing. *Malaria Journal*, **9**:125.
- Augustine- D'Israel, E. and Abah, A.E. (2018). Malaria infection among persons patronizing drugstores for malaria treatment in Port Harcourt and its environs Rivers, State Nigeria. *International Research Journal of Public Health*, **2**:20.
- Awosolu, O.B., Yahaya, Z.S., Farah, Haziqah, M.T., Simon-Oke, I.A. and Fakunle, C. (2021). A cross-sectional study of the prevalence, density and risk factors associated with malaria transmission in urban communities of Ibadan, southwestern Nigeria. *Heliyon*, **20** (7): e05975
- Ayanlade, A., Adeoye, N.O. and Babatimehin, O. (2013). Intra-annual climate variability and malaria transmission in Nigeria. *Bulletin of Geography. Socio-economic Series*, **21**: 7–19.
- Ayo, V. O., Obafemi, A. and Ogoro, M. (2017). Mapping Land Cover Determinants of Malaria in Obio-Akpor Local Government of Rivers State, Nigeria. *IOSR Journal of Humanities and Social Science*, **22** (6): 29-40. DOI: 10.9790/0837-2206042940.
- Bassey, S.E. and Izah, S.C. (2017). Some determinant factors of Malaria Prevalence in Nigeria. *Journal of Mosquito Research*, **7**(7): 48-58.
- Bassene, H., Niang, E.H.A., Fenollar, F., Fenollar, F., Doucoure, S., Faye, O., Raoult, D., Sokhna, C. and Mediannikov, O. (2020). Role of plants in the transmission of *Asaia* sp., which potentially inhibit the *Plasmodium* sporogonic cycle in *Anopheles* mosquitoes. *Scientific Reports*, **10**: 7144 (2020). <https://doi.org/10.1038/s41598-020-64163-5>
- Coleman, M., Mabuza, A.M., Kok, G., Coetzee, M. and Durrheim, D.N. (2009). Using the SaTScan method to

- detect local malaria clusters for guiding malaria control programmes. *Malaria Journal*, **8**:68.
- Egbom, S.E. and Nzeako, S.O. (2017). Malaria parasitaemia amongst military personnel households in a military formation in Port Harcourt, Nigeria. *International Journal of Scientific Research in Environmental Sciences*; **5** (1):0010-0016.
- Egbom, S.E., Ogidi, M., Nduka, F.O. and Nzeako, S.O (2021). Malaria prevalence and its demographic determinants in Oyigbo LGA, Rivers State, South south Nigeria. *Asian Journal of Biology*, **12** (4): 26-33.
- Egbom, S.E., Nduka, F.O., Nzeako, S.O., (2022). Point-Prevalence Mapping of Malaria in Rivers State, Nigeria. *Tanzania Journal of Health Research*, **23** (4):1-9
- Feng, J., Zhang, L., Huang, F., Yin, J., Tu, H., Xia, Z., Zhou, S., Xiao, N. and Zhou, X. (2018). Ready for malaria elimination: zero indigenous case reported in the People's Republic of China. *Malaria Journal*, **17**: 315
- Hay, S.I. and Snow, R.W. (2006). The Malaria Atlas Project: developing global maps of malaria risk. *PLoS Med*, **3**:e473
- Kabaria, C.W., Molteni, F., Mandike, R., Chacky, F., Noor, A.M., Snow, R.W. and Linard, C. (2016). Mapping intra-urban malaria risk using high resolution satellite imagery: a case study of Dar es Salaam. *International Journal of Health Geographics*, **15**:26. DOI 10.1186/s12942-016-0051-y
- Kigozi, R., Zinszer, K., Mpimbaza, A., Sserwanga, A., Kigozi, S.P. and Kanya, M. (2016). Assessing temporal associations between environmental factors and malaria morbidity at varying transmission settings in Uganda. *Malaria Journal*, **15**:511. DOI 10.1186/s12936-016-1549-2
- Machault, V., Vignolles, C., Pages, F., Gadiaga, L., Tourre, Y.M., Gaye, A., Sokhna, C., Trape, J.F., Lacaux, J.P. and Rogier, C. (2012). Risk mapping of *Anopheles gambiaes.l* densities using remotely-sensed environmental and meteorological data in an urban area: Dakar, Senegal. *PLoS ONE*, **7**(11):e50674.
- Ndiaye A, Niang E.H.A., Diène, A.N., Nourdine, M.A., Sarr, P.C., Konate, L., Faye, O., Gaye, O. and Sy, O. (2020). Mapping the breeding sites of *Anopheles gambiae s. l* in areas of residual malaria transmission in central western Senegal. *PLoS ONE*, **15** (12): e0236607. <https://doi.org/10.1371/journal.pone.0236607>.
- Nikbakhtzadeh, M. R., Terbot, J. W. 2nd, Otienoburu, P. E. & Foster, W. A. (2014). Olfactory basis of floral preference of the malaria vector *Anopheles gambiae* (Diptera: Culicidae) among common African plants. *Journal of Vector Ecology: Journal of The Society for Vector Ecology*, **39**: 372–383. <https://doi.org/10.1111/jvec.12113>.
- Nmadu P. M., Peter E., Alexander P., Koggie A. Z., Maikenti J. I., (2015). The Prevalence of Malaria in Children between the Ages 2-15 Visiting Gwarinpa General Hospital Life-Camp, Abuja, Nigeria. *Journal of Health Science*, **5**(3): 47-51.
- Ngom, R., and Siegmund, A. (2015). The key role of socio-demographic and socioenvironmental factors in urban malaria occurrence and control - An illustration using the city of Yaoundé. *Social Science and Medicine*, **133**:269–79.
- Nzeako SO, Nduka FO and Origie OA. (2013). Prevalence of malaria in pregnant women attending ante natal care at University of Port Harcourt Primary Health Care Centre Aluu, Port Harcourt, Rivers State, Nigeria. *International Journal of Scientific Research in Environmental Sciences*, **1** (10): 268-272
- Okogun, .G.R.A. Life table analysis of Anopheles malaria vectors: Generational mortality as tool in mosquito vector abundance and control studies. *J Vec Borne Dis*. 2005;**42**: 45-53
- Okunlola, O.A. and Oyeyemi, O.T. (2019). Spatio-temporal analysis of association between incidence of malaria and environmental predictors Of malaria transmission in Nigeria. *Scientific Reports*, **9**:17500.
- Onyiri, N. (2015). Estimating Malaria Burden in Nigeria: A Geostatistical Modelling Approach. *Geospatial Health*, **10**(2):306.
- Oluwole, A.S., Adeniran, A.A., Mogaji, H.O., Olabinke, D.B., Abe, E.M., Bankole, S.O., Sam-Wobo, S.O. and Ekpo, U.F. (2018). Prevalence, intensity and spatial co-distribution of schistosomiasis and soil transmitted helminths infections in Ogun state, Nigeria. *Parasitology Open*, **4**(e8): 1–9.
- Palaniyandi, V., Anand, P.H., Maniyosai, R., Mariappan, T. and Das, P.K. (2016). The integrated remote sensing and GIS for mapping of potential vector breeding habitats, and the Internet GIS surveillance for epidemic transmission control, and management. *Journal of Entomology and Zoological Studies*, **4** (2): 310-31.
- Pam, DD, Omalu ICJ, Akintola AA, Dan Azumi Y, Kalesanwo AO, Babagana M, Muhammad SA, Ocha IM, Adeniyi KA.

- The Role of GIS And Remote Sensing in the Control of Malaria. *Online J Health Allied Scs.* 2017;16(3):7.
- Paul, P., Kangalawe, R.Y.M. and Mboera, L.E.G. (2018). Land-use patterns and their implication on malaria transmission in Kilosa District, Tanzania. *Travel Medicine and Vaccines*,4:6. <https://doi.org/10.1186/s40794-018-0066-4>
- Ricotta, E.E., Frese, S.A., Choobwe, C., Louis, T.A. and Shiff, C.J. (2014). Evaluating local vegetation cover as a risk factor for malaria transmission: a new analytical approach using ImageJ. *Malaria Journal*, **13** (94):1–7.
- Stone, C. M., Taylor, R. M., Roitberg, B. D. & Foster, W. A. (2009). Sugar deprivation reduces insemination of *Anopheles gambiae* (Diptera: Culicidae), despite daily recruitment of adults, and predicts decline in model populations. *Journal of Medical Entomology*,46:1327–1337. <https://doi.org/10.1603/033.046.0611>.
- Sato, S. (2021). *Plasmodium*: A brief introduction to the parasites causing human malaria and their basic biology. *Journal of Physiological Anthropology*, **40**:1
- Weiss, D.J., Lucas, T.C.D., Nguyen, M., Nandi, A.K., Bisanzio, D., Battle, K.E., *et al.*, (2019). Mapping the global prevalence, incidence, and mortality of *Plasmodium falciparum*, 2000–17: a spatial and temporal modelling study. *Lancet*, **394**:322–31.
- Wogu, M. N., Nduka, F. O. and Wariso, K. T. (2017). Prevalence of uncomplicated and severe malaria in outpatients of a tertiary hospital in Rivers State, Nigeria. *Journal of Applied Life Sciences International*, **15** (3): 1-5.
- Wogu, M.N. and Nduka, F.O. (2016). Malaria parasitaemia among outpatients of Braithwaite Memorial Specialist Hospital (BMSH) Rivers State, Nigeria. *International Journal of Scientific and Research Publications*,6 (11): 60-62
- Wogu, M. and Onosakponome, E.O. (2021). Evaluating prevalence and misdiagnosis of plasmodium using microscopy compared with polymerase chain reaction technique in two tertiary care hospitals in Rivers State, Nigeria. *International Journal of Infection.*; **8**(1): e109411. doi: 10.5812/iji.109411
- Wokem, G.N., Christian, S.G. and Onuegbu, B. (2017). Prevalence, Attitude and Perception about Malaria in a Rural Setting in Rivers State, Nigeria. *Sokoto Journal of Medical Laboratory Science*; **2**(3): 167 – 174.
- Ye, Y., Louis, V.R., Simboro, S. and Sauerborn, R. (2007). Effect of meteorological factors on clinical malaria risk among children: an assessment using village-based meteorological stations and community-based parasitological survey. *BMC Public Health*,7:101.
- Zinszer, K., Verma, A.D., Charland, K., Brewer, T.F., Brownstein, J.S., Sun, Z. and Buckeridge, D.L. (2012). A scoping review of malaria forecasting: past work and future directions. *BMJ Open*, 2:e001992.